



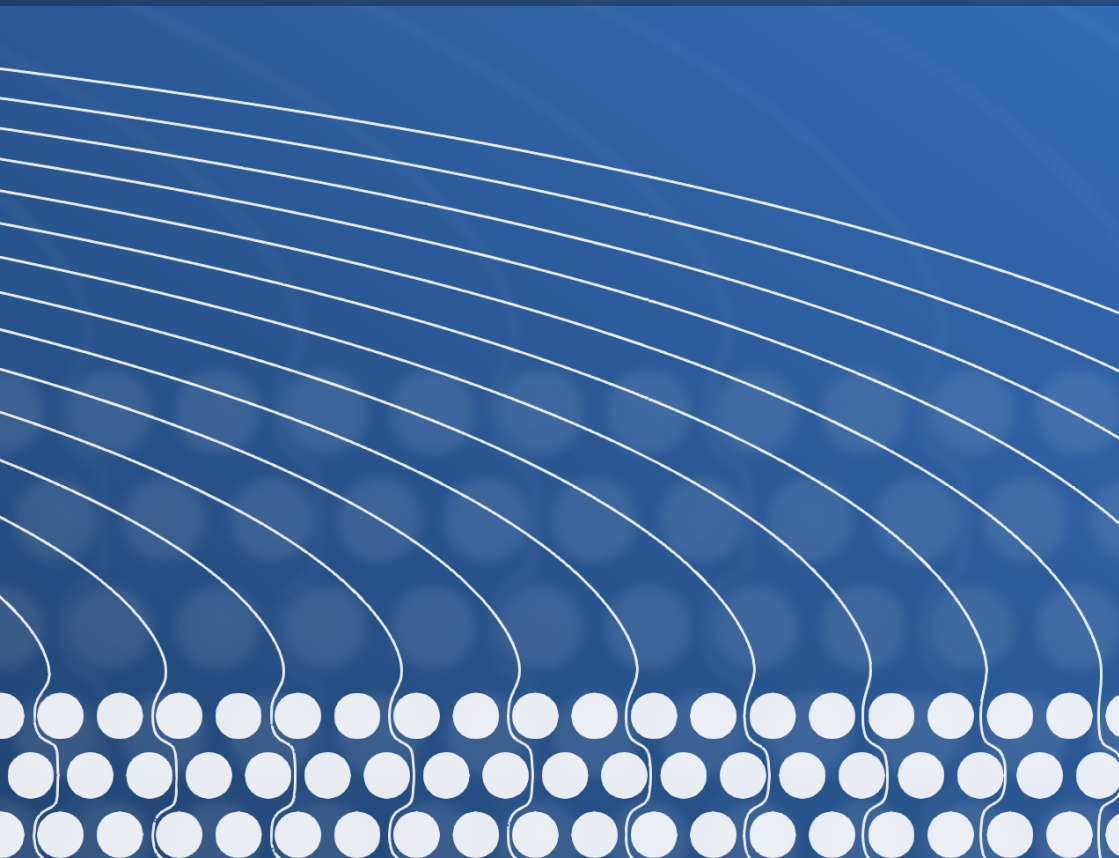
University of Stuttgart  
Germany



SFB 1313

# Interface Conditions for Arbitrary Flows in Stokes–Darcy Systems: Derivation, Analysis and Validation

Elissa Eggenweiler





# **Interface Conditions for Arbitrary Flows in Stokes–Darcy Systems: Derivation, Analysis and Validation**

Von der Fakultät Mathematik und Physik und dem  
Stuttgarter Zentrum für Simulationswissenschaft (SC SimTech)  
der Universität Stuttgart zur Erlangung der Würde eines  
*Doktors der Naturwissenschaften (Dr. rer. nat.)*  
genehmigte Abhandlung

vorgelegt von

**Maxi Elissa Zita Eggenweiler**

aus Stuttgart

Hauptberichterin:

PD Dr. Iryna Rybak

Mitberichter:

Dr. Marco Discacciati

Prof. Dr. Ben Schweizer

Tag der mündlichen Prüfung: 14. Oktober 2022

Institut für Angewandte Analysis und Numerische Simulation,  
Universität Stuttgart

2022



**University of Stuttgart**  
Germany



**SFB 1313**

Interface-Driven Multi-Field  
Processes in Porous Media



## **Acknowledgements**

This work was funded by the Deutsche Forschungsgemeinschaft (DFG, German Research Foundation) Project Number 327154368 – SFB 1313.

# Contents

<b>Abstract</b>	vii
<b>Nomenclature</b>	xi
<b>1 Introduction</b>	3
<b>2 State of the art</b>	13
2.1 Mathematical modeling of coupled problems . . . . .	13
2.1.1 Pore-scale model . . . . .	15
2.1.2 Subdomain models . . . . .	16
2.1.3 Coupling concepts . . . . .	18
2.2 Analysis, numerical methods and validation of Stokes– Darcy problems . . . . .	28
2.2.1 Well-posedness . . . . .	28
2.2.2 Numerical methods . . . . .	31
2.2.3 Model validation . . . . .	37
2.3 Homogenization and boundary layer theory . . . . .	40
2.3.1 Nondimensionalization . . . . .	41
2.3.2 Periodic homogenization: Darcy’s law . . . . .	44
2.3.3 Boundary layer theory: Interface conditions for unidirectional flows . . . . .	60

<b>3</b>	<b>Generalized interface conditions</b>	75
3.1	Derivation of interface conditions via homogenization and boundary layers . . . . .	76
3.1.1	Step 1: Geometrical setting and pore-scale model	78
3.1.2	Step 2: First approximations of pore-scale velocity and pressure . . . . .	80
3.1.3	Step 3: Improvement of first approximations . . .	84
3.1.4	Step 4: Leading order approximations and interface conditions . . . . .	109
3.2	Practical aspects . . . . .	110
3.2.1	Dimensional formulation . . . . .	111
3.2.2	Effective coefficients and interface location . . .	112
3.2.3	Comparison of generalized coupling conditions to classical ones . . . . .	120
<b>4</b>	<b>Numerical methods for coupled problems</b>	127
4.1	Pore-scale model . . . . .	127
4.1.1	Discretization scheme and solution strategy . . .	128
4.1.2	Averaging of pore-scale solutions . . . . .	131
4.2	Macroscale model . . . . .	133
4.2.1	Discretization scheme . . . . .	134
4.2.2	Monolithic approach . . . . .	146
4.3	Computation of effective properties . . . . .	147
<b>5</b>	<b>Analysis of the Stokes–Darcy problem with generalized interface conditions</b>	157
5.1	Problem setting and weak formulation . . . . .	158
5.1.1	Problem setting . . . . .	158
5.1.2	Weak formulation of the coupled problem . . . .	160
5.2	Well-posedness . . . . .	164
5.2.1	Auxiliary results . . . . .	165
5.2.2	Well-posedness of the coupled problem . . . . .	166
5.3	Numerical study of theoretical result . . . . .	171

---

<b>6</b>	<b>Model validation</b>	179
6.1	Classical coupling conditions for unidirectional flows to the interface . . . . .	184
6.1.1	Pressure driven flow . . . . .	185
6.1.2	Lid driven cavity over porous bed . . . . .	194
6.1.3	Forced infiltration . . . . .	203
6.2	Classical coupling conditions for arbitrary flows to the interface . . . . .	207
6.2.1	Filtration through T-shaped domain . . . . .	208
6.2.2	General filtration problem . . . . .	221
6.3	Generalized coupling conditions . . . . .	226
6.3.1	Pressure driven flow . . . . .	227
6.3.2	Double lid driven cavity over porous bed . . . . .	235
6.3.3	General filtration problem . . . . .	241
<b>7</b>	<b>Conclusions and perspectives</b>	255
<b>A</b>	<b>Appendix</b>	261
A.1	Functional spaces and norms . . . . .	261
A.2	Inequalities . . . . .	264
A.3	Lax–Milgram theorem . . . . .	266
	<b>Publications by the author</b>	267
	<b>Bibliography</b>	269





## Abstract

Coupled free-flow and porous-medium flow systems occur in nature as well as in a wide range of technical applications, for example, groundwater filtration or water management in fuel cells. The free flow is typically described by the Stokes equations and the flow through the porous medium by Darcy's law. One of the major challenges in modeling such flow systems is the accurate coupling of both mathematical models across the fluid-porous interface. Traditional coupling concepts are developed for unidirectional flows, parallel or perpendicular to the porous layer, however, they are not applicable if arbitrary flow directions occur, such as in industrial filtration. This fact significantly restricts the amount of applications that can be accurately modeled. Therefore, new interface conditions accounting for arbitrary flows in Stokes-Darcy systems are needed.

In this dissertation, we develop generalized coupling conditions that are valid for arbitrary flow directions to the fluid-porous interface. These conditions are rigorously derived using homogenization with two-scale asymptotic expansions and boundary layer theory. All coefficients appearing in the generalized interface conditions are computed based on the pore geometry in the vicinity of the interface. This is a great advantage over the traditionally applied coupling conditions, which are limited to unidirectional flows and contain unknown model parameters that must be fitted before the conditions can be used in numerical simulations. We derive the variational formulation of the Stokes-Darcy problem with the newly derived coupling conditions and prove existence and uniqueness of a weak solution. We develop a finite volume discretization scheme to solve the coupled problem numerically and employ finite element methods to compute all effective model parameters and to solve the pore-scale problem. To validate the generalized coupling conditions we compare microscale and macroscale numerical simulation results. We demonstrate that the derived interface conditions are more accurate than the classical conditions in case of unidirectional flows, and that they are valid in

case of arbitrary flow directions to the interface, whereas the classical conditions fail.

## Zusammenfassung

Gekoppelte Systeme von freier Strömung und Strömung durch poröses Medium kommen sowohl in der Natur als auch in einer Vielzahl von technischen Anwendungen vor, beispielsweise bei der Grundwasserfiltration oder der Wasserfiltration in Brennstoffzellen. Die freie Strömung wird üblicherweise durch die Stokes-Gleichungen beschrieben und die Strömung durch das poröse Medium mithilfe des Darcy-Gesetzes. Eine der größten Herausforderungen bei der Modellierung solcher Strömungssysteme ist die physikalisch korrekte Kopplung der beiden mathematischen Modelle an der Grenzfläche zwischen freier Strömung und poröser Schicht. Traditionelle Kopplungskonzepte wurden für unidirektionale Strömungen entwickelt, die parallel oder senkrecht zur Grenzfläche verlaufen. Allerdings sind diese Konzepte nicht für beliebige Strömungsrichtungen, welche zum Beispiel bei industriellen Filtrationsprozessen auftreten, anwendbar. Diese Tatsache beschränkt die Anwendungsmöglichkeiten erheblich. Daher werden neue Kopplungsbedingungen für Stokes–Darcy-Probleme benötigt, die für beliebige Strömungsrichtungen gültig sind.

In dieser Dissertation entwickeln wir verallgemeinerte Kopplungsbedingungen, die für Strömungen mit beliebiger Richtung zur Grenzfläche zwischen freier Strömung und porösem Medium gelten. Diese Bedingungen werden mithilfe von Homogenisierung und der Grenzschichttheorie rigoros hergeleitet. Die Koeffizienten, die in den verallgemeinerten Kopplungsbedingungen erscheinen, werden anhand der Porengeometrie in der Nähe der Grenzfläche berechnet. Dies ist ein enormer Vorteil gegenüber den traditionell verwendeten Kopplungsbedingungen, die auf unidirektionale Strömungen beschränkt sind und unbekannte Modellparameter enthalten, welche bestimmt werden müssen bevor die Bedingungen in numerischen Simulationen verwendet werden können. Wir leiten die

schwache Formulierung des Stokes–Darcy-Problems mit den neu entwickelten Kopplungsbedingungen her und beweisen Existenz und Eindeutigkeit einer schwachen Lösung. Zur numerischen Lösung des gekoppelten Problems entwickeln wir eine Finite-Volumen-Diskretisierung und zur Berechnung der effektiven Modellparameter sowie zur Lösung des Porenskalenproblems verwenden wir die Finite-Elemente-Methode. Um die verallgemeinerten Kopplungsbedingungen zu validieren, vergleichen wir numerische Simulationsergebnisse auf der Poren- und Makroskala. Wir zeigen, dass die hergeleiteten Kopplungsbedingungen präziser sind als die klassischen Bedingungen im Falle unidirektionaler Strömungen und, dass sie für beliebige Strömungsrichtungen zur Grenzfläche geeignet sind, im Gegensatz zu den klassischen Kopplungsbedingungen.



# Nomenclature

## Abbreviations

$Fr$	Froude number
$Re$	Reynolds number
DD	domain decomposition
DG	discontinuous Galerkin
FEM	finite element method
FVM	finite volume method
LBM	lattice Boltzmann method
MPFA	multipoint flux approximation
PDE	partial differential equation
REV	representative elementary volume

## Greek letters

$\alpha_{\text{BJ}}$	Beavers–Joseph parameter
$\alpha_{\text{BJ}}^{\text{opt}}$	optimal value of the Beavers–Joseph parameter
$\Gamma$	subset of $\partial\Omega$ , i.e., $\Gamma \subset \partial\Omega$
$\gamma$	vertical position of interface $\Sigma$
$\varepsilon$	scale separation parameter/nondimensional characteristic pore size, $\varepsilon = \ell/\mathcal{L}$
$\mu$	dynamic viscosity
$\rho$	mass density
$\Sigma$	sharp fluid–porous interface
$\Sigma_{\text{bot}}$	interface between transition zone and porous medium

$\Sigma_{\text{top}}$	interface between transition zone and free-flow region
$\boldsymbol{\tau}$	unit tangential vector on $\Sigma$
$\phi$	porosity
$\boldsymbol{\varphi}$	vector-valued test function
$\varphi$	scalar-valued test function
$\Omega$	spatial domain

### Roman letters

$a$	distance between interface $S$ and line tangent to first row of solid inclusions
$C$	general positive constant, $C > 0$
$\mathbf{C}$	general constant vector, $\mathbf{C} = (C_1, C_2)$ with $C_1, C_2 > 0$
$\tilde{C}$	positive constant defined in (5.24)
$C_{\text{tr,ff}}$	positive constant from inequality (A2.6)
$C_{\text{tr,pm}}$	positive constant from inequality (A2.7)
$C_{\text{tr},\tau}$	positive constant from inequality (5.20)
$\mathbf{D}$	rate of strain tensor, $\mathbf{D}(\mathbf{v}) = \frac{1}{2} (\nabla \mathbf{v} + (\nabla \mathbf{v})^\top)$
$d$	number of space dimensions
$d^*$	size of solid inclusion in $y_2$ -direction
$d^\varepsilon$	size of solid inclusion within domain $\Omega$ , $d^\varepsilon = \varepsilon d^*$
$\mathbf{e}_i$	Cartesian unit vector for $i = 1, \dots, d$
$\mathbf{f}$	nondimensional external force vector
$\mathcal{G}$	standard value of gravitational acceleration, $\mathcal{G} = 9.80665$ [m · s <sup>-2</sup> ]
$\mathbf{g}$	gravitational acceleration
$H$	height of the porous medium $\Omega_{\text{pm}}$
$h$	height of the free-flow region $\Omega_{\text{ff}}$
$\bar{\mathbf{h}}$	prescribed stress on $\Gamma_{\text{ff},N}$
$H_{\text{tot}}$	total dimensional height of the coupled domain $\Omega_{\text{ff}} \cup \Omega_{\text{pm}}$
$\mathbf{I}$	identity tensor
$\mathbf{K}$	dimensional permeability tensor, $\mathbf{K} = (k_{ij})_{1 \leq i, j \leq d}$
$\tilde{k}$	nondimensional scalar permeability, $\tilde{\mathbf{K}} = \tilde{k} \mathbf{I}$
$\tilde{\mathbf{K}}$	nondimensional permeability tensor, $\tilde{\mathbf{K}} = (\tilde{k}_{ij})_{1 \leq i, j \leq d}$ , given by (2.79)
$L$	nondimensional length of the coupled domain $\Omega_{\text{ff}} \cup \Omega_{\text{pm}}$

$\ell$	dimensional pore size
$\mathcal{L}$	characteristic length scale
$M^{j,\text{bl}}$	boundary layer constant, defined in (3.45)
$M_\omega^{j,\text{bl}}$	boundary layer constant, defined in (3.47)
$\mathbf{n}$	unit normal vector on $\partial\Omega/\Sigma$ pointing outward $\Omega/\Omega_{\text{pm}}$
$\mathbf{N}^{\text{bl}}$	boundary layer constant, defined in (3.23)
$N_s^{\text{bl}}$	boundary layer constant, defined in (3.24)
$p$	fluid pressure
$\bar{p}$	prescribed pressure on $\Gamma_{\text{pm},D}$
$P^\varepsilon$	pressure error function
$r$	radius of solid inclusion within the unit cell $Y$
$r^\varepsilon$	radius of solid inclusion within computational domain $\Omega$ , $r^\varepsilon = \varepsilon r$
$S$	interface within the boundary layer stripe $Z^{\text{bl}}$
$S^\varepsilon$	amount of solid obstacles in the nondimensional setting
$S_a$	interface $S$ positioned at distance $a$ above the solid inclusions
$\mathbf{T}$	general notation for the stress tensor (symmetric/nonsymmetric)
$\mathbf{U}^\varepsilon$	velocity error function
$\mathcal{V}$	characteristic velocity
$\bar{\mathbf{v}}$	prescribed velocity on $\Gamma_{\text{pm},N}$
$\bar{\mathbf{v}}$	prescribed velocity on $\Gamma_{\text{ff},D}$
$\mathbf{v}$	fluid velocity
$W$	dimensional length of coupled domain $\Omega_{\text{ff}} \cup \Omega_{\text{pm}}$
$\mathbf{x}$	(slow) spatial variable
$\mathbf{y}$	(fast) spatial variable, $\mathbf{y} = \mathbf{x}/\varepsilon$
$Y$	unit cell, $Y = (0, 1)^2$
$Y_{\text{f}}$	fluid part of unit cell $Y$
$Y_{\text{s}}$	solid part of unit cell $Y$
$Z^+$	free-flow part of the boundary layer stripe $Z^{\text{bl}}$ , $Z^+ = (0, 1) \times (0, \infty)$
$Z^-$	porous-medium part of the boundary layer stripe $Z^{\text{bl}}$ , $Z^- = Z^{\text{bl}} \setminus Z^+$
$Z^{\text{bl}}$	boundary layer stripe, $Z^{\text{bl}} = Z^+ \cup Z^-$

**Sub- and superscripts**

$a$	qualifier that interface $S_a$ is considered within the boundary layer stripe $Z^{\text{bl}}$
$\text{bl}$	boundary layer qualifier
$D$	Dirichlet boundary condition
$\varepsilon$	pore-scale qualifier in the nondimensional setting
$\text{ff}$	free-flow qualifier
$N$	Neumann boundary condition
$\text{pm}$	porous-medium qualifier
$\text{ps}$	pore-scale qualifier in the dimensional setting

**Other mathematical symbols**

$\nabla_{\mathbf{x}}$	gradient with respect to $\mathbf{x}$
$\nabla_{\mathbf{y}}$	gradient with respect to $\mathbf{y}$
$\nabla \mathbf{v}$	gradient of a vector function $\mathbf{v} \in \mathbb{R}^d, \mathbb{R}^{d \times d} \ni \nabla \mathbf{v} = \left( \frac{\partial v_i}{\partial x_j} \right)_{i,j=1,\dots,d}$
$\nabla \mathbf{v} : \nabla \boldsymbol{\varphi}$	inner product for tensors $\nabla \mathbf{v}$ and $\nabla \boldsymbol{\varphi} \in \mathbb{R}^{d \times d}, \mathbb{R} \ni \nabla \mathbf{v} : \nabla \boldsymbol{\varphi} = \sum_{j=1,\dots,d} \nabla v_j \cdot \nabla \varphi_j$
$\nabla \cdot \mathbf{T}$	divergence of a tensor $\mathbf{T} = (t_{ij})_{i,j=1,\dots,d} \in \mathbb{R}^{d \times d}, \mathbb{R}^d \ni \nabla \cdot \mathbf{T} = \sum_{i,j=1,\dots,d} \frac{\partial t_{ij}}{\partial x_j} \mathbf{e}_i$



# **1 Introduction**



# Introduction



Coupled free-flow and porous-medium systems appear in many technical applications, biological and environmental settings. Examples in the context of technical applications include water/gas management in fuel cells, industrial filtration, drying of food, wood or other wet porous materials [18, 46, 77, 79, 116, 158]. Exchange processes between body tissues and blood vessels such as nutrient transport or drug delivery are determined by coupled fluid flows within the human body [37, 57, 131, 148, 166]. Evaporation from soil, surface water influenced by wind or precipitation of salt in drying porous materials are examples for soil-atmospheric processes arising from the environmental interaction of free fluid flows with porous media [14, 58, 83, 85, 129]. Due to their importance for industry, biology and environment, coupled free-flow and porous-medium systems have become a topic of high research activity. Especially in the last two decades many theoretical, experimental and numerical investigations have been made to better understand the complex flow and transport phenomena in coupled systems.

Physical processes in the free-flow region and the porous medium evolve on different spatial scales (microscale, macroscale). Due to this multiscale nature, development of mathematical and numerical models for coupled flow systems is challenging. At the microscale (pore scale), the pore geometry of the porous medium is resolved, and the entire flow region consists of the free-flow region and the pore space of the porous medium

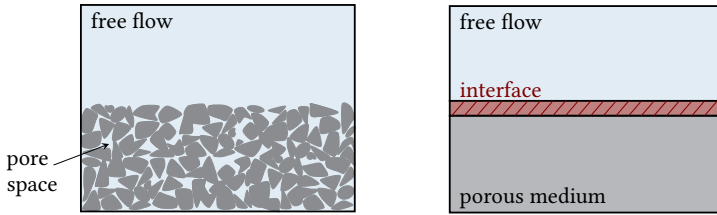


Figure 1.1: Coupled flow system at the pore scale (left) and the macroscale (right).

(Figure 1.1, left). Experimental works are based on the pore scale, e.g., measurement techniques such as (fluorescent) particle image velocimetry are used to obtain pore-scale velocity and pressure fields [11, 12]. From the modeling and numerical side, one system of equations is solved in the fully resolved flow domain. In the most general case the Navier–Stokes equations with the no-slip condition on the boundaries of the solid obstacles are used to model the fluid flow at the pore scale. For steady-state creeping flows (low Reynolds number) the Navier–Stokes equations reduce to the Stokes equations. However, pore-scale resolved simulations are often infeasible for practical applications due to two main reasons. First, the exact pore geometry is usually unknown, except if it is reconstructed by means of imaging techniques [19, 20, 121, 150, 164], or if the porous medium is artificially produced [76, 151] using, e.g., the software GeoDict ([www.geodict.com](http://www.geodict.com)). Second, even if the microscale structure of the flow domain is available, resolving the detailed pore geometry and performing pore-scale simulations is computationally very expensive. Hence, such simulations are feasible for rather small computational domains only, if at all. Therefore, in order to overcome the enormous computational demand when solving the problems at the pore scale, an average representation (macroscale model) of the flow and transport phenomena in coupled systems based on the concept of a representative elementary volume (REV) is required.

At the macroscale (REV scale) the free-flow region and the porous medium are treated as two continuum flow domains separated by an interface

---

(Figure 1.1, right), which can be a sharp interface or a transition zone. Macroscale flow models are obtained by upscaling the microscale equations, thus, they include the pore-scale information and account for microscale quantities and processes in an averaged sense [2, 56, 74, 95, 163]. There exist two different approaches to handle the coupling of free-flow and porous-medium flow from a macroscale perspective: the single-domain and the two-domain approach.

In the single-domain approach, first introduced in [26, 125], the free-flow region and the porous medium are considered as a continuum flow domain where one set of equations is supposed to be valid. The momentum transport is usually governed by the Brinkman equation [26], which requires the determination of effective properties such as permeability, porosity and effective viscosity both inside the free-flow region and in the porous medium. The transition between the two flow domains is either realized via a sharp lower-dimensional interface or an equi-dimensional transition zone presented in Figure 1.2, where the models  $F$ ,  $P$  and  $T$  are based on the same flow equations with different coefficients. In the first case, effective coefficients are discontinuous across the sharp fluid–porous interface, and in the second case, the coefficients vary continuously within the transition zone between the free-flow domain and the porous medium. The single-domain approach has been widely used in numerical studies for practical aspects due to its advantage that continuity of velocity and stress are automatically satisfied. Thus, no explicit coupling conditions are needed. However, the determination of the effective parameters, that highly affects the overall behavior of the coupled flow system, is very challenging [73]. A further difficulty is the determination of the transition zone thickness. For simplicity, this unknown model parameter is typically assumed to be of the same order as the solid obstacles [10, 36, 72, 133].

Considering the two-domain approach, the free-flow region and the porous-medium domain are treated as two different continua and in each flow domain a different model is used to describe the fluid flow (models  $F$  and  $P$  in Figure 1.2). The two flow models are typically coupled via appropriate boundary conditions at a sharp fluid–porous interface (Fig-

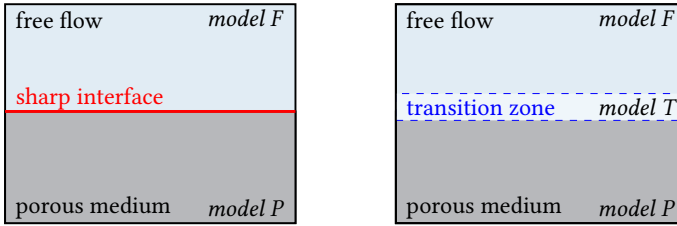


Figure 1.2: Schematic representation of the macroscopic two-domain approach with a sharp interface (left) and with a transition region (right).

ure 1.2, left). Alternatively, as for the single-domain approach, a transition zone between the free-flow region and the porous medium is considered (Figure 1.2, right). In this case, a third flow model  $T$  in form of transition region equations is needed [73, 84, 94, 126]. The two-domain approach has the advantage that no spatial variation of any physical parameters needs to be described. However, the challenging task is to find effective boundary conditions to couple the different flow models such that the complex transfer processes at the interface are represented appropriately.

In the literature, there exist several mathematical models to describe fluid flows in the two flow domains depending on the application of interest. In the most general case, the Navier–Stokes equations are used in the free-flow domain, while the fluid flow in the porous medium is described by multiphase Darcy’s law [87, 130]. For low Reynolds numbers when the fluid flow is dominated by viscous forces, the Navier–Stokes equations can be simplified to the Stokes equations. For coupled flow problems, where the vertical length scale is much smaller than the horizontal one, e.g., when simulating ocean flows in coastal regions, the shallow water equations can be used to model the free flow [159]. These equations are obtained from averaging the Navier–Stokes equations over the depth of the free-flow domain. There exist several modifications of the shallow water equations which can be used to model surface flows, for example, the dynamic wave equation or the kinematic wave equation [41, 103, 113, 149, 159]. The

---

latter is used to model one-dimensional water flows where inertial and pressure forces are negligible, e.g., in case of overland flows on plane surfaces [113]. The porous medium is often assumed to be fully saturated and the single-phase Darcy law [43] instead of its multiphase version is applied to describe the subsurface flow. Other alternative porous-medium flow models are the Forchheimer law [61] in case of high velocities, the Brinkman equation [26, 54] for porous media with high porosity  $\phi > 0.95$  or the Richards equation [128, 130, 134] in case of unsaturated porous media.

In this dissertation, we consider laminar, steady-state flows of a single viscous fluid phase in coupled free-flow and porous-medium systems. We use the two-domain approach with a sharp interface (Figure 1.2, left), where the free flow is described by the Stokes equations and in the porous medium by the single-phase Darcy law. This combination of flow models is the most widely used one in the literature both for mathematical modeling, analysis and numerical simulations of realistic applications, e.g., [15, 30, 50, EE4, 71, 95, 106, 107, 127]. Since the two mathematical models are systems of partial differential equations (PDE) of different orders, the formulation of appropriate coupling conditions at the fluid–porous interface is very challenging. Already in the 1960s, Beavers and Joseph [15] postulated a coupling condition for the tangential velocity component based on experimental observations of a Poiseuille flow over a porous bed. The classical set of interface conditions consisting of the conservation of mass across the interface, the balance of normal forces and the Beavers–Joseph coupling condition [15] or one of its modifications is typically used for analysis of the Stokes–Darcy problem as well as in numerical simulations of coupled flow systems. However, the classical conditions are restricted to flows parallel to the fluid–porous interface [10, EE3, EE4, 152, 165]. Alternative coupling concepts available in the literature, that are supposed to account for arbitrary (multidimensional) flows in Stokes–Darcy systems, i.e., for fluid flows neither parallel nor perpendicular to the interface, are either only theoretically derived and contain undetermined parameters [10] or are not validated for arbitrary flow directions [105, 123, 152]. An exception is the coupling concept recently developed in [EE4]

that is also one of the key results of this dissertation.

The main objectives of this thesis are the i) rigorous derivation of generalized interface conditions, that are free of undetermined parameters and applicable for multidimensional flows in Stokes–Darcy systems; ii) analysis of the resulting coupled macroscale problem; and iii) validation of the derived conditions using pore-scale resolved simulations.

### Outline of the thesis

In the first chapter, we highlighted the relevance of coupled free-flow and porous-medium systems for industry, biology and environment, provided an overview of different modeling approaches for such coupled systems and motivated the research topic of the thesis.

In Chapter 2, we present the state of the art related to coupled Stokes–Darcy problems. In Section 2.1, we specify the assumptions on the flow, the fluid and the porous medium and provide the underlying flow system description at the pore scale. The Stokes and Darcy subdomain models for the macroscale problem formulation are presented and existing coupling concepts are evaluated concerning their advantages and drawbacks. In Section 2.2, we give an overview of existing numerical methods, analytical results and model validation with respect to the Stokes–Darcy problem. An introduction to the theory of periodic homogenization and boundary layers is provided in Section 2.3, where examples from the literature are used in order to explain the main ideas of this averaging strategy for upscaling pore-scale equations.

Generalized coupling conditions valid for arbitrary flows in Stokes–Darcy systems are rigorously derived via periodic homogenization with boundary layer theory in Chapter 3. The derivation procedure is divided in several steps presented in Section 3.1. In Section 3.2, the dimensional form of the derived interface condition is given, the freedom in positioning the sharp interface is discussed and a comparison to the classical coupling conditions is provided.



Chapter 4 focuses on numerical methods for coupled flow problems. In Section 4.1, we present the numerical solution of the pore-scale resolved model and in Section 4.2, we provide the implementation of the coupled Stokes–Darcy problem. The computation of effective properties for the macroscale model is discussed in Section 4.3.

In Chapter 5, the Stokes–Darcy problem with the newly derived interface conditions from Chapter 3 is analyzed with respect to existence and uniqueness of its solution. In Section 5.1, we provide the problem setting including geometrical assumptions and boundary conditions for the coupled Stokes–Darcy problem, and we derive the corresponding weak formulation. In Section 5.2, we prove the well-posedness of the Stokes–Darcy problem with the generalized interface conditions under a suitable relationship between the permeability and two effective constants appearing in the coupling conditions. The obtained result is then numerically analyzed with respect to its applicability for realistic problems in Section 5.3.

Chapter 6 is devoted to model validation and calibration using pore-scale resolved simulations. In Section 6.1, we validate the Stokes–Darcy model with the classical coupling conditions for unidirectional flows, i.e., parallel or perpendicular to the porous layer. The unsuitability of the classical interface conditions for arbitrary flow directions to the porous medium is demonstrated in Section 6.2. The generalized coupling conditions derived in Chapter 3 are validated in Section 6.3 for various flow problems with different flow directions to the interface.

We close the thesis with the conclusions, where we summarize the results of the thesis and discuss the perspectives for further development and improvement of the mathematical models, numerical schemes and analytical results.



# **2 State of the art**



## State of the art

# 2

In this chapter, we first provide the mathematical models to describe the fluid flow in coupled systems at the micro- and macroscale. For the macroscopic flow description, we use the two-domain modeling approach with a sharp fluid–porous interface and consider the Stokes equations in the free-flow region and Darcy’s law in the porous medium. The underlying pore-scale model is needed for the derivation of effective coupling conditions and the numerical validation of macroscale models. Second, a review on analytical results, numerical methods and model validation is presented for the coupled Stokes–Darcy problem. In the third part of this chapter, the main ideas of periodic homogenization and boundary layer theory are presented based on examples from the literature since these averaging techniques are later used in Chapter 3 for the derivation of generalized interface conditions.

### 2.1 Mathematical modeling of coupled problems

In this thesis, we consider single-phase fluid flows in coupled free-flow and porous-medium systems. We assume the fluid to be incompressible, to have constant viscosity and to fully saturate the porous medium. The temperature is supposed to be constant, and the fluid phase is considered to be composed of a single chemical species (component) such that no energy balance and no compositional effects need to be modeled. Moreover, we

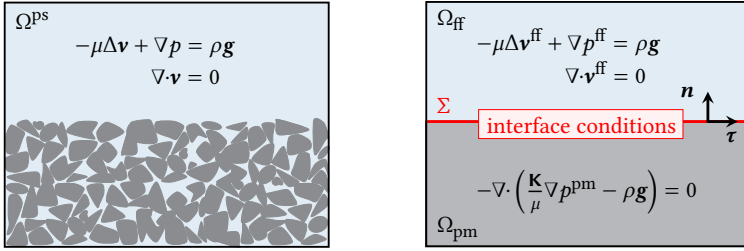


Figure 2.1: Pore-scale model (left) and macroscale coupled Stokes–Darcy model (right).

consider the porous medium to be rigid and nondeformable leading to a constant porosity. The fluid flow is supposed to be slow and laminar characterized by a low Reynolds number  $Re \ll 1$ , i.e., the viscous forces dominate the advective inertial forces. The Reynolds number is given by the following formula

$$Re = \frac{\rho\mathcal{V}\mathcal{L}}{\mu}, \quad (2.1)$$

where  $\rho$  is the fluid density,  $\mu$  is the dynamic viscosity,  $\mathcal{V}$  and  $\mathcal{L}$  are characteristic velocity and length, respectively.

From the pore-scale perspective (Figure 2.1, left), the entire flow domain  $\Omega^{\text{PS}} = \Omega_{\text{ff}} \cup \Omega_{\text{pm}}^{\text{PS}} \subset \mathbb{R}^d$  consists of the free-flow region  $\Omega_{\text{ff}} \subset \mathbb{R}^d$  and the pore space  $\Omega_{\text{pm}}^{\text{PS}} \subset \mathbb{R}^d$  of the porous medium, where  $d = 2, 3$  denotes the number of space dimensions. In this case, the fluid flow in the perforated domain  $\Omega^{\text{PS}}$  is described by one set of partial differential equations, namely the Stokes equations. At the macroscale, we consider the free-flow region  $\Omega_{\text{ff}} \subset \mathbb{R}^d$  and the porous medium  $\Omega_{\text{pm}} \subset \mathbb{R}^d$  as two different continuum flow domains which are separated by a sharp fluid–porous interface  $\Sigma = \Omega_{\text{ff}} \cap \Omega_{\text{pm}}$  (Figure 2.1, right). The latter is void of thermodynamic properties, i.e., it cannot store or transport any mass and momentum. In this case, the flow in the two subdomains is described by two different sets of equations (Stokes and Darcy equations), which need to be coupled

at the fluid–porous interface.

In Section 2.1.1, based on the given assumptions above, we present the pore-scale model describing the fluid flow in the microscopic domain  $\Omega^{\text{Ps}}$ . It consists of the Stokes equations with the no-slip condition on the boundaries of the solid obstacles. In Section 2.1.2, we provide the macroscale Stokes and Darcy flow equations in the two subdomains  $\Omega_{\text{ff}}$  and  $\Omega_{\text{pm}}$  and, in Section 2.1.3, we present different sets of interface conditions that are available in the literature.

### 2.1.1 Pore-scale model

Under the assumptions on the fluid, the porous medium and the flow, prescribed in the beginning of this section, the stationary Stokes equations are used to model the fluid motion in the perforated domain  $\Omega^{\text{Ps}}$ :

$$-\nabla \cdot \mathbf{T}(\mathbf{v}, p) = \rho \mathbf{g} \quad \text{in } \Omega^{\text{Ps}}, \quad (2.2)$$

$$\nabla \cdot \mathbf{v} = 0 \quad \text{in } \Omega^{\text{Ps}}. \quad (2.3)$$

Here,  $\mathbf{T}(\mathbf{v}, p)$  denotes the stress tensor,  $\mathbf{v}$  and  $p$  are the fluid velocity and pressure and  $\mathbf{g}$  is the gravitational acceleration. The stress tensor can be either considered in its nonsymmetric form  $\mathbf{T}(\mathbf{v}, p) = \mu \nabla \mathbf{v} - p \mathbf{I}$ , or in its symmetrized version  $\mathbf{T}(\mathbf{v}, p) = 2\mu \mathbf{D}(\mathbf{v}) - p \mathbf{I}$ , where  $\mathbf{D}(\mathbf{v}) = \frac{1}{2} (\nabla \mathbf{v} + (\nabla \mathbf{v})^\top)$  is the rate of strain tensor and  $\mathbf{I}$  is the identity tensor. In addition to the mass and momentum balance equations (2.3) and (2.2), the no-slip condition is applied on the boundary of the solid inclusions

$$\mathbf{v} = \mathbf{0} \quad \text{on } \partial\Omega^{\text{Ps}} \setminus \partial\Omega, \quad (2.4)$$

where  $\Omega = \Omega_{\text{ff}} \cup \Omega_{\text{pm}}$ . Making use of the incompressibility condition (2.3) and the fact that  $\mu$  is constant, the momentum conservation equation (2.2) can be reformulated as follows

$$-\mu \Delta \mathbf{v} + \nabla p = \rho \mathbf{g} \quad \text{in } \Omega^{\text{Ps}}. \quad (2.5)$$

In order to obtain a closed problem formulation conditions on the external boundary need to be set. We impose the following boundary conditions on  $\partial\Omega$ :

$$\mathbf{v} = \bar{\mathbf{v}} \quad \text{on } \Gamma_D, \quad \mathbf{T}(\mathbf{v}, p)\mathbf{n} = \bar{\mathbf{h}} \quad \text{on } \Gamma_N, \quad (2.6)$$

where  $\bar{\mathbf{v}}$  and  $\bar{\mathbf{h}}$  are given functions and  $\mathbf{n}$  is the unit normal vector on  $\partial\Omega = \Gamma_D \cup \Gamma_N$  pointing outward the domain  $\Omega$ .

As already mentioned, the microscale model is used for the derivation of effective interface conditions and for model validation, however, for practical applications it is often infeasible or rather impossible to solve the pore-scale problem (2.2)–(2.4). Therefore, macroscale models presented in Sections 2.1.2 and 2.1.3 are needed.

## 2.1.2 Subdomain models

In this section, we present the two subdomain models, which are used within this thesis to describe the fluid flow in the free-flow region and in the porous-medium domain, respectively. Effective coupling conditions at the fluid porous-interface are provided in Section 2.1.3.

### Free-flow model

To model the fluid flow in the free-flow region  $\Omega_{\text{ff}}$  we use the stationary Stokes equations

$$-\nabla \cdot \mathbf{T}(\mathbf{v}^{\text{ff}}, p^{\text{ff}}) = \rho \mathbf{g} \quad \text{in } \Omega_{\text{ff}}, \quad (2.7)$$

$$\nabla \cdot \mathbf{v}^{\text{ff}} = 0 \quad \text{in } \Omega_{\text{ff}}, \quad (2.8)$$

where  $\mathbf{v}^{\text{ff}}$  and  $p^{\text{ff}}$  denote the fluid velocity and pressure.



On the external boundary  $\partial\Omega_{\text{ff}} \setminus \Sigma$  of the free-flow region the following conditions are applied

$$\mathbf{v}^{\text{ff}} = \bar{\mathbf{v}} \quad \text{on } \Gamma_{\text{ff},D}, \quad \mathbf{T}(\mathbf{v}^{\text{ff}}, p^{\text{ff}})\mathbf{n} = \bar{\mathbf{h}} \quad \text{on } \Gamma_{\text{ff},N}. \quad (2.9)$$

Here,  $\mathbf{n}$  is the unit normal vector from the free-flow domain  $\Omega_{\text{ff}}$  on its outer boundary  $\partial\Omega_{\text{ff}} \setminus \Sigma = \Gamma_{\text{ff},D} \cup \Gamma_{\text{ff},N}$ .

### Porous-medium model

The motion of an incompressible fluid through the porous medium  $\Omega_{\text{pm}}$  is described by the Darcy flow equations

$$\mathbf{v}^{\text{pm}} = -\frac{\mathbf{K}}{\mu} (\nabla p^{\text{pm}} - \rho \mathbf{g}) \quad \text{in } \Omega_{\text{pm}}, \quad (2.10)$$

$$\nabla \cdot \mathbf{v}^{\text{pm}} = 0 \quad \text{in } \Omega_{\text{pm}}, \quad (2.11)$$

with the following conditions on the external boundary  $\partial\Omega_{\text{pm}} \setminus \Sigma = \Gamma_{\text{pm},D} \cup \Gamma_{\text{pm},N}$  of the porous-medium domain

$$p^{\text{pm}} = \bar{p} \quad \text{on } \Gamma_{\text{pm},D}, \quad \mathbf{v}^{\text{pm}} \cdot \mathbf{n} = \bar{v} \quad \text{on } \Gamma_{\text{pm},N}. \quad (2.12)$$

Here,  $\mathbf{K}$  is the dimensional permeability tensor,  $\mathbf{v}^{\text{pm}}$  and  $p^{\text{pm}}$  are the velocity and pressure in the porous medium,  $\bar{p}$  and  $\bar{v}$  are given functions and  $\mathbf{n}$  is the outward unit normal vector on  $\partial\Omega_{\text{pm}}$ . The tensor  $\mathbf{K} = (k_{ij})_{i,j=1,\dots,d} \subset \mathbb{R}^{d \times d}$  is symmetric and positive definite, thus, for all  $\mathbf{x} \in \mathbb{R}^d \setminus \{\mathbf{0}\}$  it holds

$$\mathbf{K} = \mathbf{K}^\top, \quad \mathbf{x}^\top \mathbf{K} \mathbf{x} > 0. \quad (2.13)$$

In case of isotropic porous media the permeability tensor reads

$$\mathbf{K} = k\mathbf{I}, \quad k > 0, \quad (2.14)$$

and for orthotropic porous media we have

$$\mathbf{K} = \text{diag}(k_1, \dots, k_d). \quad (2.15)$$

If the permeability tensor  $\mathbf{K}$  has nonzero entries  $k_{ij} \neq 0$  for  $i \neq j$  the porous material is called anisotropic.

System (2.10)–(2.11) is called the mixed form of the Darcy problem. Combination of equations (2.10) and (2.11) yields the elliptic formulation of the Darcy equations, also called primal form, often used for analysis purposes

$$-\nabla \cdot \left( \frac{\mathbf{K}}{\mu} (\nabla p^{\text{pm}} - \rho \mathbf{g}) \right) = 0 \quad \text{in } \Omega_{\text{pm}}. \quad (2.16)$$

In order to obtain a complete macroscale formulation of the Stokes–Darcy problem appropriate conditions on the fluid–porous interface are required.

### 2.1.3 Coupling concepts

The correct specification of coupling conditions for the Stokes–Darcy problem is essential for a complete and precise mathematical description of fluid flows in coupled systems as well as for accurate numerical simulations of applications [50, 52, 80, 96, 107]. In the last decades investigations to find appropriate coupling conditions for Stokes–Darcy problems that represent the physical processes at the contact surface have been made both from the experimental, numerical and rigorous mathematical side, e.g., [10, 15, 95, 127, 142, 152]. Most of the studies deal with one-dimensional flows, either parallel or perpendicular to the interface. In contrast, modeling the interactions between the free flow and the porous medium in case of arbitrary flow direction to the porous bed, where both normal and tangential velocity components are nonzero on the fluid–porous interface, is not well established yet.

Below, we present the following coupling concepts for the Stokes–Darcy problem: classical coupling conditions, which are most often used in the literature and are based on the Beavers–Joseph condition; interface conditions derived via homogenization theory for one-dimensional flows to the interface; and two alternative coupling concepts, which have been recently developed for arbitrary flow directions to the porous medium. For clarity and consistency we consider a two-dimensional geometrical setting with a horizontal fluid–porous interface. We denote by  $\mathbf{n}$  the unit normal vector on  $\Sigma$  pointing outward the porous medium and by  $\boldsymbol{\tau}$  the unit tangential vector on  $\Sigma$  (Figure 2.1, right), if not stated otherwise.

### Classical coupling conditions

Interface conditions for the Stokes–Darcy coupling, that are most commonly applied in the literature, are the conservation of mass across the fluid–porous interface (2.17), the balance of normal forces (2.18) and the Beavers–Joseph condition (2.19) on the tangential component of velocity

$$\mathbf{v}^{\text{ff}} \cdot \mathbf{n} = \mathbf{v}^{\text{pm}} \cdot \mathbf{n} \quad \text{on } \Sigma, \quad (2.17)$$

$$p^{\text{pm}} = -\mathbf{n} \cdot \mathbf{T}(\mathbf{v}^{\text{ff}}, p^{\text{ff}}) \mathbf{n} \quad \text{on } \Sigma, \quad (2.18)$$

$$(\mathbf{v}^{\text{ff}} - \mathbf{v}^{\text{pm}}) \cdot \boldsymbol{\tau} = \frac{\sqrt{K}}{\alpha_{\text{BJ}}} \boldsymbol{\tau} \cdot \nabla \mathbf{v}^{\text{ff}} \mathbf{n} \quad \text{on } \Sigma. \quad (2.19)$$

The slip boundary condition (2.19) was proposed by Beavers and Joseph in [15] based on experiments where a Poiseuille flow over a naturally permeable medium was studied. It includes the Beavers–Joseph parameter  $\alpha_{\text{BJ}} > 0$ , a dimensionless and a priori unknown constant that needs to be determined before condition (2.19) can be used for numerical simulations of realistic flow scenarios. In the literature, the parameter is typically chosen  $\alpha_{\text{BJ}} = 1$  even if this is not the correct choice [EE3, EE4, EE6]. Different approaches to compute  $\sqrt{K}$  exist, namely,  $\sqrt{K} = \sqrt{k}$  for  $\mathbf{K} = k\mathbf{I}$ ,  $k > 0$  [10, 15, 52],  $\sqrt{K} = \sqrt{\text{tr}(\mathbf{K})/d}$  [30, 50, 91] or  $\sqrt{K} = \sqrt{\boldsymbol{\tau} \cdot \mathbf{K} \boldsymbol{\tau}}$  [44,

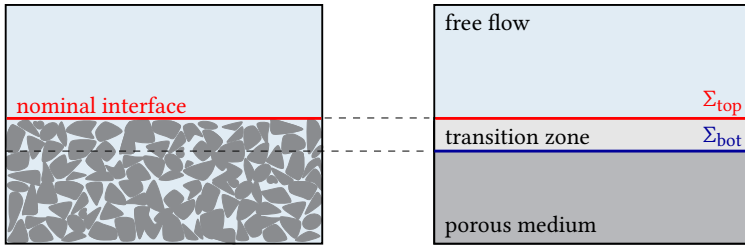


Figure 2.2: Position of the nominal interface based on the pore-scale perspective (left) and position of  $\Sigma_{top}$  and  $\Sigma_{bot}$  (right).

107, 141]. In this thesis, we use the latter interpretation, if not stated otherwise.

Beavers and Joseph already noted that there is an ambiguity of the correct interface position within the near interfacial region and that the model parameter  $\alpha_{BJ}$  is affected by a change of the interface location. This observation was also confirmed later in, e.g., [EE4, 96, EE6, 142, EE7], and makes a specification of the exact interface location when applying condition (2.19) necessary. In the pioneering work [15] the nominal interface, which is positioned directly at the outermost row of solid obstacles as shown in Figure 2.2 (left), was defined and considered in order to determine  $\alpha_{BJ}$ . Besides the dependence on the interface position the parameter  $\alpha_{BJ}$  also contains information about the permeability of the near interfacial region and the pore-scale surface roughness [EE3, 105, 117, EE6, 165].

In [15] the Beavers–Joseph slip coefficient was found to be in the range  $\alpha_{BJ} \in [0.1, 4.0]$ . Further investigations on the correct value of  $\alpha_{BJ}$  in case of flows parallel to the porous bed were made in [117] for circular solid grains and in [EE7] for several more porous-medium geometrical configurations (see Section 6.1.1). However, in case of porous materials different from the ones discussed in [15, 117, EE7] the correct value of the effective coefficient  $\alpha_{BJ}$  is uncertain. For further details on how to find the optimal Beavers–Joseph parameter we refer the reader to Section 6.1.1.

Since the experimental investigations by Beavers and Joseph many coupling concepts have been developed, most of them based on their work. The first modification of the Beavers–Joseph coupling condition (2.19) was proposed by Saffman [142] who neglected the porous-medium velocity. The Beavers–Joseph–Saffman condition reads

$$\mathbf{v}^{\text{ff}} \cdot \boldsymbol{\tau} = \frac{\sqrt{K}}{\alpha_{\text{BJ}}} \boldsymbol{\tau} \cdot \nabla \mathbf{v}^{\text{ff}} \mathbf{n} \quad \text{on } \Sigma. \quad (2.20)$$

Condition (2.20) is no more a coupling condition between the free flow and the porous-medium flow, but a boundary condition for the Stokes problem. The Saffman simplification of the Beavers–Joseph condition is only reasonable if the porous-medium velocity at the interface is much smaller than the free-flow velocity.

Jones [100] further modified Saffman’s interface condition considering the rate of strain tensor in (2.20) yielding the Beavers–Joseph–Saffman–Jones condition

$$\mathbf{v}^{\text{ff}} \cdot \boldsymbol{\tau} = \frac{2\sqrt{K}}{\alpha_{\text{BJ}}} \boldsymbol{\tau} \cdot \mathbf{D}(\mathbf{v}^{\text{ff}}) \mathbf{n} \quad \text{on } \Sigma. \quad (2.21)$$

As a further variant of the Beavers–Joseph interface condition (2.19) the following symmetrized form can be considered to couple the Stokes and Darcy problems

$$(\mathbf{v}^{\text{ff}} - \mathbf{v}^{\text{pm}}) \cdot \boldsymbol{\tau} = \frac{2\sqrt{K}}{\alpha_{\text{BJ}}} \boldsymbol{\tau} \cdot \mathbf{D}(\mathbf{v}^{\text{ff}}) \mathbf{n} \quad \text{on } \Sigma. \quad (2.22)$$

Although the original Beavers–Joseph condition was proposed for flows parallel to the porous layer, all its versions (2.19)–(2.22) are nevertheless routinely applied for flows nonparallel to the interface [22, 42, 49, 82, 101]. However, in [EE3] it is demonstrated that these interface conditions are unsuitable for filtration problems with multidimensional flows to the porous layer. This finding was confirmed in [EE4] and for higher Reynolds number flows in [165].

Conditions (2.19)–(2.22) for the tangential velocity on the fluid–porous interface were postulated based on experimental observations and ad hoc assumptions, e.g., filtration velocity is negligible small. Some decades later the first mathematical justification of the Beavers–Joseph–Saffman condition was obtained by Jäger and Mikelić [95] by means of periodic homogenization and boundary layer theory (see below and Section 2.3). Starting from this work a lot of effort was put into the development of interface concepts via averaging techniques, and the most important results are presented in the next paragraphs.

### Coupling conditions derived via homogenization

Jäger and Mikelić [95] rigorously derived coupling concepts for the Stokes–Darcy problem by means of homogenization theory with two-scale asymptotic expansions and boundary layers. In the last two decades, the proposed interface conditions were analyzed, further developed and validated [33, 34, 96–98, 120]. Since all these works are based on homogenization theory the porous medium is assumed to be periodic. More details on this averaging technique and on the derivation of coupling concepts are provided in Section 2.3.3. The main advantage of the interface conditions derived via homogenization is that all effective coefficients are computed based on the pore geometry and are independent of the macroscopic flow behavior. Thus, no uncertain parameters are present in the model. However, the proposed coupling concepts are valid for one-dimensional flows, parallel or perpendicular to the porous medium, only. In the following, we present the two sets of coupling conditions proposed in, e.g., [34, 95, 98] considering  $\tau = \mathbf{e}_1$ .

Effective coupling conditions on the fluid–porous interface for flows

parallel to the porous medium, derived and analyzed in [33, 96, 98], read

$$\mathbf{v}^{\text{ff}} \cdot \mathbf{n} = 0 \quad \text{on } \Sigma, \quad (2.23)$$

$$p^{\text{pm}} = p^{\text{ff}} + \mu C_\omega^{\text{bl}} \boldsymbol{\tau} \cdot \nabla \mathbf{v}^{\text{ff}} \mathbf{n} \quad \text{on } \Sigma, \quad (2.24)$$

$$\mathbf{v}^{\text{ff}} \cdot \boldsymbol{\tau} = -\ell C_1^{\text{bl}} \boldsymbol{\tau} \cdot \nabla \mathbf{v}^{\text{ff}} \mathbf{n} \quad \text{on } \Sigma. \quad (2.25)$$

Here,  $\ell$  is the characteristic pore size,  $C_\omega^{\text{bl}}$  and  $C_1^{\text{bl}}$  are effective coefficients depending on the pore geometry. The latter are obtained by solving additional Stokes problems on a vertical cut-off stripe of the domain and integrating their solutions (for details, see Section 2.3.3). Since the authors assume parallel flow to the interface [96, 98] the normal velocity component is zero both in the free-flow region and in the porous-medium domain and, therefore, condition (2.23) is reasonable. Equation (2.24) is a coupling condition for the pressure which reduces to the pressure continuity across the interface for isotropic porous media due to the boundary layer constant  $C_\omega^{\text{bl}} = 0$  in this case. Interface condition (2.25) is a confirmation of the Beavers–Joseph–Saffman condition (2.20) taking  $\alpha_{\text{BJ}} = -(\ell C_1^{\text{bl}})^{-1} \sqrt{K}$ .

Coupling conditions for Stokes–Darcy problems in case of perpendicular flow to the porous medium are developed in [34]:

$$\mathbf{v}^{\text{ff}} \cdot \mathbf{n} = \mathbf{v}^{\text{pm}} \cdot \mathbf{n} \quad \text{on } \Sigma, \quad (2.26)$$

$$p^{\text{pm}} = 0 \quad \text{on } \Sigma, \quad (2.27)$$

$$\mathbf{v}^{\text{ff}} \cdot \boldsymbol{\tau} = \mu^{-1} C_1^{2,\text{bl}} \nabla p^{\text{pm}} \cdot \mathbf{n} \quad \text{on } \Sigma. \quad (2.28)$$

The parameter  $C_1^{2,\text{bl}}$  is obtained by solving an additional cell problem and integrating its solution afterwards. Equation (2.26) states the mass balance across the interface. In addition, the authors [34] derived the zero Darcy pressure on the interface (2.27) and the slip condition (2.28) for the tangential velocity, which simplifies to the no-slip condition in case of isotropic porous media since it is  $C_1^{2,\text{bl}} = 0$  in this case.

For further details on the sets (2.23)–(2.25) and (2.26)–(2.28) of coupling

conditions and the computation of the effective coefficients we refer the reader to Section 2.3.3.

### Jump embedded boundary conditions

In [10] two sets of generalized interface conditions supposed to be valid for multidimensional flows are theoretically derived using the method of volume averaging in the interfacial transition zone similar to [127] and asymptotic modeling for thin layers as in [9]. The proposed sets of coupling conditions are formulated based on the position of the fluid–porous interface  $\Sigma$  within the transition zone.

When the interface  $\Sigma = \Sigma_{\text{top}}$  is chosen at the top of the transition zone (Figure 2.2, right) the interface conditions for the Stokes–Darcy system read

$$\mathbf{v}^{\text{ff}} \cdot \mathbf{n} = \mathbf{v}^{\text{pm}} \cdot \mathbf{n} \quad \text{on } \Sigma = \Sigma_{\text{top}}, \quad (2.29)$$

$$p^{\text{pm}} \mathbf{n} = -\mathbf{T}(\mathbf{v}^{\text{ff}}, p^{\text{ff}}) \mathbf{n} + \frac{\mu}{\sqrt{K}} \boldsymbol{\beta}_{\Sigma} \mathbf{v}^{\text{ff}} \quad \text{on } \Sigma = \Sigma_{\text{top}}, \quad (2.30)$$

$$(\mathbf{v}^{\text{ff}} - \mathbf{v}^{\text{pm}}) \cdot \boldsymbol{\tau} = \frac{2\sqrt{K}}{\alpha_{\Sigma}} \boldsymbol{\tau} \cdot \nabla \mathbf{v}^{\text{ff}} \mathbf{n} \quad \text{on } \Sigma = \Sigma_{\text{top}}. \quad (2.31)$$

Here,  $\alpha_{\Sigma} > 0$  is a dimensionless constant and  $\boldsymbol{\beta}_{\Sigma}$  is the dimensionless friction tensor, which is symmetric, uniformly bounded and positive semi-definite. In the two-dimensional framework, the developed coupling concept (2.29)–(2.31) consists of four conditions, but only three are needed for the Stokes–Darcy coupling. The authors [10] claim that the conservation of mass across the interface (2.29) and the normal component of equation (2.30) need to be set on the fluid–porous interface and for the third coupling condition one can choose between the two remaining ones. The tangential component of equation (2.30) relates tangential free-flow velocity and shear stress whereas its second component is an extension of the classical momentum balance (2.18) with an additional term on the right hand side accounting for arbitrary flow directions to



the interface [10]. Coupling condition (2.31) for the tangential component of velocity corresponds to the Beavers–Joseph–Jones condition (2.22) considering  $\alpha_{\text{BJ}} = \alpha_{\Sigma}$ .

When we consider the interface  $\Sigma = \Sigma_{\text{bot}}$  located at the bottom of the transition region (Figure 2.2, right), the following interface conditions are proposed in [10]:

$$\mathbf{v}^{\text{ff}} = \mathbf{v}^{\text{pm}} \quad \text{on } \Sigma = \Sigma_{\text{bot}}, \quad (2.32)$$

$$p^{\text{pm}} \mathbf{n} = \mathbf{T}(\mathbf{v}^{\text{ff}}, p^{\text{ff}}) \mathbf{n} - \frac{\mu}{\sqrt{K}} \boldsymbol{\beta}_{\Sigma} \mathbf{v}^{\text{ff}} \quad \text{on } \Sigma = \Sigma_{\text{bot}}. \quad (2.33)$$

Here, the symmetric, uniformly bounded, semi-definite friction tensor  $\boldsymbol{\beta}_{\Sigma}$  might be different from the one in (2.30). In case of a two-dimensional flow problem, we have again four coupling conditions, where the first component of condition (2.32) is needed to find the position of  $\Sigma_{\text{bot}}$  and the three remaining conditions are used to couple the Stokes and Darcy equations. In case of  $\Sigma = \Sigma_{\text{bot}}$  the authors [10] state that both velocity components are continuous across the interface (2.32) and that the free-flow stress satisfies condition (2.33) similar to the case when  $\Sigma = \Sigma_{\text{top}}$ .

For both coupling concepts (2.29)–(2.31) and (2.32)–(2.33) the effective model parameters  $\alpha_{\Sigma}$  and  $\boldsymbol{\beta}_{\Sigma}$  need to be determined before the interface conditions can be used in numerical simulations. In [5] the proposed conditions are calibrated for a few benchmarks dealing with flows parallel to the porous layer. However, it is still an open question how to determine  $\alpha_{\Sigma}$  and  $\boldsymbol{\beta}_{\Sigma}$  in general and whether these conditions are suitable for multidimensional flows to the fluid–porous interface.

### Higher-order homogenized coupling conditions

Recently, coupling conditions for the Stokes–Darcy problem in case of multidimensional flows over periodic porous structures are derived in [105, 152] using a multiscale homogenization method. This homogenization approach is different from the one applied by Jäger and Mikelić [95, 96] in the

sense that the asymptotic expansions are formulated only on perturbation quantities and not on the whole flow field, which is modeled as the sum of the perturbations due to porous structure and the flow field without the presence of the porous medium. For the sake of clarity, we present the interface conditions developed in [152] for the two-dimensional case with  $\boldsymbol{\tau} = \mathbf{e}_1$ :

$$\mathbf{v}^{\text{ff}} \cdot \mathbf{n} = \mathbf{v}^{\text{pm}} \cdot \mathbf{n} + \ell^2 (M_{211} + K_{21}^{\text{int}} \langle B_1^- \rangle) [\nabla (2\boldsymbol{\tau} \mathbf{D}(\mathbf{v}^{\text{ff}}) \mathbf{n}) \cdot \boldsymbol{\tau}] \quad \text{on } \Sigma, \quad (2.34)$$

$$\begin{aligned} p^{\text{pm}} = & -\mathbf{n} \cdot \mathbf{T}(\mathbf{v}^{\text{ff}}, p^{\text{ff}}) \mathbf{n} - \underbrace{2\mu B_1 \boldsymbol{\tau} \mathbf{D}(\mathbf{v}^{\text{ff}}) \mathbf{n}}_{T_1} + \underbrace{\ell \mathbf{A} \cdot \nabla p^{\text{pm}}}_{T_2} \\ & - \underbrace{\mu \ell (C_{11} + 2L_{11} + A_1 \langle B_1^- \rangle)}_{T_3} [\nabla (2\boldsymbol{\tau} \mathbf{D}(\mathbf{v}^{\text{ff}}) \mathbf{n}) \cdot \boldsymbol{\tau}] \quad \text{on } \Sigma, \quad (2.35) \end{aligned}$$

$$\begin{aligned} \mathbf{v}^{\text{ff}} \cdot \boldsymbol{\tau} = & \mathbf{v}_{\text{int}}^{\text{pm}} \cdot \boldsymbol{\tau} + 2\ell L_{11} \boldsymbol{\tau} \mathbf{D}(\mathbf{v}^{\text{ff}}) \mathbf{n} \\ & + \ell^2 (M_{111} + K_{11}^{\text{int}} \langle B_1^- \rangle) [\nabla (2\boldsymbol{\tau} \mathbf{D}(\mathbf{v}^{\text{ff}}) \mathbf{n}) \cdot \boldsymbol{\tau}] \quad \text{on } \Sigma. \quad (2.36) \end{aligned}$$

Here,  $\mathbf{v}_{\text{int}}^{\text{pm}}$  is understood as an interfacial porous-medium velocity, where the permeability tensor  $\mathbf{K}$  is replaced by the interfacial permeability tensor  $\mathbf{K}^{\text{int}} = \ell^2 (K_{ij}^{\text{int}})_{i,j=1,2}$ , which can be computed based on the pore geometry. Further,  $\ell$  denotes the microscopic pore size and the coefficients  $M_{111}$ ,  $M_{211}$ ,  $L_{11}$ ,  $B_1$ ,  $\mathbf{A} = (A_1, A_2)$ ,  $C_{11}$  and  $\langle B_1^- \rangle$  are nondimensional model parameters, which are dependent on the microscale structure of the interfacial zone including the information about the exact interface position.

Coupling condition (2.34) is similar to the mass conservation equation (2.17) but includes an extra term accounting for the variation in shear along the fluid–porous interface. Condition (2.35) is the momentum conservation equation (2.18) with three additional contributions corresponding to the interface normal forces due to the slip velocity (term  $T_1$ ), the wall normal velocity (term  $T_2$ ) and the shear stress variation (term  $T_3$ ). Interface condition (2.36) is a variant of the Beavers–Joseph condition where  $\mathbf{v}^{\text{pm}}$  in (2.19) is substituted by  $\mathbf{v}_{\text{int}}^{\text{pm}}$  and an additional term that accounts for shear stress variation is appearing on the right hand side of (2.36). Slightly modified coupling conditions in comparison to (2.34)–(2.36) are proposed in [106]

based on more restrictive assumptions on the fluid flow.

The advantage of conditions (2.34)–(2.36) is that all the effective coefficients depend only on the microscale geometry and the location of the sharp fluid–porous interface. They can be computed numerically by solving several Stokes problems in a periodicity stripe, which is only a small part of the computational domain. For more details on the computation of effective coefficients and the derivation of conditions (2.34)–(2.36), we refer the reader to [105, 106, 152]. The conditions have been validated only for the lid driven cavity over the porous bed, where the flow is almost parallel to the interface. In this case, the difference between the classical coupling conditions (2.17)–(2.19) and the conditions (2.34)–(2.36) is small (e.g., see Figure 11 in [152]). Up to now, it is not investigated whether these conditions are also valid for arbitrary flows to the fluid–porous interface. Moreover, in [152, Appendix] the authors noted that condition (2.35) is not optimal yet and needs to be improved.

In [123] similar techniques as in [152] have been used to develop effective interface conditions for the Stokes and Darcy flow equations in case of isotropic porous media. The authors recovered the conservation of mass (2.17) and momentum (2.18) across the fluid–porous interface and developed a modification of the Beavers–Joseph condition, where an interfacial porous-medium velocity instead of the Darcy velocity is present, similar to equation (2.36).

To summarize, classical coupling conditions for the Stokes–Darcy problem, i.e., equations (2.17) and (2.18) together with one of the conditions (2.19)–(2.22), are limited to flows parallel to the fluid–porous interface. Alternative coupling concepts supposed to account also for multidimensional flows to the porous bed are either only theoretically derived and need to be calibrated before they can be used in numerical simulations [5, 10] or are not validated for arbitrary flow directions to the porous medium [105, 106, 152]. Therefore, generalized interface conditions are needed, which are valid for multidimensional fluid flows and do not contain undetermined model parameters. In this thesis, we derive such coupling conditions in Chapter 3, analyze the resulting coupled problem in Chapter 5 and

conduct numerical simulations to validate the derived conditions in Chapter 6.

## 2.2 Analysis, numerical methods and validation of Stokes–Darcy problems

This section is devoted to well-posedness, numerical solution and model validation of the macroscale Stokes–Darcy problem with different sets of coupling conditions.

### 2.2.1 Well-posedness

During the last two decades the coupled Stokes–Darcy problem has received enormous attention both from the modeling side and the numerical point of view. Different interface conditions depending on the flow regime and flow direction were proposed (see Section 2.1.3) and various numerical methods to solve the coupled problem were developed (see Section 2.2.2). However, from the mathematical analysis side in terms of well-posedness, the macroscale model is still not completely understood. For many choices of interface conditions the existence of a unique solution to the corresponding coupled Stokes–Darcy problem is still an open question. In the following, we present results from the literature regarding the well-posedness of the Stokes–Darcy problem with different sets of coupling conditions.

First analytical studies were made in [47, 50], where the authors showed that the Stokes–Darcy problem completed with the continuity of normal velocity (2.17), the momentum balance equation (2.18) and the condition of zero tangential free-flow stress  $\boldsymbol{\tau} \cdot \mathbf{T}(\mathbf{v}^{\text{ff}}, p^{\text{ff}})\mathbf{n} = 0$  on the fluid–porous interface is well-posed. This set of interface conditions, however, leads to a poor representation of the transfer processes between the two flow domains. Based on these first analytical results, further investigations

were made [31, 52, 107] to prove the well-posedness of the Stokes–Darcy problem also for the classical coupling conditions given by (2.17), (2.18) and one of the formulas (2.19)–(2.22).

Most of the works that made contribution to the well-posedness of the coupled problem deal with the classical coupling concept including the Saffman simplification (2.21) of the Beavers–Joseph condition [52, 63, 67, 107]. For this simplified coupled Stokes–Darcy problem Layton et al. [107] have proven existence of a weak solution for the first time. They considered the mixed formulation of the Darcy equations and realized the coupling using Lagrange multipliers. The mixed form of the Stokes–Darcy problem is also analyzed in [63, 67]. Unlike that, in [52] the authors used the primal form of Darcy’s law in order to prove that the coupled problem with Saffman’s boundary condition (2.21) is well-posed.

Dealing with the original Beavers–Joseph coupling condition (2.19) instead of Saffman’s version (2.21) results in a much more complicated problem and proving the well-posedness becomes challenging [10, 30, 31]. There are two main mathematical difficulties arising in this case. First, without any additional assumptions, the Darcy velocity has no well-defined trace on the porous-medium boundary including the fluid–porous interface [10, 30]. Second, the integral term over the interface, in which the tangential porous-medium velocity appears, cannot be absorbed in other terms appearing in the weak formulation of the coupled Stokes–Darcy problem [30, 31, 91]. This makes proving the coercivity of the bilinear form denoted by  $\mathcal{A}$  (see, e.g., equation (5.12) in Section 5.1) that includes the above-mentioned integral term extremely difficult.

Cao et al. [30] proved the well-posedness for the Stokes–Darcy problem with the Beavers–Joseph condition (2.19) under the assumption

$$\alpha_{\text{BJ}}^2 \lambda_{\max}(\mathbf{K})^2 \leq C_1 C_2 \lambda_{\min}(\mathbf{K})^2.$$

Here,  $\lambda_{\min}(\mathbf{K})$  and  $\lambda_{\max}(\mathbf{K})$  denote the smallest respectively the largest eigenvalue of the permeability tensor  $\mathbf{K}$ ,  $C_1$  and  $C_2$  are positive constants coming from trace inequalities [30]. Thus, well-posedness of the coupled

problem is only guaranteed for very small values of the Beavers–Joseph slip coefficient  $\alpha_{\text{BJ}}$ .

Angot [7] considered the classical coupling concept (2.17)–(2.19) with the original condition proposed by Beavers and Joseph on an immersed, Lipschitz continuous fluid–porous interface, where the porous-medium domain is surrounded by the free-flow region. Using the general framework for proving global solvability developed in [6] the well-posedness of the Stokes–Darcy problem for any  $\alpha_{\text{BJ}} > 0$  was obtained [7]. The assumption on the geometry that the porous medium is totally bordered by the sharp interface is not realistic for many applications, however, with this assumption the well-posedness of the Stokes–Darcy problem with the Beavers–Joseph coupling condition without restriction on  $\alpha_{\text{BJ}}$  was proven for the first time. Using the same technique, Angot has proven [8] that the Stokes and Darcy equations coupled with the jump embedded interface conditions (2.29)–(2.31) or (2.32)–(2.33) proposed in [10] yield a well-posed problem.

Recently, existence and uniqueness of the Stokes–Darcy problem with the Beavers–Joseph condition (2.19) was proven in [91] for any choice of the parameter  $\alpha_{\text{BJ}} > 0$  and without geometrical restrictions on the interface. The authors expand the coupled system to a larger flow system yielding additional bilinear terms appearing in the weak formulation of the macroscale problem. These supplementary terms absorb the integral term including the tangential Darcy velocity on the interface and enable to prove the coercivity of the bilinear form  $\mathcal{A}$ .

The well-posedness of the coupled problem with the higher-order homogenized interface conditions (2.34)–(2.36) is not proven yet and is still an open question. Due to many additional terms appearing in these coupling conditions compared to the classical ones, proving the well-posedness of the resulting Stokes–Darcy problem is a challenging task.

### 2.2.2 Numerical methods

Fluid flow in the free-flow region and the porous-medium domain is described using two distinct models, the Stokes and Darcy equations. From the numerical point of view, different space discretization schemes, that suit better for the individual subdomain models, can be considered and a variety of numerical algorithms to solve the coupled problem were developed. In this section, we discuss the most widely used space discretization techniques for the Stokes–Darcy system and give an overview of numerical algorithms for the efficient and robust solution of the coupled problem.

#### Discretization techniques

In each flow domain, the most appropriate discretization approach can be applied, and different meshes can be used that do not need to be conforming at the interface [17, 63, 64, 136, 137, 157]. Various discretization schemes for the coupled Stokes–Darcy problem have been developed and analyzed during the last decades and several sets of interface conditions have been considered. Each coupling condition serves as a boundary condition on the fluid–porous interface in the numerical model, either for the Stokes system (2.7)–(2.9) or the Darcy problem (2.10)–(2.12). Most often, the classical coupling concept with the Beavers–Joseph–Saffman condition (2.20) is applied, e.g., [52, 71, 107, 111, 160]. Discretization methods concerning the Beavers–Joseph condition (2.19) are proposed in, e.g., [8, 30, 31, 91]. In the following, we give an overview of discretization schemes for the coupled Stokes–Darcy problem including continuous or mixed finite element methods [50, 51, 65, 66, 107], finite volume schemes [44, 144, 145] and discontinuous Galerkin methods [62, 71, 101, 111, 136, 137]. If not stated otherwise, the classical set of coupling conditions with the Saffman simplification (2.17), (2.18) and (2.20) is considered.

Most of the existing space discretization schemes for the Stokes–Darcy problem are based on the finite element method (FEM) with an appro-

priate combination of stable elements. For both, the Stokes equations and the Darcy equations a variety of finite element schemes exist and the main challenge is to incorporate the interface conditions. First finite element schemes for the Stokes–Darcy problem are proposed in [50, 107]. Layton et al. [107] apply a continuous finite element formulation in the free-flow region and discretize the Darcy problem via mixed finite elements. They use Lagrange multipliers to impose the coupling conditions on the interface leading to a nonconforming FEM. In [50] the Stokes equations in the free-flow region and the second order elliptic Darcy problem in the porous medium are discretized using continuous finite elements. The coupled problem is then solved using a subdomain iterative domain decomposition scheme. Gatica et al. [65, 67] consider the Stokes equations coupled to the mixed form of the Darcy problem and introduce a new fully-mixed, conforming finite element discretization for the primal/dual-mixed formulation from [107]. Karper et al. [102] discretize the entire flow domain using standard Stokes elements such as the MINI element or the Taylor–Hood finite element. In [157], standard Stokes finite elements are applied in the free-flow region only, while standard continuous piecewise polynomials (P1 or P2) are used for velocity and pressure in the Darcy region. Burman and Hansbo [27, 28] employ a mixed stabilized FEM for both flow models in form of a standard Galerkin formulation with an additional penalization term. Recently, a new FEM for the coupled Stokes–Darcy problem on quadrilateral meshes is developed in [82]. They use piecewise constant approximants for the Darcy pressure, the lowest order Arbogast–Correa element for the Darcy velocity (mixed FEM) and classical Bernardi–Raugel elements for the Stokes equations. Compared to triangular or tetrahedral meshes, quadrilateral meshes are equally flexible for partitioning domains with complicated geometries, but usually involve fewer degrees of freedom.

A finite element discretization scheme for the coupled Stokes–Darcy problem with the original Beavers–Joseph interface condition (2.19) is employed in [30, 31]. Here, quadratic elements (P2) are used for the discretization of the Darcy problem and Taylor–Hood finite elements for the Stokes part.



Another discretization technique is the finite volume method (FVM). It is very attractive for coupled free-flow and porous-medium flow problems due its property of being locally conservative in both flow domains and across interface that is highly valued by the computational fluid dynamics community. Moreover, finite volume discretization schemes are stable, i.e., oscillation-free solutions are guaranteed without any stabilization, and the coupling conditions can be implemented naturally without the need of interpolation. In [44] a FVM on staggered grids, also known as the marker and cell (MAC) method [81], is applied to solve the flow problem in the coupled domain using a Cartesian mesh. Similar schemes for the Stokes–Darcy problem based on the MAC method are developed in [139, 147] for nonuniform grids. Schneider et al. [145] apply a staggered-grid finite volume discretization for the Stokes equations in the free-flow region and a multipoint flux approximation (MPFA) finite volume scheme for the Darcy problem. The latter is needed in case of anisotropic porous media. In [144], the finite volume method is applied for the Stokes equations and the porous-medium model is discretized using the Box method, which was proposed in [93].

Other approaches are based on Discontinuous Galerkin (DG) methods. These are robust finite element methods which allow the construction of discontinuous numerical solutions. The use of DG methods received more attention in the last two decades since these methods are locally mass conservative, stable, higher-order accurate and are easy to implement on unstructured grids. However, due to its higher-order accuracy DG methods are computationally very expensive. Rivière and Yotov [137] formulate a locally conservative numerical scheme employing the DG method in the free-flow region and mixed finite elements to discretize the Darcy problem, whereas in [71, 136] the DG method is used to approximate both the Stokes and Darcy flow equations. The proposed schemes are locally (cellwise) conservative, however, not strongly (pointwise) conservative. In order to avoid the mass loss, Kanschat and Rivière [101] propose a new, strongly conservative scheme based on DG using a globally divergence-conforming velocity space. In this way, mass conservation is achieved in the sense of  $H(\text{div})$ . Gatica and Sequeira [68] introduce and

analyze a hybridizable DG method for the coupled Stokes–Darcy problem. In [62] a strongly conservative discretization scheme is developed, using a divergence-conforming finite element for the velocity in both flow domains. For the discretization of the Stokes problem hybridizable DG techniques are used and mixed finite elements for the Darcy problem.

### Numerical algorithms

After the Stokes–Darcy problem has been discretized, the resulting system of linear equations is solved numerically. There are two different ways to compute the approximate solution of the macroscale problem, either using coupled monolithic (all-at-once) methods or via decoupled (partitioning) methods [138, Chapter 4]. Both solution approaches are discussed in the following.

Using the monolithic approach, the discrete systems of linear equations corresponding to the Stokes and Darcy problems are assembled together with a set of coupling conditions into one large linear system  $\mathbf{A}_h \mathbf{x}_h = \mathbf{b}_h$ , which is schematically presented in Figure 2.3. Here, matrix  $\mathbf{A}_h$  is obtained after space discretization, matrix blocks  $\mathbf{A}_{\text{ff}}$  and  $\mathbf{A}_{\text{pm}}$  correspond to the problems in the free-flow domain and porous medium, respectively, and blocks  $\mathbf{B}$  and  $\mathbf{C}$  contain the coupling conditions. Further,  $\mathbf{x}_h = (\mathbf{v}^{\text{ff}}, \mathbf{p}^{\text{ff}}, \mathbf{v}_{\Sigma}^{\text{ff}}, \mathbf{p}^{\text{pm}}, \mathbf{p}_{\Sigma}^{\text{pm}})^{\top}$  is the solution vector, including the velocity

$$\left( \begin{array}{|c|c|} \hline \mathbf{A}_{\text{ff}} & \mathbf{B} \\ \hline \mathbf{C} & \mathbf{A}_{\text{pm}} \\ \hline \end{array} \right) \begin{pmatrix} \mathbf{v}^{\text{ff}} \\ \mathbf{p}^{\text{ff}} \\ \mathbf{v}_{\Sigma}^{\text{ff}} \\ \mathbf{p}^{\text{pm}} \\ \mathbf{p}_{\Sigma}^{\text{pm}} \end{pmatrix} = \begin{pmatrix} \mathbf{b}_v \\ 0 \\ 0 \\ \mathbf{b}_p \\ 0 \end{pmatrix}$$

Figure 2.3: System of linear equations resulting from the discretization of the coupled Stokes–Darcy problem.

and pressure solution in the Stokes region, the velocity on the interface as well as the Darcy pressure solution in the porous medium and on the interface, e.g., [28, 29, 157]. The right hand side vector  $\mathbf{b}_h = (\mathbf{b}_v, \mathbf{0}, \mathbf{0}, \mathbf{b}_p, \mathbf{0})^\top$  is composed of the right hand sides  $\mathbf{b}_v$  and  $\mathbf{b}_p$  from the discrete free-flow and porous-medium problem, respectively. For further details on the monolithic solution strategy we refer to Section 4.

In case the Stokes–Darcy problem is solved monolithically all components of the discrete solution  $\mathbf{x}_h$  are obtained at once. However, the matrix  $\mathbf{A}_h$  is large, sparse and ill-conditioned that leads to a computationally costly solution of the flow problem, especially in case of large-scale coupled problems. Due to this reason and the naturally decoupled structure of the flow system it is often convenient to solve the Stokes–Darcy problem using partitioning schemes, for example, based on two-grid methods [40, 122] or domain decomposition methods [21, 38, 49, 50, 52]. Decoupled methods reduce the size of the coupled problem by dividing it into two (or more) subproblems that are smaller than the system of equations in the fully coupled approach. This allows the use of already developed optimized solvers for the individual problems, and it makes solving the global system computationally less expensive than using the monolithic solution strategy. Below, we present the main ideas of domain decomposition methods since they are most often used in the literature for the decoupled solution of the Stokes–Darcy problem, e.g., [21, 38, 48–50, 52, 53].

Domain decomposition (DD) schemes are based on the partition of the computational domain  $\Omega$  into  $N \geq 2$  subdomains  $\Omega_i$ ,  $i = 1, \dots, N$ , such that  $\bar{\Omega} = \bigcup_{i=1}^N \Omega_i$ . Depending on the type of the subdomain intersections  $\Omega_i \cap \Omega_j$  one differentiates between two types of methods. In case the subdomains intersect only on the interfaces, i.e.,  $\Omega_i \cap \Omega_j = \emptyset$  for all  $i \neq j$  and  $i, j \in \{1, \dots, N\}$ , we obtain a nonoverlapping strategy, otherwise we have an overlapping DD method. In context with coupled flow problems, nonoverlapping DD methods are typically used [21, 49, 50, 52]. For both approaches the original problem is reformulated in the way that for each subdomain a subproblem is defined, which is coupled to the other sub-

$$\begin{array}{c}
 \left( \begin{array}{c} \boxed{\mathbf{A}_{\text{ff}}} \end{array} \right) \left( \begin{array}{c} \mathbf{v}^{\text{ff}} \\ \mathbf{p}^{\text{ff}} \\ \mathbf{v}_{\Sigma}^{\text{ff}} \end{array} \right) = \left( \begin{array}{c} \mathbf{b}_v \\ \mathbf{b}_B \\ \mathbf{0} \end{array} \right) \\
 \left( \begin{array}{c} \boxed{\mathbf{A}_{\text{pm}}} \end{array} \right) \left( \begin{array}{c} \mathbf{p}^{\text{pm}} \\ \mathbf{p}_{\Sigma}^{\text{pm}} \end{array} \right) = \left( \begin{array}{c} \mathbf{b}_p \\ \mathbf{b}_C \end{array} \right)
 \end{array}$$

Figure 2.4: Schematic of partitioning methods based on domain decomposition.

problems through boundary conditions at the subdomain interfaces. In our case, we naturally have  $N = 2$  with the Stokes equations in the free-flow region, Darcy’s law in the porous medium and, in case of two space dimensions, three coupling conditions at the fluid–porous interface.

The solution of the original coupled problem is then obtained by introducing an iterative scheme, where the flow problems in the subdomains are solved separately and information is exchanged only through boundary conditions on the fluid–porous interface. The main challenge of DD methods is to guarantee convergence and robustness of the iterations [48, 50, 52]. A schematic representation of the nonoverlapping approach for the Stokes–Darcy solution having  $N = 2$  subproblems is presented in Figure 2.4. Here, the coupling is realized via the terms  $\mathbf{b}_B$  and  $\mathbf{b}_C$  on the right hand side of the two systems of equations and all other notations are the same as in case of the monolithic solution strategy.

There exist also preconditioning techniques for the efficient solution of the Stokes–Darcy problem, both for the monolithic approach and for decoupled numerical algorithms, e.g., [29, 39, 89]. However, the aspect of preconditioning is beyond the scope of this thesis and, therefore, it is not addressed here.

### 2.2.3 Model validation

Although several sets of interface conditions for the Stokes–Darcy coupling were proposed and a variety of numerical methods to solve the coupled problem were developed, only a few investigations were made with respect to model validation. Most of the existing validation studies [33, 34, EE3, EE4, EE6, 152] are based on the comparison of macroscale numerical simulation results to pore-scale resolved models. Alternative ways to validate the Stokes–Darcy model are either based on experimental data [92] or the single-domain approach as a reference solution [108].

First attempts to validate the coupled Stokes–Darcy model are made in [108], where two analytically tractable flows are studied: a Poiseuille flow in the free-flow region over a porous layer with a constant porosity according to the Beavers and Joseph case [15] and a corner flow in a fluid overlying a porous bed, where also a normal flux through the interface takes place. Numerical simulation results for the macroscale model with the classical coupling conditions (2.17)–(2.19) taking  $\alpha_{\text{BJ}} = 1$  and with the coupling approach developed in [108] are compared to the single-domain Darcy–Brinkman model. The coupling concept for the Stokes and Darcy equations proposed by the authors [108], i.e., the continuity of velocity and pressure, is derived using the volume averaging method and assumes a transition zone, below the nominal interface inside the porous medium, where the Stokes equations are still valid. The coupling to Darcy’s law then takes place at the lower boundary of the transition region. In case of the Poiseuille flow validation case both coupled Stokes–Darcy models provide a good agreement with the Darcy–Brinkman simulation results, as expected. For the corner flow test case, the simulation results for the Stokes–Darcy problem with the classical coupling conditions taking  $\alpha_{\text{BJ}} = 1$  do not agree with the single-domain simulation results, whereas the coupled model postulated in [108] provide a good agreement. This finding is a first hint that the classical coupling concept including the Beavers–Joseph condition (2.19) is not suitable to represent arbitrary flows in coupled systems.

An experimental validation of the classical Stokes–Darcy model given by (2.7)–(2.11), (2.17)–(2.19) for matrix–conduit flows such as groundwater flows in karst aquifers is provided in [92] using experimental results from [60]. In the experiments made by Faulkner et al. [60] the fluid flows parallel to the interface between the rectangular free-flow region and the overlying porous-medium domain. The comparison of numerical simulation results for the coupled Stokes–Darcy model to experimental data yield a very good agreement [92]. Thus, the classical interface conditions are experimentally proven to be suitable for the coupling of Stokes and Darcy flow equations in case of flows parallel to the interface.

In [33] the authors validate the Stokes–Darcy problem completed with the interface conditions (2.106)–(2.108) derived using homogenization and boundary layer theory for flows parallel to the porous layer. Two validation cases are studied, namely pressure driven flow corresponding to the experiments by Beavers and Joseph and flow in a periodic setting, where the boundary conditions and microstructure of the porous domain are periodic. In both cases the flow is parallel to the fluid–porous interface. Carraro et al. [33] perform pore-scale resolved and macroscale simulations, and compute the errors between the pore-scale solutions and the solutions to the effective problem. The authors show that the errors increase appropriately with respect to increasing dimensionless pore size  $\varepsilon = \ell/\mathcal{L}$ , where  $\mathcal{L}$  denotes a characteristic length scale (for details, see Section 2.3). In this way, the Stokes–Darcy problem with coupling conditions (2.106)–(2.108) is validated for the considered flow problems.

Conditions (2.117)–(2.119) postulated for flows perpendicular to the interface are analyzed with respect to their validity in [34]. The authors consider the forced infiltration into the porous structure on a small free-flow and porous-medium stripe containing one column of identical solid inclusions. By comparison of pore-scale and macroscale numerical simulations and computation of the errors between the two solutions similar as in [33] the proposed coupling conditions are shown to be valid for this simple validation case.

Interface conditions (2.34)–(2.36) for the Stokes–Darcy problem developed in [106, 152] are validated and compared to the classical coupling approach in [152]. The authors study the lid driven cavity over a porous bed considering different types of porous materials. Pore-scale resolved models are compared to macroscale numerical simulation results to confirm the proposed conditions (2.34)–(2.36), which are supposed to account for multidimensional flows in Stokes–Darcy systems. For the lid driven cavity test cases, where the flow is almost parallel to the porous layer, the macroscale simulation results agree well with the microscale results. However, a more interesting validation case, where the flow is strongly nonparallel to the fluid–porous interface, is not investigated yet.

Coupling conditions for the Stokes–Darcy problem derived in [123] for isotropic porous media are validated by comparison of macroscale numerical simulation results to pore-scale resolved models. The authors consider two validation scenarios, stagnation point flow (Hiemenz boundary layer flow) overlying a porous bed and flow past a backward-facing step, where the step region is a porous medium. In the first test case, the porosity is assumed to be very large ( $\phi = 0.9999$ ) resulting in flow around particles rather than flow through a porous medium. For this considered problem, the Stokes–Darcy model with the conditions derived in [123] is shown to be a good approximation of the pore-scale model. Also, for the second validation scenario, where the porosity is taken more realistic, comparison of numerical simulation results confirms the validity of the proposed conditions. However, the authors [123] do not compare their developed interface conditions to the classical conditions, although, this would be interesting to see if their conditions are preferable over the classical ones in order to model coupled flow systems accurately.

Our contribution with respect to validation and calibration of the coupled Stokes–Darcy model with different sets of interface conditions is presented in Chapter 6 of this thesis based on the articles [EE3, EE4, EE6, EE7], where we compare pore-scale resolved models to macroscale numerical simulation results.

## 2.3 Homogenization and boundary layer theory

Homogenization theory with multiscale expansions was first developed for periodic porous media [1, 2, 99, 109, 118, 143, 153] for which it is also most often applied, e.g., [34, 88, 95, 96, 114, 146]. Later on, this theory was modified such that one could also upscale pore-scale equations in random porous materials [16]. Considering the Stokes equations describing the flow in a perforated domain at the pore scale both homogenization approaches yield the same type of filtration law, the Darcy law. In this thesis, we deal with periodic homogenization, where the porous medium is assumed to be constructed by a periodic arrangement of solid obstacles. In such periodic structures, there are naturally two length scales present: the sample size of the porous domain  $W$  (macroscopic length scale) and the characteristic dimensional pore size  $\ell$  (microscopic length scale), which is most often very small compared to the macroscopic length (Figure 2.5, left). In order to quantify the differences in the two length scales we make use of the scale separation parameter  $\varepsilon = \ell/\mathcal{L}$ , where  $\mathcal{L}$  is a characteristic length scale, e.g., often  $\mathcal{L} = W$ . The first step is then, to make the pore-scale equations dimensionless. Then, starting from the nondimensional pore-scale problem formulation involving the dimensionless quantity  $\varepsilon$ , we make an asymptotic analysis in order to find macroscale (effective) models.

The assumption on periodicity, which is necessary to apply homogenization, breaks down close to the boundaries of the porous structure. Here, so-called boundary layers appear and deviations from the effective model obtained inside the porous medium are expected. Indeed, for several flow problems it was shown [33, 95, 97] that these boundary layers significantly influence the boundary conditions, which are applied for the macroscale problem. To take into account the porous-medium boundary effects into the effective model, boundary layer theory is needed.

In this section, we introduce the theory of periodic homogenization and boundary layers using as an example the Stokes equations describing the flow at the pore scale through periodic porous media. In Section 2.3.1,



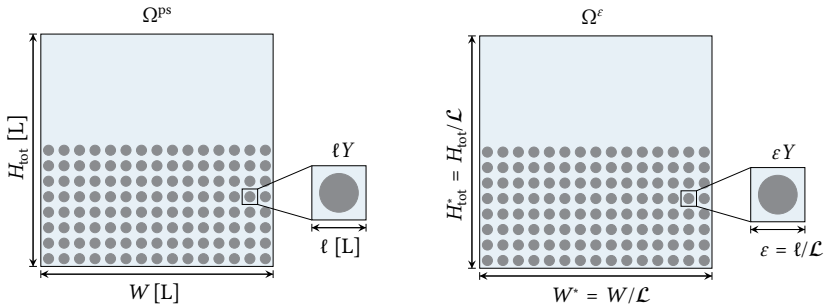


Figure 2.5: Pore-scale flow domain  $\Omega^{\text{ps}}$  (left) and dimensionless flow domain  $\Omega^{\epsilon}$  (right).

we present the nondimensionalization of the Stokes equations which is the starting point for the homogenization procedure thereafter. In Section 2.3.2 we provide an introduction to periodic homogenization by the derivation of Darcy’s law. The main ideas of boundary layer theory are explained by demonstrating how effective coupling conditions for unidirectional flows in Stokes–Darcy systems are derived, based on examples from the literature, e.g., [33, 34, 95, 98].

### 2.3.1 Nondimensionalization

Equations (2.3)–(2.5) are presented in the dimensional form, i.e., each variable and property is given in physical dimensions (Figure 2.5, left). However, we are interested in working with the dimensionless formulation of a mathematical problem because it is often necessary to bring large-scale flow problems in a numerically feasible setting, and it is the more general formulation. For example, the solution of a problem in dimensional form is the solution to one specific problem, whereas a nondimensional solution depends on a set of dimensionless parameters, e.g., the Reynolds or Prandtl number, and describes different dimensional solutions. Moreover, the nondimensionalization of mathematical problems allows the identification of significant and insignificant terms. Therefore, we transform

Quantity	Scaling parameter	Primary dimensions
Characteristic length	$\mathcal{L}$	[L]
Characteristic velocity	$\mathcal{V}$	[LT <sup>-1</sup> ]
Gravitational acceleration	$\mathcal{G}$	[LT <sup>-2</sup> ]

*Table 2.1: Scaling parameters and their primary dimensions for nondimensionalization of the Stokes equations.*

the stationary Stokes equations (2.3)–(2.5) into their dimensionless form. Within this thesis, the words ‘dimensionless’ and ‘nondimensional’ are interchangeable and indicate that no physical dimensions are involved.

In order to nondimensionalize the momentum equation (2.5) we choose the scaling parameters presented in Table 2.1. For scaling the pressure, we choose the parameter  $\mu\mathcal{V}/\mathcal{L}$  since we consider viscous fluid flows. Then, the nondimensional variables denoted by the superscript  $*$  read

$$\mathbf{x}^* = \frac{\mathbf{x}}{\mathcal{L}}, \quad \mathbf{v}^* = \frac{\mathbf{v}}{\mathcal{V}}, \quad p^* = \frac{p\mathcal{L}}{\mu\mathcal{V}}, \quad \mathbf{g}^* = \frac{\mathbf{g}}{\mathcal{G}}, \quad \nabla^* = \mathcal{L}\nabla. \quad (2.37)$$

We define the nondimensional length and height of the coupled domain as  $W^* = W/\mathcal{L}$  and  $H_{\text{tot}}^* = H_{\text{tot}}/\mathcal{L}$ , respectively. If the porous structure is periodic the nondimensional characteristic pore size is denoted by  $\varepsilon = \ell/\mathcal{L}$  (Figure 2.5, right) which is also referred as the scale separation parameter. In the nondimensional setting, we use the notations  $\Omega = \Omega_{\text{ff}} \cup \Omega_{\text{pm}}$  and  $\Omega^\varepsilon$  to relate to the macroscale and pore-scale domain, respectively, to be consistent with the notations typically used in homogenization theory.

We rearrange equations (2.37) in terms of the dimensional variables, substitute them into the momentum equation (2.5) and obtain

$$-\mu \frac{\Delta^*}{\mathcal{L}^2} (\mathbf{v}^* \mathcal{V}) + \frac{\nabla^*}{\mathcal{L}} \left( \frac{p^* \mu \mathcal{V}}{\mathcal{L}} \right) = \rho \mathbf{g}^* \mathcal{G} \quad \text{in } \Omega^\varepsilon. \quad (2.38)$$

All terms in equation (2.38) are of primary dimension [ML<sup>-2</sup>T<sup>-2</sup>]. Next, we multiply (2.38) by  $\mathcal{L}/(\rho\mathcal{V}^2)$  such that the dimensions cancel. This leads

to

$$-\frac{\mu}{\rho\mathcal{L}\mathcal{V}}\Delta^*\mathbf{v}^* + \frac{\mu}{\rho\mathcal{V}\mathcal{L}}\nabla^*p^* = \frac{\mathcal{G}\mathcal{L}}{\mathcal{V}^2}\mathbf{g}^* \quad \text{in } \Omega^\varepsilon. \quad (2.39)$$

Multiplication of equation (2.39) with the Reynolds number  $Re$  given by (2.1) yields the following nondimensional momentum equation

$$-\Delta^*\mathbf{v}^* + \nabla^*p^* = \left[ \frac{Re}{Fr^2} \right] \mathbf{g}^* \quad \text{in } \Omega^\varepsilon. \quad (2.40)$$

Here,  $Fr = \mathcal{V}/\sqrt{\mathcal{G}\mathcal{L}}$  denotes the Froude number being the ratio of the flow inertia to the gravitational acceleration.

For nondimensionalization of the mass conservation equation (2.3) and the no-slip condition (2.4) we use the scaling parameter  $\mathcal{V}$  and obtain

$$\nabla^* \cdot \mathbf{v}^* = 0 \quad \text{in } \Omega^\varepsilon, \quad \mathbf{v}^* = \mathbf{0} \quad \text{on } \partial S^\varepsilon,$$

where  $S^\varepsilon = \Omega \setminus \Omega^\varepsilon$  denotes the solid part of the porous medium in the dimensionless setting.

In the rest of the thesis, we usually work with the dimensionless flow equations, if not stated otherwise. For clarity, we drop the superscript  $*$  and the nondimensional form of equations (2.3)–(2.5) reads

$$-\Delta\mathbf{v} + \nabla p = \mathbf{f} \quad \text{in } \Omega^\varepsilon, \quad (2.41)$$

$$\nabla \cdot \mathbf{v} = 0 \quad \text{in } \Omega^\varepsilon, \quad (2.42)$$

$$\mathbf{v} = \mathbf{0} \quad \text{on } \partial S^\varepsilon, \quad (2.43)$$

where the nondimensional quantity  $\mathbf{f}$  represents the effects of external forces and corresponds to the physical force term multiplied by the ratio of Reynolds' number to Froude's number squared, i.e.,  $\mathbf{f} = ReFr^{-2}\mathbf{g}^*$ .

For slow, viscous flows when the advective inertial forces compared to the viscous forces are very small ( $Re \rightarrow 0$ ), the force term  $\mathbf{f}$  in equation (2.41)

is neglected leading to

$$-\Delta \mathbf{v} + \nabla p = \mathbf{0} \quad \text{in } \Omega^\varepsilon. \quad (2.44)$$

In the context of homogenization theory the pore-scale velocity and pressure in (2.41)–(2.44) are typically marked with the superscript  $\varepsilon$  since they depend on the dimensionless pore size. This notation is adopted in the following sections.

### 2.3.2 Periodic homogenization: Darcy's law

This section is devoted to an introduction to periodic homogenization with two-scale asymptotic expansions. We explain the main features of this averaging technique by means of upscaling the Stokes equations which govern fluid flow in a porous material from the pore-scale perspective. For a more general presentation of homogenization theory we refer the reader to [1, 90, 109, 118, 143, 153].

The two basic assumptions needed to apply periodic homogenization in context with porous media are i) the porous material is periodic and ii) the length scales are separated, i.e., the characteristic pore size is much smaller than the characteristic size of the macroscopic domain, yielding  $\varepsilon \ll 1$ . In general, scale separation holds and homogenization is applicable for  $\varepsilon < 0.1$ . The main idea of homogenization is to consider a family of functions  $f^\varepsilon$  with respect to the scale separation parameter  $\varepsilon > 0$  and then, passing to the limit

$$f = \lim_{\varepsilon \rightarrow 0} f^\varepsilon \quad (2.45)$$

as the final step of the upscaling procedure. In the limit (2.45) the microscale structure will be 'averaged out' (Figure 2.6) and we obtain a homogenized model that describes the considered process. As we will see in Section 2.3.2 the homogenized model can significantly differ from the original partial differential equation.

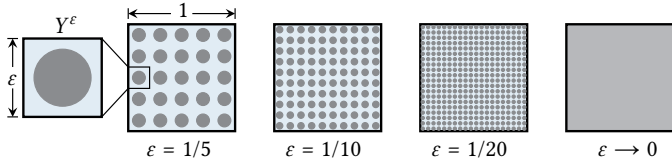


Figure 2.6: Schematic idea of homogenization.

The classical homogenization procedure presented in [2, 90, 120] comprises the following steps.

*Step 1:* Give a precise description of the porous-medium geometry.

*Step 2:* Specify the mathematical model valid at the pore scale and obtain *a priori* estimates for the solutions of the pore-scale problem with respect to the dimensionless parameter  $\varepsilon$ .

*Step 3:* Formulate the two-scale asymptotic expansion for all pore-scale functions, e.g., assume that  $f^\varepsilon$  can be written as follows

$$f^\varepsilon(\mathbf{x}) = \sum_{j=a}^{\infty} \varepsilon^j f_j(\mathbf{x}, \mathbf{y}), \quad \mathbf{y} = \frac{\mathbf{x}}{\varepsilon},$$

where  $a \in \mathbb{N}_0$  depends on the problem of interest and  $f_j$  are  $\mathbf{y}$ -periodic functions.

*Step 4:* Formulate macroscale model containing effective coefficients.

*Step 5:* Study the homogenized problem (prove uniqueness and regularity).

*Step 6:* Prove convergence of the homogenization procedure, if possible (e.g. prove two-scale convergence, obtain rigorous error estimates).

In the next section, we apply Step 1–Step 6 to the Stokes equations describing the flow in the pore space of a porous medium in order to obtain the corresponding effective flow model.

## Derivation of Darcy's law

In this section, we present the rigorous derivation of by means of periodic homogenization following Step 1–Step 6. Darcy's law was derived for the first time by Ene and Sanchez-Palencia [143, Chapters 5] via homogenization, Tartar [153] then obtained error estimates for the two-dimensional case and Allaire [2] extended Tartar's work to the three-dimensional case.

### Step 1: Description of porous-medium geometry

We consider a smooth, bounded and connected domain  $\Omega_{\text{pm}} \subset \mathbb{R}^d$ ,  $d = 2, 3$ , representing a regular porous medium, which is constructed by a periodic arrangement of solid obstacles as described hereinafter. The domain  $\Omega_{\text{pm}}$  is covered by a Cartesian mesh of size  $\varepsilon$  and the grid cells are denoted by  $Y_k^\varepsilon$ , where  $1 \leq k \leq N(\varepsilon)$  and  $N(\varepsilon) = \varepsilon^{-d} |\Omega_{\text{pm}}| (1 + o(1))$  is the number of cells. Each grid cell  $Y_k^\varepsilon$  is constructed from a translation of the unit cell  $Y = (0, 1)^d$  and a rescaling with  $\varepsilon$ . In the two-dimensional case we have

$$Y_k^\varepsilon = \varepsilon(Y + \{y_{1,k}, y_{2,k}\}), \quad 1 \leq k \leq N(\varepsilon), \quad (2.46)$$

where the translation of the unit cell  $Y = (0, 1)^2$  by  $y_{1,k} \in \mathbb{Z}$  in horizontal and  $y_{2,k} \in \mathbb{Z}$  in vertical direction corresponding to the cell number  $k$  is defined as

$$Y + \{y_{1,k}, y_{2,k}\} = (y_{1,k}, 1 + y_{1,k}) \times (y_{2,k}, 1 + y_{2,k}). \quad (2.47)$$

The unit cell  $Y$  contains a solid part  $Y_s$ , representing one or more solid obstacles, and a complementary fluid part  $Y_f = Y \setminus Y_s$ . We assume that  $Y_s$  is a closed subset of  $\bar{Y}$  with a piecewise smooth boundary and  $Y_f$  is open and connected. The fluid part  $\Omega_{\text{pm}}^\varepsilon$  of the porous medium  $\Omega_{\text{pm}}$  is the union of all pores, i.e.,  $\Omega_{\text{pm}}^\varepsilon = \bigcup_{1 \leq k \leq N(\varepsilon)} \varepsilon(Y_f + \{y_{1,k}, y_{2,k}\})$ . The domain  $S^\varepsilon = \Omega_{\text{pm}} \setminus \Omega_{\text{pm}}^\varepsilon$  represents the solid part of the porous structure.

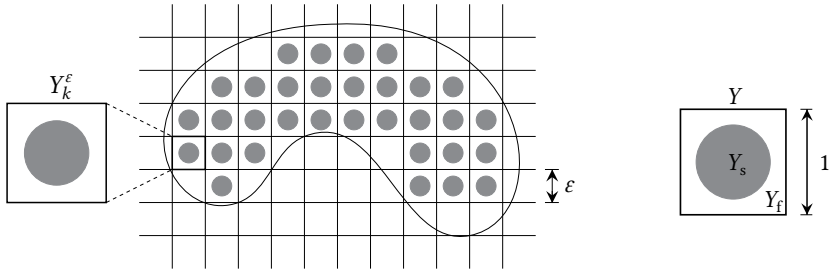


Figure 2.7: Example of an idealized, periodic porous medium (left) and the corresponding unit cell  $Y = (0, 1)^2$  (right).

An example of an idealized, periodic porous medium constructed as described above and the corresponding unit cell  $Y$  are presented in Figure 2.7 for the two-dimensional case. In this thesis, we consider rectangular porous-medium domains  $\Omega_{\text{pm}} = (0, L_j)^d$  with  $L_j \in \mathbb{R}^+$  for  $j = 1, \dots, d$  and, for simplicity, we assume  $L_j/\varepsilon \in \mathbb{N}$  for all  $j$ .

### Step 2: Pore-scale model and *a priori* estimates

After we have given a precise description of the porous domain we now specify the flow problem we are interested in. We consider slow, viscous flow at low Reynolds numbers through a rigid porous medium  $\Omega_{\text{pm}} = (0, L)^d$ , where  $L > 0$  is a dimensionless length scale with  $L/\varepsilon \in \mathbb{N}$ , such that the flow at the pore scale is described by the nondimensional stationary Stokes equations

$$-\Delta \mathbf{v}^\varepsilon + \nabla p^\varepsilon = \mathbf{f}, \quad \nabla \cdot \mathbf{v}^\varepsilon = 0 \quad \text{in } \Omega_{\text{pm}}^\varepsilon \quad (2.48)$$

with the no-slip condition on the boundaries of the solid obstacles and periodic boundary conditions on the external boundary of the porous domain

$$\mathbf{v}^\varepsilon = \mathbf{0} \quad \text{on } \partial S^\varepsilon, \quad \{\mathbf{v}^\varepsilon, p^\varepsilon\} \text{ is } L\text{-periodic}. \quad (2.49)$$

We define the test function space for the velocity

$$W_{\text{per}}(\Omega_{\text{pm}}^\varepsilon)^d = \left\{ \boldsymbol{\varphi} \in H^1(\Omega_{\text{pm}}^\varepsilon)^d : \boldsymbol{\varphi} = \mathbf{0} \text{ on } \partial S^\varepsilon, \boldsymbol{\varphi} \text{ is } L\text{-periodic} \right\}, \quad (2.50)$$

and the one for the pressure

$$L_{\text{per}}^2(\Omega_{\text{pm}}^\varepsilon) = \left\{ p \in L^2(\Omega_{\text{pm}}^\varepsilon) : p \text{ is } L\text{-periodic} \right\}. \quad (2.51)$$

Then, the variational formulation of the Stokes problem (2.48)–(2.49) is: Find  $\mathbf{v}^\varepsilon \in W_{\text{per}}(\Omega_{\text{pm}}^\varepsilon)^d$  with  $\nabla \cdot \mathbf{v}^\varepsilon = 0$  in  $\Omega_{\text{pm}}^\varepsilon$  and  $p^\varepsilon \in L_{\text{per}}^2(\Omega_{\text{pm}}^\varepsilon)$  such that

$$\int_{\Omega_{\text{pm}}^\varepsilon} \nabla \mathbf{v}^\varepsilon : \nabla \boldsymbol{\varphi} \, dx - \int_{\Omega_{\text{pm}}^\varepsilon} p^\varepsilon (\nabla \cdot \boldsymbol{\varphi}) \, dx = \int_{\Omega_{\text{pm}}^\varepsilon} \mathbf{f} \cdot \boldsymbol{\varphi} \, dx \quad (2.52)$$

for all  $\boldsymbol{\varphi} \in W_{\text{per}}(\Omega_{\text{pm}}^\varepsilon)^d$ . For  $\mathbf{f} \in L^2(\Omega_{\text{pm}}^\varepsilon)^d$  the existence of a velocity field  $\mathbf{v}^\varepsilon \in W_{\text{per}}(\Omega_{\text{pm}}^\varepsilon)^d$  with  $\nabla \cdot \mathbf{v}^\varepsilon = 0$  and a pressure field  $p^\varepsilon \in L_{\text{per}}^2(\Omega_{\text{pm}}^\varepsilon)$ , and the uniqueness of the velocity is guaranteed [155]. To make the pressure field unique, we set  $\int_{\Omega_{\text{pm}}^\varepsilon} p^\varepsilon \, dx = 0$ . This is equivalent to proving uniqueness in

$$L_{\text{per}}^2(\Omega_{\text{pm}}^\varepsilon)/\mathbb{R} = \left\{ p^\varepsilon \in L_{\text{per}}^2(\Omega_{\text{pm}}^\varepsilon) : \int_{\Omega_{\text{pm}}^\varepsilon} p^\varepsilon \, dx = 0 \right\}. \quad (2.53)$$

Since we consider  $\varepsilon \rightarrow 0$  the pore-scale functions  $\mathbf{v}^\varepsilon$ ,  $p^\varepsilon$  are not defined in a fixed domain but in varying sets  $\Omega_{\text{pm}}^\varepsilon$ . However, we want to obtain error estimates for  $\mathbf{v}^\varepsilon$ ,  $p^\varepsilon$  that are independent of  $\varepsilon$  and, in order to prove convergence of the homogenization procedure, we have to extract weakly convergent subsequences of the sequence of solutions  $(\mathbf{v}^\varepsilon, p^\varepsilon)$ . The latter is only possible in fixed Sobolev spaces (independent of  $\varepsilon$ ), thus, we need to have  $\mathbf{v}^\varepsilon$  and  $p^\varepsilon$  defined in the macroscopic flow domain  $\Omega_{\text{pm}}$ . Therefore, we make an extension  $\{\tilde{\mathbf{v}}^\varepsilon, \tilde{p}^\varepsilon\} \in H^1(\Omega_{\text{pm}}^\varepsilon)^d \times L^2(\Omega_{\text{pm}}^\varepsilon)$  to the porous-medium domain  $\Omega_{\text{pm}}$  as described below.

We extend the pore-scale velocity  $\mathbf{v}^\varepsilon$  by zero in  $\Omega_{\text{pm}} \setminus \Omega_{\text{pm}}^\varepsilon$  and define the



velocity extension

$$\tilde{\mathbf{v}}^\varepsilon = \begin{cases} \mathbf{v}^\varepsilon & \text{in } \Omega_{\text{pm}}^\varepsilon, \\ \mathbf{0} & \text{in } \Omega_{\text{pm}} \setminus \Omega_{\text{pm}}^\varepsilon. \end{cases} \quad (2.54)$$

This extension is in agreement with the no-slip condition on the solid boundaries and preserves the  $L^2$ - and  $H^1$ -norms. The extension of the pressure, which has been proven successful for obtaining an *a priori* pressure estimate, is more complicated and reads [112]:

$$\tilde{p}^\varepsilon = \begin{cases} p^\varepsilon & \text{in } \Omega_{\text{pm}}^\varepsilon, \\ \frac{1}{|Y_{fk}^\varepsilon|} \int_{Y_{fk}^\varepsilon} p^\varepsilon \, d\mathbf{y} & \text{in } Y_{sk}^\varepsilon, \, 1 \leq k \leq N(\varepsilon), \end{cases} \quad (2.55)$$

where  $Y_{fk}^\varepsilon$  is the fluid part and  $Y_{sk}^\varepsilon$  the solid part of the periodicity cell  $Y_k^\varepsilon$ . In the following, if not stated otherwise, we always deal with the extensions, but we omit the tilde symbol for the sake of clarity.

To obtain *a priori* estimates for the velocity, we take  $\boldsymbol{\varphi} = \mathbf{v}^\varepsilon$  in (2.52) and use the mass conservation equation in (2.48) and get

$$\int_{\Omega_{\text{pm}}^\varepsilon} |\nabla \mathbf{v}^\varepsilon|^2 \, d\mathbf{x} = \int_{\Omega_{\text{pm}}^\varepsilon} \mathbf{f} \cdot \mathbf{v}^\varepsilon \, d\mathbf{x} \leq \|\mathbf{f}\|_{L^2(\Omega_{\text{pm}}^\varepsilon)^d} \|\mathbf{v}^\varepsilon\|_{L^2(\Omega_{\text{pm}}^\varepsilon)^d}. \quad (2.56)$$

Applying the Poincaré inequality (A2.1) and inequality (A2.2), using estimate  $\|\mathbf{f}\|_{L^2(\Omega_{\text{pm}}^\varepsilon)^d} \leq C$ , and replacing  $\Omega_{\text{pm}}^\varepsilon$  by  $\Omega_{\text{pm}}$  leads to the following *a priori* estimates for the pore-scale velocity

$$\|\mathbf{v}^\varepsilon\|_{L^2(\Omega_{\text{pm}})^d} \leq C\varepsilon^2, \quad \|\nabla \mathbf{v}^\varepsilon\|_{L^2(\Omega_{\text{pm}})^{d \times d}} \leq C\varepsilon, \quad (2.57)$$

where  $C > 0$ . Obtaining an *a priori* error estimate for the pressure is more challenging. From the momentum conservation equation in (2.48) and inequalities (2.57) we get that  $\nabla p^\varepsilon$  is uniformly bounded in  $H^{-1}(\Omega_{\text{pm}}^\varepsilon)^d$  as

follows

$$\|\nabla p^\varepsilon\|_{H^{-1}(\Omega_{\text{pm}}^\varepsilon)^d} = \sup_{\boldsymbol{\varphi} \in W_{\text{per}}(\Omega_{\text{pm}}^\varepsilon)^d} \frac{\langle \nabla p^\varepsilon, \boldsymbol{\varphi} \rangle_{H^{-1}(\Omega_{\text{pm}}^\varepsilon)^d, H^1(\Omega_{\text{pm}}^\varepsilon)^d}}{\|\boldsymbol{\varphi}\|_{H^1(\Omega_{\text{pm}}^\varepsilon)^d}} \leq C\varepsilon.$$

Here, we denote the dual space of  $H^1(\Omega_{\text{pm}}^\varepsilon)^d$  by  $H^{-1}(\Omega_{\text{pm}}^\varepsilon)^d$  and define

$$\langle \nabla p^\varepsilon, \boldsymbol{\varphi} \rangle_{H^{-1}(\Omega_{\text{pm}}^\varepsilon)^d, H^1(\Omega_{\text{pm}}^\varepsilon)^d} := \int_{\Omega_{\text{pm}}^\varepsilon} \boldsymbol{f} \cdot \boldsymbol{\varphi} \, dx - \int_{\Omega_{\text{pm}}^\varepsilon} \nabla \boldsymbol{v}^\varepsilon : \nabla \boldsymbol{\varphi} \, dx.$$

Then, from [155, Chapter 1, Proposition 1.2] we know that the following estimate holds true

$$\|p^\varepsilon\|_{L^2(\Omega_{\text{pm}}^\varepsilon)/\mathbb{R}} \leq C(\Omega_{\text{pm}}^\varepsilon) \|\nabla p^\varepsilon\|_{H^{-1}(\Omega_{\text{pm}}^\varepsilon)^d}. \quad (2.58)$$

However, estimate (2.58) is not useful because the constant  $C(\Omega_{\text{pm}}^\varepsilon)$  depends on  $\varepsilon$ , hence, it may not be uniformly bounded for  $\varepsilon \rightarrow 0$ . There are two possibilities to overcome this problem: i) use a restriction operator and a duality argument following Tartar [153], or ii) construct a direct extension of the pressure as in [120]. We do not present the derivation of the *a priori* estimate for the pressure here, but present the main result in Lemma 2.1.

**Lemma 2.1:** *The extensions  $\boldsymbol{v}^\varepsilon$  and  $p^\varepsilon$  given by (2.54) and (2.55) of the pore-scale solutions satisfy the following a priori estimates*

$$\|\boldsymbol{v}^\varepsilon\|_{L^2(\Omega_{\text{pm}})}^2 + \varepsilon \|\nabla \boldsymbol{v}^\varepsilon\|_{L^2(\Omega_{\text{pm}})^{2 \times 2}} \leq C\varepsilon^2, \quad (2.59)$$

$$\|p^\varepsilon\|_{L^2(\Omega_{\text{pm}})/\mathbb{R}} \leq C, \quad (2.60)$$

where the constant  $C > 0$  is independent of  $\varepsilon$ .

*Proof.* The proof can be found in [90, Chapter 3, Lemma 1.3] via the use of Tartar's restriction operator and in [120, Chapter 1, Theorem 1.5] via the direct pressure extension.  $\square$

The next step is to establish asymptotic expansions of the pore-scale functions.

### Step 3: Asymptotic expansions

In this section, we consider  $\mathbf{f} = \mathbf{0}$  in (2.48). For the derivation of Darcy's law in the more general case, where  $\mathbf{f}$  is not necessarily zero, we refer to [90, Section 3.1] or [2, 120]. In order to derive the limit problem, we start from the ansatz that there exist asymptotic expansions of the pore-scale velocity  $\mathbf{v}^\varepsilon$  and pressure  $p^\varepsilon$ . Corresponding to the obtained *a priori* error estimates (2.59) and (2.60) we assume the following asymptotic expansions

$$\mathbf{v}^\varepsilon(\mathbf{x}) \approx \varepsilon^2 \mathbf{v}_0(\mathbf{x}, \mathbf{y}) + \varepsilon^3 \mathbf{v}_1(\mathbf{x}, \mathbf{y}) + \varepsilon^4 \mathbf{v}_2(\mathbf{x}, \mathbf{y}) + \dots, \quad (2.61)$$

$$p^\varepsilon(\mathbf{x}) \approx p_0(\mathbf{x}, \mathbf{y}) + \varepsilon p_1(\mathbf{x}, \mathbf{y}) + \varepsilon^2 p_2(\mathbf{x}, \mathbf{y}) + \dots, \quad (2.62)$$

where  $\mathbf{x}$  is the macroscopic (slow) spatial variable,  $\mathbf{y} = \mathbf{x}/\varepsilon$  is the microscopic (fast) spatial variable,  $\mathbf{v}_i$  and  $p_i$  are  $\mathbf{y}$ -periodic functions for  $i = 0, 1, 2, \dots$

Before we substitute expansions (2.61)–(2.62) into the Stokes problem (2.48)–(2.49) we transform the derivatives

$$\nabla = \nabla_{\mathbf{x}} + \frac{1}{\varepsilon} \nabla_{\mathbf{y}}, \quad \Delta = \Delta_{\mathbf{x}} + \frac{2}{\varepsilon} \nabla_{\mathbf{x}} \cdot \nabla_{\mathbf{y}} + \frac{1}{\varepsilon^2} \nabla_{\mathbf{y}} \cdot \nabla_{\mathbf{y}}. \quad (2.63)$$

Here, the subscript indicates which variable is involved in the differentiation. Inserting equations (2.61)–(2.63) into the pore-scale problem (2.48)–(2.49), combining terms with the same degree of  $\varepsilon$  and neglecting

$\mathcal{O}(\varepsilon^i)$  for  $i \in \mathbb{N}, i > 2$ , yields the following system of equations

$$\mathcal{O}(\varepsilon^{-1}) : \quad \nabla_{\mathbf{y}} p_0(\mathbf{x}, \mathbf{y}) = 0 \quad \text{in } \Omega_{\text{pm}} \times Y_{\text{f}}, \quad (2.64)$$

$$\mathcal{O}(1) : \quad -\Delta_{\mathbf{y}} \mathbf{v}_0(\mathbf{x}, \mathbf{y}) + \nabla_{\mathbf{y}} p_1(\mathbf{x}, \mathbf{y}) + \nabla_{\mathbf{x}} p_0(\mathbf{x}, \mathbf{y}) = \mathbf{0} \quad \text{in } \Omega_{\text{pm}} \times Y_{\text{f}}, \quad (2.65)$$

$$\mathcal{O}(\varepsilon) : \quad \nabla_{\mathbf{y}} \cdot \mathbf{v}_0(\mathbf{x}, \mathbf{y}) = 0 \quad \text{in } \Omega_{\text{pm}} \times Y_{\text{f}}, \quad (2.66)$$

$$-\Delta_{\mathbf{y}} \mathbf{v}_1(\mathbf{x}, \mathbf{y}) + \nabla_{\mathbf{y}} p_2(\mathbf{x}, \mathbf{y}) + \nabla_{\mathbf{x}} p_1(\mathbf{x}, \mathbf{y}) = \mathbf{0} \quad \text{in } \Omega_{\text{pm}} \times Y_{\text{f}}, \quad (2.67)$$

$$\mathcal{O}(\varepsilon^2) : \quad \nabla_{\mathbf{x}} \cdot \mathbf{v}_0(\mathbf{x}, \mathbf{y}) + \nabla_{\mathbf{y}} \cdot \mathbf{v}_1(\mathbf{x}, \mathbf{y}) = 0 \quad \text{in } \Omega_{\text{pm}} \times Y_{\text{f}}, \quad (2.68)$$

$$-\Delta_{\mathbf{y}} \mathbf{v}_2(\mathbf{x}, \mathbf{y}) + \nabla_{\mathbf{y}} p_3(\mathbf{x}, \mathbf{y}) + \nabla_{\mathbf{x}} p_2(\mathbf{x}, \mathbf{y}) = \mathbf{0} \quad \text{in } \Omega_{\text{pm}} \times Y_{\text{f}}, \quad (2.69)$$

$$\mathbf{v}_0(\mathbf{x}, \mathbf{y}) = \mathbf{0} \quad \text{on } \Omega_{\text{pm}} \times \partial Y_{\text{f}}. \quad (2.70)$$

From equation (2.64) we obtain that  $p_0$  is independent of  $\mathbf{y}$ , i.e.,  $p_0(\mathbf{x}, \mathbf{y}) = p_0(\mathbf{x})$ . Considering (2.65), (2.66) and (2.70), we have a Stokes problem for  $\{\mathbf{v}_0, p_1\}$  with the source term  $\nabla_{\mathbf{x}} p_0(\mathbf{x}, \mathbf{y})$ .

In the usual way, we write

$$\nabla_{\mathbf{x}} p_0(\mathbf{x}) = \sum_{j=1}^d \frac{\partial p_0(\mathbf{x})}{\partial x_j} \mathbf{e}_j, \quad (2.71)$$

and equation (2.65) becomes

$$-\Delta_{\mathbf{y}} \mathbf{v}_0(\mathbf{x}, \mathbf{y}) + \nabla_{\mathbf{y}} p_1(\mathbf{x}, \mathbf{y}) = - \sum_{j=1}^d \frac{\partial p_0(\mathbf{x})}{\partial x_j} \mathbf{e}_j. \quad (2.72)$$

Next, we decompose  $\mathbf{v}_0(\mathbf{x}, \mathbf{y})$  and  $p_1(\mathbf{x}, \mathbf{y})$  in products of  $\partial p_0 / \partial x_j(\mathbf{x})$  and terms  $\mathbf{w}^j(\mathbf{y})$  and  $\pi^j(\mathbf{y})$ . Such a decomposition has the advantage that if the pressure  $p_0$  is known, we only have to solve cell problems dependent on  $\mathbf{y}$  to find functions  $\mathbf{v}_0$  and  $p_1$ . Hence, we write

$$\mathbf{v}_0(\mathbf{x}, \mathbf{y}) = - \sum_{j=1}^d \mathbf{w}^j(\mathbf{y}) \frac{\partial p_0(\mathbf{x})}{\partial x_j}, \quad p_1(\mathbf{x}, \mathbf{y}) = - \sum_{j=1}^d \pi^j(\mathbf{y}) \frac{\partial p_0(\mathbf{x})}{\partial x_j}, \quad (2.73)$$

where the functions  $\mathbf{w}^j$  and  $\pi^j$  for  $j = 1, \dots, d$  are the solutions to the

following cell problem

$$-\Delta_{\mathbf{y}} \mathbf{w}^j(\mathbf{y}) + \nabla_{\mathbf{y}} \pi^j(\mathbf{y}) = \mathbf{e}_j, \quad \nabla_{\mathbf{y}} \cdot \mathbf{w}^j(\mathbf{y}) = 0 \quad \text{in } Y_f, \quad (2.74)$$

$$\mathbf{w}^j(\mathbf{y}) = \mathbf{0} \quad \text{on } \partial Y_s, \quad \{\mathbf{w}^j, \pi^j\} \text{ is } \mathbf{y}\text{-periodic}. \quad (2.75)$$

Existence and uniqueness of a solution to problem (2.74)–(2.75) is proven for  $j = 1, \dots, d$  in, e.g., [143]. System (2.74)–(2.75) is obtained by inserting formulas (2.71) and (2.73) in equations (2.65), (2.66) and (2.70). To define the pressure  $\pi^j$  uniquely, we set additionally

$$\int_{Y_f} \pi^j(\mathbf{y}) \, d\mathbf{y} = 0. \quad (2.76)$$

We have seen that decomposition (2.73) allows one to compute  $\mathbf{v}_0$  and  $p_1$  in terms of  $\nabla p_0$  that is independent of  $\mathbf{y}$ . The next step is to formulate the homogenized model.

#### Step 4: Formulation of macroscale model

We solve the cell problem (2.74)–(2.76) for  $j = 1, \dots, d$  and use solution  $\{\mathbf{w}^j, \pi^j\}$  to define the averaged velocity field

$$\mathbf{v}(\mathbf{x}) = \int_{Y_f} \mathbf{v}_0(\mathbf{x}, \mathbf{y}) \, d\mathbf{y} = - \sum_{j=1}^d \int_{Y_f} \mathbf{w}^j(\mathbf{y}) \, d\mathbf{y} \frac{\partial p_0(\mathbf{x})}{\partial x_j} \quad \text{in } \Omega_{\text{pm}}. \quad (2.77)$$

We write the  $i$ -th component of the averaged velocity  $\mathbf{v}$  as

$$v_i(\mathbf{x}) = -\tilde{k}_{ij} \frac{\partial p_0(\mathbf{x})}{\partial x_j}, \quad (2.78)$$

where the coefficients  $\tilde{k}_{ij}$  are given by

$$\tilde{k}_{ij} = \int_{Y_f} w_i^j(\mathbf{y}) \, d\mathbf{y}. \quad (2.79)$$

Here,  $w_i^j$  denotes the  $i$ -th component of the cell problem solution  $\mathbf{w}^j = (w_1^j, \dots, w_d^j)$  for  $i, j = 1, \dots, d$ . We define the tensor  $\tilde{\mathbf{K}} = (\tilde{k}_{ij})_{1 \leq i, j \leq d}$  and rewrite the averaged velocity defined in (2.77) in the following way

$$\mathbf{v}(\mathbf{x}) = -\tilde{\mathbf{K}}\nabla p_0(\mathbf{x}) \quad \text{in } \Omega_{\text{pm}}. \quad (2.80)$$

Equation (2.80) is the well-known Darcy's law in its nondimensional form with the permeability tensor  $\tilde{\mathbf{K}}$  with entries  $\tilde{k}_{ij}$  defined in (2.79).

Now, it remains to show that the averaged velocity  $\mathbf{v}$  is divergence-free, i.e.,  $\nabla \cdot \mathbf{v}(\mathbf{x}) = 0$  for  $\mathbf{x} \in \Omega_{\text{pm}}$ . Considering equations (2.66), (2.68) and (2.77) we obtain

$$\begin{aligned} \nabla \cdot \mathbf{v}(\mathbf{x}) &\stackrel{(2.77)}{=} \nabla \cdot \int_{Y_f} \mathbf{v}_0(\mathbf{x}, \mathbf{y}) \, d\mathbf{y} = \int_{Y_f} \nabla \cdot \mathbf{v}_0(\mathbf{x}, \mathbf{y}) \, d\mathbf{y} \\ &\stackrel{(2.66), (2.68)}{=} - \int_{Y_f} \nabla_{\mathbf{y}} \cdot \mathbf{v}_1(\mathbf{x}, \mathbf{y}) \, d\mathbf{y}. \end{aligned} \quad (2.81)$$

We apply Gauss's theorem to the term on the right hand side of equation (2.81) and get

$$\begin{aligned} \int_{Y_f} \nabla_{\mathbf{y}} \cdot \mathbf{v}_1(\mathbf{x}, \mathbf{y}) \, d\mathbf{y} &= \int_{\partial Y_f} \mathbf{n} \cdot \mathbf{v}_1(\mathbf{x}, \mathbf{y}) \, dS \\ &= \int_{\partial Y_s} \mathbf{n} \cdot \mathbf{v}_1(\mathbf{x}, \mathbf{y}) \, dS + \int_{\partial Y} \mathbf{n} \cdot \mathbf{v}_1(\mathbf{x}, \mathbf{y}) \, dS. \end{aligned} \quad (2.82)$$

The first integral on the right hand side of equation (2.82) is zero due to the no-slip condition given in (2.49). Due to the  $\mathbf{y}$ -periodicity of function  $\mathbf{v}_1$ , the last term in (2.82) is zero. Therefore, it holds

$$\nabla \cdot \mathbf{v}(\mathbf{x}) = 0 \quad \text{for all } \mathbf{x} \in \Omega_{\text{pm}}.$$

We summarize the obtained results in the following proposition:

**Proposition 2.2 (Darcy's law):** *Homogenization of the pore-scale problem (2.48)–(2.49) yields the nondimensional Darcy law with the conserva-*

tion of mass equation given by

$$\mathbf{v}(\mathbf{x}) = -\tilde{\mathbf{K}}\nabla p(\mathbf{x}), \quad \nabla \cdot \mathbf{v}(\mathbf{x}) = 0 \quad \text{in } \Omega_{\text{pm}}, \quad (2.83)$$

where  $\mathbf{v}$  and  $p$  are  $L$ -periodic functions.

*Proof.* This is a result of Step 1–Step 4 and the proof can be also found in [90, Chapter 3, Theorem 1.1].  $\square$

### Step 5: Study of the homogenized problem

In this section, we study the homogenized problem (2.83) concerning existence and uniqueness of a solution.

**Proposition 2.3 (Properties of the permeability tensor):** *The permeability tensor  $\tilde{\mathbf{K}}$  given by formula (2.79) is symmetric and positive definite.*

*Proof.* We integrate the momentum equation in (2.74) for  $j = 1, \dots, d$  over the fluid part  $Y_f$  of the unit cell, multiply with  $\mathbf{w}^i(\mathbf{y})$  for  $i = 1, \dots, d$ , use formula (2.79) and obtain

$$\begin{aligned} \int_{Y_f} \Delta_{\mathbf{y}} \mathbf{w}^j(\mathbf{y}) \cdot \mathbf{w}^i(\mathbf{y}) \, d\mathbf{y} - \int_{Y_f} \nabla_{\mathbf{y}} p^j(\mathbf{y}) \cdot \mathbf{w}^i(\mathbf{y}) \, d\mathbf{y} \\ \stackrel{(2.74)}{=} - \int_{Y_f} \mathbf{e}_j \cdot \mathbf{w}^i(\mathbf{y}) \, d\mathbf{y} = - \int_{Y_f} w_j^i(\mathbf{y}) \, d\mathbf{y} \stackrel{(2.79)}{=} -\tilde{k}_{ji}. \end{aligned} \quad (2.84)$$

We apply integration by parts to the first term on the left hand side of equation (2.84), make use the  $\mathbf{y}$ -periodicity of function  $\mathbf{w}^j$  for  $j = 1, \dots, d$

and the no-slip condition in (2.75), and get

$$\begin{aligned}
 & \int_{Y_f} \Delta_{\mathbf{y}} \mathbf{w}^j(\mathbf{y}) \cdot \mathbf{w}^i(\mathbf{y}) \, d\mathbf{y} \\
 &= \int_{\partial Y_f} (\nabla_{\mathbf{y}} \mathbf{w}^j(\mathbf{y}) \mathbf{w}^i(\mathbf{y})) \cdot \mathbf{n} \, dS - \int_{Y_f} \nabla_{\mathbf{y}} \mathbf{w}^j(\mathbf{y}) : \nabla_{\mathbf{y}} \mathbf{w}^i(\mathbf{y}) \, d\mathbf{y} \\
 &\stackrel{(2.75)}{=} - \int_{Y_f} \nabla_{\mathbf{y}} \mathbf{w}^j(\mathbf{y}) : \nabla_{\mathbf{y}} \mathbf{w}^i(\mathbf{y}) \, d\mathbf{y}. \tag{2.85}
 \end{aligned}$$

Integrating the second term on the left hand side of equation (2.84) by parts, using the mass conservation equation in (2.74) and boundary conditions (2.75) yields

$$\begin{aligned}
 - \int_{Y_f} \nabla_{\mathbf{y}} p^j(\mathbf{y}) \cdot \mathbf{w}^i(\mathbf{y}) \, d\mathbf{y} &= - \int_{\partial Y_f} p^j(\mathbf{y}) \mathbf{w}^i(\mathbf{y}) \cdot \mathbf{n} \, dS + \int_{Y_f} p^j(\mathbf{y}) \nabla_{\mathbf{y}} \cdot \mathbf{w}^i(\mathbf{y}) \, d\mathbf{y} \\
 &\stackrel{(2.74)}{=} - \int_{\partial Y_f} p^j(\mathbf{y}) \mathbf{w}^i(\mathbf{y}) \cdot \mathbf{n} \, dS \stackrel{(2.75)}{=} 0. \tag{2.86}
 \end{aligned}$$

We combine equations (2.84), (2.85) and (2.86) that leads to

$$\int_{Y_f} \nabla_{\mathbf{y}} \mathbf{w}^j(\mathbf{y}) : \nabla_{\mathbf{y}} \mathbf{w}^i(\mathbf{y}) \, d\mathbf{y} = \tilde{k}_{ji}. \tag{2.87}$$

Interchanging the indices  $i$  and  $j$  on the left hand side of equation (2.87) results in the same integral term, and using equality (2.87), we get for all  $i, j = 1, \dots, d$ :

$$\tilde{k}_{ij} \stackrel{(2.87)}{=} \int_{Y_f} \nabla_{\mathbf{y}} \mathbf{w}^i(\mathbf{y}) : \nabla_{\mathbf{y}} \mathbf{w}^j(\mathbf{y}) \, d\mathbf{y} = \int_{Y_f} \nabla_{\mathbf{y}} \mathbf{w}^j(\mathbf{y}) : \nabla_{\mathbf{y}} \mathbf{w}^i(\mathbf{y}) \, d\mathbf{y} \stackrel{(2.87)}{=} \tilde{k}_{ji}.$$

This implies that the permeability tensor  $\tilde{\mathbf{K}}$  given by (2.79) is symmetric.

It remains to prove that  $\tilde{\mathbf{K}} \in \mathbb{R}^{d \times d}$  is positive definite, i.e.,  $\mathbf{x} \cdot \tilde{\mathbf{K}} \mathbf{x} > 0$  for all



$\mathbf{x} \in \mathbb{R}^d \setminus \{\mathbf{0}\}$ . We use (2.79), (2.84) and (2.85), and obtain

$$\begin{aligned} \mathbf{x} \cdot \tilde{\mathbf{K}} \mathbf{x} &= \sum_{i,j=1}^d \tilde{k}_{ij} x_i x_j \stackrel{(2.79)}{=} \sum_{i,j=1}^d x_i x_j \int_{Y_f} w_i^j(\mathbf{y}) \, d\mathbf{y} \\ &\stackrel{(2.85), (2.84)}{=} \sum_{i,j=1}^d x_i x_j \int_{Y_f} \nabla_{\mathbf{y}} \mathbf{w}^i(\mathbf{y}) : \nabla_{\mathbf{y}} \mathbf{w}^j(\mathbf{y}) \, d\mathbf{y}. \end{aligned} \quad (2.88)$$

Rewriting the right hand side of (2.88) using the definition of the inner product yields

$$\begin{aligned} \sum_{i,j=1}^d \sum_{k=1}^d x_i x_j \int_{Y_f} \nabla_{\mathbf{y}} w_k^i(\mathbf{y}) \cdot \nabla_{\mathbf{y}} w_k^j(\mathbf{y}) \, d\mathbf{y} \\ &= \sum_{i,j=1}^d \sum_{k,l=1}^d \int_{Y_f} x_i \frac{\partial w_k^i}{\partial y_l}(\mathbf{y}) x_j \frac{\partial w_k^j}{\partial y_l}(\mathbf{y}) \, d\mathbf{y} \\ &= \sum_{k,l=1}^d \int_{Y_f} \left( \sum_{i=1}^d x_i \frac{\partial w_k^i}{\partial y_l}(\mathbf{y}) \right) \left( \sum_{j=1}^d x_j \frac{\partial w_k^j}{\partial y_l}(\mathbf{y}) \right) \, d\mathbf{y} \\ &= \sum_{k,l=1}^d \int_{Y_f} \left( \sum_{i=1}^d x_i \frac{\partial w_k^i}{\partial y_l}(\mathbf{y}) \right)^2 \, d\mathbf{y} \geq 0. \end{aligned} \quad (2.89)$$

The right hand side of equation (2.89) is only zero if all components  $x_i = 0$  for  $i = 1, \dots, d$ , since the partial derivatives  $(\partial w_k^i)/(\partial y_l) \neq 0$  for  $i, k, l = 1, \dots, d$  by definition of problem (2.75)–(2.76). Hence, considering equations (2.88) and (2.89), we get

$$\mathbf{x} \cdot \tilde{\mathbf{K}} \mathbf{x} = \sum_{k,l=1}^d \int_{Y_f} \left( \sum_{i=1}^d x_i \frac{\partial w_k^i}{\partial y_l}(\mathbf{y}) \right)^2 \, d\mathbf{y} > 0,$$

if at least one component  $x_i \neq 0$  for  $i = 1, \dots, d$ , and we have proven that the permeability tensor  $\tilde{\mathbf{K}}$  is positive definite.  $\square$

In order to prove existence and uniqueness of a solution to the homoge-

nized problem (2.83), we transform the dimensionless equations in their following mixed form, which is a second order elliptic equation for the pressure

$$-\nabla \cdot (\tilde{\mathbf{K}} \nabla p(\mathbf{x})) = 0 \quad \text{in } \Omega_{\text{pm}}. \quad (2.90)$$

Then, from the Lax–Milgram theorem (Appendix A.3, Theorem A.7), we get existence and uniqueness of a solution  $p \in H_{\text{per}}^1(\Omega_{\text{pm}})/\mathbb{R} = \{\varphi \in H^1(\Omega_{\text{pm}}) : \int_{\Omega_{\text{pm}}} \varphi \, d\mathbf{x} = 0, \varphi \text{ is } L\text{-periodic}\}$  of the macroscale problem (2.83).

### Step 6: Proof of two-scale convergence

From the mathematical point of view, the method of two-scale asymptotic expansions is a formal one because, a priori, there is no reason for the ansatz (2.61) and (2.62) to hold true. Thus, in order to justify the homogenization result (2.83), which has been derived based on the assumption that there exist asymptotic expansions, a further step is required. In the following, we present results on the convergence of the pore-scale solution  $\{\mathbf{v}^\varepsilon, p^\varepsilon\}$  to the homogenized one  $\{\mathbf{v}, p\}$  obtained by Allaire [2, 3] and Mikelić [120] using the two-scale convergence method. Here, the strategy is to test the weak formulation of the pore-scale problem (2.48)–(2.49) with an oscillating function  $\varphi(\mathbf{x}, \mathbf{x}/\varepsilon)$ , which admits passing to the limit  $\varepsilon \rightarrow 0$  that directly yields the homogenized result. Before we provide the convergence results, we recall the definition of the two-scale convergence in the function space  $L^2$  following [3].

**Definition 2.4 (Two-scale convergence):** *The sequence  $\{w^\varepsilon\} \subset L^2(\Omega_{\text{pm}})$  converges in the two-scale sense in  $L^2$  to a limit  $w(\mathbf{x}, \mathbf{y}) \in L^2(\Omega_{\text{pm}} \times Y)$  if for any  $\varphi(\mathbf{x}, \mathbf{y}) \in C_0^\infty(\Omega_{\text{pm}}; C_{\text{per}}^\infty(Y))$  we have*

$$\lim_{\varepsilon \rightarrow 0} \int_{\Omega_{\text{pm}}} w^\varepsilon(\mathbf{x}) \varphi\left(\mathbf{x}, \frac{\mathbf{x}}{\varepsilon}\right) \, d\mathbf{x} = \int_{\Omega_{\text{pm}}} \int_Y w(\mathbf{x}, \mathbf{y}) \varphi(\mathbf{x}, \mathbf{y}) \, d\mathbf{y} \, d\mathbf{x}, \quad (2.91)$$

where  $C_{per}^\infty(Y) = \{\varphi \in C^\infty(Y) : \varphi \text{ is } \mathbf{y}\text{-periodic}\}$  and  $\mathbf{y} = \mathbf{x}/\varepsilon$ .

In the two-scale limit  $w(\mathbf{x}, \mathbf{y})$  some oscillations of the sequence  $\{w^\varepsilon\}$  are incorporated and, in case all of them are captured, we obtain strong convergence. Hence, two-scale convergence is stronger than weak convergence in  $L^2$ , but it is weaker than strong convergence in  $L^2$ .

In Theorem 2.5, we summarize the convergence results rigorously derived in [2, 120] that justify the first terms in the expansions (2.61) and (2.62) for any bounded sequences  $\mathbf{v}^\varepsilon$  and  $p^\varepsilon$ , respectively.

**Theorem 2.5 (Convergence theorem):** *Let  $\{\mathbf{v}^\varepsilon, p^\varepsilon\}$  be the extension given by (2.54) and (2.55) of the solution to problem (2.48)–(2.49) with  $\int_{\Omega_{pm}^\varepsilon} p^\varepsilon \, d\mathbf{x} = 0$ . Let  $p = p_0$  be the solution to problem (2.83) and  $\mathbf{v}_0$  given in (2.73). Then, it holds*

$$\frac{\mathbf{v}^\varepsilon(\mathbf{x})}{\varepsilon^2} \rightarrow \mathbf{v}_0(\mathbf{x}, \mathbf{y}) \quad \text{in the two-scale sense in } L^2, \quad (2.92)$$

$$\frac{\nabla \mathbf{v}^\varepsilon(\mathbf{x})}{\varepsilon^2} \rightarrow \nabla_{\mathbf{y}} \mathbf{v}_0(\mathbf{x}, \mathbf{y}) \quad \text{in the two-scale sense in } L^2, \quad (2.93)$$

$$p^\varepsilon(\mathbf{x}) \rightarrow p(\mathbf{x}, \mathbf{y}) \quad \text{in } L^2. \quad (2.94)$$

*Proof.* See [120, proof of Theorem 1.15]. □

Theorem 2.5 states that the sequence  $\{\mathbf{v}^\varepsilon\}$  converges towards  $\mathbf{v}_0$  in the two-scale sense and that  $\{p^\varepsilon\}$  strongly converges in  $L^2$  towards  $p$ . More details on the two-scale convergence method can be found in [1–3, 90, 120].

In the literature there exist also stronger convergence results for the pore-scale velocity. For example, Allaire [1] proves the strong convergence  $U^\varepsilon \rightarrow \mathbf{0}$  in  $L^2$ , where  $U^\varepsilon = \varepsilon^{-2} \mathbf{v}^\varepsilon - \mathbf{v}_0(\mathbf{x}, \mathbf{y})$ . Further, in [120] the authors show that the  $L^2$ -norm of  $U^\varepsilon$  is bounded by  $C\varepsilon$  when adding a divergence corrector  $Q^\varepsilon$  to the approximation  $\mathbf{v}_0$ . Unfortunately, the new approximation  $\mathbf{v}_0 + Q^\varepsilon$  of the pore-scale velocity has nonzero trace on the

boundary  $\partial\Omega_{\text{pm}}$ . As long as we consider periodic boundary conditions on  $\partial\Omega_{\text{pm}}$  for the pore-scale problem (2.48)–(2.49), we do not have to adjust the boundary conditions on the external boundary for the upscaled problem (2.83). However, if nonperiodic boundary conditions are applied, it becomes more difficult in comparison to the periodic case to formulate the corresponding macroscale model, and also to prove convergence and to obtain rigorous error estimates [90, 95, 120]. In this case, additional corrections in form of boundary layers and auxiliary functions are needed that is discussed in the next section.

### 2.3.3 Boundary layer theory: Interface conditions for unidirectional flows

The assumption on the periodicity of a porous medium, which is needed to apply periodic homogenization, is not valid close to the boundaries of the domain. Therefore, the approximation, obtained using homogenization of the pore-scale equations, performs well inside the porous medium, however, this is not the case near the domain boundaries. Here, the behavior of the pore-scale functions may greatly differ from their behavior inside the porous material. However, this is not reflected in the Darcy law, which was derived in the previous section. There, we avoided addressing this issue by applying periodic boundary conditions on the external boundary.

In order to incorporate boundary layer effects into the macroscale model, corrector functions need to be added to the approximation of the pore-scale solution. In the previous section, for example, the pore-scale approximation that needs to be improved is  $\mathbf{v}_0$  given by (2.73). For the purpose of improvement, boundary layer correctors are used, which are scaled solutions to boundary layer problems. The latter are Stokes problems defined in a small vertical stripe of the domain, the so-called boundary layer stripe (Figure 2.8, right). One big advantage of boundary layer correctors is that they stabilize exponentially fast to some constants away from the boundary, i.e., their energies concentrate only near the boundary of the

porous domain. Further, in terms of computational complexity, boundary layer correctors are cheap compared to correctors defined in the entire flow domain.

Fixing the boundary conditions on the external boundary of a porous medium for a macroscopic model is a challenging problem. First attempts were made in [109] for the Laplace operator. In case of the Navier–Stokes equations, boundary layer correctors for the no-slip condition on the porous-medium boundary have been constructed in [115].

Besides problems involving porous-medium domains only, boundary layer correctors play a very important role in context with contact surfaces. In coupled Stokes–Darcy systems the sharp fluid–porous interface is such a contact surface and Darcy’s law is no longer valid there. Thus, in order to account for interfacial effects, the macroscale model needs to be improved using boundary layer correctors. Efforts to derive interface conditions for Stokes–Darcy problems by means of homogenization and boundary layer theory were first made by Jäger and Mikelić [95]. Based on their studies coupling conditions for one-dimensional flows, i.e., parallel or perpendicular to the porous layer, were rigorously derived using the same averaging strategy and analyzed in, e.g., [33, 34, 96, 98]. The main findings of these works are presented below. Generalized coupling conditions that account for multidimensional flows to the interface were derived via homogenization theory with boundary layers in [EE4] for the first time. These conditions are presented in Chapter 3 as one of the key results of this thesis.

### Interface conditions for unidirectional flows in Stokes–Darcy systems

In the following, we present two sets of interface conditions for the Stokes–Darcy problem derived via boundary layer theory and periodic homogenization [34, 95–98]. Based on the choice of external boundary condition for the pore-scale problem (2.48), one set of coupling conditions is derived for flows parallel to the fluid–porous interface, the other one for flows perpendicular to the porous layer. For both coupling concepts,

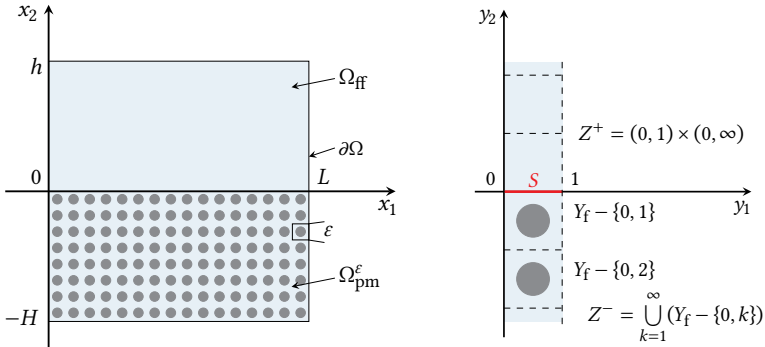


Figure 2.8: Geometrical setting of the dimensionless pore-scale domain (left) and the boundary layer stripe (right).

we present the main results obtained by the authors including the approximation of the pore-scale solution via asymptotic expansions, the most important boundary layer problems and rigorous error estimates. For further details, the interested reader is referred to [33, 34, 95–98, 114].

Before we present the aforementioned interface conditions, we provide the geometrical setting of the coupled domain and the flow models in the nondimensional framework. We consider the free-flow region  $\Omega_{\text{ff}} = (0, L) \times (0, h)$  and the porous medium  $\Omega_{\text{pm}} = (0, L) \times (-H, 0)$ , separated by the sharp interface  $\Sigma = (0, L) \times \{0\}$ , which is void of thermodynamic properties, i.e., it cannot store and transport any mass or momentum. The porous medium is constructed in the same way as described in Step 1 in Section 2.3.2, where  $\varepsilon$  is the nondimensional characteristic pore size. We chose the unit tangential vector  $\boldsymbol{\tau} = \mathbf{e}_1$  and the unit normal vector  $\mathbf{n} = \mathbf{e}_2$  on the interface  $\Sigma$ . The pore-scale flow domain is denoted by  $\Omega^\varepsilon$  consisting of the free-flow region  $\Omega_{\text{ff}}$  and the pore space  $\Omega_{\text{pm}}^\varepsilon$  of the porous-medium domain  $\Omega_{\text{pm}}$  (Figure 2.8, left). For simplicity, we assume  $L/\varepsilon, h/\varepsilon, H/\varepsilon \in \mathbb{N}$ . Further, we introduce the boundary layer stripe  $Z^{\text{bl}} = Z^+ \cup S \cup Z^-$  with its fluid part  $Z^+ = (0, 1) \times (0, \infty)$  and solid part  $Z^- = \bigcup_{k=1}^{\infty} (Y_{\text{f}} - \{0, k\})$ .

The flow at the pore scale is described by the stationary dimensionless Stokes equations with the no-slip conditions on the solid boundaries

$$-\Delta \mathbf{v}^\varepsilon + \nabla p^\varepsilon = \mathbf{0}, \quad \nabla \cdot \mathbf{v}^\varepsilon = 0 \quad \text{in } \Omega^\varepsilon, \quad \mathbf{v}^\varepsilon = \mathbf{0} \quad \text{on } \partial\Omega^\varepsilon \setminus \partial\Omega. \quad (2.95)$$

From the macroscale perspective, the nondimensional Stokes equations are used to model the free flow

$$-\Delta \cdot \mathbf{v}^{\text{ff}} + \nabla p^{\text{ff}} = \mathbf{0}, \quad \nabla \cdot \mathbf{v}^{\text{ff}} = 0 \quad \text{in } \Omega_{\text{ff}}, \quad (2.96)$$

and the dimensionless Darcy equations are applied in the porous medium

$$-\nabla \cdot (\tilde{\mathbf{K}} \nabla p^{\text{pm}}) = 0 \quad \text{in } \Omega_{\text{pm}}. \quad (2.97)$$

Conditions on the external boundary both for the pore-scale problem (2.95) and the Stokes–Darcy problem (2.96)–(2.97) are specified in the subsequent paragraphs. In addition, effective coupling conditions on the fluid–porous interface are required to close the macroscopic problem formulation. Below, the derivation of such conditions for the Stokes–Darcy coupling based on [34, 95, 96, 98] is presented for two scenarios: i) parallel flow to the interface and ii) perpendicular flow to the interface.

For the sake of clarity, we write  $\varphi$  for  $\varphi(\mathbf{x})$ ,  $\mathbf{x} \in \Omega = \Omega_{\text{ff}} \cup \Omega_{\text{pm}}$ , and  $\varphi(\mathbf{y}) = \varphi(\mathbf{x}/\varepsilon)$  if the function  $\varphi$  is evaluated at  $\mathbf{y} = \mathbf{x}/\varepsilon$ . Further, the Heaviside step function is given by

$$\mathcal{H}(x) = \begin{cases} 1 & \text{if } x \geq 0, \\ 0 & \text{else.} \end{cases} \quad (2.98)$$

### i) Parallel flow to the interface

The authors from [96, 98] study the laminar, viscous flow over a periodic porous medium, similar to the experiments of Beavers and Joseph [15]. In

this work, the pore-scale system (2.95) is completed with the following boundary conditions

$$\mathbf{v}^\varepsilon = \mathbf{0} \quad \text{on } (0, L) \times (\{-H\} \cup \{h\}), \quad v_2^\varepsilon = 0 \quad \text{on } (\{0\} \cup \{L\}) \times (-H, h), \quad (2.99)$$

$$p^\varepsilon = p_{\text{in}} \quad \text{on } \{0\} \times (-H, h), \quad p^\varepsilon = p_{\text{out}} \quad \text{on } \{L\} \times (-H, h). \quad (2.100)$$

Here,  $p_{\text{in}}$  is the prescribed pressure on the left boundary and  $p_{\text{out}}$  the one on the right boundary of the domain  $\Omega^\varepsilon$ , where  $p_{\text{in}} > p_{\text{out}}$ . Considering conditions (2.99) and (2.100) the flow is driven by a pressure gradient from the left side of the entire domain to the right side, resulting in a flow parallel to the porous layer.

From the macroscale perspective, the Poiseuille flow with  $\{\mathbf{v}^{\text{Pois}}, p^{\text{Pois}}\}$  is used to describe the fluid motion in the free-flow region. In the porous-medium domain the velocity is set to zero and the pressure is assumed to have the same form as in the free-flow region. Thus, after [96, 98] the first approximation  $\{\mathbf{v}_{\text{approx}}^{0,\varepsilon}, p_{\text{approx}}^{0,\varepsilon}\}$  of the pore-scale velocity and pressure reads

$$\begin{aligned} \mathbf{v}_{\text{approx}}^{0,\varepsilon} &= \mathcal{H}(x_2) \underbrace{\left( \frac{p_{\text{out}} - p_{\text{in}}}{2L} x_2 (x_2 - h) \right)}_{=: \mathbf{v}^{\text{Pois}}} \mathbf{e}_1, \\ p_{\text{approx}}^{0,\varepsilon} &= \underbrace{\frac{p_{\text{out}} - p_{\text{in}}}{L} x_1 + p_{\text{in}}}_{=: p^{\text{Pois}}}. \end{aligned} \quad (2.101)$$

However, this first approximation is not sufficient for the flow description in the free-flow region near the interface, due to the presence of an oscillatory boundary layer. The authors in [96, 98] consider the weak formulation of the pore-scale problem (2.95), (2.99)–(2.100) using the first approximation (2.101) and identify the terms corresponding to the physical boundary layer. Based on this investigation, the following boundary layer



problem is introduced

$$\begin{aligned}
-\Delta_{\mathbf{y}} \boldsymbol{\beta}^{\text{bl}}(\mathbf{y}) + \nabla_{\mathbf{y}} \omega^{\text{bl}}(\mathbf{y}) &= \mathbf{0}, \quad \nabla_{\mathbf{y}} \cdot \boldsymbol{\beta}^{\text{bl}}(\mathbf{y}) = 0 \quad \text{in } Z^+ \cup Z^-, \\
\llbracket \boldsymbol{\beta}^{\text{bl}}(\mathbf{y}) \rrbracket_S &= \mathbf{0}, \quad \llbracket (\nabla_{\mathbf{y}} \boldsymbol{\beta}^{\text{bl}}(\mathbf{y}) - \omega^{\text{bl}}(\mathbf{y}) \mathbf{I}) \mathbf{e}_2 \rrbracket_S = \mathbf{e}_1 \quad \text{on } S, \\
\boldsymbol{\beta}^{\text{bl}}(\mathbf{y}) &= \mathbf{0} \quad \text{on } \bigcup_{k=1}^{\infty} (\partial Y_S - \{0, k\}), \quad \{\boldsymbol{\beta}^{\text{bl}}, \omega^{\text{bl}}\} \text{ is } \mathbf{y}\text{-periodic}.
\end{aligned} \tag{2.102}$$

For existence and uniqueness of the solution to problem (2.102), we refer to [95, 96, 98].

Now, the first approximation  $\{\mathbf{v}_{\text{approx}}^{0,\varepsilon}, p_{\text{approx}}^{0,\varepsilon}\}$  is improved by adding appropriate correctors resulting from the boundary layer solution  $\{\boldsymbol{\beta}^{\text{bl}}, \omega^{\text{bl}}\}$  as follows

$$\begin{aligned}
\mathbf{v}_{\text{approx}}^{1,\varepsilon} &= \mathbf{v}_{\text{approx}}^{0,\varepsilon} - \varepsilon \boldsymbol{\beta}^{\text{bl}}(\mathbf{y}) \frac{\partial v_1^{\text{Pois}}}{\partial x_2} \Big|_{\Sigma} \\
&= \mathcal{H}(x_2) \mathbf{v}^{\text{Pois}} - \varepsilon \boldsymbol{\beta}^{\text{bl}}(\mathbf{y}) \frac{\partial v_1^{\text{Pois}}}{\partial x_2} \Big|_{\Sigma}, \\
p_{\text{approx}}^{1,\varepsilon} &= p_{\text{approx}}^{0,\varepsilon} - \omega^{\text{bl}}(\mathbf{y}) \frac{\partial v_1^{\text{Pois}}}{\partial x_2} \Big|_{\Sigma} \\
&= p^{\text{Pois}} - \omega^{\text{bl}}(\mathbf{y}) \frac{\partial v_1^{\text{Pois}}}{\partial x_2} \Big|_{\Sigma},
\end{aligned} \tag{2.103}$$

where  $(\partial v_1^{\text{Pois}} / \partial x_2)|_{\Sigma} := (\partial v_1^{\text{Pois}} / \partial x_2)(x_1, 0)$ . In [95] it is shown that the boundary layer velocity  $\boldsymbol{\beta}^{\text{bl}}(\mathbf{y})$  and pressure  $\omega^{\text{bl}}(\mathbf{y})$  stabilize exponentially fast to some constants for  $y_2 \rightarrow \infty$  and to zero for  $y_2 \rightarrow -\infty$ . The stabilizing boundary layer constants  $C^{\text{bl}}$  and  $C_{\omega}^{\text{bl}}$  for the velocity and pressure, respectively, are given by

$$\begin{aligned}
C^{\text{bl}} &= (C_1^{\text{bl}}, 0)^{\top} = \left( \int_0^1 \beta_1^{\text{bl}}(y_1, 0) \, dy_1, 0 \right)^{\top}, \\
C_{\omega}^{\text{bl}} &= \int_0^1 \omega^{\text{bl}}(y_1, 0) \, dy_1.
\end{aligned} \tag{2.104}$$

Due to the exponentially fast stabilization of the boundary layer solution  $\{\boldsymbol{\beta}^{\text{bl}}, \omega^{\text{bl}}\}$ , a counter flow in form of an Oseen–Couette system in the free-flow region is created [98, equations (7.1)–(7.4)]. In order to improve the effective approximations (2.103), the solution to the counter flow problem and the stabilizing constants are added to  $\mathbf{v}_{\text{approx}}^{1,\varepsilon}$  and  $p_{\text{approx}}^{1,\varepsilon}$ . We do not go into further details here and refer to [98].

The authors [98] propose the following final approximation of the pore-scale velocity and pressure in case of flows parallel to the porous bed

$$\begin{aligned} \mathbf{v}_{\text{approx}}^{\text{final},\varepsilon} &= \mathcal{H}(x_2)\mathbf{v}^{\text{Pois}} - \varepsilon\boldsymbol{\beta}^{\text{bl}}(\mathbf{y})\frac{\partial v_1^{\text{Pois}}}{\partial x_2}\Big|_{\Sigma} \\ &\quad + \mathcal{H}(x_2)\varepsilon C_1^{\text{bl}}\left(\frac{\partial v_1^{\text{Pois}}}{\partial x_2}\Big|_{\Sigma}\mathbf{e}_1 + \mathbf{d}\right), \\ p_{\text{approx}}^{\text{final},\varepsilon} &= \mathcal{H}(x_2)p^{\text{Pois}} + \mathcal{H}(-x_2)p^{\text{reg},\varepsilon} \\ &\quad - \left(\omega^{\text{bl}}(\mathbf{y}) - \mathcal{H}(x_2)C_{\omega}^{\text{bl}}\right)\frac{\partial v_1^{\text{Pois}}}{\partial x_2}\Big|_{\Sigma}. \end{aligned} \quad (2.105)$$

Here,  $\mathbf{d} = (1 - x_2/h)\mathbf{e}_1$  is the solution of the Couette flow and  $p^{\text{reg},\varepsilon}$  is an appropriate regularization of the pressure in the porous medium. Based on the pore-scale problem (2.95), (2.99)–(2.100) and the approximation (2.105), the following coupling conditions for the Stokes–Darcy problem (2.96)–(2.97) are derived in [95, 96, 98]:

$$\mathbf{v}^{\text{ff}} \cdot \mathbf{n} = 0 \quad \text{on } \Sigma, \quad (2.106)$$

$$p^{\text{pm}} = p^{\text{ff}} + C_{\omega}^{\text{bl}}\boldsymbol{\tau} \cdot \nabla \mathbf{v}^{\text{ff}} \mathbf{n} \quad \text{on } \Sigma, \quad (2.107)$$

$$\mathbf{v}^{\text{ff}} \cdot \boldsymbol{\tau} = -\varepsilon C_1^{\text{bl}}\boldsymbol{\tau} \cdot \nabla \mathbf{v}^{\text{ff}} \mathbf{n} \quad \text{on } \Sigma, \quad (2.108)$$

where  $\mathbf{v}^{\text{ff}} = \mathbf{v}^{\text{Pois}}$  and  $p^{\text{ff}} = p^{\text{Pois}}$ . Condition (2.106) differs from the conservation of mass equation (2.17), however, it is reasonable for flows parallel to the porous layer for which conditions (2.106)–(2.108) are developed. In this case, the normal component of the Darcy velocity is almost zero, thus, can be neglected. Interface condition (2.107) links the pressure

fields in the porous medium and in the free-flow domain. For isotropic porous media,  $C_\omega^{\text{bl}} = 0$  and we obtain continuity of pressure across the interface. Condition (2.108) is a variant of the Beavers–Joseph–Saffman law (2.20) taking  $\alpha_{\text{BJ}} = \sqrt{\widetilde{K}}/C_1^{\text{bl}}$ , where  $\sqrt{\widetilde{K}} = \sqrt{\boldsymbol{\tau} \widetilde{\mathbf{K}} \boldsymbol{\tau}}$ .

In order to provide error estimates to justify the obtained interface conditions (2.106)–(2.108), the velocity and pressure error functions are used

$$\mathbf{U}^\varepsilon = \mathbf{v}^\varepsilon - \mathbf{v}_{\text{approx}}^{\text{final},\varepsilon}, \quad P^\varepsilon = p^\varepsilon - p_{\text{approx}}^{\text{final},\varepsilon}. \quad (2.109)$$

Then, the following theorem was proven in [96]:

**Theorem 2.6:** *For the considered pore-scale problem (2.95), (2.99)–(2.100) the following error estimates hold for  $\mathbf{U}^\varepsilon$  and  $P^\varepsilon$  defined by (2.109):*

$$\begin{aligned} \|\mathbf{U}^\varepsilon\|_{L^2(\Omega_{\text{pm}}^\varepsilon)}^2 &\leq C\varepsilon^2 |\log \varepsilon|, & \|\mathbf{U}^\varepsilon\|_{L^2(\Sigma)}^2 &\leq C\varepsilon^{3/2} |\log \varepsilon|, \\ \|\mathbf{U}^\varepsilon\|_{L^2(\Omega_{\text{ff}})}^2 &\leq C\varepsilon^{3/2} |\log \varepsilon|, & \|P^\varepsilon\|_{L^2(\Omega_{\text{ff}})} &\leq C\varepsilon |\log \varepsilon|. \end{aligned}$$

*Proof.* See proof in [96, Theorem 6]. □

An error estimate for the pressure approximation in the porous medium is not obtained in [96] and the authors note that this remains an open problem which is still not solved for the considered flow problem (2.95), (2.99)–(2.100).

## ii) Perpendicular flow to the interface

In [34] a flow problem is studied where the fluid flow is perpendicular to the porous layer. The authors consider forced infiltration of a fluid into

a porous medium based on the Stokes system (2.95) with the following boundary conditions

$$\mathbf{v}^\varepsilon = \mathbf{v}^{\text{in}} \text{ on } (0, L) \times \{h\}, \quad v_2^\varepsilon = v^{\text{out}}, \quad \frac{\partial v_1^\varepsilon}{\partial x_2} = 0 \text{ on } (0, L) \times \{-H\}, \quad (2.110)$$

$$\{\mathbf{v}^\varepsilon, p^\varepsilon\} \text{ is } L\text{-periodic in } x_1. \quad (2.111)$$

Here,  $\mathbf{v}^{\text{in}} = (v_1^{\text{in}}, v_2^{\text{in}})^\top$  is a given inflow velocity and  $v^{\text{out}}$  is an outflow velocity such that

$$\int_0^L v_2^{\text{in}}(x_1) dx_1 = \int_0^L v^{\text{out}}(x_1) dx_1. \quad (2.112)$$

As before, the Stokes–Darcy model (2.96)–(2.97) is used to describe the flow at the macroscale. However, in this case the free-flow velocity and the filtration velocity in the porous medium are of the same order of magnitude, i.e., of order  $\mathcal{O}(1)$ . Taking into account the homogenization ansatz (2.61)–(2.62) and the formulas given in (2.73), the following first approximation of the pore-scale solution is proposed in [34]:

$$\begin{aligned} \mathbf{v}_{\text{approx}}^{0,\varepsilon} &= \mathcal{H}(x_2) \mathbf{v}^{\text{ff}} - \mathcal{H}(-x_2) \sum_{j=1}^2 \frac{\partial p^{\text{pm}}}{\partial x_j} \mathbf{w}^j(\mathbf{y}), \\ p_{\text{approx}}^{0,\varepsilon} &= \mathcal{H}(x_2) p^{\text{ff}} + \mathcal{H}(-x_2) \left[ \varepsilon^{-2} p^{\text{pm}} - \varepsilon^{-1} \sum_{j=1}^2 \left( \frac{\partial p^{\text{pm}}}{\partial x_j} \pi^j(\mathbf{y}) \right) \right], \end{aligned} \quad (2.113)$$

where  $\{\mathbf{w}^j, \pi^j\}$  is the solution to the cell problem (2.74)–(2.76) for  $j = 1, 2$ . With the first approximation  $\mathbf{v}_{\text{approx}}^{0,\varepsilon}$  given in (2.113), the velocity inside the two flow domains far away from the interface is approximated sufficiently well, however, this is not the case in the near interface region. Furthermore, function  $\mathbf{v}_{\text{approx}}^{0,\varepsilon}$  is not divergence free yet and the boundary conditions (2.110) on the external boundary are not fulfilled. Thus, corrections in form of boundary layer correctors are needed to resolve these problems.

In order to approximate the velocity in the near interface region, the following boundary layer problem is defined [34]:

$$\begin{aligned} -\Delta_{\mathbf{y}}\boldsymbol{\beta}^{2,\text{bl}}(\mathbf{y}) + \nabla_{\mathbf{y}}\omega^{2,\text{bl}}(\mathbf{y}) &= \mathbf{0}, & \nabla_{\mathbf{y}}\cdot\boldsymbol{\beta}^{2,\text{bl}}(\mathbf{y}) &= 0 & \text{in } Z^+ \cup Z^-, \\ \llbracket\boldsymbol{\beta}^{2,\text{bl}}(\mathbf{y})\rrbracket_S &= k_{22}\mathbf{e}_2 - \mathbf{w}^j(\mathbf{y}) & & & \text{on } S, \\ \llbracket(\nabla_{\mathbf{y}}\boldsymbol{\beta}^{2,\text{bl}}(\mathbf{y}) - \omega^{2,\text{bl}}(\mathbf{y})\mathbf{I})\mathbf{e}_2\rrbracket_S &= (\nabla_{\mathbf{y}}\mathbf{w}^j(\mathbf{y}) - \pi^j(\mathbf{y})\mathbf{I})\mathbf{e}_2 & & & \text{on } S, \\ \boldsymbol{\beta}^{2,\text{bl}}(\mathbf{y}) &= \mathbf{0} & \text{on } \bigcup_{k=1}^{\infty}(\partial Y_S - \{0, k\}), & & \{\boldsymbol{\beta}^{2,\text{bl}}, \omega^{2,\text{bl}}\} \text{ is } \mathbf{y}\text{-periodic.} \end{aligned}$$

It is shown [95] that  $\boldsymbol{\beta}^{2,\text{bl}}$  and  $\omega^{2,\text{bl}}$  stabilize exponentially to the boundary layer constants  $C^{2,\text{bl}}$  and  $C_{\pi}^2$  for  $y_2 \rightarrow \infty$  and to zero for  $y_2 \rightarrow -\infty$ . These constants are given by

$$\begin{aligned} C^{2,\text{bl}} &= (C_1^{2,\text{bl}}, 0)^{\top} = \left( \int_0^1 \beta_1^{2,\text{bl}}(y_1, 0) \, dy_1, 0 \right)^{\top}, \\ C_{\pi}^2 &= \int_0^1 \omega^{2,\text{bl}}(y_1, 0) \, dy_1. \end{aligned} \tag{2.114}$$

For further properties of the boundary layer solution  $\{\boldsymbol{\beta}^{2,\text{bl}}, \omega^{2,\text{bl}}\}$ , existence and uniqueness results we refer to [34, 95].

An improved approximation of the pore-scale solution to problem (2.95), (2.110) and (2.111) is obtained by adding boundary layer correctors and appropriately scaled boundary layer constants in the following way

$$\begin{aligned} \mathbf{v}_{\text{approx}}^{1,\varepsilon} &= \mathbf{v}_{\text{approx}}^{0,\varepsilon} + \boldsymbol{\beta}^{2,\text{bl}}(\mathbf{y}) \frac{\partial p^{\text{pm}}}{\partial x_2} \Big|_{\Sigma} - \mathcal{H}(x_2) C^{2,\text{bl}} \frac{\partial p^{\text{pm}}}{\partial x_2} \Big|_{\Sigma}, \\ p_{\text{approx}}^{1,\varepsilon} &= p_{\text{approx}}^{0,\varepsilon} + \omega^{2,\text{bl}}(\mathbf{y}) \frac{\partial p^{\text{pm}}}{\partial x_2} \Big|_{\Sigma} - C_{\pi}^2 \frac{\partial p^{\text{pm}}}{\partial x_2} \Big|_{\Sigma}, \end{aligned}$$

where  $(\partial p^{\text{pm}}/\partial x_2)|_{\Sigma} := \partial p^{\text{pm}}/\partial x_2(x_1, 0)$ . Further boundary layer problems and auxiliary functions are constructed in [34], however, we do not discuss them in this thesis since they do not contribute to the derived interface conditions. The interested reader is referred to [34].

After all corrections are done the asymptotic behavior of the pore-scale velocity and pressure is given by [34]:

$$\begin{aligned}\mathbf{v}^\varepsilon &= \mathbf{v}_{\text{approx}}^{\text{final},\varepsilon} + \mathcal{O}(\varepsilon) + \text{outer boundary layers}, \\ p^\varepsilon &= p_{\text{approx}}^{\text{final},\varepsilon} + o(\varepsilon^{-1}) + \text{outer boundary layers}.\end{aligned}$$

Hereby, the final approximation of the pore-scale velocity and pressure is

$$\begin{aligned}\mathbf{v}_{\text{approx}}^{\text{final},\varepsilon} &= \mathcal{H}(x_2) \left( \mathbf{v}^{\text{ff}} - C_1^{2,\text{bl}} \frac{\partial p^{\text{pm}}}{\partial x_2} \Big|_{\Sigma} \mathbf{e}_1 \right) \\ &\quad - \mathcal{H}(-x_2) \sum_{j=1}^2 \frac{\partial p^{\text{pm}}}{\partial x_j} \mathbf{w}^j(\mathbf{y}) + \frac{\partial p^{\text{pm}}}{\partial x_2} \Big|_{\Sigma} \boldsymbol{\beta}^{2,\text{bl}}(\mathbf{y}),\end{aligned}\quad (2.115)$$

$$\begin{aligned}p_{\text{approx}}^{\text{final},\varepsilon} &= \mathcal{H}(x_2) p^{\text{ff}} \\ &\quad + \mathcal{H}(-x_2) \left[ \varepsilon^{-2} p^{\text{pm}} - \varepsilon^{-1} \sum_{j=1}^2 \left( \frac{\partial p^{\text{pm}}}{\partial x_j} \pi^j(\mathbf{y}) + \delta_{2j} C_\pi^2 \frac{\partial p^{\text{pm}}}{\partial x_2} \Big|_{\Sigma} \right) \right] \\ &\quad + \varepsilon^{-1} \left( \omega^{2,\text{bl}} \left( \frac{\mathbf{x}}{\varepsilon} \right) - \mathcal{H}(x_2) C_\pi^2 \right) \frac{\partial p^{\text{pm}}}{\partial x_2} \Big|_{\Sigma},\end{aligned}\quad (2.116)$$

where  $\delta_{ij}$  denotes the Kronecker delta for  $i, j = 1, 2$ . Making use of the approximations (2.115) and (2.116), Carraro et al. [34] derived the subsequent coupling conditions for Stokes–Darcy systems with flows perpendicular to the porous layer

$$\mathbf{v}^{\text{ff}} \cdot \mathbf{n} = \mathbf{v}^{\text{pm}} \cdot \mathbf{n} \quad \text{on } \Sigma, \quad (2.117)$$

$$p^{\text{pm}} = 0 \quad \text{on } \Sigma, \quad (2.118)$$

$$\mathbf{v}^{\text{ff}} \cdot \boldsymbol{\tau} = C_1^{2,\text{bl}} \nabla p^{\text{pm}} \cdot \mathbf{n} \quad \text{on } \Sigma. \quad (2.119)$$

Condition (2.117) is the conservation of mass across the interface and equation (2.118) states zero Darcy pressure on  $\Sigma$ . For anisotropic porous media a jump in tangential velocities (2.119) is proposed, which reduces to  $\mathbf{v}^{\text{ff}} \cdot \boldsymbol{\tau} = 0$  for isotropic media since  $C_1^{2,\text{bl}} = 0$  in this case. The derived interface conditions (2.117)–(2.119) are valid only for the specific set of

boundary conditions (2.110)–(2.111) considered in [34] and are not applicable for general flow problems where the flow is perpendicular to the porous medium. An example of forced infiltration of a fluid into a porous medium where  $p^{\text{pm}} \neq 0$  on  $\Sigma$  and thus, interface condition (2.118) is not fulfilled, is given in [EE6, Section 6.2].

In Theorem 2.7 below, error estimates obtained in [34] are provided to justify the interface conditions (2.117)–(2.119) derived via homogenization and boundary layer theory.

**Theorem 2.7:** *Let  $\mathcal{M}$  be a neighborhood of the lower boundary  $\{x_2 = -H\}$  and  $p^\varepsilon$  extended by (2.55). Then, considering the pore-scale problem given by (2.95), (2.110) and (2.111) it holds*

$$\begin{aligned} & \left\| \mathbf{v}^\varepsilon - \mathbf{v}^{\text{ff}} + C^{2,\text{bl}} \frac{\partial p^{\text{pm}}}{\partial x_2} \Big|_\Sigma - \boldsymbol{\beta}^{2,\text{bl}}(\mathbf{y}) \frac{\partial p^{\text{pm}}}{\partial x_2} \Big|_\Sigma \right\|_{L^2(\Omega_{\text{ff}})^2} \leq C\varepsilon, \\ & \left\| \mathbf{v}^\varepsilon + (k_{22} \mathbf{e}_2 - \boldsymbol{\beta}^{2,\text{bl}}(y_1, +0)) \frac{\partial p^{\text{pm}}}{\partial x_2} \Big|_\Sigma \right\|_{L^2(\Sigma)^2} \leq C\varepsilon, \\ & \left\| \mathbf{v}^\varepsilon + \sum_{k=1}^2 \mathbf{w}^k(\mathbf{y}) - \boldsymbol{\beta}^{2,\text{bl}}(\mathbf{y}) \frac{\partial p^{\text{pm}}}{\partial x_2} \Big|_\Sigma \right\|_{L^2(\Omega_{\text{pm}} \setminus \mathcal{M})} \leq C\varepsilon, \\ & \left\| p^\varepsilon - \mathcal{H}(-x_2) \left[ \varepsilon^{-2} p^{\text{pm}} - \varepsilon^{-1} \left( C_\pi^2 \frac{\partial p^{\text{pm}}}{\partial x_2} \Big|_\Sigma + \sum_{k=1}^2 \pi^k(\mathbf{y}) \frac{\partial p^{\text{pm}}}{\partial x_j} \right) \right] \right\|_{L^2(\Omega)} \leq C\varepsilon^{-1/2}. \end{aligned}$$

*Proof.* See proof of [34, Theorem 2]. □

To summarize, we presented two sets of interface conditions (2.106)–(2.108) and (2.117)–(2.119) for the Stokes–Darcy problem that have been rigorously derived via periodic homogenization and boundary layer theory, e.g., [34, 95, 98]. Both coupling concepts are restricted to unidirectional flows, either parallel or perpendicular to the fluid–porous interface, and are not applicable for arbitrary flows in Stokes–Darcy systems. We showed that the use of homogenization and boundary layers for the derivation of

effective coupling conditions brings two benefits with it. First, all effective model parameters appearing in the resulting coupled Stokes–Darcy model can be computed based on the pore geometry. Second, rigorous error estimates between the pore-scale solution and the homogenized one are obtained. Using the presented averaging techniques, generalized coupling conditions accounting for arbitrary flow directions to the porous layer are derived in Chapter 3.



# **3** Generalized interface conditions



# Generalized interface conditions

# 3

The content of this chapter is based on the following original articles:

- [EE2] E. Eggenweiler and I. Rybak. *Interface conditions for arbitrary flows in coupled porous-medium and free-flow systems. Finite Volumes for Complex Applications IX – Methods, Theoretical Aspects, Examples. FVCA 9, Bergen, Norway, 2020.* Vol. 323. Springer Proc. Math. Stat. Springer, 2020, pp. 345–353. DOI: 10.1007/978-3-030-43651-3\\_31
- [EE4] E. Eggenweiler and I. Rybak. *Effective coupling conditions for arbitrary flows in Stokes–Darcy systems.* Multiscale Model. Simul. 19.2 (2021), pp. 731–757. DOI: 10.1137/20M1346638

In this chapter, we derive generalized coupling conditions valid for arbitrary flows in Stokes–Darcy systems via homogenization and boundary layer theory (Section 3.1) and discuss practical aspects of the newly developed conditions (Section 3.2). For this purpose we start from the pore-scale description of the coupled flow system in form of the dimensionless Stokes equations. At the macroscale, the Stokes equations remain valid in the free-flow domain and in the porous medium Darcy’s law is obtained using averaging techniques such as homogenization, volume

averaging or numerical upscaling. However, significant deviations from the macroscale models are expected close to the fluid–porous interface. In order to describe the effective flow behavior in the neighborhood of the interface in case of arbitrary flow direction to the porous layer, we rigorously derive a set of generalized coupling conditions by means of homogenization and boundary layer theory in Section 3.1. In Section 3.2, we provide the dimensional form of the derived coupling conditions and demonstrate how the exact interface location is incorporated in the effective coefficients appearing in the conditions. Finally, we compare the generalized interface conditions to the classical ones for the Stokes–Darcy problem in order to highlight similarities and differences.

### 3.1 Derivation of interface conditions via homogenization and boundary layers

In this section, we derive generalized coupling conditions for the two-dimensional Stokes–Darcy problem with a horizontal fluid–porous interface following the strategy described in the steps below.

*Step 1:* Give a precise description of the pore-scale geometry, define the pore-scale problem (Stokes problem) and the corresponding test function space  $V_{\text{per}}(\Omega^\varepsilon)^2$  (see equation (3.5)).

*Step 2:* Formulate two-scale asymptotic expansions of the pore-scale velocity  $\mathbf{v}^\varepsilon$  and pressure  $p^\varepsilon$  using auxiliary functions  $\mathbf{v}_j$  and  $p_j$  for  $j \in \mathbb{N}_0$ :

$$\begin{aligned}\mathbf{v}^\varepsilon(\mathbf{x}) &= \mathbf{v}_0(\mathbf{x}, \mathbf{y}) + \varepsilon \mathbf{v}_1(\mathbf{x}, \mathbf{y}) + \varepsilon^2 \mathbf{v}_2(\mathbf{x}, \mathbf{y}) + \mathcal{O}(\varepsilon^3), \\ p^\varepsilon(\mathbf{x}) &= p_0(\mathbf{x}, \mathbf{y}) + \varepsilon p_1(\mathbf{x}, \mathbf{y}) + \varepsilon^2 p_2(\mathbf{x}, \mathbf{y}) + \mathcal{O}(\varepsilon^3),\end{aligned}$$

where  $\mathbf{y} = \mathbf{x}/\varepsilon$ . Based on this ansatz, construct the first approximations  $\mathbf{v}_{\text{approx}}^{0,\varepsilon}$  and  $p_{\text{approx}}^{0,\varepsilon}$  of the pore-scale velocity and pressure and define the corresponding error functions  $U^{0,\varepsilon} = \mathbf{v}^\varepsilon - \mathbf{v}_{\text{approx}}^{0,\varepsilon}$  and  $P^{0,\varepsilon} = p^\varepsilon - p_{\text{approx}}^{0,\varepsilon}$ . Then, write the weak form of the momentum equation for the errors in

velocity and pressure

$$\int_{\Omega^\varepsilon} \nabla \mathbf{U}^{0,\varepsilon} : \nabla \boldsymbol{\varphi} \, d\mathbf{x} - \int_{\Omega^\varepsilon} P^{0,\varepsilon} \nabla \cdot \boldsymbol{\varphi} \, d\mathbf{x} = r.h.s. \quad \text{for all } \boldsymbol{\varphi} \in V_{\text{per}}(\Omega^\varepsilon)^2, \quad (3.1)$$

in order to detect terms of low order with respect to  $\varepsilon$  appearing in integrals on the right hand side (r.h.s.) of equation (3.1).

*Goal:* Obtain accurate approximations  $\mathbf{v}_{\text{approx}}^{N,\varepsilon}$  and  $p_{\text{approx}}^{N,\varepsilon}$  of the pore-scale solution such that we have  $\mathbf{U}^{N,\varepsilon} \in V_{\text{per}}(\Omega^\varepsilon)^2$  for one  $N \in \mathbb{N}$ . Then,  $\{\mathbf{U}^{0,\varepsilon}, P^{0,\varepsilon}\}$  appearing in the weak form (3.1) is replaced by  $\{\mathbf{U}^{N,\varepsilon}, P^{N,\varepsilon}\}$  and the velocity error  $\mathbf{U}^{N,\varepsilon}$  is inserted as a test function that is necessary to formulate effective interface conditions and to obtain rigorous error estimates for the error functions  $\mathbf{U}^{N,\varepsilon}$  and  $P^{N,\varepsilon}$ .

For the errors  $\{\mathbf{U}^{0,\varepsilon}, P^{0,\varepsilon}\}$  the above stated goal is not achieved, and thus, the first approximations  $\mathbf{v}_{\text{approx}}^{0,\varepsilon}$  and  $p_{\text{approx}}^{0,\varepsilon}$  need to be improved in the next step.

*Step 3:* Improve the first approximations  $\mathbf{v}_{\text{approx}}^{0,\varepsilon}$  and  $p_{\text{approx}}^{0,\varepsilon}$  by reducing the terms that are either reasons for  $\mathbf{U}^{0,\varepsilon} \notin V_{\text{per}}(\Omega^\varepsilon)^2$  or sources for a low estimation order with respect to the scale separation parameter  $\varepsilon$ . To reduce these terms appropriate boundary layer correctors and auxiliary functions are added to the first approximations of the pore-scale solution. This leads to updated velocity and pressure error functions. The new approximations and errors are defined by a rising index  $n \in \mathbb{N}$  as follows  $\mathbf{v}_{\text{approx}}^{n,\varepsilon}$ ,  $p_{\text{approx}}^{n,\varepsilon}$ ,  $\mathbf{U}^{n,\varepsilon}$ ,  $P^{n,\varepsilon}$ .

*Step 4:* For some index  $N \in \mathbb{N}$  our goal is achieved, i.e., we have  $\mathbf{U}^{N,\varepsilon} \in V_{\text{per}}(\Omega^\varepsilon)^2$ , and we estimated  $\nabla \cdot \mathbf{U}^{N,\varepsilon}$  as well as the integral terms appearing on the right hand side of the resulting weak formulation of the momentum equation sufficiently well with respect to  $\varepsilon$ . Then, we formulate effective interface conditions.

In Sections 3.1.1–3.1.4, we derive generalized coupling conditions for the Stokes–Darcy problem following Step 1–Step 4 for the two-dimensional case considering a flat interface. The extension of the derived conditions

to the three-dimensional space is possible by appropriate definition of the boundary layer problems and auxiliary functions.

### 3.1.1 Step 1: Geometrical setting and pore-scale model

We consider the same assumptions on the flow, the fluid and the porous medium as described in Section 2.3.2: steady-state single-phase flow at low Reynolds numbers  $Re \ll 1$ ; an incompressible fluid that contains a single chemical species and has constant temperature and constant viscosity; a nondeformable and fully saturated porous medium having the same temperature as the fluid. Since the temperature of the fluid and solid phase is assumed to be equal and constant no energy balance equation is needed. In this chapter, we use the theory of homogenization and boundary layers presented in Section 2.3 for the derivation of new coupling conditions. Thus, we work with the nondimensional formulation of the underlying flow problem (see Section 2.3.1 for details on the nondimensionalization).

At the pore scale, we consider the flow region  $\Omega^\varepsilon = ((0, L) \times (-H, h)) \setminus S^\varepsilon$ , consisting of the free-flow domain  $\Omega_{\text{ff}} = (0, L) \times (0, h)$  and the pore space  $\Omega_{\text{pm}}^\varepsilon$  of the porous medium  $\Omega_{\text{pm}} = (0, L) \times (-H, 0)$ , where  $S^\varepsilon$  denotes the solid part of the porous structure and  $h, H, L > 0$ . A schematic representation of the coupled flow domain from the microscale perspective is provided in Figure 2.8 (left). The porous-medium domain is assumed to be constructed by the periodic repetition of the scaled unit cell  $\varepsilon Y$  as described in Section 2.3.2, where  $\varepsilon$  is the scale separation parameter, and we have  $S^\varepsilon = \bigcup_k \varepsilon(Y_s + \{y_{1,k}, y_{2,k}\})$ . For simplicity, we assume that  $L/\varepsilon, h/\varepsilon, H/\varepsilon \in \mathbb{N}$ . From the macroscopic point of view, the coupled flow domain  $\Omega = (0, L) \times (-H, h)$  comprises the free-flow region  $\Omega_{\text{ff}}$  and the adjacent porous-medium region  $\Omega_{\text{pm}}$  that are separated by the sharp interface  $\Sigma = (0, L) \times \{0\}$ . We assume the fluid–porous interface to be flat and simple, meaning that it cannot store or transport any mass and momentum. We consider a horizontal interface and the unit normal vector on  $\Sigma$  pointing outward the porous-medium domain is  $\mathbf{n} = \mathbf{e}_2$ .

Under the prescribed assumptions the flow at the pore scale is described by the Stokes equations completed with the no-slip condition on the solid boundary  $\partial\Omega^\varepsilon \setminus \partial\Omega$ . In addition, we apply appropriate conditions on the external boundary of the flow domain and obtain the following nondimensional pore-scale problem

$$-\Delta \mathbf{v}^\varepsilon + \nabla p^\varepsilon = \mathbf{0}, \quad \nabla \cdot \mathbf{v}^\varepsilon = 0 \quad \text{in } \Omega^\varepsilon, \quad \int_{\Omega_{\text{ff}}^\varepsilon} p^\varepsilon \, dx = 0, \quad (3.2)$$

$$\mathbf{v}^\varepsilon = \mathbf{0} \quad \text{on } \partial\Omega^\varepsilon \setminus \partial\Omega, \quad \mathbf{v}^\varepsilon = (\mathbf{v}^{\text{in}}(x_1), 0)^\top \quad \text{on } \{x_2 = h\}, \quad (3.3)$$

$$v_2^\varepsilon = \frac{\partial v_1^\varepsilon}{\partial x_2} = 0 \quad \text{on } \{x_2 = -H\}, \quad \{\mathbf{v}^\varepsilon, p^\varepsilon\} \text{ is } L\text{-periodic in } x_1. \quad (3.4)$$

Here,  $\mathbf{v}^\varepsilon = (v_1^\varepsilon, v_2^\varepsilon)^\top$  and  $p^\varepsilon$  are the fluid velocity and pressure. The last condition in (3.2) is applied to define the pressure  $p^\varepsilon$  uniquely. On the lateral boundaries we set periodic boundary conditions (3.4) as usual when applying homogenization theory. This avoids further complications regarding the 'correct' specification of outer boundary conditions and makes the derivation of effective coupling conditions more convenient. For numerical simulations, however, the requirement for periodicity of the pore-scale solution can be relaxed (see Section 6.3.3). The condition on the upper free-flow boundary  $\{x_2 = h\}$  in (3.3) has to be chosen in such a way that  $L$ -periodicity of the pore-scale solution is fulfilled. On the lower boundary  $\{x_2 = -H\}$  we choose the boundary conditions (3.4) such that the law of conservation of mass is fulfilled and the stress in tangential direction is zero.

Corresponding to the pore-scale problem (3.2)–(3.4) we define the test function space

$$V_{\text{per}}(\Omega^\varepsilon)^2 = \{\boldsymbol{\varphi} \in H^1(\Omega^\varepsilon)^2 : \boldsymbol{\varphi} = \mathbf{0} \text{ on } \partial\Omega^\varepsilon \setminus \partial\Omega, \boldsymbol{\varphi} = \mathbf{0} \text{ on } \{x_2 = h\}, \\ \varphi_2 = 0 \text{ on } \{x_2 = -H\}, \boldsymbol{\varphi} \text{ is } L\text{-periodic in } x_1\}, \quad (3.5)$$

where  $\boldsymbol{\varphi} = (\varphi_1, \varphi_2)^\top$ . We use the notation  $H^1(\Omega^\varepsilon)^2$  for vector-valued functions, where each component is an element of  $H^1(\Omega^\varepsilon)$  and  $H^1(\Omega^\varepsilon)^{2 \times 2}$  for the gradients of vector-valued functions. Details regarding the notation

for functional spaces and norms are provided in Appendix A.1. In the following, we denote by  $C > 0$  a positive constant and by  $C = (C_1, C_2)^\top \in \mathbb{R}^2$  a constant vector with positive entries  $C_1, C_2 > 0$ , where  $C, C_1$  and  $C_2$  are all independent of  $\varepsilon$  and can have different values at different places. For simplicity, we waive writing  $dx$  and  $dS$  at the end of volume and boundary integrals, we assume  $\boldsymbol{\varphi} \in V_{\text{per}}(\Omega^\varepsilon)^2$  and we write  $q = q(\mathbf{x})$  for  $\mathbf{x} \in \Omega$ .

### 3.1.2 Step 2: First approximations of pore-scale velocity and pressure

In this section, we construct the first approximations  $\mathbf{v}_{\text{approx}}^{0,\varepsilon}$  and  $p_{\text{approx}}^{0,\varepsilon}$  of the pore-scale velocity and pressure corresponding to problem (3.2)–(3.4). In the interior of the free-flow region  $\Omega_{\text{ff}}$ , sufficient far from the interface, fluid flow is described by the dimensionless Stokes equations with the following boundary conditions on the external boundary  $\partial\Omega_{\text{ff}} \setminus \Sigma$ :

$$-\Delta \mathbf{v}^{\text{ff}} + \nabla p^{\text{ff}} = \mathbf{0}, \quad \nabla \cdot \mathbf{v}^{\text{ff}} = 0 \quad \text{in } \Omega_{\text{ff}}, \quad \int_{\Omega_{\text{ff}}} p^{\text{ff}} \, d\mathbf{x} = 0, \quad (3.6)$$

$$\mathbf{v}^{\text{ff}} = (v_1^{\text{in}}(x_1), 0)^\top \quad \text{on } \{x_2 = h\}, \quad \{\mathbf{v}^{\text{ff}}, p^{\text{ff}}\} \text{ is } L\text{-periodic in } x_1. \quad (3.7)$$

Here,  $\mathbf{v}^{\text{ff}} = (v_1^{\text{ff}}, v_2^{\text{ff}})^\top$  and  $p^{\text{ff}}$  are the free-flow velocity and pressure.

We have seen in Section 2.3 that upscaling the pore-scale equations (3.2) in the perforated domain yields the Darcy flow equations if periodic boundary conditions are applied. The authors in [119] also obtain Darcy's law as the homogenized model corresponding to the Stokes system with Dirichlet conditions on the external boundary. In our case, besides the periodic and the Dirichlet boundary conditions, we also apply the Neumann boundary condition given in (3.4) on the lower porous-medium boundary. For this specific set of boundary conditions (3.3)–(3.4) there is no corresponding macroscale model available. Nevertheless, we approximate problem (3.2)–(3.4) in the porous-medium domain away from the



interface by the following nondimensional Darcy system

$$\begin{aligned} -\nabla \cdot (\tilde{\mathbf{K}} \nabla p^{\text{pm}}) &= 0 \quad \text{in } \Omega_{\text{pm}}, \\ (\tilde{\mathbf{K}} \nabla p^{\text{pm}}) \cdot \mathbf{n} &= 0 \quad \text{on } \{x_2 = -H\}, \quad p^{\text{pm}} \text{ is } L\text{-periodic in } x_1, \end{aligned}$$

where  $p^{\text{pm}}$  is the porous-medium pressure,  $\mathbf{n}$  is the outward unit normal vector on  $\partial\Omega_{\text{pm}}$  and  $\tilde{\mathbf{K}}$  is the dimensionless permeability tensor given by (2.79).

Since we know the macroscale models that describe the fluid flow inside the two subdomains (sufficiently far from the dividing fluid–porous interface) we need to find approximations of the pore-scale velocity and pressure that are in accordance with these models. We start with the construction of a first approximation  $\{\mathbf{v}_{\text{approx}}^{0,\varepsilon}, p_{\text{approx}}^{0,\varepsilon}\}$  of the pore-scale solution  $\{\mathbf{v}^\varepsilon, p^\varepsilon\}$  which fulfills the following properties: i) it describes the flow in the interior of the free-flow region  $\Omega_{\text{ff}}$ , ii) it agrees with the boundary conditions at the upper boundary  $\{x_2 = h\}$ , and iii) it approximates the flow inside the porous medium according to the asymptotic expansions (2.61), (2.62) with (2.73) obtained via homogenization theory. Concerning the first two properties, it is obvious to use the Stokes velocity  $\mathbf{v}^{\text{ff}}$  and pressure  $p^{\text{ff}}$  for the approximation of the pore-scale quantities in the free-flow region. Based on the results of the homogenization procedure presented in Section 2.3.2 we approximate the pore-scale velocity and pressure in the porous domain according to (2.73) by

$$\mathbf{v}^\varepsilon|_{\Omega_{\text{pm}}^\varepsilon} \approx -\varepsilon^2 \sum_{j=1}^2 \mathbf{w}^{j,\varepsilon} \frac{\partial p^{\text{pm}}}{\partial x_j}, \quad p^\varepsilon|_{\Omega_{\text{pm}}^\varepsilon} \approx p^{\text{pm}} - \varepsilon \sum_{j=1}^2 \pi^{j,\varepsilon} \frac{\partial p^{\text{pm}}}{\partial x_j}. \quad (3.8)$$

Here, we set  $\mathbf{w}^{j,\varepsilon}(\mathbf{x}) = \mathbf{w}^j(\mathbf{y})$ ,  $\mathbf{y} = \mathbf{x}/\varepsilon$  and  $\pi^{j,\varepsilon}(\mathbf{x}) = \pi^j(\mathbf{y})$  where  $\{\mathbf{w}^j, \pi^j\} \in H_{\text{per}}^1(Y_f)^2 \times L^2(Y_f)$  is the solution to the cell problems (2.74)–(2.76) for  $j = 1, 2$  and the velocity  $\mathbf{w}^{j,\varepsilon}$  is extended by zero in  $\Omega_{\text{pm}} \setminus \Omega_{\text{pm}}^\varepsilon$ . Analogous notations are used for the boundary layer correctors later.

We combine the Stokes solution  $\{\mathbf{v}^{\text{ff}}, p^{\text{ff}}\}$  in the free-flow region and approximation (3.8) in the porous medium to obtain the following first

approximations of the pore-scale velocity and pressure

$$\mathbf{v}_{\text{approx}}^{0,\varepsilon} = \mathcal{H}(x_2)\mathbf{v}^{\text{ff}} + \mathcal{H}(-x_2) \left( -\varepsilon^2 \sum_{j=1}^2 \mathbf{w}^{j,\varepsilon} \frac{\partial p^{\text{pm}}}{\partial x_j} \right), \quad (3.9)$$

$$p_{\text{approx}}^{0,\varepsilon} = \mathcal{H}(x_2)p^{\text{ff}} + \mathcal{H}(-x_2) \left( p^{\text{pm}} - \varepsilon \sum_{j=1}^2 \pi^{j,\varepsilon} \frac{\partial p^{\text{pm}}}{\partial x_j} \right). \quad (3.10)$$

Here,  $\mathcal{H}$  is the Heaviside function given by (2.98). Corresponding to (3.9) and (3.10) we define the velocity and pressure errors

$$\mathbf{U}^{0,\varepsilon} = \mathbf{v}^\varepsilon - \mathbf{v}_{\text{approx}}^{0,\varepsilon}, \quad P^{0,\varepsilon} = p^\varepsilon - p_{\text{approx}}^{0,\varepsilon}.$$

In order to obtain the variational form of the momentum equation in (3.2) for the error functions  $\mathbf{U}^{0,\varepsilon}$ ,  $P^{0,\varepsilon}$  instead of  $\mathbf{v}^\varepsilon$ ,  $p^\varepsilon$ , we consider the weak formulation for the pore-scale functions  $\mathbf{v}^\varepsilon$ ,  $p^\varepsilon$  and the weak formulation for the first approximations  $\mathbf{v}_{\text{approx}}^{0,\varepsilon}$ ,  $p_{\text{approx}}^{0,\varepsilon}$  separately. The weak form corresponding to  $\mathbf{v}^\varepsilon$ ,  $p^\varepsilon$  is given by

$$\int_{\Omega^\varepsilon} \nabla \mathbf{v}^\varepsilon : \nabla \boldsymbol{\varphi} - \int_{\Omega^\varepsilon} p^\varepsilon \nabla \cdot \boldsymbol{\varphi} = 0 \quad \text{for all } \boldsymbol{\varphi} \in V_{\text{per}}(\Omega^\varepsilon)^2. \quad (3.11)$$

The Stokes velocity  $\mathbf{v}^{\text{ff}}$  and pressure  $p^{\text{ff}}$  are used for the approximation of the pore-scale solution in  $\Omega_{\text{ff}}$  and the corresponding variational formulation of the momentum conservation equation in (3.6) reads

$$\int_{\Omega_{\text{ff}}} \nabla \mathbf{v}^{\text{ff}} : \nabla \boldsymbol{\varphi} - \int_{\Omega_{\text{ff}}} p^{\text{ff}} \nabla \cdot \boldsymbol{\varphi} = - \int_{\Sigma} \underbrace{\left( \frac{\partial}{\partial x_2} \mathbf{v}^{\text{ff}} - \begin{bmatrix} 0 \\ p^{\text{ff}} \end{bmatrix} \right)}_{=: \mathbf{F}} \cdot \boldsymbol{\varphi}. \quad (3.12)$$

The weak form of the pore-scale problem corresponding to the approximation in the porous-medium domain  $\Omega_{\text{pm}}$  is given by

$$\int_{\Omega_{\text{pm}}^\varepsilon} \nabla \left( -\varepsilon^2 \sum_{j=1}^2 \mathbf{w}^{j,\varepsilon} \frac{\partial p^{\text{pm}}}{\partial x_j} \right) : \nabla \boldsymbol{\varphi} - \int_{\Omega_{\text{pm}}^\varepsilon} \left( p^{\text{pm}} - \varepsilon \sum_{j=1}^2 \pi^{j,\varepsilon} \frac{\partial p^{\text{pm}}}{\partial x_j} \right) \nabla \cdot \boldsymbol{\varphi}$$

$$\begin{aligned}
&= - \int_{\Sigma} \varepsilon \sum_{j=1}^2 \underbrace{\left( (\varepsilon \nabla \mathbf{w}^{j,\varepsilon} - \pi^{j,\varepsilon} \mathbf{1}) \frac{\partial p^{\text{pm}}}{\partial x_j} \mathbf{e}_2 \right)}_{=: \mathbf{B}_\varepsilon^j} \cdot \boldsymbol{\varphi} \\
&\quad - \int_{\Sigma} \varepsilon^2 \sum_{j=1}^2 \left( \left( \mathbf{w}^{j,\varepsilon} \otimes \nabla \frac{\partial p^{\text{pm}}}{\partial x_j} \right) \mathbf{e}_2 \right) \cdot \boldsymbol{\varphi} - \int_{\Sigma} p^{\text{pm}} \mathbf{e}_2 \cdot \boldsymbol{\varphi} \\
&\quad + \int_{\{x_2=-H\}} \varepsilon^2 \sum_{j=1}^2 \left( \nabla \mathbf{w}^{j,\varepsilon} \frac{\partial p^{\text{pm}}}{\partial x_j} \mathbf{e}_2 + \left( \mathbf{w}^{j,\varepsilon} \otimes \nabla \frac{\partial p^{\text{pm}}}{\partial x_j} \right) \mathbf{e}_2 \right) \cdot \boldsymbol{\varphi} \\
&\quad + \int_{\Omega_{\text{pm}}^\varepsilon} \sum_{j=1}^2 \underbrace{\left( \varepsilon^2 \mathbf{w}^{j,\varepsilon} \Delta \frac{\partial p^{\text{pm}}}{\partial x_j} + 2\varepsilon^2 \nabla \mathbf{w}^{j,\varepsilon} \nabla \frac{\partial p^{\text{pm}}}{\partial x_j} - \varepsilon \pi^{j,\varepsilon} \nabla \frac{\partial p^{\text{pm}}}{\partial x_j} \right)}_{=: \mathbf{A}_\varepsilon^j} \cdot \boldsymbol{\varphi}.
\end{aligned} \tag{3.13}$$

The weak formulation for the error functions results from subtraction of (3.12) and (3.13) from (3.11). In order to obtain estimates for the velocity and pressure errors later, e.g., in Corollary 3.1, we use the Poincaré-type inequalities (A2.2) provided in the Appendix A.2 to estimate the second term, the fourth term partially and the last term on the right hand side of (3.13) as follows

$$\left| \int_{\Sigma} \varepsilon^2 \sum_{j=1}^2 \left( \left( \mathbf{w}^{j,\varepsilon} \otimes \nabla \frac{\partial p^{\text{pm}}}{\partial x_j} \right) \mathbf{e}_2 \right) \cdot \boldsymbol{\varphi} \right| \leq C \varepsilon^{5/2} \|\nabla \boldsymbol{\varphi}\|_{L^2(\Omega_{\text{pm}}^\varepsilon)^{2 \times 2}}, \tag{3.14}$$

$$\left| \int_{\{x_2=-H\}} \varepsilon^2 \sum_{j=1}^2 \left( \left( \mathbf{w}^{j,\varepsilon} \otimes \nabla \frac{\partial p^{\text{pm}}}{\partial x_j} \right) \mathbf{e}_2 \right) \cdot \boldsymbol{\varphi} \right| \leq C \varepsilon^2 \|\nabla \boldsymbol{\varphi}\|_{L^2(\Omega_{\text{pm}}^\varepsilon)^{2 \times 2}}, \tag{3.15}$$

$$\left| \int_{\Omega_{\text{pm}}^\varepsilon} \sum_{j=1}^2 \mathbf{A}_\varepsilon^j \cdot \boldsymbol{\varphi} \right| \leq C \varepsilon^2 \|\nabla \boldsymbol{\varphi}\|_{L^2(\Omega_{\text{pm}}^\varepsilon)^{2 \times 2}}. \tag{3.16}$$

The integrals which are not estimated yet, vanish later either due to the newly derived coupling conditions or are absorbed by the boundary layer correctors which are added to the approximations of the pore-scale solutions.

### 3.1.3 Step 3: Improvement of first approximations

Approximations (3.9) and (3.10) of the pore-scale velocity and pressure have several issues that need to be addressed. First, the velocity approximation  $\mathbf{v}_{\text{approx}}^{0,\varepsilon}$  of order  $\mathcal{O}(1)$  in the free-flow region is not sufficient for the flow problems we consider, and we need to improve it by adding higher-order (with respect to  $\varepsilon$ ) boundary layer correctors (Section 3.1.3.1). Second, with the definition of  $\{\mathbf{v}_{\text{approx}}^{0,\varepsilon}, p_{\text{approx}}^{0,\varepsilon}\}$  we created a boundary layer in the neighborhood of the fluid–porous interface that needs to be reflected in the improved pore-scale approximations. This includes fixing the traces of the velocity approximation on the fluid–porous interface (Section 3.1.3.2). Third, the function  $\mathbf{v}_{\text{approx}}^{0,\varepsilon}$  does not fulfill the boundary conditions on the lower boundary (Section 3.1.3.3). Fourth, nonphysical compressibility effects coming from the pore-scale velocity approximation  $\mathbf{v}_{\text{approx}}^{0,\varepsilon}$  need to be corrected (Section 3.1.3.4). In the following, these issues will be addressed by adding boundary layer correctors and auxiliary functions to the first approximations (3.9) and (3.10) of the pore-scale velocity and pressure.

#### 3.1.3.1 Next order velocity approximation in the free-flow region

The first approximation (3.9) leads to  $\mathbf{v}_{\text{approx}}^{0,\varepsilon} = \mathbf{v}^{\text{ff}}$  in  $\Omega_{\text{ff}}$  and a shear stress jump across the interface which is given by  $F \cdot \boldsymbol{\tau} = \partial v_1^{\text{ff}} / \partial x_2$ , where  $F$  is defined in (3.12). For many coupled flow problems this approximation of the pore-scale velocity in the free-flow region is not accurate enough and construction of the appropriate boundary layer corrector is required [15, 95, 98, 142]. Even in case of parallel flows to the interface, the velocity approximation for the free flow needs to be at least  $\mathcal{O}(\varepsilon)$  as it is the case in, e.g., the Beavers–Joseph interface condition (2.19). Therefore, we continue the asymptotic expansions and incorporate terms of order  $\varepsilon$  for the velocity and of order 1 for the pressure in form of boundary layer correctors corresponding to problem (3.17)–(3.21) introduced below. The boundary layer problem (3.17)–(3.21) is defined on an infinite stripe  $Z^{\text{bl}} = Z^+ \cup S \cup Z^-$ , consisting of the free-flow part  $Z^+ = (0, 1) \times (0, \infty)$ ,

the porous-medium part  $Z^- = \bigcup_{k=1}^{\infty} (Y_f - \{0, k\})$  and the sharp interface  $S = (0, 1) \times \{0\}$  (Figure 2.8, right). We denote the jump of function  $u$  across the fluid–porous interface  $S$  within the boundary layer stripe  $Z^{\text{bl}}$  by  $[[u]]_S := u(\cdot, +0) - u(\cdot, -0)$ , where  $u(\cdot, +0) = \lim_{y \in Z^+, y_2 \rightarrow 0} u(\cdot, y_2)$  and  $u(\cdot, -0) = \lim_{y \in Z^-, y_2 \rightarrow 0} u(\cdot, y_2)$ .

The boundary layer problem corresponding to the next order velocity approximation in the free-flow region and the correction of the shear stress is given by

$$-\Delta_{\mathbf{y}} \mathbf{t}^{\text{bl}} + \nabla_{\mathbf{y}} s^{\text{bl}} = \mathbf{0} \quad \text{in } Z^+ \cup Z^-, \quad (3.17)$$

$$\nabla_{\mathbf{y}} \cdot \mathbf{t}^{\text{bl}} = 0 \quad \text{in } Z^+ \cup Z^-, \quad (3.18)$$

$$[[\mathbf{t}^{\text{bl}}]]_S = \mathbf{0} \quad \text{on } S, \quad (3.19)$$

$$[[\langle \nabla_{\mathbf{y}} \mathbf{t}^{\text{bl}} - s^{\text{bl}} \mathbf{I} \rangle \mathbf{e}_2]]_S = \mathbf{e}_1 \quad \text{on } S, \quad (3.20)$$

$$\mathbf{t}^{\text{bl}} = \mathbf{0} \quad \text{on } \bigcup_{k=1}^{\infty} (\partial Y_s - \{0, k\}), \quad \{\mathbf{t}^{\text{bl}}, s^{\text{bl}}\} \text{ is } \gamma_1\text{-periodic}. \quad (3.21)$$

Problem (3.17)–(3.21) was first constructed and analyzed by Jäger and Mikelić [95, Proposition 3.22]. The authors used the Lax–Milgram theorem (Appendix, Theorem A.7) to prove existence and uniqueness of  $\mathbf{t}^{\text{bl}} \in L^2_{\text{loc}}(Z^{\text{bl}})^2 \cap C^{\infty}_{\text{loc}}(Z^+ \cup Z^-)^2$ ,  $\nabla_{\mathbf{y}} \mathbf{t}^{\text{bl}} \in L^2(Z^+ \cup Z^-)^{2 \times 2}$  and uniqueness up to a constant of  $s^{\text{bl}} \in L^2_{\text{loc}}(Z^{\text{bl}}) \cap C^{\infty}_{\text{loc}}(Z^+ \cup Z^-)$  that satisfy (3.17)–(3.21). We set  $\lim_{\mathbf{y} \rightarrow -\infty} s^{\text{bl}}(\mathbf{y}) = 0$  to make the boundary layer pressure  $s^{\text{bl}}$  uniquely

defined. Moreover, in the vicinity of the interface  $S$  we have  $\mathbf{t}^{\text{bl}} - (0.5(\gamma_2 - \gamma_2^2)e^{-\gamma_2} \mathcal{H}(\gamma_2), 0) \in W^{2,q}(Y \cup S \cup (Y - \{0, 1\}))^2$  and  $s^{\text{bl}} \in W^{1,q}(Y \cup S \cup (Y - \{0, 1\}))$  for all  $q \in [1, \infty)$ , as shown in [95].

Setting the jump condition (3.20) enables the correction of the shear stress at the fluid–porous interface coming from the free-flow region. Condition (3.19) guarantees that no additional contribution at the interface is added to the velocity approximation yet. As shown in [95, 98] the boundary layer velocity  $\mathbf{t}^{\text{bl}} = (t_1^{\text{bl}}, t_2^{\text{bl}})$  and pressure  $s^{\text{bl}}$  stabilize exponentially towards some boundary layer constants for  $|\gamma_2| \rightarrow \infty$ . The stabilizing

constant for the velocity  $\mathbf{t}^{\text{bl}}$  was proven to be zero for  $y_2 \rightarrow -\infty$  and to have a zero second component for  $y_2 \rightarrow \infty$ . Concerning the boundary layer pressure  $s^{\text{bl}}$ , it was shown in [95] that a nonzero boundary layer constant is present in the free-flow region.

Following [95], there exist a constant  $\gamma \in (0, 1)$  and the boundary layer constants  $\mathbf{N}^{\text{bl}}$  and  $N_s^{\text{bl}}$  for the velocity and pressure such that

$$\begin{aligned} e^{\gamma|y_2|} \nabla_{\mathbf{y}} \mathbf{t}^{\text{bl}} &\in L^2(Z^+ \cup Z^-)^{2 \times 2}, & e^{\gamma|y_2|} \mathbf{t}^{\text{bl}} &\in L^2(Z^-)^2, \\ e^{\gamma|y_2|} s^{\text{bl}} &\in L^2(Z^-), \end{aligned} \quad (3.22)$$

and

$$\mathbf{N}^{\text{bl}} = (N_1^{\text{bl}}, 0)^\top = \left( \int_S t_1^{\text{bl}}(y_1, +0) \, dy_1, 0 \right)^\top, \quad (3.23)$$

$$N_s^{\text{bl}} = \int_S s^{\text{bl}}(y_1, +0) \, dy_1, \quad (3.24)$$

$$|\mathbf{t}^{\text{bl}} - \mathbf{N}^{\text{bl}}| \leq C e^{-\gamma y_2}, \quad |s^{\text{bl}} - N_s^{\text{bl}}| \leq C e^{-\gamma y_2}, \quad y_2 > 0. \quad (3.25)$$

Here, in case of a vector-valued function  $\boldsymbol{\varphi} = (\varphi_1, \varphi_2)^\top$ ,  $|\cdot|$  is meant to be the Euclidian norm, i.e.,  $|\boldsymbol{\varphi}| := \|\boldsymbol{\varphi}\|_2 = (\varphi_1^2 + \varphi_2^2)^{1/2}$ . From (3.22) we get that  $\nabla_{\mathbf{y}} \mathbf{t}^{\text{bl}} \rightarrow \mathbf{0}$  exponentially fast for  $|y_2| \rightarrow \infty$  and  $\{\mathbf{t}^{\text{bl}}, s^{\text{bl}}\} \rightarrow \{\mathbf{0}, 0\}$  exponentially fast for  $y_2 \rightarrow -\infty$ . As before for the cell problem solution  $\{\mathbf{w}^j, \pi^j\}$  we introduce  $\mathbf{t}^{\text{bl},\varepsilon}(\mathbf{x}) = \mathbf{t}^{\text{bl}}(\mathbf{y})$  and  $s^{\text{bl},\varepsilon}(\mathbf{x}) = s^{\text{bl}}(\mathbf{y})$  for  $\mathbf{x} \in \Omega^\varepsilon$  and extend the velocity  $\mathbf{t}^{\text{bl},\varepsilon}$  by zero in  $\Omega \setminus \Omega^\varepsilon$ . In [95] it is proven that the following inequalities hold

$$\|\mathbf{t}^{\text{bl},\varepsilon} - \mathcal{H}(x_2) \mathbf{N}^{\text{bl}}\|_{L^2(\Omega)^2} \leq C \varepsilon^{1/2}, \quad \|\nabla \mathbf{t}^{\text{bl},\varepsilon}\|_{L^2(\Omega_{\text{ff}} \cup \Omega_{\text{pm}})^{2 \times 2}} \leq C \varepsilon^{-1/2}, \quad (3.26)$$

$$\|s^{\text{bl},\varepsilon} - \mathcal{H}(x_2) N_s^{\text{bl}}\|_{L^2(\Omega^\varepsilon)} \leq C \varepsilon^{1/2}. \quad (3.27)$$

Using the boundary layer correctors  $\mathbf{t}^{\text{bl},\varepsilon}$ ,  $s^{\text{bl},\varepsilon}$  and their corresponding boundary layer constants we obtain improved approximations of the

pore-scale velocity and pressure

$$\mathbf{v}_{\text{approx}}^{1,\varepsilon} = \mathbf{v}_{\text{approx}}^{0,\varepsilon} - \varepsilon \left( \mathbf{t}^{\text{bl},\varepsilon} - \mathcal{H}(x_2) \mathbf{N}^{\text{bl}} \right) \frac{\partial v_1^{\text{ff}}}{\partial x_2} \Big|_{\Sigma}, \quad (3.28)$$

$$p_{\text{approx}}^{1,\varepsilon} = p_{\text{approx}}^{0,\varepsilon} - \left( s^{\text{bl},\varepsilon} - \mathcal{H}(x_2) N_s^{\text{bl}} \right) \frac{\partial v_1^{\text{ff}}}{\partial x_2} \Big|_{\Sigma}, \quad (3.29)$$

leading to the following new error functions

$$\begin{aligned} \mathbf{U}^{1,\varepsilon} &= \mathbf{U}^{0,\varepsilon} + \varepsilon \left( \mathbf{t}^{\text{bl},\varepsilon} - \mathcal{H}(x_2) \mathbf{N}^{\text{bl}} \right) \frac{\partial v_1^{\text{ff}}}{\partial x_2} \Big|_{\Sigma}, \\ P^{1,\varepsilon} &= P^{0,\varepsilon} + \left( s^{\text{bl},\varepsilon} - \mathcal{H}(x_2) N_s^{\text{bl}} \right) \frac{\partial v_1^{\text{ff}}}{\partial x_2} \Big|_{\Sigma}. \end{aligned} \quad (3.30)$$

Here,  $(\partial v_1^{\text{ff}} / \partial x_2)|_{\Sigma} := (\partial v_1^{\text{ff}} / \partial x_2)(x_1, +0)$  is constant with respect to  $x_2$  and the boundary layer constants  $\mathbf{N}^{\text{bl}}$  and  $N_s^{\text{bl}}$  are given by (3.23) and (3.25). In order to obtain error estimates in Corollary 3.1 we write the weak formulation for the errors in velocity  $\mathbf{U}^{1,\varepsilon}$  and pressure  $P^{1,\varepsilon}$ . This yields

$$\begin{aligned} & \int_{\Omega^\varepsilon} \nabla \mathbf{U}^{1,\varepsilon} : \nabla \boldsymbol{\varphi} + \int_{\Sigma} P^{1,\varepsilon} \nabla \cdot \boldsymbol{\varphi} = \int_{\Omega^\varepsilon} \nabla \mathbf{U}^{0,\varepsilon} : \nabla \boldsymbol{\varphi} + \int_{\Sigma} P^{0,\varepsilon} \nabla \cdot \boldsymbol{\varphi} \\ & + \int_{\Omega^\varepsilon} \nabla \left( \varepsilon \left( \mathbf{t}^{\text{bl},\varepsilon} - \mathcal{H}(x_2) \mathbf{N}^{\text{bl}} \right) \frac{\partial v_1^{\text{ff}}}{\partial x_2} \Big|_{\Sigma} \right) : \nabla \boldsymbol{\varphi} \\ & - \int_{\Omega^\varepsilon} \left( s^{\text{bl},\varepsilon} - \mathcal{H}(x_2) N_s^{\text{bl}} \right) \frac{\partial v_1^{\text{ff}}}{\partial x_2} \Big|_{\Sigma} \nabla \cdot \boldsymbol{\varphi}. \end{aligned} \quad (3.31)$$

Since we already obtained (3.11), (3.12) and (3.13) directly giving us the weak formulation for the first errors  $\mathbf{U}^{0,\varepsilon}$  and  $P^{0,\varepsilon}$ , we now focus on the weak form corresponding to the newly added terms including the boundary layer correctors. Thus, we write

$$\int_{\Omega^\varepsilon} \nabla \left( \varepsilon \left( \mathbf{t}^{\text{bl},\varepsilon} - \mathcal{H}(x_2) \mathbf{N}^{\text{bl}} \right) \frac{\partial v_1^{\text{ff}}}{\partial x_2} \Big|_{\Sigma} \right) : \nabla \boldsymbol{\varphi}$$

$$\begin{aligned}
& - \int_{\Omega^\varepsilon} \left( s^{\text{bl},\varepsilon} - \mathcal{H}(x_2) N_s^{\text{bl}} \right) \frac{\partial v_1^{\text{ff}}}{\partial x_2} \Big|_{\Sigma} \nabla \cdot \boldsymbol{\varphi} \\
& = \int_{\Omega^\varepsilon} \underbrace{\left( \varepsilon (\mathbf{t}^{\text{bl},\varepsilon} - \mathcal{H}(x_2) \mathbf{N}^{\text{bl}}) \frac{\partial^2}{\partial x_1^2} \frac{\partial v_1^{\text{ff}}}{\partial x_2} \Big|_{\Sigma} \right)}_{=: \mathbf{A}_\varepsilon^{11}} \\
& \quad + \underbrace{\left( s^{\text{bl},\varepsilon} - \mathcal{H}(x_2) N_s^{\text{bl}} \right) \nabla \frac{\partial v_1^{\text{ff}}}{\partial x_2} \Big|_{\Sigma}}_{=: \mathbf{A}_\varepsilon^{31}} \cdot \boldsymbol{\varphi} \\
& \quad + 2 \int_{\Omega^\varepsilon} \underbrace{\varepsilon \left( (\mathbf{t}^{\text{bl},\varepsilon} - \mathcal{H}(x_2) \mathbf{N}^{\text{bl}}) \otimes \frac{\partial}{\partial x_1} \frac{\partial v_1^{\text{ff}}}{\partial x_2} \Big|_{\Sigma} \mathbf{e}_1 \right)}_{=: \mathbf{A}_\varepsilon^{21}} : \nabla \boldsymbol{\varphi} \\
& \quad - \int_{\Sigma} N_s^{\text{bl}} \frac{\partial v_1^{\text{ff}}}{\partial x_2} \Big|_{\Sigma} \mathbf{e}_2 \cdot \boldsymbol{\varphi} - \int_{\Sigma} \frac{\partial v_1^{\text{ff}}}{\partial x_2} \Big|_{\Sigma} \mathbf{e}_1 \cdot \boldsymbol{\varphi} + \text{e.s.t.} \tag{3.32}
\end{aligned}$$

Exponentially small terms are denoted by 'e.s.t.' throughout this chapter. These terms in (3.32) include the boundary layer corrector  $\mathbf{t}^{\text{bl},\varepsilon}$  and its gradient  $\nabla \mathbf{t}^{\text{bl},\varepsilon}$  appearing in the integral over the lower boundary  $\{x_2 = -H\}$  since  $\mathbf{t}^{\text{bl},\varepsilon} \rightarrow \mathbf{0}$  and  $\nabla \mathbf{t}^{\text{bl},\varepsilon} \rightarrow \mathbf{0}$  for  $x_2 \rightarrow -\infty$  what follows from (3.22) and (3.25). The first integral term over the interface  $\Sigma$  on the right hand side of equation (3.32) will later vanish due to the newly derived generalized coupling conditions. The second integral term over  $\Sigma$  appearing in (3.32) cancels out with the corresponding parts of  $\int_{\Sigma} \mathbf{F} \cdot \boldsymbol{\varphi}$  from (3.12) when we consider the weak form (3.31) for  $\{\mathbf{U}^{1,\varepsilon}, P^{1,\varepsilon}\}$ .

To obtain higher-order estimates with respect to  $\varepsilon$  for the integrals over  $\Omega^\varepsilon$  on the right hand side of (3.32) we use the following identity

$$\nabla q \otimes \mathbf{u} = \nabla(\mathbf{u}q) - q \nabla \mathbf{u}, \tag{3.33}$$

where  $q$  denotes a scalar-valued function and  $\mathbf{u}$  a vector-valued function. Taking into account (3.33), the Poincaré inequality (A2.1), the inequalities (A2.2) and the previously obtained results (3.26), (3.27), we obtain the



following estimates

$$\left| \int_{\Omega_{\text{ff}}} \mathbf{A}_\varepsilon^{11} \cdot \boldsymbol{\varphi} \right| \leq C\varepsilon^{3/2} \|\boldsymbol{\varphi}\|_{L^2(\Omega_{\text{ff}})^2}, \quad (3.34)$$

$$\left| \int_{\Omega_{\text{pm}}^\varepsilon} \mathbf{A}_\varepsilon^{11} \cdot \boldsymbol{\varphi} \right| \leq C\varepsilon^{5/2} \|\nabla \boldsymbol{\varphi}\|_{L^2(\Omega_{\text{pm}}^\varepsilon)^{2 \times 2}},$$

$$\left| \int_{\Omega^\varepsilon} \mathbf{A}_\varepsilon^{21} : \nabla \boldsymbol{\varphi} \right| \leq C\varepsilon^{3/2} \|\nabla \boldsymbol{\varphi}\|_{L^2(\Omega^\varepsilon)^{2 \times 2}}, \quad (3.35)$$

$$\left| \int_{\Omega_{\text{pm}}^\varepsilon} \mathbf{A}_\varepsilon^{31} \cdot \boldsymbol{\varphi} \right| \leq C\varepsilon^{3/2} \|\nabla \boldsymbol{\varphi}\|_{L^2(\Omega_{\text{pm}}^\varepsilon)^{2 \times 2}}.$$

It remains to estimate the integral  $\int_{\Omega_{\text{ff}}} \mathbf{A}_\varepsilon^{31} \cdot \boldsymbol{\varphi}$  in (3.32). For this purpose, we follow the ideas from [95] and construct the auxiliary problem

$$\frac{\partial V}{\partial y_1}(\mathbf{y}) = s^{\text{bl}}(\mathbf{y}) - N_s^{\text{bl}}, \quad \mathbf{y} \in (0, 1) \times (0, \infty), \quad V \text{ is } y_1\text{-periodic}. \quad (3.36)$$

From the definition (3.24) of the boundary layer constant  $N_s^{\text{bl}}$  it follows directly that

$$V(y_1, y_2) = \int_0^{y_1} s^{\text{bl}}(t, y_2) dt - N_s^{\text{bl}} y_1, \quad \mathbf{y} \in (0, 1) \times (0, \infty),$$

is a solution to problem (3.36). Further, from [95] we know that there exists a constant  $\gamma > 0$  such that  $e^{\gamma y_2} V \in L^2(Z^+)$ . Defining  $V^\varepsilon(\mathbf{x}) = \varepsilon V(\mathbf{y})$  for  $\mathbf{x} \in \Omega_{\text{ff}}$  and using estimate (3.27) directly yields

$$\frac{\partial V^\varepsilon}{\partial x_1} = s^{\text{bl}, \varepsilon} - N_s^{\text{bl}} \quad \text{in } \Omega_{\text{ff}}, \quad \|V^\varepsilon\|_{L^2(\Omega_{\text{ff}})} \leq C\varepsilon^{3/2}. \quad (3.37)$$

Next, we use the first formula in (3.37) to rewrite the integral term  $\int_{\Omega_{\text{ff}}} \mathbf{A}_\varepsilon^{31} \cdot \boldsymbol{\varphi}$  from (3.32) and apply integration by parts. We take into account the periodicity of functions  $V^\varepsilon$ ,  $v_1^{\text{ff}}$  and  $\varphi_1$ , use the estimate for  $V^\varepsilon$  given

in (3.37) and obtain

$$\begin{aligned}
\left| \int_{\Omega_{\text{ff}}} \mathbf{A}_\varepsilon^{31} \cdot \boldsymbol{\varphi} \right| &= \left| \int_{\Omega_{\text{ff}}} (s^{\text{bl},\varepsilon} - N_s^{\text{bl}}) \left( \frac{\partial}{\partial x_1} \frac{\partial v_1^{\text{ff}}}{\partial x_2} \Big|_\Sigma \right) \varphi_1 \right| \\
&= \left| \int_{\Omega_{\text{ff}}} \frac{\partial V^\varepsilon}{\partial x_1} \left( \frac{\partial}{\partial x_1} \frac{\partial v_1^{\text{ff}}}{\partial x_2} \Big|_\Sigma \right) \varphi_1 \right| \\
&= \left| \int_{\partial\Omega_{\text{ff}}} V^\varepsilon \left( \frac{\partial}{\partial x_1} \frac{\partial v_1^{\text{ff}}}{\partial x_2} \Big|_\Sigma \right) \varphi_1 \mathbf{e}_1 \cdot \mathbf{n} \right. \\
&\quad \left. - \int_{\Omega_{\text{ff}}} V^\varepsilon \frac{\partial}{\partial x_1} \left( \left( \frac{\partial}{\partial x_1} \frac{\partial v_1^{\text{ff}}}{\partial x_2} \Big|_\Sigma \right) \varphi_1 \right) \right| \\
&= \left| \int_{\Omega_{\text{ff}}} V^\varepsilon \left( \varphi_1 \left( \frac{\partial^2}{\partial x_1^2} \frac{\partial v_1^{\text{ff}}}{\partial x_2} \Big|_\Sigma \right) + \frac{\partial \varphi_1}{\partial x_1} \left( \frac{\partial}{\partial x_1} \frac{\partial v_1^{\text{ff}}}{\partial x_2} \Big|_\Sigma \right) \right) \right| \\
&\leq C\varepsilon^{3/2} \|\boldsymbol{\varphi}\|_{H^1(\Omega_{\text{ff}})^2} \leq C\varepsilon^{3/2} \|\nabla \boldsymbol{\varphi}\|_{H^1(\Omega_{\text{ff}})^{2 \times 2}}. \tag{3.38}
\end{aligned}$$

With the constructed functions  $\mathbf{v}_{\text{approx}}^{1,\varepsilon}$  and  $p_{\text{approx}}^{1,\varepsilon}$  in (3.28) and (3.29) the approximation order of the velocity in the free-flow region is improved to  $\mathcal{O}(\varepsilon)$  and the values of the stress in normal direction to the fluid–porous  $\Sigma$  are corrected. However, we do not have continuity of the velocity trace across the interface, although the principle of mass conservation should be fulfilled. Hence, in the following section we eliminate the trace jump on  $\Sigma$  to obtain a physically consistent pore-scale velocity approximation.

### 3.1.3.2 Continuity of velocity trace

With the approximations given in (3.28) and (3.29), mass conservation across the interface  $\Sigma$  is not satisfied, and we created a boundary layer that needs to be corrected. In order to do so and establish the continuity of the velocity trace across the fluid–porous interface, we add boundary layer correctors to the approximations  $\mathbf{v}_{\text{approx}}^{1,\varepsilon}$  and  $p_{\text{approx}}^{1,\varepsilon}$ . These correctors are thus also added to errors  $U^{1,\varepsilon}$  and  $P^{1,\varepsilon}$  given in (3.30) by taking the

opposite sign. The required boundary layer correctors are solutions to the following boundary layer problem for  $j = 1, 2$  constructed in [95]:

$$-\Delta_{\mathbf{y}} \boldsymbol{\beta}^{j,\text{bl}} + \nabla_{\mathbf{y}} \omega^{j,\text{bl}} = \mathbf{0} \quad \text{in } Z^+ \cup Z^-, \quad (3.39)$$

$$\nabla_{\mathbf{y}} \cdot \boldsymbol{\beta}^{j,\text{bl}} = 0 \quad \text{in } Z^+ \cup Z^-, \quad (3.40)$$

$$\llbracket \boldsymbol{\beta}^{j,\text{bl}} \rrbracket_S = \tilde{k}_2^j \mathbf{e}_2 - \mathbf{w}^j \quad \text{on } S, \quad (3.41)$$

$$\llbracket (\nabla_{\mathbf{y}} \boldsymbol{\beta}^{j,\text{bl}} - \omega^{j,\text{bl}} \mathbf{1}) \mathbf{e}_2 \rrbracket_S = -(\nabla_{\mathbf{y}} \mathbf{w}^j - \pi^j \mathbf{1}) \mathbf{e}_2 \quad \text{on } S, \quad (3.42)$$

$$\boldsymbol{\beta}^{j,\text{bl}} = \mathbf{0} \quad \text{on } \bigcup_{k=1}^{\infty} (\partial Y_s - \{0, k\}), \quad \{\boldsymbol{\beta}^{j,\text{bl}}, \omega^{j,\text{bl}}\} \text{ is } y_1\text{-periodic.} \quad (3.43)$$

Equation (3.41) establishes the continuity of normal velocity across the interface and condition (3.42) eliminates the lower-order integral term  $\int_{\Sigma} \varepsilon \sum_{j=1}^2 \mathbf{B}_\varepsilon^j \boldsymbol{\varphi}$  appearing in the variational formulation (3.13).

Uniqueness of  $\boldsymbol{\beta}^{j,\text{bl}} \in L_{\text{loc}}^2(Z^{\text{bl}})^2$  and  $\nabla_{\mathbf{y}} \boldsymbol{\beta}^{j,\text{bl}} \in L^2(Z^+ \cup Z^-)^{2 \times 2}$  satisfying equations (3.39)–(3.43) and uniqueness of  $\omega^{j,\text{bl}} \in L_{\text{loc}}^2(Z^{\text{bl}})$  up to a constant follow from the Lax–Milgram theorem. Moreover, from Proposition 3.22 in [95] we obtain  $\{\boldsymbol{\beta}^{j,\text{bl}}, \omega^{j,\text{bl}}\} \in C_{\text{loc}}^\infty(Z^+ \cup Z^-)^2 \times C_{\text{loc}}^\infty(Z^+ \cup Z^-)$ . In [95], also the behavior of the boundary layer solution in the near of the interface  $S$  is specified as  $\boldsymbol{\beta}^{j,\text{bl}}(\cdot, \pm 0) \in W^{2-1/q, q}(S)^2$  and  $(\nabla_{\mathbf{y}} \boldsymbol{\beta}^{j,\text{bl}} - \omega^{j,\text{bl}} \mathbf{1})(\cdot, \pm 0) \mathbf{e}_2 \in W^{1-1/q, q}(S)^2$  for all  $q \in (1, \infty]$ . Since (3.39)–(3.43) describe a boundary layer problem, its solutions  $\boldsymbol{\beta}^{j,\text{bl}}$  and  $\omega^{j,\text{bl}}$  stabilize exponentially towards some boundary layer constants for  $|y_2| \rightarrow \infty$ . To obtain a uniquely defined pressure in the same way as in Section 3.1.3.1, we set  $\lim_{y \rightarrow -\infty} \omega^{j,\text{bl}}(\mathbf{y}) = 0$ .

After [34, 95] there exist  $\gamma \in (0, 1)$  such that

$$\begin{aligned} e^{\gamma|y_2|} \nabla_{\mathbf{y}} \boldsymbol{\beta}^{j,\text{bl}} &\in L^2(Z^+ \cup Z^-)^{2 \times 2}, \quad e^{\gamma|y_2|} \boldsymbol{\beta}^{j,\text{bl}} \in L^2(Z^-)^2, \\ e^{\gamma|y_2|} \omega^{j,\text{bl}} &\in L^2(Z^-), \end{aligned} \quad (3.44)$$

and

$$\mathbf{M}^{j,\text{bl}} = (M_1^{j,\text{bl}}, 0)^\top = \left( \int_S \beta_1^{j,\text{bl}}(y_1, +0) \, dy_1, 0 \right)^\top, \quad (3.45)$$

$$M_\omega^{j,\text{bl}} = \int_S \omega^{j,\text{bl}}(y_1, +0) \, dy_1, \quad (3.46)$$

$$|\boldsymbol{\beta}^{j,\text{bl}} - \mathbf{M}^{j,\text{bl}}| \leq C e^{-\gamma y_2}, \quad |\omega^{j,\text{bl}} - M_\omega^{j,\text{bl}}| \leq C e^{-\gamma y_2}, \quad y_2 > 0. \quad (3.47)$$

Similar as in the sections before, we define  $\boldsymbol{\beta}^{j,\text{bl},\varepsilon}(\mathbf{x}) = \boldsymbol{\beta}^{j,\text{bl}}(\mathbf{y})$  and  $\omega^{j,\text{bl},\varepsilon}(\mathbf{x}) = \omega^{j,\text{bl}}(\mathbf{y})$ , and extend the boundary layer velocity by setting  $\boldsymbol{\beta}^{j,\text{bl},\varepsilon} = \mathbf{0}$  in  $\Omega \setminus \Omega^\varepsilon$ . Following [95], it holds

$$\|\boldsymbol{\beta}^{j,\text{bl},\varepsilon} - \mathcal{H}(x_2) \mathbf{M}^{j,\text{bl}}\|_{L^2(\Omega)^2} \leq C \varepsilon^{1/2}, \quad \|\nabla \boldsymbol{\beta}^{j,\text{bl},\varepsilon}\|_{L^2(\Omega_{\text{ff}} \cup \Omega_{\text{pm}})^{2 \times 2}} \leq C \varepsilon^{-1/2}, \quad (3.48)$$

$$\|\omega^{j,\text{bl},\varepsilon} - \mathcal{H}(x_2) M_\omega^{j,\text{bl}}\|_{L^2(\Omega^\varepsilon)} \leq C \varepsilon^{1/2}. \quad (3.49)$$

We improve the pore-scale velocity and pressure approximations  $\mathbf{v}_{\text{approx}}^{1,\varepsilon}$  and  $p_{\text{approx}}^{1,\varepsilon}$  by adding the boundary layer correctors  $\boldsymbol{\beta}^{j,\text{bl},\varepsilon}$  and  $\omega^{j,\text{bl},\varepsilon}$  and their stabilizing constants  $\mathbf{M}^{j,\text{bl}}$  and  $M_\omega^{j,\text{bl}}$ . This yields new error functions

$$\mathbf{U}^{2,\varepsilon} = \mathbf{U}^{1,\varepsilon} - \varepsilon^2 \sum_{j=1}^2 \left( \boldsymbol{\beta}^{j,\text{bl},\varepsilon} - \mathcal{H}(x_2) \mathbf{M}^{j,\text{bl}} \right) \frac{\partial p^{\text{pm}}}{\partial x_j} \Big|_{\Sigma}, \quad (3.50)$$

$$P^{2,\varepsilon} = P^{1,\varepsilon} - \varepsilon \sum_{j=1}^2 \left( \omega^{j,\text{bl},\varepsilon} - \mathcal{H}(x_2) M_\omega^{j,\text{bl}} \right) \frac{\partial p^{\text{pm}}}{\partial x_j} \Big|_{\Sigma}. \quad (3.51)$$

Here,  $(\partial p^{\text{pm}} / \partial x_j)|_{\Sigma} := (\partial p^{\text{pm}} / \partial x_j)(x_1, -0)$  is constant with respect to  $x_2$ . At this stage, we have approximated the pore-scale velocity  $\mathbf{v}^\varepsilon$  such that the approximation is continuous across the fluid–porous interface, and we obtain the following result.

**Corollary 3.1:** *We have  $\mathbf{U}^{2,\varepsilon} \in H^1(\Omega^\varepsilon)^2$  and the following estimate holds*

$$\begin{aligned} & \left| \int_{\Omega^\varepsilon} \nabla \mathbf{U}^{2,\varepsilon} : \nabla \boldsymbol{\varphi} - \int_{\Omega^\varepsilon} P^{2,\varepsilon} \nabla \cdot \boldsymbol{\varphi} + \int_{\{x_2 = -H\}} \varepsilon^2 \sum_{j=1}^2 \frac{\partial}{\partial x_2} w_1^{j,\varepsilon} \frac{\partial p^{\text{pm}}}{\partial x_j} \varphi_1 \right. \\ & \quad \left. - \int_{\Sigma} p^{\text{pm}} \varphi_2 - \int_{\Sigma} \left( \frac{\partial}{\partial x_2} \mathbf{v}^{\text{ff}} - \begin{bmatrix} 0 \\ p^{\text{ff}} \end{bmatrix} \right) \cdot \boldsymbol{\varphi} \right| \end{aligned}$$

$$\begin{aligned}
& + \int_{\Sigma} \frac{\partial v_1^{\text{ff}}}{\partial x_2} \Big|_{\Sigma} \mathbf{e}_1 \cdot \boldsymbol{\varphi} + \int_{\Sigma} N_s^{\text{bl}} \frac{\partial v_1^{\text{ff}}}{\partial x_2} \Big|_{\Sigma} \mathbf{e}_2 \cdot \boldsymbol{\varphi} \\
& \leq C\varepsilon^{3/2} \left( \|\nabla \boldsymbol{\varphi}\|_{L^2(\Omega^\varepsilon)^{2 \times 2}} + \|\boldsymbol{\varphi}\|_{H^1(\Omega_{\text{ff}}^2)} \right), \quad \text{for all } \boldsymbol{\varphi} \in V_{\text{per}}(\Omega^\varepsilon)^2. \quad (3.52)
\end{aligned}$$

*Proof.* By construction of  $U^{2,\varepsilon}$  as a sum of  $H^1$ - functions we have  $U^{2,\varepsilon} \in H^1(\Omega^\varepsilon)^2$ . Using the fact that the boundary layer velocities  $\mathbf{t}^{\text{bl},\varepsilon}$ ,  $\boldsymbol{\beta}^{j,\text{bl},\varepsilon}$ , their gradients and the pressures  $s^{\text{bl},\varepsilon}$ ,  $\omega^{j,\text{bl},\varepsilon}$  stabilize exponentially to zero for  $x_2 \rightarrow -\infty$ , we get

$$\begin{aligned}
& \int_{\Omega^\varepsilon} \nabla U^{2,\varepsilon} : \nabla \boldsymbol{\varphi} - \int_{\Omega^\varepsilon} P^{2,\varepsilon} \nabla \cdot \boldsymbol{\varphi} + \int_{\{x_2=-H\}} \varepsilon^2 \sum_{j=1}^2 \frac{\partial}{\partial x_2} w_1^{j,\varepsilon} \frac{\partial p^{\text{pm}}}{\partial x_j} \varphi_1 \\
& \quad - \int_{\Sigma} p^{\text{pm}} \varphi_2 - \int_{\Sigma} \mathbf{F} \cdot \boldsymbol{\varphi} + \int_{\Sigma} \frac{\partial v_1^{\text{ff}}}{\partial x_2} \Big|_{\Sigma} \mathbf{e}_1 \cdot \boldsymbol{\varphi} + \int_{\Sigma} N_s^{\text{bl}} \frac{\partial v_1^{\text{ff}}}{\partial x_2} \Big|_{\Sigma} \mathbf{e}_2 \cdot \boldsymbol{\varphi} \\
& = \int_{\Sigma} \varepsilon^2 \sum_{j=1}^2 \left( \left( \mathbf{w}^{j,\varepsilon} \otimes \nabla \frac{\partial p^{\text{pm}}}{\partial x_j} \right) \mathbf{e}_2 \right) \cdot \boldsymbol{\varphi} \\
& \quad - \int_{\{x_2=-H\}} \varepsilon^2 \sum_{j=1}^2 \left( \left( \mathbf{w}^{j,\varepsilon} \otimes \nabla \frac{\partial p^{\text{pm}}}{\partial x_j} \right) \mathbf{e}_2 \right) \cdot \boldsymbol{\varphi} \\
& \quad + \int_{\Omega_{\text{pm}}^\varepsilon} \sum_{j=1}^2 \mathbf{A}_\varepsilon^j \cdot \boldsymbol{\varphi} + \int_{\Omega_{\text{pm}}^\varepsilon} \mathbf{A}_\varepsilon^{11} \cdot \boldsymbol{\varphi} + \int_{\Omega_{\text{ff}}^\varepsilon} \mathbf{A}_\varepsilon^{11} \cdot \boldsymbol{\varphi} + 2 \int_{\Omega^\varepsilon} \mathbf{A}_\varepsilon^{21} : \nabla \boldsymbol{\varphi} \\
& \quad + \int_{\Omega_{\text{pm}}^\varepsilon} \mathbf{A}_\varepsilon^{31} \cdot \boldsymbol{\varphi} + \int_{\Omega_{\text{ff}}^\varepsilon} \mathbf{A}_\varepsilon^{31} \cdot \boldsymbol{\varphi} + \int_{\Sigma} \varepsilon \sum_{j=1}^2 M_\omega^{j,\text{bl}} \frac{\partial p^{\text{pm}}}{\partial x_j} \Big|_{\Sigma} \varphi_2 \\
& \quad - 2 \int_{\Omega^\varepsilon} \sum_{j=1}^2 \varepsilon^2 \underbrace{\left( \left( \boldsymbol{\beta}^{j,\text{bl},\varepsilon} - \mathcal{H}(x_2) \mathbf{M}^{j,\text{bl}} \right) \otimes \frac{\partial}{\partial x_1} \frac{\partial p^{\text{pm}}}{\partial x_j} \Big|_{\Sigma} \right)}_{=:\mathbf{A}_\varepsilon^{j,12}} \cdot \nabla \boldsymbol{\varphi} \\
& \quad - \int_{\Omega^\varepsilon} \sum_{j=1}^2 \varepsilon^2 \underbrace{\left( \boldsymbol{\beta}^{j,\text{bl},\varepsilon} - \mathcal{H}(x_2) \mathbf{M}^{j,\text{bl}} \right)}_{=:\mathbf{A}_\varepsilon^{j,22}} \frac{\partial^2}{\partial x_1^2} \frac{\partial p^{\text{pm}}}{\partial x_j} \Big|_{\Sigma} \cdot \boldsymbol{\varphi}
\end{aligned}$$

$$- \int_{\Omega^\varepsilon} \sum_{j=1}^2 \varepsilon \underbrace{\left( \omega^{j,\text{bl},\varepsilon} - \mathcal{H}(x_2) M_\omega^{j,\text{bl}} \right)}_{=: \mathbf{A}_\varepsilon^{j,32}} \frac{\partial}{\partial x_1} \frac{\partial p^{\text{pm}}}{\partial x_j} \Big|_\Sigma \mathbf{e}_1 \cdot \boldsymbol{\varphi} + \text{e.s.t.} \quad (3.53)$$

The exponentially small terms in (3.53) include the boundary layer velocities  $\mathbf{t}^{\text{bl},\varepsilon}$ ,  $\boldsymbol{\beta}^{j,\text{bl},\varepsilon}$  and their gradients  $\nabla \mathbf{t}^{\text{bl},\varepsilon}$ ,  $\nabla \boldsymbol{\beta}^{j,\text{bl},\varepsilon}$  appearing in integrals over the lower boundary  $\{x_2 = -H\}$ . Using the Poincaré inequality (A2.1), inequalities (A2.2), (3.48) and (3.49), we estimate the integral terms on the right hand side of (3.53), which have been not estimated yet, as follows

$$\left| \int_\Sigma \sum_{j=1}^2 M_\omega^{j,\text{bl}} \frac{\partial p^{\text{pm}}}{\partial x_j} \Big|_\Sigma \varphi_2 \right| \leq C \varepsilon^{1/2} \|\nabla \boldsymbol{\varphi}\|_{L^2(\Omega^\varepsilon)^{2 \times 2}}, \quad (3.54)$$

$$\left| \int_{\Omega^\varepsilon} \sum_{j=1}^2 \mathbf{A}_\varepsilon^{j,12} : \nabla \boldsymbol{\varphi} \right| \leq C \varepsilon^{5/2} \|\nabla \boldsymbol{\varphi}\|_{L^2(\Omega^\varepsilon)^{2 \times 2}},$$

$$\left| \int_{\Omega_{\text{pm}}^\varepsilon} \sum_{j=1}^2 \mathbf{A}_\varepsilon^{j,22} \cdot \boldsymbol{\varphi} \right| \leq C \varepsilon^3 \|\nabla \boldsymbol{\varphi}\|_{L^2(\Omega_{\text{pm}}^\varepsilon)^{2 \times 2}}, \quad (3.55)$$

$$\left| \int_{\Omega_{\text{pm}}^\varepsilon} \sum_{j=1}^2 \mathbf{A}_\varepsilon^{j,32} \cdot \boldsymbol{\varphi} \right| \leq C \varepsilon^2 \|\nabla \boldsymbol{\varphi}\|_{L^2(\Omega_{\text{pm}}^\varepsilon)^{2 \times 2}},$$

$$\left| \int_{\Omega_{\text{ff}}^\varepsilon} \sum_{j=1}^2 \mathbf{A}_\varepsilon^{j,22} \cdot \boldsymbol{\varphi} \right| \leq C \varepsilon^{5/2} \|\nabla \boldsymbol{\varphi}\|_{L^2(\Omega_{\text{ff}}^\varepsilon)^{2 \times 2}}, \quad (3.56)$$

$$\left| \int_{\Omega_{\text{ff}}^\varepsilon} \sum_{j=1}^2 \mathbf{A}_\varepsilon^{j,32} \cdot \boldsymbol{\varphi} \right| \leq C \varepsilon^{5/2} \|\boldsymbol{\varphi}\|_{H^1(\Omega_{\text{ff}}^\varepsilon)^2}.$$

The last estimate in (3.56) is obtained using the auxiliary function  $V^j$  for  $j = 1, 2$  given by

$$\frac{\partial V^j}{\partial y_1}(\mathbf{y}) = \omega^{j,\text{bl}}(\mathbf{y}) - M_\omega^{j,\text{bl}}, \quad \mathbf{y} \in (0, 1) \times (0, \infty), \quad V^j \text{ is } y_1\text{-periodic},$$

and proceeding in the same way as for the derivation of estimate (3.38),

where we used the auxiliary function  $V$ . Taking into account estimates (3.14)–(3.16), (3.34), (3.35), (3.38), (3.48), (3.49) and (3.54)–(3.56) we complete the proof.  $\square$

The goal of the homogenization procedure is to derive a velocity approximation  $\mathbf{v}_{\text{approx}}^{n,\varepsilon}$  such that for some  $n \in \mathbb{N}$  the corresponding velocity error  $U^{n,\varepsilon} \in V_{\text{per}}(\Omega^\varepsilon)^2$  can be used as a test function in (3.53). So far, the obtained approximation  $\mathbf{v}_{\text{approx}}^{2,\varepsilon}$  does not fulfill the boundary conditions given in (3.4) on the lower porous-medium boundary. Hence, the next task is to construct an improved approximation  $\mathbf{v}_{\text{approx}}^{3,\varepsilon}$  of the pore-scale velocity based on  $\mathbf{v}_{\text{approx}}^{2,\varepsilon}$  such that the corresponding velocity error  $U^{3,\varepsilon}$  satisfies at least

$$U_2^{3,\varepsilon} = \mathcal{O}(\varepsilon^3), \quad \frac{\partial U_1^{3,\varepsilon}}{\partial x_2} = \mathcal{O}(\varepsilon^2) \quad \text{on } \{x_2 = -H\}. \quad (3.57)$$

The orders on the right hand sides in (3.57) result from the fact that we approximated the pore-scale velocity  $\mathbf{v}^\varepsilon$  up to order  $\varepsilon^2$ .

### 3.1.3.3 Velocity correction on the lower boundary

In this section, we construct an approximation of the pore-scale velocity such that it satisfies conditions (3.3)–(3.4) up to higher-order terms with respect to  $\varepsilon$ . Then, for the resulting velocity error, conditions (3.57) on the lower boundary  $\{x_2 = -H\}$  hold true. However, up to now, this is not the case for the error function  $U^{2,\varepsilon}$  defined in (3.50) since we have

$$U_2^{2,\varepsilon}(x_1, -H) = \varepsilon^2 \sum_{j=1}^2 (w_2^j(y_1, 0) - \tilde{k}_{2j}) \frac{\partial p^{\text{pm}}}{\partial x_j}(x_1, -H) + \text{e.s.t.}, \quad (3.58)$$

$$\begin{aligned} \frac{\partial U_1^{2,\varepsilon}}{\partial x_2}(x_1, -H) &= \varepsilon \sum_{j=1}^2 \frac{\partial}{\partial y_2} w_1^j(y_1, 0) \frac{\partial p^{\text{pm}}}{\partial x_j}(x_1, -H) \\ &+ \varepsilon^2 \sum_{j=1}^2 w_1^j(y_1, 0) \frac{\partial}{\partial x_2} \frac{\partial p^{\text{pm}}}{\partial x_j}(x_1, -H) + \text{e.s.t.} \end{aligned} \quad (3.59)$$

In order to obtain (3.58) we added  $-\varepsilon^2 \sum_{j=1}^2 \tilde{k}_{2j} \partial p^{\text{pm}} / \partial x_j(x_1, -H) = 0$  to  $U_2^{2,\varepsilon}(x_1, -H)$  and used the  $y$ -periodicity of  $w^j$ , i.e.,  $w^j(y_1, -H\varepsilon^{-1}) = w^j(y_1, 0)$ . The values of the error  $U^{2,\varepsilon}$  on the lower boundary given on the right hand side of (3.58) and (3.59) are up to the factor  $\varepsilon^2$  the same as those in [34, Section 4.3]. Hence, to correct the outer boundary effects, we consider the same problem as in [34] but a different scaling for the boundary layer correctors. The boundary layer problem reads

$$-\Delta_y \mathbf{q}^{j,\text{bl}} + \nabla_y z^{j,\text{bl}} = \mathbf{0} \quad \text{in } Z^-, \quad (3.60)$$

$$\nabla_y \cdot \mathbf{q}^{j,\text{bl}} = 0 \quad \text{in } Z^-, \quad (3.61)$$

$$q_2^{j,\text{bl}} = \tilde{k}_{2j} - w_2^j \quad \text{on } S, \quad (3.62)$$

$$\frac{\partial q_1^{j,\text{bl}}}{\partial y_2} = -\frac{\partial w_1^j}{\partial y_2} \quad \text{on } S, \quad (3.63)$$

$$\mathbf{q}^{j,\text{bl}} = \mathbf{0} \quad \text{on } \bigcup_{k=1}^{\infty} (\partial Y_s - \{0, k\}), \quad \{\mathbf{q}^{j,\text{bl}}, z^{j,\text{bl}}\} \text{ is } y_1\text{-periodic}. \quad (3.64)$$

In [34, 95] it is shown that there exists a unique solution  $\mathbf{q}^{j,\text{bl}} \in H^1(Z^-)^2$ , smooth in  $Z^-$  and a constant  $\gamma \in (0, 1)$  such that  $e^{\gamma|y_2|} \mathbf{q}^{j,\text{bl}} \in L^2(Z^-)^2$ . The pressure  $z^{j,\text{bl}}$  is unique up to an additive constant and having determined this constant it holds  $e^{\gamma|y_2|} z^{j,\text{bl}} \in L^2(Z^-)$ .

Making use of the boundary layer correctors  $\mathbf{q}^{j,\text{bl}}$  and  $z^{j,\text{bl}}$  we construct new error functions

$$U^{3,\varepsilon} = U^{2,\varepsilon} + \varepsilon^2 \sum_{j=1}^2 \frac{\partial p^{\text{pm}}}{\partial x_j}(x_1, -H) \mathbf{q}^{j,\text{bl}} \left( \frac{x_1}{\varepsilon}, -\frac{x_2 + H}{\varepsilon} \right),$$



$$P^{3,\varepsilon} = P^{2,\varepsilon} + \varepsilon \sum_{j=1}^2 \frac{\partial p^{\text{pm}}}{\partial x_j}(x_1, -H) z^{j,\text{bl}} \left( \frac{x_1}{\varepsilon}, -\frac{x_2 + H}{\varepsilon} \right).$$

Considering conditions (3.62) and (3.63), and taking into account (3.58) and (3.59) we have

$$\begin{aligned} U_2^{3,\varepsilon}(x_1, -H) &= U_2^{2,\varepsilon} + \varepsilon^2 \sum_{j=1}^2 \frac{\partial p^{\text{pm}}}{\partial x_j}(x_1, -H) q_2^{j,\text{bl}} \left( \frac{x_1}{\varepsilon}, 0 \right) \\ &= U_2^{2,\varepsilon} + \varepsilon^2 \sum_{j=1}^2 \frac{\partial p^{\text{pm}}}{\partial x_j}(x_1, -H) (\tilde{k}_{2j} - w_2^j) \left( \frac{x_1}{\varepsilon}, 0 \right) = 0, \end{aligned} \tag{3.65}$$

$$\begin{aligned} \frac{\partial U_1^{3,\varepsilon}}{\partial x_2}(x_1, -H) &= \frac{\partial U_1^{2,\varepsilon}}{\partial x_2}(x_1, -H) \\ &\quad + \frac{\partial}{\partial x_2} \left( \varepsilon^2 \sum_{j=1}^2 \frac{\partial p^{\text{pm}}}{\partial x_j}(x_1, -H) q_1^{j,\text{bl}} \left( \frac{x_1}{\varepsilon}, -\frac{x_2 + H}{\varepsilon} \right) \right) (x_1, -H) \\ &= \frac{\partial U_1^{2,\varepsilon}}{\partial x_2}(x_1, -H) \\ &\quad + \varepsilon^2 \sum_{j=1}^2 \left( \underbrace{\frac{\partial}{\partial x_2} \left( \frac{\partial p^{\text{pm}}}{\partial x_j}(x_1, -H) \right)}_{=0} q_1^{j,\text{bl}} \left( \frac{x_1}{\varepsilon}, -\frac{x_2 + H}{\varepsilon} \right) \right) (x_1, -H) \\ &\quad + \varepsilon^2 \sum_{j=1}^2 \left( \frac{\partial p^{\text{pm}}}{\partial x_j}(x_1, -H) \frac{\partial}{\partial x_2} q_1^{j,\text{bl}} \left( \frac{x_1}{\varepsilon}, -\frac{x_2 + H}{\varepsilon} \right) \right) (x_1, -H) \\ &= \frac{\partial U_1^{2,\varepsilon}}{\partial x_2}(x_1, -H) - \varepsilon \sum_{j=1}^2 \frac{\partial p^{\text{pm}}}{\partial x_j}(x_1, -H) \frac{\partial}{\partial y_2} w_1^j \left( \frac{x_1}{\varepsilon}, 0 \right) \\ &= \mathcal{O}(\varepsilon^2). \end{aligned} \tag{3.66}$$

Thus, the goal  $U^{3,\varepsilon} \in V_{\text{per}}(\Omega^\varepsilon)^2$  is achieved, and we obtain the following result:

**Corollary 3.2:** *We have  $U^{3,\varepsilon} \in V_{\text{per}}(\Omega^\varepsilon)^2$ , and it holds*

$$\begin{aligned} & \left| \int_{\Omega^\varepsilon} \nabla U^{3,\varepsilon} : \nabla \boldsymbol{\varphi} - \int_{\Omega^\varepsilon} P^{3,\varepsilon} \nabla \cdot \boldsymbol{\varphi} - \int_{\Sigma} p^{\text{pm}} \varphi_2 \right. \\ & \quad \left. - \int_{\Sigma} \left( \frac{\partial v_2^{\text{ff}}}{\partial x_2} - p^{\text{ff}} \right) \varphi_2 + \int_{\Sigma} N_s^{\text{bl}} \frac{\partial v_1^{\text{ff}}}{\partial x_2} \Big|_{\Sigma} \varphi_2 \right| \\ & \leq C\varepsilon^{3/2} \left( \|\nabla \boldsymbol{\varphi}\|_{L^2(\Omega^\varepsilon)^{2 \times 2}} + \|\boldsymbol{\varphi}\|_{H^1(\Omega_{\text{ff}}^\varepsilon)} \right), \quad \text{for all } \boldsymbol{\varphi} \in V_{\text{per}}(\Omega^\varepsilon)^2. \end{aligned} \quad (3.67)$$

*Proof.* From Corollary 3.1 we know that  $U^{2,\varepsilon} \in H^1(\Omega^\varepsilon)^2$  and due to  $\mathbf{q}^{j,\text{bl}} \in H^1(Z^-)^2$  we obtain directly  $U^{3,\varepsilon} \in H^1(\Omega^\varepsilon)^2$ . The velocity error  $U^{3,\varepsilon}$  is a sum of functions, that are  $L$ -periodic and fulfill the no-slip condition (3.3) on the boundary of the solid grains  $\partial\Omega^\varepsilon \setminus \partial\Omega$ , and further, we have

$$U^{3,\varepsilon}(x_1, h) = \mathbf{0}. \quad (3.68)$$

The correction of the velocity error  $U^{2,\varepsilon}$  on the lower boundary using problem (3.60)–(3.64) yields  $U^{3,\varepsilon} \in V_{\text{per}}(\Omega^\varepsilon)^2$  since (3.65) and (3.66) hold. We have proven (3.52) in Corollary 3.1 for  $\{U^{2,\varepsilon}, P^{2,\varepsilon}\}$  and therefore, we consider only the variational form for the boundary layer correctors added to the error functions  $U^{2,\varepsilon}$  and  $P^{2,\varepsilon}$ . This yields

$$\begin{aligned} & \int_{\Omega^\varepsilon} \nabla \left( \varepsilon^2 \sum_{j=1}^2 \frac{\partial p^{\text{pm}}}{\partial x_j}(x_1, -H) \mathbf{q}^{j,\text{bl}} \left( \frac{x_1}{\varepsilon}, -\frac{x_2 + H}{\varepsilon} \right) \right) : \nabla \boldsymbol{\varphi} \\ & \quad - \int_{\Omega^\varepsilon} \varepsilon \sum_{j=1}^2 \frac{\partial p^{\text{pm}}}{\partial x_j}(x_1, -H) z^{j,\text{bl}} \left( \frac{x_1}{\varepsilon}, -\frac{x_2 + H}{\varepsilon} \right) \nabla \cdot \boldsymbol{\varphi} \\ & \quad - \int_{\{x_2 = -H\}} \varepsilon^2 \sum_{j=1}^2 \frac{\partial p^{\text{pm}}}{\partial x_j}(x_1, -H) \frac{\partial w_1^{j,\varepsilon}}{\partial x_2}(x_1, 0) \varphi_1 \\ & = - \underbrace{\int_{\Omega_{\text{pm}}^\varepsilon} \varepsilon^2 \sum_{j=1}^2 \frac{\partial^2}{\partial x_1^2} \frac{\partial p^{\text{pm}}}{\partial x_j}(x_1, -H) \mathbf{q}^{j,\text{bl}} \left( \frac{x_1}{\varepsilon}, -\frac{x_2 + H}{\varepsilon} \right) \cdot \boldsymbol{\varphi}}_{=: \mathbf{A}_\varepsilon^{j,13}} \end{aligned}$$

$$\begin{aligned}
& - 2 \int_{\Omega_{\text{pm}}^\varepsilon} \underbrace{\varepsilon^2 \sum_{j=1}^2 \nabla \frac{\partial p^{\text{pm}}}{\partial x_j}(x_1, -H) \nabla \mathbf{q}^{j,\text{bl}} \left( \frac{x_1}{\varepsilon}, -\frac{x_2 + H}{\varepsilon} \right)}_{=: \mathbf{A}_\varepsilon^{j,23}} \cdot \boldsymbol{\varphi} \\
& + \int_{\Omega_{\text{pm}}^\varepsilon} \underbrace{\varepsilon \sum_{j=1}^2 \nabla \frac{\partial p^{\text{pm}}}{\partial x_j}(x_1, -H) z^{j,\text{bl}} \left( \frac{x_1}{\varepsilon}, -\frac{x_2 + H}{\varepsilon} \right)}_{=: \mathbf{A}_\varepsilon^{j,33}} \cdot \boldsymbol{\varphi} + \text{e.s.t.} \quad (3.69)
\end{aligned}$$

Taking into account the periodicity of the cell problem solutions  $\mathbf{w}^{j,\varepsilon}$ ,  $j = 1, 2$ , we have  $\mathbf{w}^{j,\varepsilon}(x_1, 0) = \mathbf{w}^{j,\varepsilon}(x_1, -H)$  for all  $x_1 \in (0, L)$ . Therefore, the integral over the lower boundary  $\{x_2 = -H\}$  on the left hand side of equation (3.69) cancels with the corresponding integral on the left hand side of equation (3.52). Furthermore, the boundary layer functions  $\mathbf{q}^{j,\text{bl}}$  and  $z^{j,\text{bl}}$  are continuous across  $\{x_2 = -H\}$ , i.e., there is no jump in velocity or pressure. The volume integrals over the free-flow region  $\Omega_{\text{ff}}$  are incorporated in the exponentially small terms in (3.69) since  $\mathbf{q}^{j,\text{bl}} \rightarrow \mathbf{0}$  and  $z^{j,\text{bl}} \rightarrow 0$  exponentially fast for  $x_2 \rightarrow -\infty$ .

We estimate the integrals on the right hand side of (3.69) using inequalities (A2.2) and identity (3.38) as follows

$$\left| \int_{\Omega_{\text{pm}}^\varepsilon} \sum_{j=1}^2 \mathbf{A}_\varepsilon^{j,13} \cdot \boldsymbol{\varphi} \right|, \quad \varepsilon \left| \int_{\Omega_{\text{pm}}^\varepsilon} \sum_{j=1}^2 \mathbf{A}_\varepsilon^{j,23} \cdot \boldsymbol{\varphi} \right| \leq C \varepsilon^3 \|\nabla \boldsymbol{\varphi}\|_{L^2(\Omega_{\text{pm}}^\varepsilon)^{2 \times 2}}, \quad (3.70)$$

$$\left| \int_{\Omega_{\text{pm}}^\varepsilon} \sum_{j=1}^2 \mathbf{A}_\varepsilon^{j,33} \cdot \boldsymbol{\varphi} \right| \leq C \varepsilon^2 \|\nabla \boldsymbol{\varphi}\|_{L^2(\Omega_{\text{pm}}^\varepsilon)^{2 \times 2}}. \quad (3.71)$$

Using estimates (3.70)–(3.71) and the results from Corollary 3.1 we obtain (3.67) and Corollary 3.2 is proven.  $\square$

On the left hand side of equation (3.67) there are integrals over  $\Sigma$  that need to be eliminated and the most natural way to do this is to set

$$p^{\text{pm}} = p^{\text{ff}} - \frac{\partial v_2^{\text{ff}}}{\partial x_2} + N_s^{\text{bl}} \frac{\partial v_1^{\text{ff}}}{\partial x_2} \quad \text{on } \Sigma. \quad (3.72)$$

Then, the use of (3.72) in inequality (3.67) leads to

$$\left| \int_{\Omega^\varepsilon} \nabla \mathbf{U}^{3,\varepsilon} : \nabla \boldsymbol{\varphi} - \int_{\Omega^\varepsilon} p^{3,\varepsilon} \nabla \cdot \boldsymbol{\varphi} \right| \leq C\varepsilon^{3/2} \left( \|\nabla \boldsymbol{\varphi}\|_{L^2(\Omega^\varepsilon)^{2 \times 2}} + \|\boldsymbol{\varphi}\|_{H^1(\Omega_{\text{ff}}^\varepsilon)} \right). \quad (3.73)$$

Let us shortly summarize what we achieved up to now. We constructed approximations of the pore-scale functions such that the corresponding velocity error is an element of our test function space, i.e.,  $\mathbf{U}^{3,\varepsilon} \in V_{\text{per}}(\Omega^\varepsilon)^2$ , we formulated interface condition (3.72) for the pressure and obtained estimate (3.73). The problem at this stage are nonphysical compressibility effects of  $\mathbf{U}^{3,\varepsilon}$ , i.e.,  $\nabla \cdot \mathbf{U}^{3,\varepsilon}$  is of low order with respect to  $\varepsilon$ . Thus, the next task is to obtain a higher-order estimate with respect to  $\varepsilon$  for the divergence of the velocity error  $\mathbf{U}^{3,\varepsilon}$ .

### 3.1.3.4 Correction of compressibility effects

The divergence of the velocity error function  $\mathbf{U}^{3,\varepsilon}$  reads

$$\begin{aligned} \nabla \cdot \mathbf{U}^{3,\varepsilon} &= \mathcal{H}(-x_2) \varepsilon^2 \sum_{j=1}^2 \mathbf{w}^{j,\varepsilon, \nabla} \frac{\partial p^{\text{pm}}}{\partial x_j} + \varepsilon \left( t_1^{\text{bl},\varepsilon} - \mathcal{H}(x_2) N_1^{\text{bl}} \right) \frac{\partial}{\partial x_1} \frac{\partial v_1^{\text{ff}}}{\partial x_2} \Big|_{\Sigma} \\ &\quad - \varepsilon^2 \sum_{j=1}^2 \left( \beta_1^{j,\text{bl},\varepsilon} - \mathcal{H}(x_2) M_1^{j,\text{bl}} \right) \frac{\partial}{\partial x_1} \frac{\partial p^{\text{pm}}}{\partial x_j} \Big|_{\Sigma} \\ &\quad + \varepsilon^2 \sum_{j=1}^2 \frac{\partial}{\partial x_1} \frac{\partial p^{\text{pm}}}{\partial x_j} (x_1, -H) q_1^{j,\text{bl}} \left( \frac{x_1}{\varepsilon}, -\frac{x_2 + H}{\varepsilon} \right). \end{aligned} \quad (3.74)$$

We use the Minkowski inequality (A2.4) to estimate  $\nabla \cdot \mathbf{U}^{3,\varepsilon}$  as follows

$$\begin{aligned} \|\nabla \cdot \mathbf{U}^{3,\varepsilon}\|_{L^2(\Omega^\varepsilon)} &\leq \left\| \varepsilon^2 \sum_{j=1}^2 \mathbf{w}^{j,\varepsilon, \nabla} \frac{\partial p^{\text{pm}}}{\partial x_j} \right\|_{L^2(\Omega_{\text{pm}}^\varepsilon)} \\ &\quad + \left\| \varepsilon \left( t_1^{\text{bl},\varepsilon} - \mathcal{H}(x_2) N_1^{\text{bl}} \right) \frac{\partial}{\partial x_1} \frac{\partial v_1^{\text{ff}}}{\partial x_2} \Big|_{\Sigma} \right\|_{L^2(\Omega^\varepsilon)} \end{aligned}$$

$$\begin{aligned}
& + \left\| \varepsilon^2 \sum_{j=1}^2 \left( \beta_1^{j,\text{bl},\varepsilon} - \mathcal{H}(x_2) M_1^{j,\text{bl}} \right) \frac{\partial}{\partial x_1} \frac{\partial p^{\text{pm}}}{\partial x_j} \Big|_{\Sigma} \right\|_{L^2(\Omega^\varepsilon)} \\
& + \left\| \varepsilon^2 \sum_{j=1}^2 \frac{\partial}{\partial x_1} \frac{\partial p^{\text{pm}}}{\partial x_j} (x_1, -H) q_1^{j,\text{bl}} \left( \frac{x_1}{\varepsilon}, -\frac{x_2 + H}{\varepsilon} \right) \right\|_{L^2(\Omega^\varepsilon)}. \quad (3.75)
\end{aligned}$$

Then, making use of (3.26) and (3.48) we obtain the following estimates for the right hand side terms in equation (3.75):

$$\left\| \varepsilon^2 \sum_{j=1}^2 \mathbf{w}^{j,\varepsilon} \cdot \nabla \frac{\partial p^{\text{pm}}}{\partial x_j} \right\|_{L^2(\Omega_{\text{pm}}^\varepsilon)} \leq C\varepsilon^2, \quad (3.76)$$

$$\left\| \varepsilon \left( l_1^{\text{bl},\varepsilon} - \mathcal{H}(x_2) N_1^{\text{bl}} \right) \frac{\partial}{\partial x_1} \frac{\partial v_1^{\text{ff}}}{\partial x_2} \Big|_{\Sigma} \right\|_{L^2(\Omega^\varepsilon)} \leq C\varepsilon^{3/2}, \quad (3.77)$$

$$\left\| \varepsilon^2 \sum_{j=1}^2 \left( \beta_1^{j,\text{bl},\varepsilon} - \mathcal{H}(x_2) M_1^{j,\text{bl}} \right) \frac{\partial}{\partial x_1} \frac{\partial p^{\text{pm}}}{\partial x_j} \Big|_{\Sigma} \right\|_{L^2(\Omega^\varepsilon)} \leq C\varepsilon^{5/2}, \quad (3.78)$$

$$\left\| \varepsilon^2 \sum_{j=1}^2 \frac{\partial}{\partial x_1} \frac{\partial p^{\text{pm}}}{\partial x_j} (x_1, -H) q_1^{j,\text{bl}} \left( \frac{x_1}{\varepsilon}, -\frac{x_2 + H}{\varepsilon} \right) \right\|_{L^2(\Omega^\varepsilon)} \leq C\varepsilon^2. \quad (3.79)$$

Consequently, we have  $\|\nabla \cdot \mathbf{U}^{3,\varepsilon}\|_{L^2(\Omega^\varepsilon)} \leq C\varepsilon^{3/2}$ . However, due to the fact that the velocity approximation is of order  $\varepsilon^2$ , we need to have  $\|\nabla \cdot \mathbf{U}^{3,\varepsilon}\|_{L^2(\Omega^\varepsilon)} \leq C\varepsilon^i$  for some  $i > 2$ . In this section, we correct the compressibility effects of  $\mathbf{U}^{3,\varepsilon}$  coming from the different contributions in (3.76), (3.77) and (3.79). Estimate (3.78) is already sufficient, so we do not need any correction for the corresponding term appearing in (3.74). In the following, we consider each of the three remaining terms on the right hand side of (3.74) in a separate step *a* – *c*) and correct it using boundary layers and auxiliary functions.

### a) Compressibility effects coming from $\mathbf{w}^{j,\varepsilon}$

We correct the compressibility effects coming from the term including the cell problem velocity  $\mathbf{w}^{j,\varepsilon}$  using the auxiliary function  $\boldsymbol{\gamma}^{j,i}$  for  $i, j = 1, 2$  from [34, Section 4.4]. The function  $\boldsymbol{\gamma}^{j,i}$  is the solution to the following problem defined only in the porous part of the coupled domain

$$\begin{aligned} \nabla_{\mathbf{y}} \cdot \boldsymbol{\gamma}^{j,i} &= w_i^j - \frac{\tilde{k}_{ij}}{|Y_{\text{f}}|} \quad \text{in } Y_{\text{f}}, \quad \boldsymbol{\gamma}^{j,i} = \mathbf{0} \quad \text{on } \partial Y_{\text{f}} \setminus \partial Y, \\ \boldsymbol{\gamma}^{j,i} &\text{ is } \mathbf{y}\text{-periodic.} \end{aligned} \quad (3.80)$$

Following [34, 95], there exists at least one solution  $\boldsymbol{\gamma}^{j,i} \in H^1(Y_{\text{f}})^2 \cap C_{\text{loc}}^\infty(\cup_{k=1}^\infty (Y_{\text{f}} - \{0, k\}))^2$  to problem (3.80). We define  $\boldsymbol{\gamma}^{j,i,\varepsilon}(\mathbf{x}) = \varepsilon \boldsymbol{\gamma}^{j,i}(\mathbf{y})$  for  $\mathbf{x} \in \Omega_{\text{pm}}^\varepsilon$  and set  $\boldsymbol{\gamma}^{j,i,\varepsilon}(\mathbf{x}) = \mathbf{0}$  for  $\mathbf{x} \in \Omega_{\text{pm}} \setminus \Omega_{\text{pm}}^\varepsilon$ . Due to the reason that  $\boldsymbol{\gamma}^{j,i,\varepsilon}$  is defined in the porous-medium domain, it has a value on the fluid–porous interface  $\Sigma$  which needs to be corrected. In order to do this, we use the following boundary layer problem [34, 95] constructed on the whole stripe  $Z^{\text{bl}}$ :

$$-\Delta_{\mathbf{y}} \boldsymbol{\gamma}^{j,i,\text{bl}} + \nabla_{\mathbf{y}} \pi^{j,i,\text{bl}} = \mathbf{0} \quad \text{in } Z^+ \cup Z^-, \quad (3.81)$$

$$\nabla_{\mathbf{y}} \cdot \boldsymbol{\gamma}^{j,i,\text{bl}} = 0 \quad \text{in } Z^+ \cup Z^-, \quad (3.82)$$

$$\llbracket \boldsymbol{\gamma}^{j,i,\text{bl}} \rrbracket_S = \boldsymbol{\gamma}^{j,i} \quad \text{on } S, \quad (3.83)$$

$$\llbracket (\nabla_{\mathbf{y}} \boldsymbol{\gamma}^{j,i,\text{bl}} - \pi^{j,i,\text{bl}} \mathbf{1}) \mathbf{e}_2 \rrbracket_S = -\nabla_{\mathbf{y}} \boldsymbol{\gamma}^{j,i} \mathbf{e}_2 \quad \text{on } S, \quad (3.84)$$

$$\boldsymbol{\gamma}^{j,i,\text{bl}} = \mathbf{0} \quad \text{on } \bigcup_{k=1}^\infty (\partial Y_S - \{0, k\}), \quad \{\boldsymbol{\gamma}^{j,i,\text{bl}}, \pi^{j,i,\text{bl}}\} \text{ is } y_1\text{-periodic.} \quad (3.85)$$

From [95] we know that a solution  $\{\boldsymbol{\gamma}^{j,i,\text{bl}}, \pi^{j,i,\text{bl}}\} \in L_{\text{loc}}^2(Z^{\text{bl}})^2 \cap C_{\text{loc}}^\infty(Z^+ \cup Z^-)^2 \times C_{\text{loc}}^\infty(Z^+ \cup Z^-)$  to problem (3.81)–(3.85) exists, where  $\boldsymbol{\gamma}^{j,i,\text{bl}}$  is unique and  $\pi^{j,i,\text{bl}}$  is unique up to a constant. Furthermore, the authors [95] show that  $\boldsymbol{\gamma}^{j,i,\text{bl}}(\cdot, \pm 0) \in W^{2-1/q, q}(S)^2$  and  $(\nabla_{\mathbf{y}} \boldsymbol{\gamma}^{j,i,\text{bl}} - \pi^{j,i,\text{bl}} \mathbf{1})(\cdot, \pm 0) \mathbf{e}_2 \in W^{1-1/q, q}(S)^2$  for all  $q \in [1, \infty)$ , and that there exist a constant  $\gamma \in (0, 1)$

such that

$$\begin{aligned} e^{\gamma|y_2|} \nabla_{\mathbf{y}} \boldsymbol{\gamma}^{j,i,\text{bl}} &\in L^2(Z^+ \cup Z^-)^{2 \times 2}, & e^{\gamma|y_2|} \boldsymbol{\gamma}^{j,i,\text{bl}} &\in L^2(Z^-)^2, \\ e^{\gamma|y_2|} \pi^{j,i,\text{bl}} &\in L^2(Z^-). \end{aligned}$$

We introduce  $\boldsymbol{\gamma}^{j,i,\text{bl},\varepsilon}(\mathbf{x}) = \varepsilon \boldsymbol{\gamma}^{j,i,\text{bl}}(\mathbf{y})$  and  $\pi^{j,i,\text{bl},\varepsilon}(\mathbf{x}) = \pi^{j,i,\text{bl}}(\mathbf{y})$  for  $\mathbf{x} \in \Omega^\varepsilon$  and extend the boundary layer velocity  $\boldsymbol{\gamma}^{j,i,\text{bl},\varepsilon}$  by zero in  $\Omega \setminus \Omega^\varepsilon$ . After [95], there exist boundary layer constants  $C_\pi^{j,i,\text{bl}}$  and  $C^{j,i,\text{bl}}$  such that

$$|\boldsymbol{\gamma}^{j,i,\text{bl}} - C^{j,i,\text{bl}}| \leq C e^{-\gamma y_2}, \quad |\pi^{j,i,\text{bl}} - C_\pi^{j,i,\text{bl}}| \leq C e^{-\gamma y_2} \quad \text{for } y_2 > 0.$$

For details on the existence and uniqueness of a solution to problem (3.81)–(3.85) and for further properties of the boundary layer solution  $\{\boldsymbol{\gamma}^{j,i,\text{bl}}, \pi^{j,i,\text{bl}}\}$ , we refer to [34, 95].

We use problems (3.80) and (3.81)–(3.85) to define boundary layer correctors for the compressibility effects coming from the cell problems. These correctors are added to the error functions  $U^{3,\varepsilon}$  and  $P^{3,\varepsilon}$  yielding the following new errors

$$\begin{aligned} U^{4,\varepsilon} &= U^{3,\varepsilon} - \mathcal{H}(-x_2) \varepsilon^2 \sum_{i,j=1}^2 \boldsymbol{\gamma}^{j,i,\varepsilon} \frac{\partial^2 p^{\text{pm}}}{\partial x_i \partial x_j} \\ &\quad - \varepsilon^2 \sum_{i,j=1}^2 \left( \boldsymbol{\gamma}^{j,i,\text{bl},\varepsilon} - \mathcal{H}(x_2) \varepsilon C^{j,i,\text{bl}} \right) \frac{\partial^2 p^{\text{pm}}}{\partial x_i \partial x_j} \Big|_{\Sigma}, \\ P^{4,\varepsilon} &= P^{3,\varepsilon} - \varepsilon^2 \sum_{i,j=1}^2 \left( \pi^{j,i,\text{bl},\varepsilon} - C_\pi^{j,i,\text{bl}} \right) \frac{\partial^2 p^{\text{pm}}}{\partial x_i \partial x_j} \Big|_{\Sigma}. \end{aligned}$$

### b) Compressibility effects coming from $t_1^{\text{bl},\varepsilon}$

Next, we correct the compressibility effects resulting from the second term on the right hand side of (3.74) which is only bounded by  $\varepsilon^{3/2}$  in (3.77).

We consider the following boundary layer problem from [95, Section 1.2.8] to eliminate this problematic term

$$\nabla_{\mathbf{y}} \cdot \boldsymbol{\zeta}^{\text{bl}} = t_1^{\text{bl}}(\mathbf{y}) - \mathcal{H}(y_2) N_1^{\text{bl}} \quad \text{in } Z^+ \cup Z^-, \quad (3.86)$$

$$\llbracket \boldsymbol{\zeta}^{\text{bl}} \rrbracket_S = - \left( \int_{Z^{\text{bl}}} (t_1^{\text{bl}}(\mathbf{y}) - \mathcal{H}(y_2) N_1^{\text{bl}}) d\mathbf{y} \right) \mathbf{e}_2 \quad \text{on } S, \quad (3.87)$$

$$\boldsymbol{\zeta}^{\text{bl}} = \mathbf{0} \quad \text{on } \bigcup_{k=1}^{\infty} (\partial Y_s - \{0, k\}), \quad \boldsymbol{\zeta}^{\text{bl}} \text{ is } y_1\text{-periodic}. \quad (3.88)$$

After [95, Section 1.2.8], there exists at least one solution  $\boldsymbol{\zeta}^{\text{bl}} \in H^1(Z^+ \cup Z^-)^2 \cap C_{\text{loc}}^\infty(Z^+ \cup Z^-)^2$  to problem (3.86)–(3.88) such that  $\boldsymbol{\zeta}^{\text{bl}}(\cdot, \pm 0) \in W^{1-1/q, q}(S)^2$  for all  $q \in [1, \infty)$  and for  $\gamma > 0$  we have  $e^{\gamma|y_2|} \boldsymbol{\zeta}^{\text{bl}} \in H^1(Z^+ \cup Z^-)^2$ . For the definition on the macroscopic domain, we set  $\boldsymbol{\zeta}^{\text{bl}, \varepsilon}(\mathbf{x}) = \varepsilon \boldsymbol{\zeta}^{\text{bl}}(\mathbf{y})$  for  $\mathbf{x} \in \Omega^\varepsilon$  and  $\boldsymbol{\zeta}^{\text{bl}, \varepsilon}(\mathbf{x}) = \mathbf{0}$  for  $\mathbf{x} \in \Omega \setminus \Omega^\varepsilon$ , and following [95], it holds

$$\|\boldsymbol{\zeta}^{\text{bl}, \varepsilon}\|_{L^2(\Omega)^2} \leq \varepsilon^{3/2}, \quad \|\nabla \boldsymbol{\zeta}^{\text{bl}, \varepsilon}\|_{L^2(\Omega)^{2 \times 2}} \leq \varepsilon^{1/2}. \quad (3.89)$$

Before we add the boundary layer corrector  $\boldsymbol{\zeta}^{\text{bl}, \varepsilon}$  with an appropriate scaling to the velocity error function  $U^{4, \varepsilon}$  in order to correct compressibility effects, we need to eliminate the additional contribution to the velocity on the interface appearing on the right hand side of equation (3.87). For the correction of this arising term, we construct the following counter flow problem

$$\Delta \mathbf{v}^{\text{cf}} - \nabla p^{\text{cf}} = \mathbf{0}, \quad \nabla \cdot \mathbf{v}^{\text{cf}} = 0 \quad \text{in } \Omega_{\text{ff}}, \quad \int_{\Omega_{\text{ff}}} p^{\text{cf}} d\mathbf{x} = 0, \quad (3.90)$$

$$v_1^{\text{cf}} = \llbracket \zeta_1^{\text{bl}} \rrbracket_S \frac{\partial}{\partial x_1} \frac{\partial v_1^{\text{ff}}}{\partial x_2} \Big|_\Sigma, \quad v_2^{\text{cf}} = \llbracket \zeta_2^{\text{bl}} \rrbracket_S \frac{\partial}{\partial x_1} \frac{\partial v_1^{\text{ff}}}{\partial x_2} \Big|_\Sigma \quad \text{on } \Sigma, \quad (3.91)$$

$$v_1^{\text{cf}} = 0, \quad v_2^{\text{cf}} = v_2^{\text{cf}, \text{in}} \quad \text{on } \{x_2 = h\}, \quad \{\mathbf{v}^{\text{cf}}, p^{\text{cf}}\} \text{ is } L\text{-periodic in } x_1, \quad (3.92)$$



where the velocity  $\mathbf{v}^{\text{cf}}$  should satisfy the compatibility condition

$$\int_0^L v_2^{\text{cf},\text{in}} dx_1 = \int_0^L \llbracket \zeta_2^{\text{bl}} \rrbracket_S \frac{\partial}{\partial x_1} \frac{\partial v_1^{\text{ff}}}{\partial x_2} \Big|_{\Sigma} dx_1.$$

We correct the compressibility effects coming from the function  $t_1^{\text{bl},\varepsilon}$  using the boundary layer corrector  $\zeta^{\text{bl},\varepsilon}$  and the solution  $\{\mathbf{v}^{\text{cf}}, p^{\text{cf}}\}$  to the counter flow problem (3.90)–(3.92). This leads to following velocity and pressure error functions

$$U^{5,\varepsilon} = U^{4,\varepsilon} - \varepsilon \zeta^{\text{bl},\varepsilon} \frac{\partial}{\partial x_1} \frac{\partial v_1^{\text{ff}}}{\partial x_2} \Big|_{\Sigma} + \varepsilon^2 \mathcal{H}(x_2) \mathbf{v}^{\text{cf}}, \quad P^{5,\varepsilon} = P^{4,\varepsilon} + \varepsilon^2 \mathcal{H}(x_2) p^{\text{cf}}.$$

### c) Compressibility effects coming from $q_1^{j,\text{bl}}$

Finally, we address the last term on the right hand side of equation (3.74) involving the boundary layer corrector  $q_1^{j,\text{bl}}$ . For the correction of this term, we need an auxiliary problem which is defined in the porous medium only, similar to (3.60)–(3.64). We consider the following boundary layer problem defined in [95] for our purpose

$$\begin{aligned} \nabla_{\mathbf{y}} \cdot \mathbf{Z}^{j,\text{bl}} &= q_1^{j,\text{bl}} \quad \text{in } Z^-, \\ \mathbf{Z}^{j,\text{bl}}(\cdot, -0) &= - \left( \int_{Z^-} q_1^{j,\text{bl}} d\mathbf{y} \right) \mathbf{e}_2 \quad \text{on } S, \\ \mathbf{Z}^{j,\text{bl}} &= \mathbf{0} \quad \text{on } \bigcup_{k=1}^{\infty} (\partial Y_s - \{0, k\}), \quad \mathbf{Z}^{j,\text{bl}} \text{ is } y_1\text{-periodic.} \end{aligned}$$

We obtain existence of a solution  $\mathbf{Z}^{j,\text{bl}} \in H^1(Z^+ \cup Z^-)^2 \cap C_{\text{loc}}^{\infty}(Z^+ \cup Z^-)^2$  by applying Proposition 3.20 from [95]. Moreover, we have  $\mathbf{Z}^{j,\text{bl}} \in W^{1,q}(Y)^2$  and  $\mathbf{Z}^{j,\text{bl}} \in W^{1,q}(Y - \{0, 1\})^2$  for all  $q \in [1, \infty)$ , and there exists a constant  $\gamma \in (0, 1)$  such that  $e^{\gamma|\cdot|} \mathbf{Z}^{j,\text{bl}} \in H^1(Z^+ \cup Z^-)^2$ . We introduce the boundary

layer corrector

$$\mathbf{Z}^{j,\text{bl},\varepsilon}(\mathbf{x}) = \varepsilon \mathbf{Z}^{j,\text{bl}} \left( \frac{x_1}{\varepsilon}, -\frac{x_2 + H}{\varepsilon} \right) \quad \text{for } \mathbf{x} \in \Omega^\varepsilon,$$

and extend it by zero in  $\Omega \setminus \Omega^\varepsilon$ . Using corrector  $\mathbf{Z}^{j,\text{bl},\varepsilon}$  for the compressibility effects coming from  $q_1^{j,\text{bl}}$  we obtain the following velocity and pressure errors

$$\begin{aligned} \mathbf{U}^{6,\varepsilon} &= \mathbf{U}^{5,\varepsilon} - \varepsilon^2 \sum_{j=1}^2 \frac{\partial}{\partial x_1} \frac{\partial p^{\text{pm}}}{\partial x_j}(x_1, -H) \left( \mathbf{Z}^{j,\text{bl},\varepsilon} + \varepsilon R^\varepsilon \mathbf{e}_2 \int_{Z^-} q_1^{j,\text{bl}} \, d\mathbf{y} \right), \\ p^{6,\varepsilon} &= p^{5,\varepsilon}. \end{aligned}$$

Here,  $R^\varepsilon$  is the restriction operator first introduced by Tartar in [153, Lemma 4]. In this work, we consider  $R^\varepsilon : H^1(\Omega)^2 \rightarrow H^1(\Omega^\varepsilon)^2$  for  $\mathbf{v} \in H^1(\Omega)^2$  by  $R^\varepsilon \mathbf{v} = \mathbf{v}|_{\Omega^\varepsilon}$ , hence, we have

$$\mathbf{v} \in H^1(\Omega^\varepsilon)^2 \quad \Rightarrow \quad R^\varepsilon \mathbf{v} = \mathbf{v}, \quad \nabla \cdot \mathbf{v} = 0 \quad \Rightarrow \quad \nabla \cdot (R^\varepsilon \mathbf{v}) = 0.$$

The integral term  $\varepsilon R^\varepsilon \mathbf{e}_2 \int_{Z^-} q_1^{j,\text{bl}} \, d\mathbf{y}$ , included in the velocity error function  $\mathbf{U}^{6,\varepsilon}$ , corrects the value of  $\mathbf{Z}^{j,\text{bl},\varepsilon}$  on the lower boundary  $\{x_2 = -H\}$ .

By construction of  $\mathbf{U}^{6,\varepsilon}$  we reduce nonphysical compressibility effects of the velocity error  $\mathbf{U}^{3,\varepsilon}$  that appeared due to the corrections made in Sections 3.1.2 and 3.1.3.1–3.1.3.3. Moreover,  $\mathbf{U}^{6,\varepsilon}$  is derived in such a way that it fulfills boundary conditions (3.57) and (3.68), the no-slip condition  $\mathbf{U}^{6,\varepsilon} = \mathbf{0}$  on  $\partial\Omega^\varepsilon \setminus \partial\Omega$  and that it is  $L$ -periodic in  $x_1$ , leading to  $\mathbf{U}^{6,\varepsilon} \in V_{\text{per}}(\Omega^\varepsilon)^2$ . We summarize the obtained results in the following corollaries.

**Corollary 3.3:** *It is  $\mathbf{U}^{6,\varepsilon} \in V_{\text{per}}(\Omega^\varepsilon)^2$  and it holds  $\|\nabla \cdot \mathbf{U}^{6,\varepsilon}\|_{L^2(\Omega^\varepsilon)} \leq C\varepsilon^{5/2}$ .*

*Proof.* From Corollary 3.2 we know that  $\mathbf{U}^{3,\varepsilon} \in V_{\text{per}}(\Omega^\varepsilon)^2$ . Moreover, all correctors added to the velocity error  $\mathbf{U}^{3,\varepsilon}$  are elements of  $V_{\text{per}}(\Omega^\varepsilon)^2$ , thus,

by construction  $\mathbf{U}^{6,\varepsilon} \in V_{\text{per}}(\Omega^\varepsilon)^2$ . Furthermore, we have

$$\begin{aligned} \nabla \cdot \mathbf{U}^{6,\varepsilon} = & -\varepsilon^2 \sum_{j=1}^2 \left( \beta_1^{j,\text{bl},\varepsilon} - \mathcal{H}(x_2) M_1^{j,\text{bl}} \right) \frac{\partial}{\partial x_1} \frac{\partial p^{\text{pm}}}{\partial x_j} \Big|_{\Sigma} \\ & + \frac{\mathcal{H}(-x_2)}{|Y_{\text{f}}|} \varepsilon^2 \underbrace{\sum_{j=1}^2 \tilde{k}_{ij} \frac{\partial^2 p^{\text{pm}}}{\partial x_i \partial x_j}}_{= \nabla \cdot (\tilde{\mathbf{K}} \nabla p^{\text{pm}}) = 0} - \mathcal{H}(-x_2) \varepsilon^3 \sum_{j=1}^2 \boldsymbol{\gamma}^{j,i}(\mathbf{y}) \cdot \nabla \frac{\partial^2 p^{\text{pm}}}{\partial x_i \partial x_j} \\ & - \varepsilon^3 \sum_{j=1}^2 \left( \boldsymbol{\gamma}^{j,i,\text{bl}}(\mathbf{y}) - \mathcal{H}(x_2) \mathbf{C}^{j,i,\text{bl}} \right) \cdot \nabla \frac{\partial^2 p^{\text{pm}}}{\partial x_i \partial x_j} \Big|_{\Sigma} - \varepsilon \zeta_1^{\text{bl},\varepsilon} \frac{\partial}{\partial x_1} \frac{\partial v_1^{\text{ff}}}{\partial x_2} \Big|_{\Sigma} \\ & - \varepsilon^3 \sum_{j=1}^2 \nabla \frac{\partial}{\partial x_1} \frac{\partial p^{\text{pm}}}{\partial x_j} (x_1, -H) \cdot \left( \mathbf{Z}^{j,\text{bl}} \left( \frac{x_1}{\varepsilon}, -\frac{x_2 + H}{\varepsilon} \right) \right. \\ & \quad \left. + R^\varepsilon \mathbf{e}_2 \int_{Z^-} q_1^{j,\text{bl}} d\mathbf{y} \right). \end{aligned}$$

Considering estimates (3.48) and (3.89) we obtain  $\|\nabla \cdot \mathbf{U}^{6,\varepsilon}\|_{L^2(\Omega^\varepsilon)} \leq C\varepsilon^{5/2}$ .  $\square$

**Corollary 3.4:** For all  $\boldsymbol{\varphi} \in V_{\text{per}}(\Omega^\varepsilon)^2$  it holds that

$$\left| \int_{\Omega^\varepsilon} \nabla \mathbf{U}^{6,\varepsilon} : \nabla \boldsymbol{\varphi} - \int_{\Omega^\varepsilon} P^{6,\varepsilon} \nabla \cdot \boldsymbol{\varphi} \right| \leq C\varepsilon^{3/2} \left( \|\nabla \boldsymbol{\varphi}\|_{L^2(\Omega^\varepsilon)^{2 \times 2}} + \|\boldsymbol{\varphi}\|_{H^1(\Omega_{\text{ff}}^\varepsilon)} \right). \quad (3.93)$$

*Proof.* For the error functions  $\mathbf{U}^{6,\varepsilon}$  and  $P^{6,\varepsilon}$  we write the weak formulation

$$\begin{aligned} \int_{\Omega^\varepsilon} \nabla \mathbf{U}^{6,\varepsilon} : \nabla \boldsymbol{\varphi} - \int_{\Omega^\varepsilon} P^{6,\varepsilon} \nabla \cdot \boldsymbol{\varphi} &= \int_{\Omega^\varepsilon} \nabla \mathbf{U}^{3,\varepsilon} : \nabla \boldsymbol{\varphi} - \int_{\Omega^\varepsilon} P^{3,\varepsilon} \nabla \cdot \boldsymbol{\varphi} \\ & - \int_{\Omega_{\text{pm}}^\varepsilon} \varepsilon^2 \sum_{i,j=1}^2 \left( \nabla_{\mathbf{y}} \boldsymbol{\gamma}^{j,i}(\mathbf{y}) \frac{\partial^2 p^{\text{pm}}}{\partial x_i \partial x_j} + \boldsymbol{\gamma}^{j,i,\varepsilon} \nabla \frac{\partial^2 p^{\text{pm}}}{\partial x_i \partial x_j} \right) : \nabla \boldsymbol{\varphi} \\ & + \int_{\Sigma} \varepsilon^2 \sum_{i,j=1}^2 \left( \nabla_{\mathbf{y}} \boldsymbol{\gamma}^{j,i}(\mathbf{y}_1, -0) \frac{\partial^2 p^{\text{pm}}}{\partial x_i \partial x_j} \Big|_{\Sigma} \mathbf{e}_2 - \left( \boldsymbol{\gamma}^{j,i,\varepsilon} \otimes \nabla \frac{\partial^2 p^{\text{pm}}}{\partial x_i \partial x_j} \Big|_{\Sigma} \right) \mathbf{e}_2 \right) \cdot \boldsymbol{\varphi} \end{aligned}$$

$$\begin{aligned}
& + \int_{\Sigma} \varepsilon^3 \sum_{i,j=1}^2 \left( \left( C^{j,i,\text{bl}} \otimes \nabla \frac{\partial^2 p^{\text{pm}}}{\partial x_i \partial x_j} \Big|_{\Sigma} \right) \mathbf{e}_2 \right) \cdot \boldsymbol{\varphi} \\
& - \int_{\Omega^\varepsilon} 2\varepsilon^2 \sum_{i,j=1}^2 \left( \left( \boldsymbol{\gamma}^{j,i,\text{bl},\varepsilon} - \mathcal{H}(x_2) \varepsilon C^{j,i,\text{bl}} \right) \otimes \nabla \frac{\partial^2 p^{\text{pm}}}{\partial x_i \partial x_j} \Big|_{\Sigma} \right) : \nabla \boldsymbol{\varphi} \\
& - \int_{\Omega^\varepsilon} \varepsilon^2 \sum_{i,j=1}^2 \left( \boldsymbol{\gamma}^{j,i,\text{bl},\varepsilon} - \mathcal{H}(x_2) \varepsilon C^{j,i,\text{bl}} \right) \frac{\partial^2}{\partial x_1^2} \frac{\partial^2 p^{\text{pm}}}{\partial x_i \partial x_j} \Big|_{\Sigma} \cdot \boldsymbol{\varphi} \\
& - \int_{\Omega^\varepsilon} \varepsilon^2 \left( \nabla \boldsymbol{\zeta}^{\text{bl}}(\mathbf{y}) \frac{\partial}{\partial x_1} \frac{\partial v_1^{\text{ff}}}{\partial x_2} \Big|_{\Sigma} + \boldsymbol{\zeta}^{\text{bl}}(\mathbf{y}) \otimes \nabla \frac{\partial}{\partial x_1} \frac{\partial v_1^{\text{ff}}}{\partial x_2} \Big|_{\Sigma} \right) : \nabla \boldsymbol{\varphi} \\
& - \int_{\Omega^\varepsilon} \varepsilon^2 \sum_{i,j=1}^2 \left( \boldsymbol{\pi}^{j,i,\text{bl},\varepsilon} - C_\pi^{j,i,\text{bl}} \right) \nabla \frac{\partial^2 p^{\text{pm}}}{\partial x_i \partial x_j} \Big|_{\Sigma} \cdot \boldsymbol{\varphi} \\
& - \int_{\Sigma} \varepsilon^2 \left( (\nabla \mathbf{v}^{\text{cf}} - p^{\text{cf}} \mathbf{1}) \mathbf{e}_2 \right) \cdot \boldsymbol{\varphi} \\
& - \int_{\Omega^\varepsilon} \varepsilon^2 \sum_{j=1}^2 \nabla \left( \frac{\partial}{\partial x_1} \frac{\partial p^{\text{pm}}}{\partial x_j} (x_1, -H) \left( Z^{j,\text{bl},\varepsilon} + \varepsilon R^\varepsilon \mathbf{e}_2 \int_{Z^-} q_1^{j,\text{bl}} d\mathbf{y} \right) \right) : \nabla \boldsymbol{\varphi} \\
& + \text{e.s.t.} \tag{3.94}
\end{aligned}$$

Taking into account estimate (3.73) for the first two terms on the right hand side of (3.94) and noting that all the other integrals are at least of order  $\varepsilon^2$ , we prove inequality (3.93).  $\square$

Now, the approximations of the pore-scale velocity and pressure given by  $\mathbf{v}_{\text{approx}}^{6,\varepsilon} = \mathbf{U}^{6,\varepsilon} - \mathbf{v}^\varepsilon$  and  $p_{\text{approx}}^{6,\varepsilon} = P^{6,\varepsilon} - p^\varepsilon$  is accurate enough such that the goal of the homogenization procedure is achieved and the divergence of the velocity error  $\mathbf{U}^{6,\varepsilon} \in V_{\text{per}}(\Omega^\varepsilon)^2$  is estimated sufficiently well,  $\|\nabla \cdot \mathbf{U}^{6,\varepsilon}\|_{L^2(\Omega^\varepsilon)} \leq C\varepsilon^{5/2}$ . Hence, we can formulate effective conditions on the fluid-porous interface.

### 3.1.4 Step 4: Leading order approximations and interface conditions

We constructed a higher-order approximation of the pore-scale solution corresponding to problem (3.2)–(3.4) yielding the error functions  $U^{6,\varepsilon}$  and  $P^{6,\varepsilon}$ . The leading order approximation of the pore-scale velocity and pressure is used for the formulation of effective interface conditions and reads

$$\begin{aligned} \mathbf{v}_{\text{approx}}^{6,\varepsilon} &= \mathcal{H}(x_2)\mathbf{v}^{\text{ff}} - \mathcal{H}(-x_2)\varepsilon^2 \sum_{j=1}^2 \mathbf{w}^{j,\varepsilon} \frac{\partial p^{\text{pm}}}{\partial x_j} - \varepsilon \left( \mathbf{t}^{\text{bl},\varepsilon} - \mathcal{H}(x_2)\mathbf{N}^{\text{bl}} \right) \frac{\partial v_1^{\text{ff}}}{\partial x_2} \Big|_{\Sigma} \\ &\quad + \varepsilon^2 \boldsymbol{\zeta}^{\text{bl}}(\mathbf{y}) \frac{\partial}{\partial x_1} \frac{\partial v_1^{\text{ff}}}{\partial x_2} \Big|_{\Sigma} + \varepsilon^2 \sum_{j=1}^2 \left( \boldsymbol{\beta}^{j,\text{bl},\varepsilon} - \mathcal{H}(x_2)\mathbf{M}^{j,\text{bl}} \right) \frac{\partial p^{\text{pm}}}{\partial x_j} \Big|_{\Sigma} \\ &\quad - \varepsilon^2 \sum_{j=1}^2 \frac{\partial p^{\text{pm}}}{\partial x_j} (x_1, -H) \mathbf{q}^{j,\text{bl}} \left( \frac{x_1}{\varepsilon}, -\frac{x_2+H}{\varepsilon} \right) - \varepsilon^2 \mathcal{H}(x_2) \mathbf{v}^{\text{cf}} + \mathcal{O}(\varepsilon^3), \\ p_{\text{approx}}^{6,\varepsilon} &= \mathcal{H}(x_2)p^{\text{ff}} + \mathcal{H}(-x_2)p^{\text{pm}} - \left( s^{\text{bl},\varepsilon} - \mathcal{H}(x_2)N_s^{\text{bl}} \right) \frac{\partial v_1^{\text{ff}}}{\partial x_2} \Big|_{\Sigma} + \mathcal{O}(\varepsilon). \end{aligned}$$

The coupling conditions for the velocity components are obtained by taking into account the definition of  $\mathbf{v}_{\text{approx}}^{6,\varepsilon}$  and the fact that the pore-scale velocity  $\mathbf{v}^\varepsilon$  is continuous across the interface, thus, the same should also be true for its approximation, i.e.,  $[[\mathbf{v}_{\text{approx}}^{6,\varepsilon}]]_{\Sigma} = \mathbf{0}$ . The coupling condition for the pressure is given by equation (3.72) and was already derived in Section 3.1.3.3.

Below, we present the generalized coupling conditions derived via homogenization and boundary layer theory in this chapter

$$\mathbf{v}^{\text{ff}} \cdot \mathbf{n} = \mathbf{v}^{\text{pm}} \cdot \mathbf{n} \quad \text{on } \Sigma, \quad (3.95)$$

$$p^{\text{pm}} = p^{\text{ff}} - \frac{\partial v_2^{\text{ff}}}{\partial x_2} + N_s^{\text{bl}} \frac{\partial v_1^{\text{ff}}}{\partial x_2} \quad \text{on } \Sigma, \quad (3.96)$$

$$\mathbf{v}^{\text{ff}} \cdot \boldsymbol{\tau} = -\varepsilon \mathbf{N}^{\text{bl}} \cdot \boldsymbol{\tau} \frac{\partial v_1^{\text{ff}}}{\partial x_2} + \varepsilon^2 \sum_{j=1}^2 \mathbf{M}^{j,\text{bl}} \cdot \boldsymbol{\tau} \frac{\partial p^{\text{pm}}}{\partial x_j} \quad \text{on } \Sigma. \quad (3.97)$$

The physical interpretation and dimensional formulation of coupling conditions (3.95)–(3.97) is given in Section 3.2, where we also explain how the exact position of the fluid–porous interface  $\Sigma$  is incorporated in the derived conditions (3.95)–(3.97) and provide a comparison to the classical interface conditions for the Stokes–Darcy problem.

Taking into account the derived interface conditions (3.95)–(3.97) and inserting the velocity error  $\mathbf{U}^{6,\varepsilon}$  as a test function in (3.93) yields the following corollary.

**Corollary 3.5:** *For  $\mathbf{U}^{6,\varepsilon} \in V_{per}(\Omega^\varepsilon)^2$  we have*

$$\begin{aligned} \|\nabla \mathbf{U}^{6,\varepsilon}\|_{L^2(\Omega^\varepsilon)^{2 \times 2}}^2 &\leq C\varepsilon^{5/2} \|P^{6,\varepsilon}\|_{L^2(\Omega^\varepsilon)} \\ &\quad + C\varepsilon^{3/2} \left( \|\nabla \mathbf{U}^{6,\varepsilon}\|_{L^2(\Omega_{pm}^\varepsilon)^{2 \times 2}} + \|\mathbf{U}^{6,\varepsilon}\|_{H^1(\Omega_{fl}^\varepsilon)^2} \right). \end{aligned}$$

*Proof.* We use the estimates proven in Corollaries 3.3 and 3.4, and substitute  $\mathbf{U}^{6,\varepsilon}$  as a test function in the weak form (3.93) to complete the proof.  $\square$

**Remark 3.6:** *The next step towards rigorous error estimates for the error functions  $\mathbf{U}^{6,\varepsilon}$ ,  $P^{6,\varepsilon}$  is to estimate the pressure error  $P^{6,\varepsilon}$  using the velocity error  $\mathbf{U}^{6,\varepsilon}$  similar to, e.g., [34, 95]. However, such error estimates are beyond the scope of this work. In this thesis, we focus on the derivation of the generalized coupling conditions (3.95)–(3.97), the numerical validation and the well-posedness of the resulting coupled Stokes–Darcy problem.*

## 3.2 Practical aspects

This section is dedicated to aspects that are useful for applying the newly derived conditions in numerical simulations of free-flow and porous-medium flow systems. In Section 3.2.1, we write the generalized interface conditions (3.95)–(3.97) in terms of SI units to account for the physical

dimensions of all quantities. In Section 3.2.2, we explain how the information about the exact interface position is included in the boundary layer constants. We show that the interface location is not uncertain in this case, contrary to the classical conditions (2.17)–(2.19). In Section 3.2.3, we compare the generalized interface conditions to the classical ones, highlight their differences and similarities to make it easier to adopt the new coupling conditions in already existing frameworks.

### 3.2.1 Dimensional formulation

The generalized interface conditions (3.95)–(3.97) are derived from the dimensionless pore-scale problem (3.2)–(3.4). However, for numerical simulations of applications involving physical quantities, the dimensional form of the derived coupling conditions is needed. In order to formulate the conditions for the dimensional setting we use the scale separation parameter  $\varepsilon = \ell/\mathcal{L}$ , and the same quantities and scaling parameters as in Section 2.3.1. Moreover, we write the generalized coupling conditions in terms of the stress tensor  $\mathbf{T}(\mathbf{v}^{\text{ff}}, p^{\text{ff}}) = \nabla \mathbf{v}^{\text{ff}} - p^{\text{ff}} \mathbf{I}$  and the tangential respective normal vector  $\boldsymbol{\tau}$  and  $\mathbf{n}$  on the horizontal fluid–porous interface  $\Sigma$  which is considered to be flat. The generalized interface conditions (3.95)–(3.97) in their dimensional form read

$$\mathbf{v}^{\text{ff}} \cdot \mathbf{n} = \mathbf{v}^{\text{pm}} \cdot \mathbf{n} \quad \text{on } \Sigma, \quad (3.98)$$

$$p^{\text{pm}} = -\mathbf{n} \cdot \mathbf{T}(\mathbf{v}^{\text{ff}}, p^{\text{ff}}) \mathbf{n} + N_s^{\text{bl}} \boldsymbol{\tau} \cdot \mathbf{T}(\mathbf{v}^{\text{ff}}, p^{\text{ff}}) \mathbf{n} \quad \text{on } \Sigma, \quad (3.99)$$

$$\mathbf{v}^{\text{ff}} \cdot \boldsymbol{\tau} = -\ell \mu^{-1} (\mathbf{N}^{\text{bl}} \cdot \boldsymbol{\tau}) \boldsymbol{\tau} \cdot \mathbf{T}(\mathbf{v}^{\text{ff}}, p^{\text{ff}}) \mathbf{n} + \ell^2 \mu^{-1} \sum_{j=1}^2 \frac{\partial p^{\text{pm}}}{\partial x_j} \mathbf{M}^{j,\text{bl}} \cdot \boldsymbol{\tau} \quad \text{on } \Sigma. \quad (3.100)$$

Here, the unit normal vector  $\mathbf{n}$  points outward the porous medium and the unit tangential vector  $\boldsymbol{\tau}$  is oriented in the positive  $x_1$ -direction, i.e.,  $\boldsymbol{\tau} = \mathbf{e}_1$ . All quantities appearing in the coupling conditions (3.98)–(3.100) are dimensional, except for the boundary layer constants  $N_s^{\text{bl}}$ ,  $\mathbf{N}^{\text{bl}}$ ,  $\mathbf{M}^{j,\text{bl}}$ . We provide the corresponding primary dimensions and SI units in Table 3.1.

Quantity	Primary dimensions	SI units
Velocity $\mathbf{v}^{\text{ff}}, \mathbf{v}^{\text{pm}}$	$[\text{LT}^{-1}]$	$\text{m} \cdot \text{s}^{-1}$
Pressure $p^{\text{ff}}, p^{\text{pm}}$	$[\text{MLT}^{-2}]$	$\text{Pa} = \text{kg} \cdot \text{m}^{-1} \cdot \text{s}^{-2}$
Stress tensor $\mathbf{T}(\mathbf{v}^{\text{ff}}, p^{\text{ff}})$	$[\text{ML}^{-1}\text{T}^{-2}]$	Pa
Viscosity $\mu$	$[\text{ML}^{-1}\text{T}^{-1}]$	$\text{Pa} \cdot \text{s}$
Permeability $\mathbf{K}$	$[\text{L}^2]$	$\text{m}^2$
Pore size $\ell$	$[\text{L}]$	m
Boundary layer constants $N_s^{\text{bl}}, \mathbf{N}^{\text{bl}}, \mathbf{M}^{j,\text{bl}}$	$[-]$	–

Table 3.1: Quantities appearing in the generalized coupling conditions (3.98)–(3.100) with their corresponding primary dimensions and SI units.

The dimensional Darcy velocity in condition (3.98) has the following form

$$\mathbf{v}^{\text{pm}} = -\frac{\varepsilon^2 \mathcal{L}^2 \tilde{\mathbf{K}}}{\mu} \nabla p^{\text{pm}} = -\frac{\ell^2 \tilde{\mathbf{K}}}{\mu} \nabla p^{\text{pm}} = -\frac{\mathbf{K}}{\mu} \nabla p^{\text{pm}}, \quad (3.101)$$

where  $\mathbf{K} = \ell^2 \tilde{\mathbf{K}}$  is the physical permeability tensor that was already introduced in equation (2.13). Note that  $\mathbf{K}$  has primary dimension  $[\text{L}^2]$  (Table 3.1) and  $\tilde{\mathbf{K}}$  is a dimensionless quantity.

Before comparing the generalized interface conditions (3.98)–(3.100) to the classical conditions (2.17)–(2.19) in Section 3.2.3, we take a closer look at the effective coefficients (permeability and boundary layer constants) appearing in the generalized conditions in Section 3.2.2.

### 3.2.2 Effective coefficients and interface location

Effective coefficients appearing both in the dimensionless and dimensional form of the generalized interface conditions are the permeability tensor



$\tilde{\mathbf{K}}$  in the Darcy velocity  $\mathbf{v}^{\text{pm}}$  appearing in (3.95) and (3.98), and the boundary layer constants  $\mathbf{N}^{\text{bl}}$ ,  $N_s^{\text{bl}}$  and  $\mathbf{M}^{j,\text{bl}}$  in (3.96)–(3.97) and (3.99)–(3.100), respectively. The nondimensional permeability  $\tilde{\mathbf{K}}$  depends only on the porous-medium geometry within the unit cell  $Y = (0, 1)^2$  and is given by (2.79). The physical permeability  $\mathbf{K} = \ell^2 \tilde{\mathbf{K}}$  depends additionally on the number of solid obstacles and the size of the coupled flow domain. Note that both coefficients  $\tilde{\mathbf{K}}$  and  $\mathbf{K}$  are not affected by a change of the fluid–porous interface location.

From Section 3.1 we know that the boundary layer constants  $\mathbf{N}^{\text{bl}}$ ,  $N_s^{\text{bl}}$  and  $\mathbf{M}^{j,\text{bl}}$  are obtained by solving problems (3.17)–(3.21) and (3.39)–(3.43) defined on the boundary layer stripe  $Z^{\text{bl}}$  (Figure 2.8, right) and integrating the solutions over the interface  $S$  as described in (3.23)–(3.24) and (3.45)–(3.46). Hence, these effective coefficients depend both on the pore geometry within the boundary layer stripe  $Z^{\text{bl}}$  and the exact location of the fluid–porous interface  $S$ . For the derivation of coupling conditions (3.95)–(3.97) we considered a horizontal interface  $S$  positioned at  $y_2 = 0$  within the stripe  $Z^{\text{bl}}$  according to the geometry of the coupled flow system (Figure 2.8). Indeed, this can be made more general. The sharp interface  $S$  within the stripe  $Z^{\text{bl}}$  can be located at any distance  $a \in (0, 1 - d^*)$  from the top of the first row of solid inclusions, where  $d^*$  denotes the height of solid inclusions. In case of circular or quadratic inclusions, for example,  $d^*$  is the diameter or side length of the solid grains. A schematic representation of two possible locations for the interface  $S$  within the vertical boundary layer stripe  $Z^{\text{bl}}$  is provided in Figure 3.1.

In order to show that the generalized interface conditions derived in Section 3.1 include the information about the chosen interface position, we introduce the following notations. We denote the sharp interface that is located at distance  $a \in (0, 1 - d^*)$  above the top of the first row of solid inclusions within the infinite boundary layer stripe  $Z^{\text{bl}}$  by

$$S_a = (0, 1) \times \left\{ \frac{d^* - 1}{2} + a \right\}.$$

Then, the free-flow part of the boundary layer stripe  $Z^{\text{bl}}$  is given by

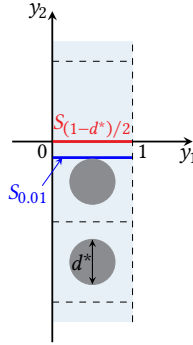


Figure 3.1: Two possible locations of the fluid–porous interface within the boundary layer stripe  $Z^{\text{bl}}$ .

$Z^{a,+} = (0, 1) \times \left( \left\{ \frac{d^*-1}{2} + a \right\}, \infty \right)$  and the solid part by  $Z^{a,-} = Z^{\text{bl}} \setminus (Z^{a,+} \cup S_a)$ . In view of these notations, the boundary layer problems (3.17)–(3.21) and (3.39)–(3.43) and the constants (3.23)–(3.24) and (3.45)–(3.46) are defined based on the interface  $S = S_{(d^*-1)/2}$  located at  $y_2 = 0$ . Since we are not restricted to this choice of interface location, we reformulate the boundary layer problems and the corresponding constants such that any interface  $S_a$  for  $a \in (0, 1 - d^*)$  can be considered. For this purpose, we replace  $S$ ,  $Z^+$  and  $Z^-$  in problems (3.17)–(3.21) and (3.39)–(3.43) by  $S_a$ ,  $Z^{a,+}$  and  $Z^{a,-}$ , respectively, and denote the solutions by  $\{t^{\text{bl},a}, s^{\text{bl},a}\}$  and  $\{\beta^{j,\text{bl},a}, \omega^{j,\text{bl},a}\}$  for  $j = 1, 2$ . Then, the boundary layer constants are given by

$$\mathbf{N}^{\text{bl},a} = \left( \int_0^1 t_1^{\text{bl},a} \left( y_1, \frac{d^*-1}{2} + a \right) dy_1, 0 \right)^\top, \quad (3.102a)$$

$$N_s^{\text{bl},a} = \int_0^1 s^{\text{bl},a} \left( y_1, \frac{d^*-1}{2} + a \right) dy_1, \quad (3.102b)$$

$$\mathbf{M}^{j,\text{bl},a} = \left( \int_0^1 \beta_1^{j,\text{bl},a} \left( y_1, \frac{d^*-1}{2} + a \right) dy_1, 0 \right)^\top. \quad (3.103)$$

According to the chosen  $a$  that determines the vertical position of the interface  $S_a$  within the boundary layer stripe  $Z^{\text{bl}}$  for the computation of the boundary layer constants, we locate the sharp interface  $\Sigma$  within the coupled flow domain  $\Omega = \Omega_{\text{ff}} \cup \Omega_{\text{pm}}$  at  $x_2 = \ell \left( \frac{d^k - 1}{2} + a \right)$ . The boundary layer constants  $\mathbf{N}^{\text{bl}}$ ,  $N_s^{\text{bl}}$  and  $\mathbf{M}^{j,\text{bl}}$  in the generalized conditions given by (3.95)–(3.97) or (3.98)–(3.100) are then replaced by  $\mathbf{N}^{\text{bl},a}$ ,  $N_s^{\text{bl},a}$  and  $\mathbf{M}^{j,\text{bl},a}$  defined in (3.102a)–(3.103). In this way, the exact location of the fluid–porous interface  $\Sigma$  is incorporated in the Stokes–Darcy model with the generalized coupling conditions.

Next, we investigate how the values of  $N_s^{\text{bl},a}$ ,  $\mathbf{N}^{\text{bl},a}$  and  $\mathbf{M}^{j,\text{bl},a}$ ,  $j = 1, 2$ , change with respect to the variation of the interface location. Note that we consider the unit normal and tangential vectors  $\mathbf{n} = \mathbf{e}_2$  and  $\boldsymbol{\tau} = \mathbf{e}_1$  on the horizontal interface. Independent of the pore geometry and the chosen interface  $S_a$ , we have  $\mathbf{N}^{\text{bl},a} \cdot \mathbf{n} = 0$  and  $\mathbf{M}^{j,\text{bl},a} \cdot \mathbf{n} = 0$  as is proven in [95, Section 3] and for isotropic and orthotropic porous media, i.e.,  $\mathbf{K} = \text{diag}(k_{11}, k_{22})$ , we obtain  $N_s^{\text{bl},a} = 0$  and  $M_1^{2,\text{bl},a} = \mathbf{M}^{2,\text{bl},a} \cdot \boldsymbol{\tau} = 0$ . The two latter equations follow from the axisymmetry of the solid part within the stripe  $Z^{\text{bl}}$  to  $y_1 = 0.5$  and the definition of the boundary layer problems (3.17)–(3.21) and (3.39)–(3.43). For further details, we refer to [34, 98]. In Section 5.3, we numerically study the behavior of  $N_1^{\text{bl},a} = \mathbf{N}^{\text{bl},a} \cdot \boldsymbol{\tau}$  and  $M_1^{1,\text{bl},a} = \mathbf{M}^{1,\text{bl},a} \cdot \boldsymbol{\tau}$  for various isotropic porous media and different interface locations. There, we observe that these two constants, regarded as functions of the interface position  $S_a$ , are monotonic functions that both become larger for decreasing  $a$ , i.e.,  $a \rightarrow 0$  (see Figure 5.3). Similarly, we performed numerical experiments for anisotropic porous media, where all the boundary layer constants  $N_s^{\text{bl},a}$ ,  $N_1^{\text{bl},a}$ ,  $M_1^{1,\text{bl},a}$  and  $M_1^{2,\text{bl},a}$  appear as nonzero coefficients in the generalized coupling conditions. In Figure 3.2 (top) we provide the values of these constants with respect to different interface locations  $S_a$  in case of an elliptical solid inclusion within the unit cell  $Y$  (Figure 3.2, bottom). The border of the elliptical solid grain is given by the ellipse with center at  $(0.5, 0.5)$  and semi-axes  $r_b = 0.4$  and  $r_c = 0.2$ , rotated clockwise by  $45^\circ$ . We observe from Figure 3.2 (top) that the constants  $N_1^{\text{bl},a} < 0$  and  $M_1^{1,\text{bl},a} < 0$  behave similarly to the isotropic

$$\tilde{\mathbf{K}} = \begin{pmatrix} 1.22787e-2 & 2.68921e-3 \\ 2.68921e-3 & 1.22787e-2 \end{pmatrix}$$

	$M_1^{1,bl,a}$	$M_1^{2,bl,a}$	$N_1^{bl,a}$	$N_s^{bl,a}$
$S_{0,34}$	$-8.06716e-2$	$-3.33709e-3$	$-3.95818e-1$	$-2.71778e-1$
$S_{0,26}$	$-5.22061e-2$	$-3.33709e-3$	$-3.15818e-1$	$-2.71778e-1$
$S_{0,18}$	$-3.01407e-2$	$-3.33709e-3$	$-2.35818e-1$	$-2.71778e-1$
$S_{0,1}$	$-1.44752e-2$	$-3.33709e-3$	$-1.55818e-1$	$-2.71778e-1$
$S_{0,02}$	$-5.20972e-3$	$-3.33709e-3$	$-7.58185e-2$	$-2.71778e-1$

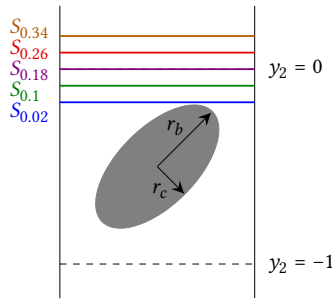


Figure 3.2: Boundary layer constants  $M_1^{1,bl,a}$ ,  $M_1^{2,bl,a}$ ,  $N_1^{bl,a}$  and  $N_s^{bl,a}$  for five interface locations (top) and illustration of these interface locations (bottom) for elliptical solid grains.

case, i.e., they increase monotonically for  $a \rightarrow 0$ . The constants  $N_s^{bl,a}$  and  $M_1^{2,bl,a}$ , which are nonzero only for anisotropic porous media, are not affected by a change of the interface location within the boundary layer stripe. We observed the same behavior of the boundary layer constants also for other anisotropic porous-medium geometries.

Apart from the observations we made above, we prove Lemma 3.7 that explicitly describes the behavior of  $N_1^{bl,a}$  with respect to a changing interface position. We show that the coefficient  $N_1^{bl,a}$  for some  $a \in (0, 1 - d^*)$  is obtained from the boundary layer constant  $N_1^{bl,(1-d^*)/2}$  corresponding to the interface  $S_{(1-d^*)/2}$  by adding a constant.

**Lemma 3.7:** Consider the interface  $S_{(1-d^*)/2}$  located directly on top of unit cell at  $y_2 = 0$  (Figure 3.1, red line) and any second interface location  $S_a$  for  $a \in (0, 1 - d^*)$ . Then it holds

$$N_1^{\text{bl},a} = N_1^{\text{bl},(1-d^*)/2} - a + \frac{1-d^*}{2}.$$

*Proof.* We follow the ideas in [120, Lemma 4.20] where a similar result is proven. We consider the vertical boundary layer stripe  $Z^{\text{bl}}$  where the solid part is given by  $Z_s^{\text{bl}} = \bigcup_{k=1}^{\infty} (Y_s - \{0, k\})$ , and a fixed, but arbitrary chosen  $a \in (0, 1 - d^*)$ . Then, the solution to problem (3.17)–(3.21) with interface  $S_a$  is denoted by  $t^{\text{bl},a}$ . For clarity, we define  $\theta = (1 - d^*)/2$ , where  $d^*$  is the size of the solid part  $Y_s$  in  $y_2$ -direction corresponding to the unit cell  $Y$ . From [98, Lemma 3.2] we deduce directly that for all  $b > c \geq a - \theta$  it holds

$$\int_0^1 t_1^{\text{bl},a}(y_1, b) \, dy_1 = \int_0^1 t_1^{\text{bl},a}(y_1, c) \, dy_1,$$

and thus, for all  $d \geq a - \theta$  we have

$$N_1^{\text{bl},a} = \int_0^1 t_1^{\text{bl},a}(y_1, d) \, dy_1. \quad (3.104)$$

Let  $-\theta \leq c_1 \leq a - \theta \leq c_2$ . We integrate the first component of equation (3.17) over the domain  $(0, 1) \times (c_1, c_2)$ , use the  $y_1$ -periodicity of the boundary layer solution  $t^{\text{bl},a}$  and get

$$\int_0^1 \left( \frac{\partial t_1^{\text{bl},a}}{\partial y_2}(y_1, c_2) - \frac{\partial t_1^{\text{bl},a}}{\partial y_2}(y_1, (a - \theta) + 0) \right. \\ \left. + \frac{\partial t_1^{\text{bl},a}}{\partial y_2}(y_1, (a - \theta) - 0) - \frac{\partial t_1^{\text{bl},a}}{\partial y_2}(y_1, c_1) \right) dy_1 = 0.$$

Considering jump condition (3.20) across  $S_a$ , this reduces to

$$\int_0^1 \left( \frac{\partial t_1^{\text{bl},a}}{\partial y_2}(y_1, c_2) - \frac{\partial t_1^{\text{bl},a}}{\partial y_2}(y_1, c_1) \right) dy_1 = 1.$$

Making use of the Leibniz integral rule for differentiation and using (3.104) since  $c_2 \geq a - \theta$ , we get for  $c_1 < y_2 < a - \theta$ :

$$\frac{\partial}{\partial y_2} \int_0^1 t_1^{\text{bl},a}(y_1, y_2) dy_1 = -1.$$

We apply the fundamental theorem of calculus and obtain for  $0 \leq y_2 \leq a - \theta$ :

$$\int_0^1 t_1^{\text{bl},a}(y_1, y_2) dy_1 = N_1^{\text{bl},a} - y_2. \quad (3.105)$$

We consider the interface  $S_a$  for the boundary layer problem (3.17)–(3.21) and substitute velocity  $\mathbf{t}^{\text{bl},a}$  and pressure  $s^{\text{bl},a}$  by  $(-\mathbf{t}^{\text{bl},a} + \mathbf{t}^{\text{bl},\theta})$  and  $(-s^{\text{bl},a} + s^{\text{bl},\theta})$ , respectively. Then, we multiply the resulting equation (3.17) by a test function  $\boldsymbol{\varphi} \in V(Z^{\text{bl}})^2$ , where  $V(Z^{\text{bl}})^2$  is defined in the Appendix A.1, integrate over  $Z^{\text{bl}}$  and obtain

$$\begin{aligned} & \int_{Z^{\text{bl}}} \nabla_{\mathbf{y}}(-\mathbf{t}^{\text{bl},a} + \mathbf{t}^{\text{bl},\theta}) : \nabla_{\mathbf{y}} \boldsymbol{\varphi} \, d\mathbf{y} - \int_{Z^{\text{bl}}} (-s^{\text{bl},a} + s^{\text{bl},\theta}) \nabla_{\mathbf{y}} \cdot \boldsymbol{\varphi} \, d\mathbf{y} \\ &= - \int_{Z^{\text{bl}}} \nabla_{\mathbf{y}} \cdot (\nabla_{\mathbf{y}}(-\mathbf{t}^{\text{bl},a} + \mathbf{t}^{\text{bl},\theta})) \cdot \boldsymbol{\varphi} \, d\mathbf{y} + \int_{\partial Z^{\text{bl}}} \nabla_{\mathbf{y}}(-\mathbf{t}^{\text{bl},a} + \mathbf{t}^{\text{bl},\theta}) \mathbf{n} \cdot \boldsymbol{\varphi} \, dS \\ & \quad - \int_{\partial Z^{\text{bl}}} (-s^{\text{bl},a} + s^{\text{bl},\theta}) \mathbf{n} \cdot \boldsymbol{\varphi} \, dS + \int_{Z^{\text{bl}}} \nabla_{\mathbf{y}}(-s^{\text{bl},a} + s^{\text{bl},\theta}) \cdot \boldsymbol{\varphi} \, d\mathbf{y} \\ &= \int_0^1 (-\varphi_1(y_1, 0) + \varphi_1(y_1, a - \theta)) dy_1. \end{aligned} \quad (3.106)$$

Without the loss of generality we assume that  $a < \theta$ . The case of  $a > \theta$  can be treated analogously. Then, testing equation (3.106) with  $\boldsymbol{\varphi} = -\mathbf{t}^{\text{bl},a} + \mathbf{t}^{\text{bl},\theta}$

and using the result in (3.105) yields

$$\begin{aligned}
& \int_{Z^{\text{bl}}} (\nabla_{\mathbf{y}}(-\mathbf{t}^{\text{bl},a} + \mathbf{t}^{\text{bl},\theta}))^2 \, d\mathbf{y} \\
&= \int_0^1 (t_1^{\text{bl},a} - t_1^{\text{bl},\theta})(y_1, 0) + (-t_1^{\text{bl},a} + t_1^{\text{bl},\theta})(y_1, a - \theta) \, dy_1 \\
&= \int_0^1 t_1^{\text{bl},a}(y_1, 0) \, dy_1 - N_1^{\text{bl},\theta} - N_1^{\text{bl},a} + \int_0^1 t_1^{\text{bl},\theta}(y_1, a - \theta) \, dy_1 \\
&= N_1^{\text{bl},a} - N_1^{\text{bl},\theta} - N_1^{\text{bl},a} + N_1^{\text{bl},\theta} - (a - \theta) = -a + \theta. \tag{3.107}
\end{aligned}$$

Next, we integrate (3.17) over  $Z^{\text{bl}}$  considering  $\mathbf{t}^{\text{bl},a}$ , test the resulting equation with  $\boldsymbol{\varphi} = \mathbf{t}^{\text{bl},a}$  and obtain

$$\int_0^1 t_1^{\text{bl},a}(y_1, a - \theta) \, dy_1 = - \int_{Z^{\text{bl}}} |\nabla_{\mathbf{y}} \mathbf{t}^{\text{bl},a}|^2 \, d\mathbf{y}.$$

Using this result in (3.107) we get

$$\begin{aligned}
-a + \theta &= \int_{Z^{\text{bl}}} |\nabla_{\mathbf{y}}(-\mathbf{t}^{\text{bl},a} + \mathbf{t}^{\text{bl},\theta})|^2 \, d\mathbf{y} \\
&= -N_1^{\text{bl},a} - N_1^{\text{bl},\theta} - 2 \int_{Z^{\text{bl}}} \nabla_{\mathbf{y}} \mathbf{t}^{\text{bl},a} \nabla_{\mathbf{y}} \mathbf{t}^{\text{bl},\theta} \, d\mathbf{y}. \tag{3.108}
\end{aligned}$$

The last term in (3.108) is reformulated using (3.17), (3.18) and (3.20) as follows

$$\begin{aligned}
\int_{Z^{\text{bl}}} \nabla_{\mathbf{y}} \mathbf{t}^{\text{bl},a} \nabla_{\mathbf{y}} \mathbf{t}^{\text{bl},\theta} \, d\mathbf{y} &= \int_{Z^{\text{bl}}} \nabla_{\mathbf{y}} \cdot (\mathbf{t}^{\text{bl},a} \nabla_{\mathbf{y}} \mathbf{t}^{\text{bl},\theta}) \, d\mathbf{y} - \int_{Z^{\text{bl}}} t^{\text{bl},a} \Delta_{\mathbf{y}} \mathbf{t}^{\text{bl},\theta} \, d\mathbf{y} \\
&= \int_{Z^{\text{bl}}} \nabla_{\mathbf{y}} \cdot (\mathbf{t}^{\text{bl},a} \nabla_{\mathbf{y}} \mathbf{t}^{\text{bl},\theta}) \, d\mathbf{y} - \int_{Z^{\text{bl}}} \mathbf{t}^{\text{bl},a} \nabla_{\mathbf{y}} s^{\text{bl},\theta} \, d\mathbf{y} \\
&= - \int_0^1 t_1^{\text{bl},a}(y_1, 0) \, dy_1 \\
&= -N_1^{\text{bl},a}.
\end{aligned}$$

We substitute this reformulation in (3.108) and obtain

$$-a + \theta = -N_1^{\text{bl},a} - N_1^{\text{bl},\theta} + 2N_1^{\text{bl},a},$$

which completes the proof.  $\square$

Throughout this thesis, we usually omit the super- and subscript  $a$  for the interface within the boundary layer stripe and for the boundary layer constants due to clarity. If not stated otherwise, the interface  $S$  at distance  $a = (1 - d^*)/2$  above the solid inclusions is considered in the boundary layer problems (3.17)–(3.21) and (3.39)–(3.43) and in the definitions of the boundary layer constants (3.23)–(3.24) and (3.45)–(3.46).

**Remark 3.8:** *Before the generalized coupling conditions (3.98)–(3.100) are used for numerical simulations of applications, the exact location of the fluid–porous interface has to be chosen. We remark that this choice fully determines the position of the interface  $\Sigma$  within the computational domain  $\Omega = \Omega_{\text{ff}} \cup \Omega_{\text{pm}}$  as well as the position of  $S_a$  within the boundary layer stripe  $Z^{\text{bl}}$ . Dependent on the chosen  $S_a$  the boundary layer constants  $\mathbf{N}^{\text{bl}}$ ,  $N_s^{\text{bl}}$  and  $\mathbf{M}^{j,\text{bl}}$  for  $j = 1, 2$  appearing in conditions (3.98)–(3.100) are computed. In this way the information about the exact interface position within the coupled flow domain  $\Omega$  or, equivalently, within the stripe  $Z^{\text{bl}}$ , is incorporated in these effective coefficients. Thus, if the generalized coupling conditions are applied, the sharp interface location is not an unknown model parameter for the Stokes–Darcy problem as it is the case for the classical coupling approach.*

### 3.2.3 Comparison of generalized coupling conditions to classical ones

In this section, we compare the generalized interface conditions to the classical coupling conditions for the Stokes–Darcy problem. For ease of comparison, we provide both coupling concepts in their dimensional form below. As before, the unit normal vector  $\mathbf{n}$  on the fluid–porous interface  $\Sigma$



is pointing outward the porous medium and the unit tangential vector is  $\boldsymbol{\tau} = \mathbf{e}_1$ . The classical conditions (2.17)–(2.19) read

$$\mathbf{v}^{\text{ff}} \cdot \mathbf{n} = \mathbf{v}^{\text{pm}} \cdot \mathbf{n} \quad \text{on } \Sigma, \quad (3.109)$$

$$p^{\text{pm}} = -\mathbf{n} \cdot \mathbf{T}(\mathbf{v}^{\text{ff}}, p^{\text{ff}}) \mathbf{n} \quad \text{on } \Sigma, \quad (3.110)$$

$$(\mathbf{v}^{\text{ff}} - \mathbf{v}^{\text{pm}}) \cdot \boldsymbol{\tau} = \frac{\sqrt{K}}{\alpha_{\text{BJ}} \mu} \boldsymbol{\tau} \cdot \mathbf{T}(\mathbf{v}^{\text{ff}}, p^{\text{ff}}) \mathbf{n} \quad \text{on } \Sigma. \quad (3.111)$$

The generalized interface conditions (3.98)–(3.100) are given by

$$\mathbf{v}^{\text{ff}} \cdot \mathbf{n} = \mathbf{v}^{\text{pm}} \cdot \mathbf{n} \quad \text{on } \Sigma, \quad (3.112)$$

$$p^{\text{pm}} = -\mathbf{n} \cdot \mathbf{T}(\mathbf{v}^{\text{ff}}, p^{\text{ff}}) \mathbf{n} + N_s^{\text{bl}} \boldsymbol{\tau} \cdot \mathbf{T}(\mathbf{v}^{\text{ff}}, p^{\text{ff}}) \mathbf{n} \quad \text{on } \Sigma, \quad (3.113)$$

$$\mathbf{v}^{\text{ff}} \cdot \boldsymbol{\tau} = -\frac{\ell}{\mu} \left( \mathbf{N}^{\text{bl}} \cdot \boldsymbol{\tau} \right) \boldsymbol{\tau} \cdot \mathbf{T}(\mathbf{v}^{\text{ff}}, p^{\text{ff}}) \mathbf{n} + \frac{\ell^2}{\mu} \sum_{j=1}^2 \frac{\partial p^{\text{pm}}}{\partial x_j} M^{j,\text{bl}} \cdot \boldsymbol{\tau} \quad \text{on } \Sigma. \quad (3.114)$$

Equation (3.109) is identical with (3.112) and both equations describe the conservation of mass across the fluid–porous interface. Coupling condition (3.113) is an extension of the classical momentum balance equation (3.110). In case of a diagonal permeability tensor  $\mathbf{K}$ , i.e., when the porous medium is isotropic or orthotropic, we have  $N_s^{\text{bl}} = 0$  and condition (3.113) reduces to the classical balance of normal forces (3.110) across the interface. Interface condition (3.114) is a generalization of the original Beavers–Joseph coupling condition (3.111). This becomes apparent if we consider  $-\ell \mathbf{N}^{\text{bl}} \cdot \boldsymbol{\tau} = \sqrt{K} \alpha_{\text{BJ}}^{-1}$  and notice that the tangential Darcy velocity  $\mathbf{v}^{\text{pm}} \cdot \boldsymbol{\tau}$  in (3.111) is replaced by the tangential component of the interfacial porous-medium velocity which is given by

$$\mathbf{v}_{\text{int}}^{\text{pm}} = -\frac{\ell^2 \tilde{\mathbf{K}}^{\text{int}}}{\mu} \nabla p^{\text{pm}}, \quad \tilde{\mathbf{K}}^{\text{int}} = (\tilde{k}_{ij}^{\text{int}})_{i,j=1,2} = \begin{pmatrix} -M_1^{1,\text{bl}} & -M_1^{2,\text{bl}} \\ -M_2^{1,\text{bl}} & -M_2^{2,\text{bl}} \end{pmatrix}. \quad (3.115)$$

The tensor  $\tilde{\mathbf{K}}^{\text{int}}$  can be understood as an interfacial permeability tensor. We note that we always have  $\mathbf{N}^{\text{bl}} \cdot \boldsymbol{\tau} < 0$  and  $(\boldsymbol{\tau} \tilde{\mathbf{K}}^{\text{int}} \boldsymbol{\tau}) > 0$  for the coefficients appearing in the generalized interface condition (3.114). Fur-

thermore, in case of a horizontal interface  $\Sigma$  we have  $M_2^{j,\text{bl}} = 0$  for  $j = 1, 2$  (see Section 3.2.2).

For orthotropic porous structures, which are characterized by permeability tensors of the form  $\mathbf{K} = \text{diag}(k_{11}, k_{22})$ , the interfacial permeability tensor reads  $\tilde{\mathbf{K}}^{\text{int}} = \text{diag}(-M_1^{1,\text{bl}}, -M_2^{2,\text{bl}})$  since we have  $M_1^{2,\text{bl}} = M_2^{1,\text{bl}} = 0$ . Then, if the fluid–porous interface  $\Sigma$  is positioned horizontally we obtain  $\tilde{\mathbf{K}}^{\text{int}} = \text{diag}(-M_1^{1,\text{bl}}, 0)$  due to  $M_2^{2,\text{bl}} = 0$ . Consequently, in this case the tangential component of the Darcy velocity respective interfacial porous-medium velocity reads

$$\mathbf{v}^{\text{pm}} \cdot \boldsymbol{\tau} = -\frac{k_{11}}{\mu} \frac{\partial p^{\text{pm}}}{\partial x_1}, \quad \mathbf{v}_{\text{int}}^{\text{pm}} \cdot \boldsymbol{\tau} = \frac{\ell^2 M_1^{1,\text{bl}}}{\mu} \frac{\partial p^{\text{pm}}}{\partial x_1}.$$

We show in Section 6.3.1.2 that for orthotropic porous media with porosity  $\phi > \phi_0^{\text{shape, arrangement}}$  it is possible to find a position of the horizontal interface  $\Sigma$  such that

$$-\ell^2 M_1^{1,\text{bl}} = k_{11} \left( = \ell^2 \tilde{k}_{11} \right), \quad (3.116)$$

where  $\phi_0^{\text{shape, arrangement}}$  is a critical porosity value dependent on the shape and arrangement of solid obstacles. The interface determined in this way is located at a certain distance  $a$  above the first row of solid inclusions dependent on the permeability  $\tilde{\mathbf{K}}$ , the porosity  $\phi$  and the shape of the solid grains of the considered porous-medium domain. Thus, in case of porous materials having a diagonal permeability tensor  $\mathbf{K}$  and porosity  $\phi > \phi_0^{\text{shape, arrangement}}$ , condition (3.100) can recover the original Beavers–Joseph coupling condition (2.19) by taking  $\alpha_{\text{BJ}} = \sqrt{\tilde{K}} / (-N_1^{\text{bl}} \ell)$ . Furthermore, we demonstrate in Section 6.3.1.2 that in case of porous media with  $\phi < \phi_0^{\text{shape, arrangement}}$  it is not possible to find an interface position such that (3.116) is fulfilled. In this case, condition (3.100) cannot be rewritten in form of the Beavers–Joseph condition (2.19). The same holds true for anisotropic porous structures since in this case the interfacial permeability  $\tilde{\mathbf{K}}^{\text{int}}$  is always different from the dimensionless permeability

$\tilde{\mathbf{K}}$  inside the porous medium.

## Summary

In this chapter, we rigorously derived a set of generalized coupling conditions (3.95)–(3.97) for the Stokes–Darcy problem using homogenization theory and boundary layer correctors. These conditions are suitable for arbitrary flow directions to the fluid–porous interface. All effective coefficients appearing in the conditions are computed based on the sharp interface location and the porous-medium geometry in the vicinity of the fluid–porous interface. Besides the nondimensional formulation of the generalized interface conditions, which is obtained from the theoretical derivation, we also provided the dimensional form, needed for numerical simulations of realistic flow scenarios. We explained how the information about the exact location of the sharp interface is incorporated into the resulting coupled Stokes–Darcy model. Finally, we compared the generalized interface conditions to the classical ones and highlighted their differences.



# **4 Numerical methods for cou- pled problems**



# Numerical methods for coupled problems

# 4

This chapter is devoted to the numerical treatment of the coupled flow system both from the microscale and macroscale perspective, whereby the latter requires computation of effective model parameters. In Section 4.1, we present the numerical method for solving the pore-scale problem and introduce two different averaging approaches to reduce oscillations in the microscale solution. These oscillations appear due to the presence of solid inclusions in the porous domain and averaging microscale quantities becomes necessary to compare pore-scale and macroscale numerical simulation results in a fair and reasonable way. In Section 4.2, the discretization scheme and solution strategy for the macroscale coupled Stokes–Darcy problem are presented. The numerical algorithm for the computation of effective coefficients appearing in the macroscale model dependent on the set of coupling conditions is introduced in Section 4.3.

## 4.1 Pore-scale model

In the following, we present the numerical method for solving the Stokes system (2.2)–(2.4) with (2.6) in the perforated domain and introduce two averaging strategies to reduce physical oscillations in the pore-scale velocity and pressure due to solid obstacles present in the porous region.

### 4.1.1 Discretization scheme and solution strategy

To solve the pore-scale problem (2.2)–(2.4), (2.6) we perform numerical simulations using FREEFEM++ [86], which is a high level multiphysics finite element software. Therefore, the variational formulation of the problem is needed. We define the following test function spaces for the velocity and pressure

$$V = \{\boldsymbol{\varphi} \in H^1(\Omega^{\text{ps}})^2 : \boldsymbol{\varphi} = \mathbf{0} \text{ on } \Gamma_D \cup (\partial\Omega^{\text{ps}} \setminus \partial\Omega)\}, \quad Q = L^2(\Omega^{\text{ps}}).$$

We recall that  $\Gamma_D$  and  $\Gamma_N$  denote the external boundaries of the partially perforated domain  $\Omega^{\text{ps}}$  where Dirichlet respective Neumann boundary conditions are set. Note that we assume  $\Gamma_N \neq \emptyset$ , otherwise, in case  $\Gamma_N = \emptyset$ , one would need to consider the pressure test function space  $\{\psi \in L^2(\Omega^{\text{ps}}) : \int_{\Omega^{\text{ps}}} \psi \, d\mathbf{x} = 0\}$  instead of space  $Q$ . Furthermore, as in the rest of this thesis, we set  $\mathbf{g} = \mathbf{0}$  in (2.2).

We multiply the momentum conservation equation (2.2) by a test function  $\boldsymbol{\varphi} \in V$ , integrate the resulting equation by parts over domain  $\Omega^{\text{ps}}$  and apply the Gauss's theorem. This yields

$$\begin{aligned} 0 &= - \int_{\Omega^{\text{ps}}} (\nabla \cdot \mathbf{T}(\mathbf{v}, p)) \cdot \boldsymbol{\varphi} \, d\mathbf{x} \\ &= - \int_{\partial\Omega^{\text{ps}}} \mathbf{T}(\mathbf{v}, p) \mathbf{n} \cdot \boldsymbol{\varphi} \, dS + \int_{\Omega^{\text{ps}}} \mu \nabla \mathbf{v} : \nabla \boldsymbol{\varphi} \, d\mathbf{x} - \int_{\Omega^{\text{ps}}} (\nabla \cdot \boldsymbol{\varphi}) p \, d\mathbf{x}. \end{aligned}$$

By taking into account the Neumann boundary condition (2.6) and the fact that  $\boldsymbol{\varphi} = \mathbf{0}$  on  $\Gamma_D \cup (\partial\Omega^{\text{ps}} \setminus \partial\Omega)$ , we obtain

$$\int_{\Omega^{\text{ps}}} \mu \nabla \mathbf{v} : \nabla \boldsymbol{\varphi} \, d\mathbf{x} - \int_{\Omega^{\text{ps}}} (\nabla \cdot \boldsymbol{\varphi}) p \, d\mathbf{x} = \int_{\Gamma_N} \mathbf{T}(\mathbf{v}, p) \mathbf{n} \cdot \boldsymbol{\varphi} \, dS = \int_{\Gamma_N} \bar{\mathbf{h}} \cdot \boldsymbol{\varphi} \, dS.$$

This yields the following weak formulation of the pore-scale problem (2.2)–(2.4) and (2.6):



Find  $\{\mathbf{v}, p\} \in V \times Q$  such that

$$\mathcal{A}(\mathbf{v}, \boldsymbol{\varphi}) + \mathcal{B}(\boldsymbol{\varphi}, p) = \langle \bar{\mathbf{h}}, \boldsymbol{\varphi} \rangle_{\Gamma_N} \quad \text{for all } \boldsymbol{\varphi} \in V, \quad (4.1)$$

$$\mathcal{B}(\mathbf{v}, q) = 0 \quad \text{for all } q \in Q, \quad (4.2)$$

where we define the duality pairing  $\langle \cdot, \cdot \rangle_{\Gamma_N} : H^{-1/2}(\Gamma_N) \times H^{1/2}(\Gamma_N) \rightarrow \mathbb{R}$  and the bilinear forms

$$\mathcal{A}(\mathbf{v}, \boldsymbol{\varphi}) = \int_{\Omega^{\text{ps}}} \mu \nabla \mathbf{v} : \nabla \boldsymbol{\varphi} \, dx, \quad \mathcal{B}(\boldsymbol{\varphi}, p) = - \int_{\Omega^{\text{ps}}} (\nabla \cdot \boldsymbol{\varphi}) p \, dx.$$

The next step towards the numerical solution of the pore-scale problem is to partition the flow domain  $\Omega^{\text{ps}}$  into triangles. We make use of the adaptive mesh refinement method available in `FREEFEM++` that is based on the Delaunay–Voronoi algorithm [69, 70]. We generate a mesh such that for each porous-medium geometrical configuration considered in this thesis we have at least three triangles between two solid inclusions. The exact number of triangular elements, which is used for the numerical examples in Chapter 6, is provided in the corresponding sections. We denote the triangulation of the domain  $\Omega^{\text{ps}}$  by  $\mathcal{T}_h$  with  $h$  being the maximum edge size of triangular grid cells.

Now, we introduce the discrete finite element spaces  $V_h \subset V$  and  $Q_h \subset Q$ . Since these are subspaces of the solution spaces  $V$  and  $Q$  we obtain a conforming finite element method. The discrete spaces contain functions of the following form

$$V_h \ni \mathbf{v}^h = \sum_{j=1}^{N_{v,1}+N_{v,2}} \mathbf{v}_j^h \boldsymbol{\phi}_j, \quad Q_h \ni p^h = \sum_{j=1}^{N_p} p_j^h \zeta_j,$$

where  $\{\boldsymbol{\phi}_j\}_{j=1, \dots, N_{v,1}+N_{v,2}}$  and  $\{\zeta_j\}_{j=1, \dots, N_p}$  are the respective bases for the spaces  $V_h$  and  $Q_h$ , and  $\{\mathbf{v}_j^h\}_{j=1, \dots, N_{v,1}+N_{v,2}}$  and  $\{p_j^h\}_{j=1, \dots, N_p}$  are the respective real-valued coefficients. The degrees of freedom for  $\mathbf{v}^h$  and  $p^h$ , which are equal to the number of basis functions of the corresponding discrete

finite element space, are given by  $N_{v,1} + N_{v,2}$ , where  $N_{v,1}, N_{v,2} \in \mathbb{N}$ , and  $N_p \in \mathbb{N}$ , respectively.

We denote by  $\mathcal{B}^h : V_h \times Q_h \rightarrow \mathbb{R}$  the discrete form of  $\mathcal{B}$  and by  $\mathcal{A}^h : V_h \times V_h \rightarrow \mathbb{R}$  the discrete variant of  $\mathcal{A}$ . Since we consider conforming finite elements we have

$$\mathcal{A}^h(\mathbf{v}^h, \boldsymbol{\varphi}^h) = \mathcal{A}(\mathbf{v}^h, \boldsymbol{\varphi}^h), \quad \mathcal{B}^h(\mathbf{v}^h, q^h) = \mathcal{B}(\mathbf{v}^h, q^h),$$

for all  $\mathbf{v}^h, \boldsymbol{\varphi}^h \in V_h, q^h \in Q_h$ . Then, the discrete weak form corresponding to problem (2.2)–(2.4) and (2.6) reads:

Find  $\{\mathbf{v}^h, p^h\} \in V_h \times Q_h$  such that

$$\mathcal{A}(\mathbf{v}^h, \boldsymbol{\varphi}^h) + \mathcal{B}(\boldsymbol{\varphi}^h, p^h) = \langle \bar{\mathbf{h}}, \boldsymbol{\varphi}^h \rangle_{\Gamma_N} \quad \text{for all } \boldsymbol{\varphi}^h \in V_h, \quad (4.3)$$

$$\mathcal{B}(\mathbf{v}^h, q^h) = 0 \quad \text{for all } q^h \in Q_h. \quad (4.4)$$

Rewriting problem (4.3)–(4.4) using the basis functions  $\boldsymbol{\phi}_j \in V_h$  for  $j = 1, \dots, N_{v,1} + N_{v,2}$  and  $\zeta_j \in Q_h$  for  $j = 1, \dots, N_p$  yields the following matrix formulation of the Stokes equations (2.2)–(2.4) with the boundary conditions (2.6):

$$\begin{pmatrix} \mathbf{A} & \mathbf{B}^\top \\ \mathbf{B} & \mathbf{0} \end{pmatrix} \begin{pmatrix} \tilde{\mathbf{v}} \\ \tilde{p} \end{pmatrix} = \begin{pmatrix} \tilde{\mathbf{f}} \\ \mathbf{0} \end{pmatrix}. \quad (4.5)$$

Here, we define the matrix blocks  $\mathbf{A} = (A_{ij})_{i,j=1,\dots,N_{v,1}+N_{v,2}}$  with  $A_{ij} = \mathcal{A}(\boldsymbol{\phi}_j, \boldsymbol{\phi}_i)$  and  $\mathbf{B} = (B_{kl})_{k=1,\dots,N_p; l=1,\dots,N_{v,1}+N_{v,2}}$  with  $B_{kl} = \mathcal{B}(\boldsymbol{\phi}_l, \zeta_k)$ . Furthermore, we set  $\tilde{\mathbf{v}} = (v_1^h, \dots, v_{N_{v,1}+N_{v,2}}^h)^\top$ ,  $\tilde{p} = (p_1^h, \dots, p_{N_p}^h)^\top$  and  $\tilde{\mathbf{f}} = (f_1, \dots, f_{N_{v,1}+N_{v,2}})^\top$  with  $f_i = \langle \bar{\mathbf{h}}, \boldsymbol{\phi}_i \rangle_{\Gamma_N}$  for  $i = 1, \dots, N_{v,1} + N_{v,2}$ . The system of linear equations (4.5) is then solved numerically.

Within this thesis, we use the Taylor–Hood  $(P_1, P_2)$  finite elements to solve the pore-scale problem (2.2)–(2.4), (2.6), i.e., we have continuous bi-quadratic interpolation functions for the velocity ( $P_2$ ) and continuous bi-linear functions for the pressure ( $P_1$ ). Thus, the finite element function

spaces read

$$\begin{aligned} V_h &= \{\mathbf{v}^h \in H^1(\Omega^{\text{ps}})^2 : \mathbf{v}^h|_T \in P_2 \text{ for all } T \in \mathcal{T}_h\}, \\ Q_h &= \{p^h \in L^2(\Omega^{\text{ps}}) : p^h|_T \in P_1 \text{ for all } T \in \mathcal{T}_h\}, \end{aligned}$$

where  $T$  denotes a triangular element. The Taylor–Hood finite element pair is stable for the Stokes equations [25], thus, no additional stabilization for the pressure is needed. We implement the weak formulation (4.3)–(4.4) in the FREFEM++ software, which internally solves the linear system (4.5) using the direct sparse solver MUMPS (multifrontal massively parallel solver) [4].

### 4.1.2 Averaging of pore-scale solutions

Due to the presence of solid obstacles in the porous part of the coupled domain, the results obtained from microscale simulations contain both microscopic and macroscopic details of the flow field. For a fair and reasonable comparison of pore-scale resolved models and macroscale numerical simulation results, averaging of pore-scale solutions needs to be performed to eliminate the microscopic oscillations. Different averaging approaches exist in the literature, e.g., volume averaging [133, 163], line averaging [135] (also called plane or horizontal averaging) or ensemble averaging [106, 152]. However, it is still an open question which technique is the most appropriate one to obtain accurate, physically reasonable averaged microscale simulation results. We investigate two different averaging approaches, adaptive volume averaging and ensemble averaging, which we introduce in the following.

#### Adaptive volume averaging

When we apply adaptive volume averaging, the local pore-scale velocity and pressure fields are averaged over representative volumes  $V^{\text{avg}}$  of varying sizes dependent on their location within the coupled domain. In

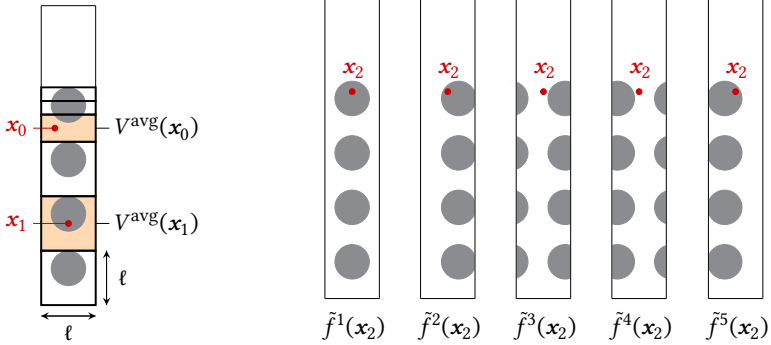


Figure 4.1: Schematic of adaptive volume averaging (left) and ensemble averaging with  $N_{\text{avg}} = 5$  (right) presented on a vertical stripe of the domain only.

the porous medium away from the fluid–porous interface, the representative volume  $V^{\text{avg}}$  is identical with the scaled unit cell  $\ell Y$  (Figure 4.1, left) as in the case of classical volume averaging [163]. When approaching the interfacial region especially the pore-scale velocity undergoes rapid changes. In this case, the volume  $\ell Y$  is too large such that it cannot capture the velocity’s behavior and its size needs to be adjusted. Therefore, we consider smaller averaging volumes  $V^{\text{avg}}$  near the interface, i.e., we multiply the height of the scaled cell  $\ell Y$  by factor 0.5 and 0.25, accordingly (Figure 4.1, left). The averaged function  $f^{\text{avg}}$  of the pore-scale quantity  $f$  at point  $\mathbf{x}_0 \in \Omega^f$  is then given by

$$f^{\text{avg}}(\mathbf{x}_0) = \frac{1}{|V^{\text{avg}}(\mathbf{x}_0)|} \int_{V_f^{\text{avg}}(\mathbf{x}_0)} f(\mathbf{x}) \, d\mathbf{x},$$

where  $V^{\text{avg}}(\mathbf{x}_0)$  is the averaging volume corresponding to  $\mathbf{x}_0$  and  $V_f^{\text{avg}}(\mathbf{x}_0)$  is its fluid part. Using the presented adaptive volume averaging method, all the microscopic oscillations of the pore-scale solution are averaged out, and the resulting functions can be compared to macroscale numerical simulation results.

### Ensemble averaging

The idea of ensemble averaging is to gradually move the solid inclusions in horizontal direction, solve the pore-scale problem after each step of movement, and obtain the averaged pore-scale quantities as the arithmetic mean of all computed solutions. We denote by  $N_{\text{avg}} \in \mathbb{N}$  the number of samples used for the averaging process. Samples are generated by moving the solid obstacles horizontally by distance  $\ell/N_{\text{avg}}$ . Thus, after  $N_{\text{avg}}$  steps of movement the solid inclusions are shifted by the microscopic length scale  $\ell$ . For each sample, we compute the Stokes problem (2.2)–(2.4), (2.6) based on the underlying pore geometry. The averaged function  $f^{\text{avg}}$  of any pore-scale quantity  $f$  at  $\mathbf{x}_0 \in \Omega^\ell$  is obtained by

$$f^{\text{avg}}(\mathbf{x}_0) = \frac{1}{N_{\text{avg}}} \sum_{j=1}^{N_{\text{avg}}} \tilde{f}^j(\mathbf{x}_0),$$

where  $\tilde{f}^j$  represents the pore-scale result corresponding to sample  $j$ . Figure 4.1 (right) provides a schematic of ensemble averaging with  $N_{\text{avg}} = 5$  samples. For the numerical simulation results presented in Chapter 6 we have chosen  $N_{\text{avg}} = 50$  sufficiently large such that details of the flow field at the microscopic scale in horizontal direction are completely neglected. Note that microscopic variations in vertical direction still remain in the averaged results.

## 4.2 Macroscale model

We solve the Stokes–Darcy problem monolithically using our in-house C++ code based on the finite volume method (FVM). Below, we present the corresponding discretization scheme and the monolithic solution strategy.

### 4.2.1 Discretization scheme

We discretize the Stokes and Darcy problems (2.7)–(2.9), (2.12) and (2.16) using the second order finite volume method on staggered grids [78, Chapter 6.2, 6.3]. This discretization scheme is stable, i.e., we do not need additional stabilization terms to avoid numerical oscillations [44]. Concerning the free-flow model we have the velocity and pressure as primary variables and applying staggered grids leads to separate control volumes for each of those variables. Since we consider the primal form of the Darcy problem (2.16), the pressure is the only primary variable in the porous-medium domain and the velocity is computed in a post-processing step. Finite volume discretization is conducted over individual control volumes for each variable, and therefore, it is guaranteed that the flux which enters a volume is equal to the one which leaves the volume. Hence, the scheme is locally mass conservative in the two flow domains and across the fluid–porous interface.

In the following, we explain how the staggered grid is constructed, present the discretized form of the conservation equations describing the free flow and the porous-medium flow, and provide the approximation of coupling conditions. Parts of this section are based on [140]. For clarity, we write  $u$ ,  $v$  and  $p$  for the free-flow primary variables and  $\psi$  for the porous-medium pressure. Further, we indicate the horizontal direction by  $x$  and the vertical direction by  $y$ . Moreover, for the discretization of the coupled Stokes–Darcy system, we consider both the dynamic viscosity  $\mu$  and the entries  $k_{ij}$ ,  $i, j = 1, 2$  of the permeability tensor  $\mathbf{K}$  to be constant.

#### Grid generation

We divide the free-flow region  $\Omega_{\text{ff}}$  and the porous-medium domain  $\Omega_{\text{pm}}$  into rectangular blocks of size  $h_x \times h_y$ , leading uniform Cartesian grids conforming on the fluid–porous interface (dashed lines in Figure 4.2). We use staggered grids in the free-flow region, i.e., the velocities are computed at the centers of grid cell edges and the pressures, both in the Stokes and

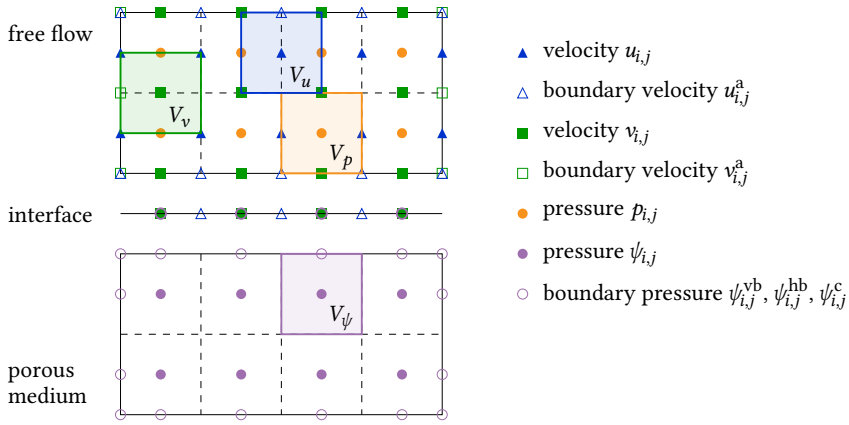


Figure 4.2: Schematic depiction of the staggered grid for the coupled flow domain, position of primary variables and corresponding control volumes  $V_u, V_v, V_p, V_\psi$ , based on [140, Figure 2.5].

Darcy region, are computed in the cell centers [78, Chapter 6.2, 6.3]. In addition to these 'natural' nodes, we compute the free-flow velocities  $u, v$  and the Darcy pressure  $\psi$  on the fluid–porous interface and on the external boundaries of the free-flow domain and the porous medium, respectively. For the 'natural' nodes we introduce the following notation

$$\begin{aligned}
 u_{i,j} &= u(ih_x, (j-0.5)h_y), & i &= 0, \dots, N_x^{\text{ff}}, & j &= 1, \dots, N_y^{\text{ff}}, \\
 v_{i,j} &= v((i-0.5)h_x, jh_y), & i &= 1, \dots, N_x^{\text{ff}}, & j &= 0, \dots, N_y^{\text{ff}}, \\
 p_{i,j} &= p((i-0.5)h_x, (j-0.5)h_y), & i &= 1, \dots, N_x^{\text{ff}}, & j &= 1, \dots, N_y^{\text{ff}}, \\
 \psi_{i,j} &= \psi((i-0.5)h_x, (j-0.5)h_y), & i &= 1, \dots, N_x^{\text{pm}}, & j &= 1, \dots, N_y^{\text{pm}},
 \end{aligned}$$

where  $N_x^{\text{ff}}, N_x^{\text{pm}}, N_y^{\text{ff}}$  and  $N_y^{\text{pm}}$  denote the number of grid cells in  $x$ - and  $y$ -direction in the free-flow region and in the porous-medium domain, respectively. 'Natural' nodes emerge directly from the staggered grid approach. They are called inner nodes if they do not lie on the boundary of the computational domain. All inner nodes corresponding to the primary variables  $u, v, p, \psi$  are surrounded by their corresponding control volumes

$V_u, V_v, V_p, V_\psi$ , schematically presented in Figures 4.2, 4.3 and 4.5. The control volumes for  $u$  and  $v$  corresponding to 'natural nodes' that lie on the external boundary of the domain, e.g.  $u_{0,j}$  for  $j = 1, \dots, N_y^{\text{ff}}$ , are half of the size compared to control volumes for inner nodes (Figure 4.4). For the pressures  $p$  and  $\psi$  all 'natural' nodes are also inner nodes.

For the remaining nodes on the external boundary that do not appear naturally due to staggered grid and thus, do not correspond to any control volume, we write

$$\begin{aligned} u_{i,j}^a &= u(ih_x, jh_y), & i &= 0, \dots, N_x^{\text{ff}}, & j &= 0, N_y^{\text{ff}}, \\ v_{i,j}^a &= v(ih_x, jh_y), & i &= 0, N_x^{\text{ff}}, & j &= 0, \dots, N_y^{\text{ff}}, \\ \psi_{i,j}^{\text{vb}} &= \psi(ih_x, (j-0.5)h_y), & i &= 0, N_x^{\text{pm}}, & j &= 1, \dots, N_y^{\text{pm}}, \\ \psi_{i,j}^{\text{hb}} &= \psi((i-0.5)h_x, jh_y), & i &= 1, \dots, N_x^{\text{pm}}, & j &= 0, N_y^{\text{pm}}, \\ \psi_{i,j}^c &= \psi(ih_x, jh_y), & i &= 0, N_x^{\text{pm}}, & j &= 0, N_y^{\text{pm}}. \end{aligned}$$

Here, the superscript 'a' indicates the additional boundary nodes for  $u$  and  $v$ , the superscripts 'vb' respective 'hb' stand for the vertical respective horizontal boundaries of the porous medium (without the corner points) and the superscript 'c' reveals that the pressure nodes  $\psi_{i,j}^c$  are located at the corners of the porous-medium domain.

In the following, we usually omit the sub- and superscript corresponding to nodes for the primary variables due to clarity. We denote a nodal point in the center of a control volume by  $P$  and the centering nodes in the neighboring volumes are denoted by  $N, E, S, W, NE, NW, SE$  and  $SW$  corresponding to the compass directions, the center of edges and the corners of the control volume are denoted by  $n, e, s, w$  and  $ne, nw, se, sw$ , accordingly (e.g., Figures 4.3 and 4.5).



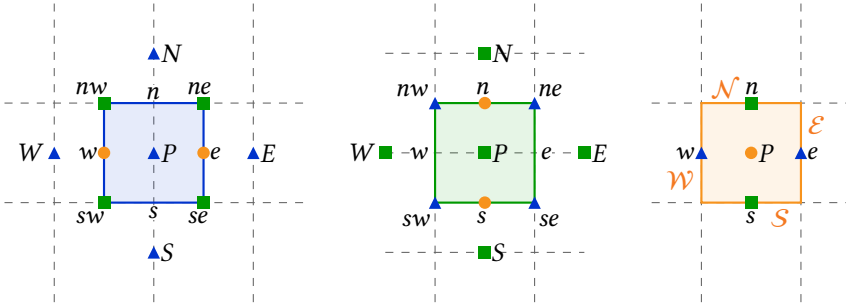


Figure 4.3: Inner control volumes  $V_u$  (left),  $V_v$  (middle),  $V_p$  (right) for the respective primary variables  $u$ ,  $v$ ,  $p$  including the nodes for the corresponding discretization procedure.

### Free-flow discretization

The first step using the FVM is to write the conservation equations in integral form over the corresponding control volumes. Next, we transform the obtained volume integrals including a divergence term into surface integrals over the control volume boundary making use of the divergence theorem. Then, the resulting surface integrals are approximated via the midpoint rule which is second order accurate.

The mass balance equation (2.8) integrated over a control volume  $V_p$  (Figure 4.3, right) corresponding to the free-flow pressure node  $p_{i,j}$  reads

$$\int_{V_p} \nabla \cdot \mathbf{v} dV = \int_{\partial V_p} \mathbf{n} \cdot \mathbf{v} dS = \sum_{k=\mathcal{N}, \mathcal{E}, \mathcal{S}, \mathcal{W}} \int_k \mathbf{n}_k \cdot \mathbf{v} dS = 0.$$

Here,  $\mathbf{n}$  is the unit normal vector on  $\partial V_p$  pointing outward the control volume,  $\mathcal{N}$ ,  $\mathcal{E}$ ,  $\mathcal{S}$  and  $\mathcal{W}$  denote the control volume edges and  $\mathbf{n}_k$  is the specific unit normal vector on edge  $k \subset \partial V_p$ . The discretized form of (2.8) is then obtained using the midpoint rule to approximate the integrals over

the control volume edges

$$(u_e - u_w)h_y + (v_n - v_s)h_x = 0. \quad (4.6)$$

For the discretization of the momentum conservation equation (2.7) we integrate its tangential component over the control volumes for  $u_{i,j}$ , the normal component over the volumes for  $v_{i,j}$ , respectively, and approximate the resulting integrals. For both components, we need to distinguish between inner control volumes and control volumes which lie on the external boundary or on the interface.

The discrete form of the tangential component of the momentum balance equation (2.7) in case of an inner control volume (Figure 4.3, left) reads

$$(F_{x,e}^u - F_{x,w}^u)h_y + (F_{y,n}^u - F_{y,s}^u)h_x = f_P^u h_x h_y. \quad (4.7)$$

Here,  $f_P^u$  denotes the tangential component of the external force  $\mathbf{f} = \rho\mathbf{g}$  at center  $P$  of the control volume  $V_u$  and the momentum fluxes are approximated at the centers  $n, e, s, w$  of the control volume edges and are given by

$$\begin{aligned} F_{x,e}^u &= p_e - 2\mu \frac{u_E - u_P}{h_x}, & F_{y,n}^u &= -\mu \left( \frac{u_N - u_P}{h_y} + \frac{v_{ne} - v_{nw}}{h_x} \right), \\ F_{x,w}^u &= p_w - 2\mu \frac{u_P - u_W}{h_x}, & F_{y,s}^u &= -\mu \left( \frac{u_P - u_S}{h_y} + \frac{v_{se} - v_{sw}}{h_x} \right). \end{aligned} \quad (4.8)$$

For the momentum fluxes in (4.8) we consider the symmetric stress tensor and use central differences to approximate the derivatives, e.g.

$$\left. \frac{\partial u}{\partial x} \right|_e \approx \frac{u_E - u_P}{h_x}, \quad \left. \frac{\partial u}{\partial y} \right|_n \approx \frac{u_N - u_P}{h_y}, \quad \left. \frac{\partial v}{\partial x} \right|_s \approx \frac{v_{se} - v_{sw}}{h_x}.$$

In case the nonsymmetric stress tensor is applied in (2.7) the fluxes given in (4.8) reduce to, e.g.,  $F_{x,e}^u = p_e - \mu(u_E - u_P)/h_x$  and  $F_{y,n}^u = -\mu(u_N - u_P)/h_y$ .

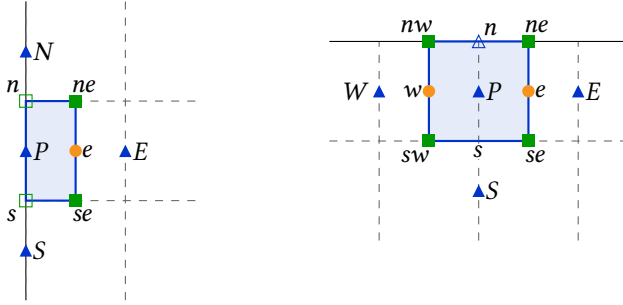


Figure 4.4: Control volumes  $V_u$  located on the left boundary (left) and on the upper boundary (right) of the free-flow domain.

For control volumes  $V_u$  of size  $h_x \times h_y$  lying on the top boundary of the free-flow domain or on the interface, the approximation of the fluxes  $F_{y,n}^u$  respective  $F_{y,s}^u$  appearing in (4.8), where the symmetric stress tensor is considered, has to be adjusted. For example, in case of a control volume on the upper boundary (Figure 4.4, right), we get

$$F_{y,n}^u = -\mu \left( \frac{u_n - u_P}{0.5h_y} + \frac{v_{ne} - v_{nw}}{h_x} \right), \quad \text{where} \quad \frac{\partial u}{\partial y} \Big|_n \approx \frac{u_n - u_P}{0.5h_y}. \quad (4.9)$$

In case of the nonsymmetric stress tensor approximation of the momentum fluxes in case of control volumes lying on the top or bottom boundary is the same as for inner control volumes.

For natural nodes  $u_{0,j}$  or  $u_{N_x^{\text{ff}},j}$ ,  $j = 1, \dots, N_y^{\text{ff}}$  lying on the left or right boundary of the free-flow domain, the corresponding control volumes are of size  $0.5h_x \times h_y$  as schematically presented in Figure 4.4 (left). For these nodes one can either consider the Neumann or Dirichlet boundary conditions presented in (2.9). In case we apply the Neumann boundary condition on the left boundary of the domain, for example, integration of the momentum equation (2.7) over the control volume  $V_u$  of reduced size  $0.5h_x \times h_y$  and approximating the surface integrals via the midpoint rule

as usual yields

$$F_{x,e}^u h_y + 0.5 (F_{y,n}^u - F_{y,s}^u) h_x = 0.5 f_P^u h_x h_y + \bar{h}_P^u h_y.$$

Here,  $\bar{h}_P^u$  denotes the prescribed flux  $\bar{\mathbf{h}} = (\bar{h}^u, \bar{h}^v)$  given in (2.9) at node  $P$ , and we have

$$\begin{aligned} F_{x,e}^u &= p_e - 2\mu \frac{u_E - u_P}{h_x}, & F_{y,n}^u &= -\mu \left( \frac{u_N - u_P}{h_y} + \frac{v_{ne} - v_n}{0.5h_x} \right), \\ F_{y,s}^u &= -\mu \left( \frac{u_P - u_S}{h_y} + \frac{v_{se} - v_s}{0.5h_x} \right). \end{aligned} \quad (4.10)$$

In case the Dirichlet boundary condition in (2.9) is set on the external boundary the corresponding values for the velocity  $u$  enter the right hand side of the resulting linear system given in (4.20).

The approximation of the normal component of the momentum equation (2.7) is obtained analogously to tangential case. For an inner control volume  $V_v$  (Figure 4.3, middle) the discrete equation considering the symmetric stress tensor reads

$$(F_{x,e}^v - F_{x,w}^v) h_y + (F_{y,n}^v - F_{y,s}^v) h_x = f_P^v h_x h_y, \quad (4.11)$$

where the external forces in the center of  $V_v$  are denoted by  $f_P^v$  and the fluxes at the centers of the control volume edges are given by

$$\begin{aligned} F_{x,e}^v &= -\mu \left( \frac{u_{ne} - u_{se}}{h_y} + \frac{v_E - v_P}{h_x} \right), & F_{y,n}^v &= p_n - 2\mu \frac{v_N - v_P}{h_y}, \\ F_{x,w}^v &= -\mu \left( \frac{u_{nw} - u_{sw}}{h_y} + \frac{v_P - v_W}{h_x} \right), & F_{y,s}^v &= p_s - 2\mu \frac{v_P - v_S}{h_y}. \end{aligned} \quad (4.12)$$

In case the nonsymmetric stress tensor is considered in (2.7) the fluxes in (4.12) reduce to, e.g.,  $F_{x,e}^v = -\mu(v_E - v_P)/h_x$  and  $F_{y,n}^v = p_n - \mu(v_N - v_P)/h_y$ . For control volumes lying on the left and right boundary, we need to adjust the momentum fluxes  $F_{x,w}^v$  and  $F_{x,e}^v$ , respectively, in an analogous

manner to (4.9). Control volumes  $V_v$  lying on the top boundary and on the interface are of size  $h_x \times 0.5h_y$  and the fluxes are computed similar as we did it in (4.10), where the fluxes across the edges of the control volumes  $V_u$  corresponding to the tangential component of the momentum equation are provided.

Boundary conditions on the lateral external boundaries either enter the right hand side of the linear system directly (Dirichlet boundary condition) or are implemented using finite differences (Neumann boundary condition). Dirichlet boundary conditions for the natural nodes  $v_{i,N_y^{\text{ff}}}$  with  $i = 1, \dots, N_x^{\text{ff}}$  that are located on the upper free-flow boundary are incorporated into the right hand side.

### Porous-medium flow discretization

We follow the same steps as for the discretization in the free-flow domain: we integrate the Darcy flow equation (2.16) over control volumes  $V_\psi$  (Figure 4.5) corresponding to the Darcy pressure nodes  $\psi_{i,j}$ , apply the divergence theorem and approximate the surface integrals. To allow for anisotropic permeability tensors  $\mathbf{K}$ , we develop a numerical scheme based on multipoint flux approximation (MPFA) which has been proposed in, e.g., [55] for second order elliptic equations. The flux stencil using MPFA is increased to the 9-point stencil compared to the standard two-point flux approximation with the 5-point stencil (Figure 4.5, left).

We obtain the following discrete form of the Darcy flow equation (2.16):

$$(a_e - a_w)h_y + (b_n - b_s)h_x = 0. \quad (4.13)$$

Here,  $a_e, a_w, b_n$  and  $b_s$  denote the approximated Darcy velocities at the control volume edges by means of central differences. For an inner control

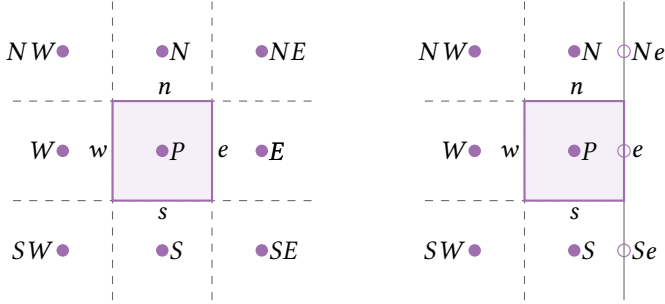


Figure 4.5: Inner control volume and nine-point stencil (left) and control volume on the right boundary (right) for the porous-medium pressure  $\psi$ .

volume  $V_\psi$ , we have

$$\begin{aligned}
 a_e &= -\frac{k_{11}}{\mu} \frac{\psi_E - \psi_P}{h_x} - \frac{k_{12}}{\mu} \frac{1}{4} \left( \frac{\psi_{NE} - \psi_{SE} + \psi_N - \psi_S}{h_y} \right), \\
 a_w &= -\frac{k_{11}}{\mu} \frac{\psi_P - \psi_W}{h_x} - \frac{k_{12}}{\mu} \frac{1}{4} \left( \frac{\psi_{NW} - \psi_{SW} + \psi_N - \psi_S}{h_y} \right), \\
 b_n &= -\frac{k_{21}}{\mu} \frac{1}{4} \left( \frac{\psi_{NE} - \psi_{NW} + \psi_E - \psi_W}{h_x} \right) - \frac{k_{22}}{\mu} \frac{\psi_N - \psi_P}{h_y}, \\
 b_s &= -\frac{k_{21}}{\mu} \frac{1}{4} \left( \frac{\psi_{SE} - \psi_{SW} + \psi_E - \psi_W}{h_x} \right) - \frac{k_{22}}{\mu} \frac{\psi_P - \psi_S}{h_y}.
 \end{aligned}$$

For control volumes located on the external boundary of the porous domain or on the interface, the corresponding fluxes need to be adjusted. We consider the case of a volume  $V_\psi$  located on the right external boundary as depicted in Figure 4.5 (right). In this case  $a_w$  is the same as above and the remaining approximations of the Darcy velocities are

$$a_e = -\frac{k_{11}}{\mu} \frac{\psi_e - \psi_P}{0.5h_x} - \frac{k_{12}}{\mu} \frac{1}{2} \left( \frac{\psi_{Ne} - \psi_{Se}}{h_y} \right),$$

$$b_n = -\frac{k_{21}}{\mu} \frac{1}{3} \left( \frac{\psi_{Ne} - \psi_{NW} + \psi_e - \psi_W}{h_x} \right) - \frac{k_{22}}{\mu} \frac{\psi_N - \psi_P}{h_y},$$

$$b_s = -\frac{k_{21}}{\mu} \frac{1}{3} \left( \frac{\psi_{Se} - \psi_{SW} + \psi_e - \psi_W}{h_x} \right) - \frac{k_{22}}{\mu} \frac{\psi_P - \psi_S}{h_y}.$$

For control volumes lying on other boundaries of the porous-medium domain the fluxes are adapted analogously. The Dirichlet boundary conditions in (2.12) are directly incorporated into the right hand side of the resulting linear system of equations (4.20). Since there exist no control volumes for the pressure nodes  $\psi_{i,j}^{vb}$ ,  $\psi_{i,j}^{hb}$ ,  $\psi_{i,j}^c$  on the external boundary, the Neumann boundary condition in (2.12) is approximated using finite differences.

### Discretization of coupling conditions

For the numerical simulations presented in Chapter 6 we consider two different sets of interface conditions, the classical conditions (2.17)–(2.19) and the generalized conditions (3.98)–(3.100). The corresponding nodes used for the implementation of the two coupling concepts are presented in Figure 4.6.

Both sets of coupling conditions contain the conservation of mass across the fluid–porous interface, which is given by (2.17) and (3.98). This condition is approximated using the stencil presented in Figure 4.6 (right) for nodes  $\psi_{i,N_y}^{hb}$  with  $1 < i < N_x^{pm}$  as follows

$$v_P = -\frac{k_{21}}{\mu} \frac{\psi_E - \psi_W}{2h_x} - \frac{k_{22}}{\mu} \frac{\psi_P - \psi_S}{0.5h_y}. \quad (4.14)$$

For the pressure nodes at  $(0.5h_x, N_y^{pm}h_y)$  and  $((N_x^{pm} - 0.5)h_x, N_y^{pm}h_y)$  we use one-sided finite differences instead of the central one. For example,

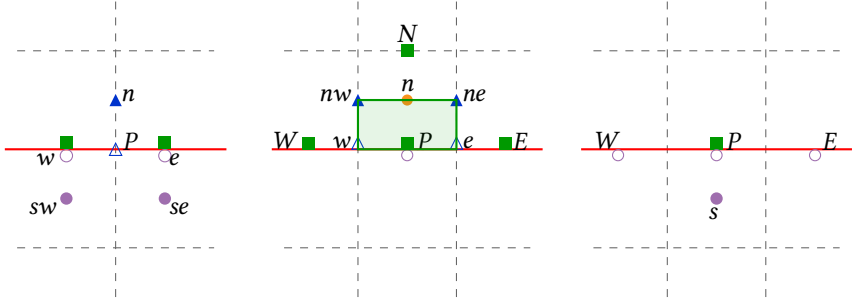


Figure 4.6: Stencil for the coupling condition for the tangential velocity (left), the normal velocity (middle) and the pressure (right).

for node  $\psi_{1, N_y^{\text{pm}}}$  the conservation of mass across the interface reads

$$v_P = -\frac{k_{21}}{\mu} \frac{\psi_E - \psi_P}{h_x} - \frac{k_{22}}{\mu} \frac{\psi_P - \psi_s}{0.5h_y}.$$

The discrete form of the balance of normal forces (2.18) in case of the symmetric stress tensor  $\mathbf{T}(\mathbf{v}, p) = \mu (\nabla \mathbf{v} + (\nabla \mathbf{v})^\top) - p \mathbf{I}$  is obtained considering a control volume of size  $h_x \times 0.5h_y$  for the velocity  $v_P$  on the interface (Figure 4.6, middle), and it reads

$$(F_{x,e}^v - F_{x,w}^v)0.5h_y + (F_{y,n}^v - F_{y,p}^v)h_x = 0.5f_P^v h_x h_y. \quad (4.15)$$

Here, the fluxes across the control volume edges corresponding to nodes  $v_{i,0}$  for  $1 < i < N_x^{\text{ff}}$  have the following form

$$\begin{aligned} F_{x,e}^v &= -\mu \left( \frac{u_{ne} - u_e}{0.5h_y} + \frac{v_E - v_P}{h_x} \right), & F_{y,n}^v &= p_n - 2\mu \frac{v_N - v_P}{h_y}, \\ F_{x,w}^v &= -\mu \left( \frac{u_{nw} - u_w}{0.5h_y} + \frac{v_P - v_W}{h_x} \right), & F_{y,p}^v &= \psi_P. \end{aligned}$$

At nodes  $v_{1,0}$  and  $v_{N_x^{\text{ff}},0}$  the fluxes  $F_{x,w}^v$  and  $F_{x,e}^v$  need to be adjusted, respectively. Considering  $v_{1,0}$  located at  $(0.5h_x, 0)$ , for example, we obtain a



modified flux

$$F_{x,w}^v = -\mu \left( \frac{u_{nw} - u_w}{0.5h_y} + \frac{v_p - v_w}{0.5h_x} \right).$$

In case the nonsymmetric tensor  $\mathbf{T}(\mathbf{v}, p) = \mu \nabla \mathbf{v} - p \mathbf{I}$  is considered in (2.18), we discretize the balance of normal forces using finite differences. This leads to

$$p_n - \mu \frac{v_N - v_P}{h_y} = \psi_P.$$

Discretization of the generalized balance of normal forces (3.99), that includes the nonsymmetric stress tensor, using the stencil presented in Figure 4.6 (middle) yields

$$p_n - \mu \frac{v_N - v_P}{h_y} + \mu N_s^{\text{bl}} \left( \frac{u_{nw} - u_w}{h_y} + \frac{u_{ne} - u_e}{h_y} \right) = \psi_P. \quad (4.16)$$

We approximate the Beavers–Joseph coupling condition (2.19) by

$$u_P + \frac{k_{11}}{\mu} \frac{\psi_w - \psi_e}{h_x} + \frac{k_{12}}{\mu} \left( \frac{\psi_w - \psi_{sw}}{h_y} + \frac{\psi_e - \psi_{se}}{h_y} \right) = \frac{\sqrt{k_{11}}}{\alpha_{\text{BJ}}} \frac{u_n - u_P}{0.5h_y}, \quad (4.17)$$

the Beavers–Joseph–Jones condition (2.22) by

$$\begin{aligned} u_P + \frac{k_{11}}{\mu} \frac{\psi_w - \psi_e}{h_x} + \frac{k_{12}}{\mu} \left( \frac{\psi_w - \psi_{sw}}{h_y} + \frac{\psi_e - \psi_{se}}{h_y} \right) \\ = \frac{\sqrt{k_{11}}}{\alpha_{\text{BJ}}} \left( \frac{u_n - u_P}{0.5h_y} + \frac{v_e - v_w}{h_x} \right), \end{aligned} \quad (4.18)$$

and the Saffman simplifications (2.20) and (2.21) are obtained by neglecting the terms on the left hand side in (4.17) and (4.18) except for  $u_P$ . The

discrete form of the generalized condition (3.100) reads

$$\begin{aligned}
 u_P - \frac{\ell^2 M_1^{1,\text{bl}}}{\mu} \frac{\psi_w - \psi_e}{h_x} - \frac{\ell^2 M_1^{2,\text{bl}}}{\mu} \left( \frac{\psi_w - \psi_{sw}}{h_y} + \frac{\psi_e - \psi_{se}}{h_y} \right) \\
 = -\ell N_1^{\text{bl}} \frac{u_n - u_P}{0.5h_y}. \quad (4.19)
 \end{aligned}$$

For the implementation of coupling conditions (2.19)–(2.22) and (3.100) we used the stencil presented in Figure 4.6 (left).

## 4.2.2 Monolithic approach

We solve the coupled Stokes–Darcy problem monotonically, i.e., all equations including a set of interface conditions are assembled together into the global matrix  $\mathbf{A}_h$ . The monolithic approach allows us to solve the strongly coupled problem without developing any subdomain iteration scheme for which we would need to prove convergence and robustness before the scheme could be used for numerical solution. Partitioning schemes become necessary and beneficial in case of large-scale applications or nonstationary problems to handle different scales in time in the free-flow region and the porous-medium domain. However, in this work we deal with stationary flows in coupled systems which can be solved in a monolithic way. After having discretized problem (2.7)–(2.9), (2.12) and (2.16) with an appropriate set of interface conditions (2.17)–(2.19) or (3.98)–(3.100) as described in Section 4.2.1, the resulting equations are put together into one sparse matrix  $\mathbf{A}_h$ . The latter is composed of four submatrices that are schematically separated by the dashed lines in (4.20). Two of these submatrices correspond to the Stokes and Darcy equations in the subdomains and the two remaining ones enable the coupling of the two flow models. The discrete coupled system has the following form

$$\mathbf{A}_h \mathbf{x}_h = \mathbf{b}_h \quad \Leftrightarrow \quad \left( \begin{array}{ccc|cc} \mathbf{A} & \mathbf{B}_1 & \mathbf{C}_1 & & \\ \mathbf{B}_2 & \mathbf{0} & \mathbf{0} & & \\ \mathbf{C}_2 & \mathbf{0} & \mathbf{D} & & \end{array} \right) \begin{pmatrix} \mathbf{w} \\ \mathbf{p} \\ \boldsymbol{\psi} \end{pmatrix} = \begin{pmatrix} \mathbf{b}_w \\ \mathbf{0} \\ \mathbf{b}_\psi \end{pmatrix}. \quad (4.20)$$

Here,  $\mathbf{w} = (\mathbf{u}, \mathbf{v})$ ,  $\mathbf{p}$ ,  $\boldsymbol{\psi}$  are the solution vectors for the primary variables in the two flow domains that are put together into vector  $x_h$ . The upper left  $2 \times 2$  block in matrix  $\mathbf{A}_h$  corresponds to the Stokes problem, where  $\mathbf{A}$  and  $\mathbf{B}_1$  incorporate the discrete form of the momentum conservation equation given by (4.7) and (4.11), and  $\mathbf{B}_2$  includes the discrete mass conservation equation (4.6). The Darcy flow problem (4.13) is represented by matrix  $\mathbf{D}$ . Coupling condition (4.17) respective (4.19) for the tangential velocity component, and condition (4.15) respective (4.16) for the momentum coupling are incorporated in  $\mathbf{C}_1$ . The conservation of mass across the fluid–porous interface (4.14) is given by  $\mathbf{C}_2$ . Vector  $\mathbf{b}_h$  denotes the right hand side of the system of linear equations and contains vectors  $\mathbf{b}_w$  and  $\mathbf{b}_\psi$  that include values corresponding to the applied conditions on the external boundary of the coupled domain (see Section 4.2.1). The discrete Stokes–Darcy problem (4.20) is then solved monolithically using the sparse supernodal LU factorization for general matrices available in EIGEN [75].

### 4.3 Computation of effective properties

Before the coupled Stokes–Darcy problem is solved we need to determine effective coefficients (permeability, Beavers–Joseph parameter, boundary layer constants) that appear in the macroscale model depending on the set of interface conditions. For the classical set of coupling conditions (2.17)–(2.19) the permeability tensor  $\mathbf{K}$  and the Beavers–Joseph slip coefficient  $\alpha_{\text{BJ}}$  are required, whereas the generalized interface conditions (3.98)–(3.100) contain the permeability  $\mathbf{K}$  and the boundary layer constants  $N_1^{\text{bl}}$ ,  $N_s^{\text{bl}}$  and  $M_1^{j,\text{bl}}$ . The Beavers–Joseph slip coefficient  $\alpha_{\text{BJ}}$  cannot be computed in general but needs to be fitted experimentally dependent on the pore geometry, the exact interface location and the flow regime. However, since it is not well studied how to find the optimal Beavers–Joseph parameter and available methods to determine this coefficient are often computationally expensive [117], it is typically taken  $\alpha_{\text{BJ}} = 1$  in the literature. Within this thesis we also use this value, if not stated otherwise.

Regarding permeability and boundary layer constants we obtained formulas in Sections 2.3.2 and 3.1.3 that enable us to compute these coefficients based on the pore geometry and the sharp interface location as described below.

Independent of the set of coupling conditions the permeability of the porous medium appearing in the Darcy flow equation (2.16) needs to be determined. This can be done in various ways, e.g., using the Kozeny–Carman equation [32, 104] which provides a semi-analytical porosity–permeability relation, via upscaling of the pore-scale simulations (FEM, Lattice Boltzman method or smoothed-particle hydrodynamics) or using homogenization. For a thorough study on different methods to obtain the permeability of an isotropic porous medium with a periodic microstructure, we refer the reader to [EE8]. In this work, we compute the dimensionless permeability tensor  $\tilde{\mathbf{K}}$  of a periodic porous medium numerically by means of homogenization theory [90, 95]. We solve the cell problems (2.74)–(2.76) in the unit cell  $Y$  (Figure 4.7, left) using the PDE solver FREEFEM++ with Taylor–Hood finite elements (see Section 4.1.1). Hereby, the fluid part  $Y_f$  of the unit cell  $Y$  is partitioned into triangular elements and the exact number of elements depends on the shape of solid obstacles and is given in Chapter 6 for the considered geometries. The entries of the permeability tensor are then obtained by integrating the cell problem solutions as described by (2.79).

When the generalized interface conditions (3.98)–(3.100) are applied, in addition to the permeability tensor  $\tilde{\mathbf{K}}$ , the boundary layer constants  $N_1^{\text{bl}}$ ,  $N_s^{\text{bl}}$  and  $M_1^{j,\text{bl}}$  need to be computed. We obtain these dimensionless effective coefficients from the boundary layer problems (3.17)–(3.21) and (3.39)–(3.43) defined in the infinite stripe  $Z^{\text{bl}}$ . As explained in Section 3.2, we have freedom to choose the exact position of the sharp fluid–porous interface within the boundary layer stripe. Based on the chosen interface location at distance  $a$  (Figure 4.7, right) above the top row of solid inclusions, the boundary layer problems need to be solved in  $Z^{\text{bl}} = Z^{a,+} \cup Z^{a,-}$ . The corresponding boundary layer constants are then defined as integrals of the solutions over the interface  $S_a$  as given by (3.102a)–(3.103).

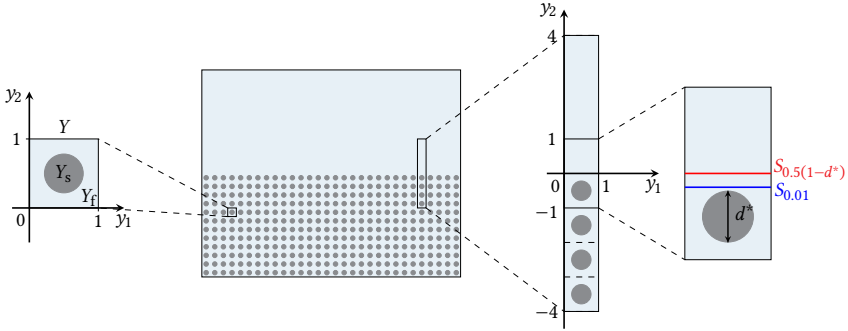


Figure 4.7: Unit cell  $Y$  (left) and cut-off stripe  $Z_{4,4}$  with two possible interface locations  $S_a$  (right) where  $a = 0.01$  (blue line) and  $a = 0.5(1 - d^*)$  (red line), respectively, and  $d^*$  denotes the size of solid obstacles within the unit cell  $Y$ .

Since we cannot handle infinitely large domains for the numerical solution of boundary layer problems (3.17)–(3.21) and (3.39)–(3.43) we define a vertical cut-off stripe

$$Z_{k,m} = Z_m^{a,+} \cup Z_k^{a,-} = Z^{\text{bl}} \cap ((0, 1) \times (-k, m)), \quad k, m \in \mathbb{N},$$

where  $Z_m^{a,+} = (0, 1) \times (\frac{d^*-1}{2} + a, m)$  and  $Z_k^{a,-} = Z_{k,m} \setminus Z_m^{a,+}$ . By cutting the infinite boundary layer stripe  $Z^{\text{bl}}$  such that the cut-off domain  $Z_{k,m}$  is obtained, two additional boundaries are created where appropriate boundary conditions need to be applied: the upper boundary  $\Gamma_m = (0, 1) \times \{m\}$  and the lower boundary  $\Gamma_k = (0, 1) \times \{-k\}$ . We follow [33, 34, 98] to define the cut-off boundary layer problems (4.21)–(4.23) and (4.24)–(4.26), that are used for the computation of  $N_1^{\text{bl}}$ ,  $N_s^{\text{bl}}$  and  $M_1^{j,\text{bl}}$ , according to problems (3.17)–(3.21) and (3.39)–(3.43).

The following system of equations corresponds to boundary layer problem

(3.17)–(3.21) defined on the cut-off stripe  $Z_{k,m}$ :

$$\begin{aligned}
 -\Delta_{\mathbf{y}} \mathbf{t}^{\text{bl},k,m,a} + \nabla_{\mathbf{y}} s^{\text{bl},k,m,a} &= \mathbf{0} & \text{in } Z_m^{a,+} \cup Z_k^{a,-}, \\
 \nabla_{\mathbf{y}} \cdot \mathbf{t}^{\text{bl},k,m,a} &= 0 & \text{in } Z_m^{a,+} \cup Z_k^{a,-}, \\
 \llbracket \mathbf{t}^{\text{bl},k,m,a} \rrbracket_{S_a} &= \mathbf{0} & \text{on } S_a, \\
 \llbracket (\nabla_{\mathbf{y}} \mathbf{t}^{\text{bl},k,m,a} - s^{\text{bl},k,m,a} \mathbf{1}) \mathbf{e}_2 \rrbracket_{S_a} &= \mathbf{e}_1 & \text{on } S_a, \\
 \mathbf{t}^{\text{bl},k,m,a} &= \mathbf{0} & \text{on } \bigcup_{i=1}^k (\partial Y_s - \{0, i\}), \quad \{\mathbf{t}^{\text{bl},k,m,a}, s^{\text{bl},k,m,a}\} \text{ is } y_1\text{-periodic},
 \end{aligned} \tag{4.21}$$

with the following additional boundary conditions on the upper respective lower boundary of the cut-off stripe  $Z_{k,m}$  proposed in [98]:

$$\frac{\partial t_1^{\text{bl},k,m,a}}{\partial y_2} = t_2^{\text{bl},k,m,a} = 0 \quad \text{on } \Gamma_m, \quad \mathbf{t}^{\text{bl},k,m,a} = \mathbf{0} \quad \text{on } \Gamma_k. \tag{4.22}$$

In addition, to obtain a uniquely defined pressure, we set

$$\int_{\Gamma_k} s^{\text{bl},k,m,a}(y_1, -k) dy_1 = 0. \tag{4.23}$$

The cut-off boundary layer problem corresponding to (3.39)–(3.43) for  $j = 1, 2$  reads

$$\begin{aligned}
 -\Delta_{\mathbf{y}} \boldsymbol{\beta}^{j,\text{bl},k,m,a} + \nabla_{\mathbf{y}} \omega^{j,\text{bl},k,m,a} &= \mathbf{0} & \text{in } Z_m^{a,+} \cup Z_k^{a,-}, \\
 \nabla_{\mathbf{y}} \cdot \boldsymbol{\beta}^{j,\text{bl},k,m,a} &= 0 & \text{in } Z_m^{a,+} \cup Z_k^{a,-}, \\
 \llbracket \boldsymbol{\beta}^{j,\text{bl},k,m,a} \rrbracket_{S_a} &= k_2^j \mathbf{e}_2 - \mathbf{w}^j & \text{on } S_a, \\
 \llbracket (\nabla_{\mathbf{y}} \boldsymbol{\beta}^{j,\text{bl},k,m,a} - \omega^{j,\text{bl},k,m,a} \mathbf{1}) \mathbf{e}_2 \rrbracket_{S_a} &= -(\nabla_{\mathbf{y}} \mathbf{w}^j - \pi^j \mathbf{1}) \mathbf{e}_2 & \text{on } S_a, \\
 \boldsymbol{\beta}^{j,\text{bl},k,m,a} &= \mathbf{0} & \text{on } \bigcup_{i=1}^k (\partial Y_s - \{0, i\}), \quad \{\boldsymbol{\beta}^{j,\text{bl},k,m,a}, \omega^{j,\text{bl},k,m,a}\} \text{ is } y_1\text{-periodic},
 \end{aligned} \tag{4.24}$$

with the additional conditions on the cut-off boundaries  $\Gamma_m$  and  $\Gamma_k$  and the condition to obtain a uniquely defined pressure

$$\frac{\partial \beta_1^{j,\text{bl},k,m,a}}{\partial y_2} = \beta_2^{j,\text{bl},k,m,a} = 0 \quad \text{on } \Gamma_m, \quad \beta^{j,\text{bl},k,m,a} = \mathbf{0} \quad \text{on } \Gamma_k, \quad (4.25)$$

$$\int_{\Gamma_k} \omega^{j,\text{bl},k,m,a}(y_1, -k) dy_1 = 0. \quad (4.26)$$

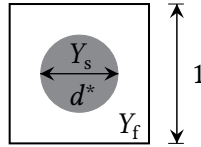
Then, we define the following cut-off boundary layer constants

$$N_1^{\text{bl},k,m,a} = \int_0^1 t_1^{\text{bl},k,m,a} \left( y_1, \frac{d^*-1}{2} + a \right) dy_1, \quad (4.27)$$

$$N_s^{\text{bl},k,m,a} = \int_0^1 s^{\text{bl},k,m,a} \left( y_1, \frac{d^*-1}{2} + a \right) dy_1, \quad (4.28)$$

$$M_1^{j,\text{bl},k,m,a} = \int_0^1 \beta_1^{j,\text{bl},k,m,a} \left( y_1, \frac{d^*-1}{2} + a \right) dy_1. \quad (4.29)$$

The use of cut-off solutions  $t^{\text{bl},k,m,a}$ ,  $s^{\text{bl},k,m,a}$  and  $\beta^{j,\text{bl},k,m,a}$  for the computation of the boundary layer constants (4.28) and (4.29) leads to two different sources of error, i.e., the discretization error and the cut-off error (approximation error introduced by cutting the infinite stripe). In order to reduce the latter one, we need to set  $k, m \in \mathbb{N}$  large enough such that exponential decay of the solutions to the cut-off boundary layer problems is guaranteed. As proposed in [34], we use  $k = 4$  solid inclusions in the porous part and  $m = 4$  cells in the free-flow part resulting in the cut-off stripe  $Z_{4,4}$  (Figure 4.7, right) for the computation of boundary layer constants in Chapter 6. With this choice for  $k$  and  $m$ , the two different errors are balanced in an optimal way such that the computational costs are minimal and the cut-off error in the computed constants  $N_1^{\text{bl},k,m,a}$ ,  $N_s^{\text{bl},k,m,a}$  and  $M_1^{j,\text{bl},k,m,a}$  can be neglected. We solve problems (4.21)–(4.23) and (4.24)–(4.26) via `FREEFEM++` using Taylor–Hood finite elements and an adaptive mesh. In Tables 4.1 and 4.2 we provide the boundary layer constants computed on cut-off domains  $Z_{k,k}$  of different sizes for circular



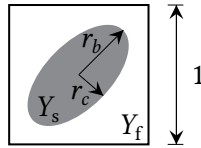
$k$	$N_1^{\text{bl},k,m,a}$	$N_s^{\text{bl},k,m,a}$	$M_1^{1,\text{bl},k,m,a}$	$M_1^{2,\text{bl},k,m,a}$
1	-0.303821777	-	-0.045066533	-
2	-0.303825416	-	-0.047673166	-
3	-0.303825412	-	-0.047673168	-
4	-0.303825307	-	-0.047673169	-
5	-0.303825364	-	-0.047673165	-
6	-0.303825360	-	-0.047673165	-

Table 4.1: Boundary layer constants for the presented circular solid inclusion ( $d^* = 0.5$ ) depending on the size of the cut-off stripe  $Z_{k,k}$  for the interface  $S_{0.5(1-d^*)}$ .

and elliptical solid inclusions, respectively. The radius of the circular inclusion within the unit cell  $Y = (0, 1)^2$  is  $r = 0.25$ , and the inclusion is centered at  $(0.5, 0.5)$ . The geometry of the elliptical solid grain is the same as in [33, 98], i.e., the semi-axes of the ellipse are  $r_b = 0.4$  and  $r_c = 0.2$ , it is rotated clockwise by  $45^\circ$  and the center is at  $(0.5, 0.5)$ . We observe that for  $k \geq 4$  at least the 7 digits after decimal point are the same for all boundary layer constants in case of circular solid obstacles (Table 4.1), and in case of elliptical inclusions, at least the 4 digits after decimal point are equal (Table 4.2).

In this thesis, for the computation of boundary layer constants we consider the cut-off boundary layer stripe  $Z_{4,4}$  and the interface  $S_{0.5(1-d^*)}$  (Figure 4.7, right), if not stated otherwise. For clarity, we usually waive writing the superscripts  $k, m, a$  and denote the effective coefficients computed using cut-off problems (4.21)–(4.23) and (4.24)–(4.26) by  $\mathbf{N}^{\text{bl}}$ ,  $N_s^{\text{bl}}$  and  $\mathbf{M}^{j,\text{bl}}$ .





$k$	$N_1^{\text{bl},k,m,a}$	$N_s^{\text{bl},k,m,a}$	$M_1^{\text{bl},k,m,a}$	$M_1^{\text{bl},k,m,a}$
1	-0.239631077	-0.271181957	-0.029993521	-0.003336630
2	-0.239630149	-0.271327915	-0.031028758	-0.003337094
3	-0.239630412	-0.271327977	-0.031028758	-0.003337094
4	-0.239629929	-0.271327434	-0.031028758	-0.003337094
5	-0.239630267	-0.271329321	-0.031028758	-0.003337094
6	-0.239629975	-0.271329853	-0.031028758	-0.003337094

Table 4.2: Boundary layer constants for the presented elliptical solid inclusion ( $r_b = 0.4$ ,  $r_c = 0.2$ ) depending on the size of the cut-off stripe  $Z_{k,k}$  for the interface  $S_{0.5(1-d^*)}$ .

## Summary

In this chapter, we presented the numerical method for solving the pore-scale problem based on a finite element discretization. We introduced two averaging techniques to reduce oscillations in the pore-scale solution that appear naturally due to the presence of solid obstacles in the porous medium. Averaging of pore-scale quantities is useful for a better comparison of microscale and macroscale simulation results as we will see in Chapter 6. We discretized the coupled Stokes–Darcy model with different sets of interface conditions based on the finite volume method. Hereby, we used staggered grids in the free-flow region to prevent pressure oscillations, and multipoint flux approximation in the porous medium to account for anisotropic permeability. The resulting discrete Stokes–Darcy problem is then solved monolithically. Further, we provided information on the computation of effective coefficients (permeability, boundary layer constants) in the macroscale model.



# 5 Analysis of the Stokes–Darcy prob- lem with generalized interface conditions



# Analysis of the Stokes–Darcy problem with generalized interface conditions

# 5

The content of this chapter is based on the following original article:

- [EE1] E. Eggenweiler, M. Discacciati, and I. Rybak. *Analysis of the Stokes–Darcy problem with generalised interface conditions*. ESAIM Math. Model. Numer. Anal. 56 (2022), pp. 727–742.  
DOI: 10.1051/m2an/2022025

In this chapter, we analyze the Stokes–Darcy problem with the generalized interface conditions developed in Chapter 3 with respect to existence and uniqueness of a weak solution. In Section 5.1, we introduce the problem setting and derive the corresponding weak formulation. In Section 5.2, we prove that the Stokes–Darcy problem with the generalized coupling conditions is well-posed for orthotropic porous media, where the well-posedness is guaranteed under a suitable relationship between the permeability and the boundary layer constants. In Section 5.3, we analyze the validity of the obtained relationship, i.e., we compute the effective coefficients for various porous-medium geometrical configurations and show that the resulting assumption is not restrictive.

## 5.1 Problem setting and weak formulation

In this section, we introduce the problem setting (geometry, assumptions, flow models, boundary conditions) and derive the weak formulation of the corresponding Stokes–Darcy problem with the generalized interface conditions developed in Chapter 3.

### 5.1.1 Problem setting

We consider the coupled domain  $\Omega \subset \mathbb{R}^2$  consisting of the free-flow region  $\Omega_{\text{ff}}$  and the porous-medium domain  $\Omega_{\text{pm}}$  separated by a sharp fluid–porous interface  $\Sigma$ . The interface is assumed to be straight such that the tangential and normal vectors on the interface denoted by  $\boldsymbol{\tau}$  and  $\boldsymbol{n}$  are constant (Figure 5.1). Therefore, taking the tangential and normal components  $\boldsymbol{v}\boldsymbol{\tau}$  respective  $\boldsymbol{v}\boldsymbol{n}$  of a suitable vector function  $\boldsymbol{v}$  on the interface  $\Sigma$  does not reduce the regularity of the trace  $\boldsymbol{v}|_{\Sigma}$ . The porous medium is constructed by a periodic repetition of solid obstacles as described in Section 2.3.2.

As in the rest of this thesis, we consider slow, viscous fluid flow at low Reynolds numbers ( $Re \ll 1$ ) through a nondeformable porous medium.

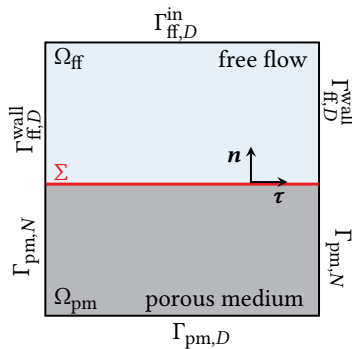


Figure 5.1: Schematic representation of the computational domain.

Thus, fluid motion in the free-flow region is described by the Stokes equations

$$-\nabla \cdot \mathbf{T}(\mathbf{v}^{\text{ff}}, p^{\text{ff}}) = \mathbf{0}, \quad \nabla \cdot \mathbf{v}^{\text{ff}} = 0 \quad \text{in } \Omega_{\text{ff}}, \quad (5.1)$$

where  $\mathbf{T}(\mathbf{v}^{\text{ff}}, p^{\text{ff}}) = \mu \nabla \mathbf{v}^{\text{ff}} - p^{\text{ff}} \mathbf{I}$  denotes the nonsymmetric stress tensor. To describe the flow in the porous-medium domain we use the Darcy flow model

$$-\nabla \cdot \left( \frac{\mathbf{K}}{\mu} \nabla p^{\text{pm}} \right) = 0 \quad \text{in } \Omega_{\text{pm}}. \quad (5.2)$$

On the fluid–porous interface  $\Sigma$ , we apply the generalized coupling conditions developed in Chapter 3 (see equations (3.98)–(3.100)) for arbitrary flows to the porous bed, which read

$$\mathbf{v}^{\text{ff}} \cdot \mathbf{n} = \mathbf{v}^{\text{pm}} \cdot \mathbf{n} \quad \text{on } \Sigma, \quad (5.3)$$

$$p^{\text{pm}} = -\mathbf{n} \cdot \mathbf{T}(\mathbf{v}^{\text{ff}}, p^{\text{ff}}) \mathbf{n} + N_s^{\text{bl}} \boldsymbol{\tau} \cdot \mathbf{T}(\mathbf{v}^{\text{ff}}, p^{\text{ff}}) \mathbf{n} \quad \text{on } \Sigma, \quad (5.4)$$

$$\mathbf{v}^{\text{ff}} \cdot \boldsymbol{\tau} = -\ell \mu^{-1} (N^{\text{bl}} \cdot \boldsymbol{\tau}) \boldsymbol{\tau} \cdot \mathbf{T}(\mathbf{v}^{\text{ff}}, p^{\text{ff}}) \mathbf{n} + \ell^2 \mu^{-1} \sum_{j=1}^2 \frac{\partial p^{\text{pm}}}{\partial x_j} M^{j,\text{bl}} \cdot \boldsymbol{\tau} \quad \text{on } \Sigma. \quad (5.5)$$

The Stokes–Darcy problem (5.1)–(5.5) is completed with the following boundary conditions on the external boundary  $\partial\Omega$  of the coupled domain

$$\mathbf{v}^{\text{ff}} = \mathbf{v}_{\text{in}} \quad \text{on } \Gamma_{\text{ff},D}^{\text{in}}, \quad \mathbf{v}^{\text{ff}} = \mathbf{0} \quad \text{on } \Gamma_{\text{ff},D}^{\text{wall}}, \quad (5.6)$$

$$p^{\text{pm}} = 0 \quad \text{on } \Gamma_{\text{pm},D}, \quad \mathbf{v}^{\text{pm}} \cdot \mathbf{n}^{\text{pm}} = 0 \quad \text{on } \Gamma_{\text{pm},N}. \quad (5.7)$$

Here,  $\mathbf{v}_{\text{in}}$  is the prescribed velocity on  $\Gamma_{\text{ff},D}^{\text{in}}$ ,  $\mathbf{n}^{\text{pm}}$  denotes the unit vector on  $\Gamma_{\text{pm},N}$  pointing outward the porous-medium domain,  $\partial\Omega_{\text{ff}} \setminus \Sigma = \Gamma_{\text{ff},D}^{\text{in}} \cup \Gamma_{\text{ff},D}^{\text{wall}}$  and  $\partial\Omega_{\text{pm}} \setminus \Sigma = \Gamma_{\text{pm},D} \cup \Gamma_{\text{pm},N}$ ,  $\Gamma_{\text{pm},D} \cap \Gamma_{\text{pm},N} = \emptyset$ , and  $\Gamma_{\text{pm},D} \neq \emptyset$  (Figure 5.1).

### 5.1.2 Weak formulation of the coupled problem

In order to obtain the weak formulation of the coupled Stokes–Darcy problem (5.1)–(5.7) we introduce the following functional spaces

$$\begin{aligned} \mathbf{H}_{\text{ff}} &:= \{ \mathbf{u} \in H^1(\Omega_{\text{ff}})^2 : \mathbf{u} = \mathbf{0} \text{ on } \partial\Omega_{\text{ff}} \setminus \Sigma \}, \\ \mathbf{H}_{\text{ff},\Sigma} &:= \{ \mathbf{u} \in H^1(\Omega_{\text{ff}})^2 : \mathbf{u} = \mathbf{0} \text{ on } \Gamma_{\text{ff},D}^{\text{wall}} \cup \Sigma \}, \\ \mathbf{H}_{\text{pm}} &:= \{ \psi \in H^1(\Omega_{\text{pm}}) : \psi = 0 \text{ on } \Gamma_{\text{pm},D} \}, \\ \mathbf{Q}_{\text{ff}} &:= L^2(\Omega_{\text{ff}}), \quad \mathbf{W} := \mathbf{H}_{\text{ff}} \times \mathbf{H}_{\text{pm}}, \end{aligned}$$

and define the norm of the Hilbert space  $\mathbf{W}$  as

$$\|\underline{\mathbf{w}}\|_{\mathbf{W}} := \left( \|\mathbf{w}\|_{H^1(\Omega_{\text{ff}})^2}^2 + \|\psi\|_{H^1(\Omega_{\text{pm}})}^2 \right)^{1/2} \quad \text{for all } \underline{\mathbf{w}} = (\mathbf{w}, \psi) \in \mathbf{W}.$$

Further, we consider the trace spaces [110, Chapters 8, 11, 12]:

$$\begin{aligned} H^{1/2}(\partial\Omega_{\text{pm}}) &= \{ v \in L^2(\partial\Omega_{\text{pm}}) : \text{there exists } u \in H^1(\Omega_{\text{pm}}) \\ &\quad \text{such that } \text{tr}(u) = v \}, \\ H_0^{1/2}(\Sigma) &= \{ u \in H^{1/2}(\partial\Omega_{\text{pm}}) : \text{supp } u \subset \bar{\Sigma} \}, \end{aligned}$$

and denote their dual spaces by  $H^{-1/2}(\partial\Omega_{\text{pm}})$  and  $(H_0^{1/2}(\Sigma))'$ , respectively. Below, for the sake of simplicity, we waive the symbols  $\mathrm{d}\mathbf{x}$  and  $\mathrm{d}\mathbf{S}$  in volume and boundary integrals, and we write  $q = q(\mathbf{x})$  for  $\mathbf{x} \in \Omega$ .

As a first step towards the weak formulation of problem (5.1)–(5.7), we multiply the momentum conservation equation given in (5.1) by a test function  $\mathbf{u} \in \mathbf{H}_{\text{ff}}$  and apply integration by parts over  $\Omega_{\text{ff}}$ . This yields

$$\begin{aligned} 0 &= - \int_{\Omega_{\text{ff}}} (\nabla \cdot \mathbf{T}(\mathbf{v}^{\text{ff}}, p^{\text{ff}})) \cdot \mathbf{u} \\ &= - \int_{\partial\Omega_{\text{ff}}} \mathbf{T}(\mathbf{v}^{\text{ff}}, p^{\text{ff}}) \mathbf{n}^{\text{ff}} \cdot \mathbf{u} + \int_{\Omega_{\text{ff}}} \mu \nabla \mathbf{v}^{\text{ff}} : \nabla \mathbf{u} - \int_{\Omega_{\text{ff}}} p^{\text{ff}} \nabla \cdot \mathbf{u} \end{aligned}$$



$$= \int_{\Sigma} \mathbf{T}(\mathbf{v}^{\text{ff}}, p^{\text{ff}}) \mathbf{n} \cdot \mathbf{u} + \int_{\Omega_{\text{ff}}} \mu \nabla \mathbf{v}^{\text{ff}} : \nabla \mathbf{u} - \int_{\Omega_{\text{ff}}} p^{\text{ff}} \nabla \cdot \mathbf{u}, \quad (5.8)$$

where  $\mathbf{n}^{\text{ff}}$  denotes the unit normal vector on  $\partial\Omega_{\text{ff}}$  pointing outward the free-flow region, thus,  $\mathbf{n}^{\text{ff}} = -\mathbf{n}$  on  $\Sigma$ . Next, we rewrite condition (5.5) as follows

$$\boldsymbol{\tau} \mathbf{T}(\mathbf{v}^{\text{ff}}, p^{\text{ff}}) \mathbf{n} = -\mu \ell^{-1} (N_1^{\text{bl}})^{-1} \mathbf{v}^{\text{ff}} \cdot \boldsymbol{\tau} + \ell (N_1^{\text{bl}})^{-1} \sum_{j=1}^2 M_1^{j,\text{bl}} \frac{\partial p^{\text{pm}}}{\partial x_j}, \quad (5.9)$$

where we set  $N_1^{\text{bl}} = \mathbf{N}^{\text{bl}} \cdot \boldsymbol{\tau}$  and  $M_1^{j,\text{bl}} = \mathbf{M}^{j,\text{bl}} \cdot \boldsymbol{\tau}$  as in Section 3.2.2. Splitting the stress tensor  $\mathbf{T}(\mathbf{v}^{\text{ff}}, p^{\text{ff}})$  in its normal and tangential component and substituting conditions (5.4) and (5.9) in the integral term over  $\Sigma$  in the weak form (5.8), we obtain

$$\begin{aligned} \int_{\Sigma} \mathbf{T}(\mathbf{v}^{\text{ff}}, p^{\text{ff}}) \mathbf{n} \cdot \mathbf{u} &= \int_{\Sigma} (\mathbf{n} \cdot \mathbf{T}(\mathbf{v}^{\text{ff}}, p^{\text{ff}}) \mathbf{n}) (\mathbf{u} \mathbf{n}) + \int_{\Sigma} (\boldsymbol{\tau} \mathbf{T}(\mathbf{v}^{\text{ff}}, p^{\text{ff}}) \mathbf{n}) (\mathbf{u} \boldsymbol{\tau}) \\ &= \int_{\Sigma} (-p^{\text{pm}} + N_s^{\text{bl}} \boldsymbol{\tau} \mathbf{T}(\mathbf{v}^{\text{ff}}, p^{\text{ff}}) \mathbf{n}) (\mathbf{u} \mathbf{n}) \\ &\quad + \int_{\Sigma} (\boldsymbol{\tau} \mathbf{T}(\mathbf{v}^{\text{ff}}, p^{\text{ff}}) \mathbf{n}) (\mathbf{u} \boldsymbol{\tau}) \\ &= - \int_{\Sigma} p^{\text{pm}} (\mathbf{u} \mathbf{n}) + \int_{\Sigma} (\boldsymbol{\tau} \mathbf{T}(\mathbf{v}^{\text{ff}}, p^{\text{ff}}) \mathbf{n}) ((\mathbf{u} \boldsymbol{\tau}) + N_s^{\text{bl}} (\mathbf{u} \mathbf{n})) \\ &= - \int_{\Sigma} p^{\text{pm}} (\mathbf{u} \mathbf{n}) \\ &\quad + \int_{\Sigma} \left( -\mu \ell^{-1} (N_1^{\text{bl}})^{-1} (\mathbf{v}^{\text{ff}} \cdot \boldsymbol{\tau}) \right. \\ &\quad \left. + \ell (N_1^{\text{bl}})^{-1} \sum_{j=1}^2 M_1^{j,\text{bl}} \frac{\partial p^{\text{pm}}}{\partial x_j} \right) ((\mathbf{u} \boldsymbol{\tau}) + N_s^{\text{bl}} (\mathbf{u} \mathbf{n})) \\ &= - \int_{\Sigma} p^{\text{pm}} (\mathbf{u} \mathbf{n}) - \int_{\Sigma} \mu \ell^{-1} (N_1^{\text{bl}})^{-1} N_s^{\text{bl}} (\mathbf{v}^{\text{ff}} \cdot \boldsymbol{\tau}) (\mathbf{u} \mathbf{n}) \\ &\quad - \int_{\Sigma} \mu \ell^{-1} (N_1^{\text{bl}})^{-1} (\mathbf{v}^{\text{ff}} \cdot \boldsymbol{\tau}) (\mathbf{u} \boldsymbol{\tau}) \end{aligned}$$

$$\begin{aligned}
 & + \int_{\Sigma} \left( \ell(N_1^{\text{bl}})^{-1} N_s^{\text{bl}} \sum_{j=1}^2 M_1^{j,\text{bl}} \frac{\partial p^{\text{pm}}}{\partial x_j} \right) (\mathbf{u}\mathbf{n}) \\
 & + \int_{\Sigma} \left( \ell(N_1^{\text{bl}})^{-1} \sum_{j=1}^2 M_1^{j,\text{bl}} \frac{\partial p^{\text{pm}}}{\partial x_j} \right) (\mathbf{u}\boldsymbol{\tau}) \tag{5.10}
 \end{aligned}$$

for all  $\mathbf{u} \in H_{\text{ff}}$ . We introduce the continuous lifting operator  $E_{\text{ff}} : H^{1/2}(\Gamma_{\text{ff},D}^{\text{in}})^2 \rightarrow H_{\text{ff},\Sigma}$  and split the free-flow velocity  $\mathbf{v}^{\text{ff}} = \mathbf{v}_0^{\text{ff}} + E_{\text{ff}}\mathbf{v}_{\text{in}}$ , where  $\mathbf{v}_0^{\text{ff}} \in H_{\text{ff}}$ . We make use of this lifting, substitute (5.10) in the weak formulation (5.8) and get

$$\begin{aligned}
 - \int_{\Omega_{\text{ff}}} \mu \nabla (E_{\text{ff}}\mathbf{v}_{\text{in}}) : \nabla \mathbf{u} & = \int_{\Omega_{\text{ff}}} \mu \nabla \mathbf{v}_0^{\text{ff}} : \nabla \mathbf{u} - \int_{\Omega_{\text{ff}}} p^{\text{ff}} (\nabla \cdot \mathbf{u}) - \int_{\Sigma} p^{\text{pm}} (\mathbf{u}\mathbf{n}) \\
 & - \int_{\Sigma} \mu \ell^{-1} (N_1^{\text{bl}})^{-1} N_s^{\text{bl}} (\mathbf{v}_0^{\text{ff}} \cdot \boldsymbol{\tau}) (\mathbf{u}\mathbf{n}) \\
 & - \int_{\Sigma} \mu \ell^{-1} (N_1^{\text{bl}})^{-1} (\mathbf{v}_0^{\text{ff}} \cdot \boldsymbol{\tau}) (\mathbf{u}\boldsymbol{\tau}) \\
 & + \int_{\Sigma} \left( \ell(N_1^{\text{bl}})^{-1} N_s^{\text{bl}} \sum_{j=1}^2 M_1^{j,\text{bl}} \frac{\partial p^{\text{pm}}}{\partial x_j} \right) (\mathbf{u}\mathbf{n}) \\
 & + \int_{\Sigma} \left( \ell(N_1^{\text{bl}})^{-1} \sum_{j=1}^2 M_1^{j,\text{bl}} \frac{\partial p^{\text{pm}}}{\partial x_j} \right) (\mathbf{u}\boldsymbol{\tau}) \tag{5.11}
 \end{aligned}$$

for all  $\mathbf{u} \in H_{\text{ff}}$ . The weak form of the mass conservation equation given in (5.1) reads

$$- \int_{\Omega_{\text{ff}}} (\nabla \cdot \mathbf{v}_0^{\text{ff}}) q = \int_{\Omega_{\text{ff}}} (\nabla \cdot (E_{\text{ff}}\mathbf{v}_{\text{in}})) q$$

for all  $q \in Q_{\text{ff}}$ .

In order to derive the variational formulation in the porous-medium domain  $\Omega_{\text{pm}}$ , we multiply (5.2) by a test function  $\psi \in H_{\text{pm}}$ , integrate over  $\Omega_{\text{pm}}$  and incorporate the coupling condition (5.3) in the integral over  $\Sigma$ .

This yields

$$\int_{\Omega_{\text{pm}}} (\mu^{-1} \mathbf{K} \nabla p^{\text{pm}}) \cdot \nabla \psi + \int_{\Sigma} (\mathbf{v}^{\text{ff}} \cdot \mathbf{n}) \psi = 0$$

for all  $\psi \in H_{\text{pm}}$ .

For all  $\underline{v} = (\mathbf{v}, \varphi)$ ,  $\underline{w} = (\mathbf{w}, \psi) \in W$  and  $q \in Q_{\text{ff}}$ , we define the following bilinear forms

$$\begin{aligned} \mathcal{A}(\underline{v}, \underline{w}) &= \int_{\Omega_{\text{ff}}} \mu \nabla \mathbf{v} : \nabla \mathbf{w} + \int_{\Omega_{\text{pm}}} (\mu^{-1} \mathbf{K} \nabla \varphi) \cdot \nabla \psi - \int_{\Sigma} \varphi (\mathbf{w} \cdot \mathbf{n}) + \int_{\Sigma} (\mathbf{v} \cdot \mathbf{n}) \psi \\ &\quad - \int_{\Sigma} \mu \ell^{-1} (N_1^{\text{bl}})^{-1} N_s^{\text{bl}} (\mathbf{v} \cdot \boldsymbol{\tau}) (\mathbf{w} \cdot \mathbf{n}) - \int_{\Sigma} \mu \ell^{-1} (N_1^{\text{bl}})^{-1} (\mathbf{v} \cdot \boldsymbol{\tau}) (\mathbf{w} \cdot \boldsymbol{\tau}) \\ &\quad + \int_{\Sigma} \left( \ell (N_1^{\text{bl}})^{-1} N_s^{\text{bl}} \sum_{j=1}^2 M_1^{j, \text{bl}} \frac{\partial \varphi}{\partial x_j} \right) (\mathbf{w} \cdot \mathbf{n}) \\ &\quad + \int_{\Sigma} \left( \ell (N_1^{\text{bl}})^{-1} \sum_{j=1}^2 M_1^{j, \text{bl}} \frac{\partial \varphi}{\partial x_j} \right) (\mathbf{w} \cdot \boldsymbol{\tau}), \end{aligned} \quad (5.12)$$

$$\mathcal{B}(\underline{w}, q) = - \int_{\Omega_{\text{ff}}} (\nabla \cdot \mathbf{w}) q, \quad (5.13)$$

and the linear functionals

$$\mathcal{F}(\underline{w}) = - \int_{\Omega_{\text{ff}}} \mu \nabla (E_{\text{ff}} \mathbf{v}_{\text{in}}) : \nabla \mathbf{w}, \quad \mathcal{G}(q) = \int_{\Omega_{\text{ff}}} (\nabla \cdot (E_{\text{ff}} \mathbf{v}_{\text{in}})) q. \quad (5.14)$$

Making use of these notations, the weak formulation of the coupled Stokes–Darcy problem (5.1)–(5.7) reads:

Find  $\underline{u} = (\mathbf{u}_0^{\text{ff}}, p^{\text{pm}}) \in W$  and  $p^{\text{ff}} \in Q_{\text{ff}}$  such that

$$\mathcal{A}(\underline{u}, \underline{w}) + \mathcal{B}(\underline{w}, p^{\text{ff}}) = \mathcal{F}(\underline{w}) \quad \text{for all } \underline{w} = (\mathbf{w}, \psi) \in W, \quad (5.15)$$

$$\mathcal{B}(\underline{u}, q) = \mathcal{G}(q) \quad \text{for all } q \in Q_{\text{ff}}. \quad (5.16)$$

## 5.2 Well-posedness

In this section, we prove the well-posedness of the coupled Stokes–Darcy problem (5.15)–(5.16) with the generalized interface conditions for isotropic porous media having permeability  $\mathbf{K} = k\mathbf{I}$  with  $k > 0$  constant. This leads to the boundary layer constants  $N_s^{\text{bl}} = 0$  and  $M_1^{2,\text{bl}} = 0$  (see Section 3.2.3). Since the porous-medium domain is periodic the dimensional permeability has the form  $k = \ell^2 \tilde{k}$  as in (3.101) where the dimensionless quantity  $\tilde{k}$  is given by (2.79). We consider the straight interface  $\Sigma$  to be horizontal resulting in  $\boldsymbol{\tau} = \mathbf{e}_1$  and  $\mathbf{n} = \mathbf{e}_2$  as schematically presented in Figure 5.1. The case of a vertical fluid–porous interface can be treated in an analogous way. Under these geometrical assumptions, the bilinear form  $\mathcal{A}(\underline{\mathbf{u}}, \underline{\mathbf{w}})$  in (5.15) given by (5.12) reduces to

$$\begin{aligned} \mathcal{A}(\underline{\mathbf{u}}, \underline{\mathbf{w}}) &= \int_{\Omega_{\text{ff}}} \mu \nabla \mathbf{v}_0^{\text{ff}} : \nabla \mathbf{w} + \int_{\Omega_{\text{pm}}} (\mu^{-1} k \nabla p^{\text{pm}}) \cdot \nabla \psi \\ &\quad - \int_{\Sigma} p^{\text{pm}} (\mathbf{w} \cdot \mathbf{n}) + \int_{\Sigma} (\mathbf{v}_0^{\text{ff}} \cdot \mathbf{n}) \psi \\ &\quad - \int_{\Sigma} \mu \ell^{-1} (N_1^{\text{bl}})^{-1} (\mathbf{v}_0^{\text{ff}} \cdot \boldsymbol{\tau}) (\mathbf{w} \cdot \boldsymbol{\tau}) \\ &\quad + \int_{\Sigma} \ell (N_1^{\text{bl}})^{-1} \left( M_1^{1,\text{bl}} \frac{\partial p^{\text{pm}}}{\partial x_1} \right) (\mathbf{w} \cdot \boldsymbol{\tau}) . \end{aligned} \quad (5.17)$$

The first three integrals over  $\Sigma$  in the bilinear form  $\mathcal{A}$  in (5.17) are understood as scalar products in  $H_{00}^{1/2}(\Sigma)$  since  $\mathbf{v}_0^{\text{ff}}, \mathbf{w} \in \mathbf{H}_{\text{ff}}$  and  $p^{\text{pm}}, \psi \in \mathbf{H}_{\text{pm}}$  have well-defined traces on  $\Sigma$ . However, this is a priori not the case for the gradient of the porous-medium pressure  $\nabla p^{\text{pm}} \in L^2(\Omega_{\text{pm}})^2$  whose tangential component  $\partial p^{\text{pm}} / \partial x_1$  appears in the last term in formula (5.17). Before proving the well-posedness of the coupled Stokes–Darcy problem with the generalized interface conditions (5.3)–(5.5) in Theorem 5.1, we provide auxiliary results that are required for the definition of the integral over  $\Sigma$  involving the term  $\partial p^{\text{pm}} / \partial x_1$ .

### 5.2.1 Auxiliary results

Without further argumentation or additional regularity of the porous-medium pressure  $p^{\text{pm}}$ , we have  $\nabla p^{\text{pm}} \in L^2(\Omega_{\text{pm}})^2$ , thus,  $\nabla p^{\text{pm}}$  has no well-defined trace on the fluid–porous interface  $\Sigma$ . Therefore, the definition of the last term in (5.17) including the gradient of the porous-medium pressure  $(\nabla p^{\text{pm}} \cdot \boldsymbol{\tau})|_{\Sigma} = (\partial p^{\text{pm}} / \partial x_1)|_{\Sigma}$  needs to be discussed. In the following, we investigate this integral term and show that it should be understood as a duality pairing between the trace space  $H_{00}^{1/2}(\Sigma)$  and its dual space  $(H_{00}^{1/2}(\Sigma))'$ .

Since we consider two space dimensions the curl of a scalar function  $\varphi \in H^1(\Omega_{\text{pm}})$  is obtained by rotating its gradient and changing the sign as follows

$$\mathbf{curl} \varphi = \left( \frac{\partial \varphi}{\partial x_2}, -\frac{\partial \varphi}{\partial x_1} \right)^{\top}.$$

For any  $\varphi \in H^1(\Omega_{\text{pm}})$  it is  $\nabla \varphi \in L^2(\Omega_{\text{pm}})^2$  and, thus, we get  $\mathbf{curl} \varphi \in L^2(\Omega_{\text{pm}})^2$ . Further, we have  $\nabla \cdot (\mathbf{curl} \varphi) = 0$  that yields

$$\mathbf{curl} \varphi \in H(\text{div}; \Omega_{\text{pm}})^2 := \{\mathbf{u} \in L^2(\Omega_{\text{pm}})^2 : \nabla \cdot \mathbf{u} \in L^2(\Omega_{\text{pm}})\}.$$

From classical trace results in  $H(\text{div}; \Omega_{\text{pm}})^2$ , see e.g., [154, Lemma 20.2] and [45, Chapter IX, Theorem 1], we know that there exists a positive constant  $C > 0$  such that

$$\begin{aligned} \|\mathbf{curl} \varphi \cdot \mathbf{n}^{\text{pm}}\|_{H^{-1/2}(\partial\Omega_{\text{pm}})} &\leq C \|\mathbf{curl} \varphi\|_{H(\text{div}; \Omega_{\text{pm}})^2} \\ &= C \|\mathbf{curl} \varphi\|_{L^2(\Omega_{\text{pm}})^2} \\ &= C \|\nabla \varphi\|_{L^2(\Omega_{\text{pm}})^2} \leq C \|\varphi\|_{H^1(\Omega_{\text{pm}})}. \end{aligned} \quad (5.18)$$

Due to the fact that  $\Sigma \subsetneq \partial\Omega_{\text{pm}}$ , by definition it is  $H^{-1/2}(\partial\Omega_{\text{pm}}) \subset (H_{00}^{1/2}(\Sigma))'$ .

Therefore, we have  $(\mathbf{curl} \varphi \cdot \mathbf{n})|_{\Sigma} \in (H_{00}^{1/2}(\Sigma))'$  and it holds

$$\|(\mathbf{curl} \varphi \cdot \mathbf{n})|_{\Sigma}\|_{(H_{00}^{1/2}(\Sigma))'} \leq \|\mathbf{curl} \varphi \cdot \mathbf{n}^{\text{pm}}\|_{H^{-1/2}(\partial\Omega_{\text{pm}})}. \quad (5.19)$$

Furthermore, we obviously have  $\nabla\varphi \cdot \boldsymbol{\tau} = -\mathbf{curl} \varphi \cdot \mathbf{n}$  on  $\Sigma$ , and considering inequalities (5.18) and (5.19) we conclude that there exists a constant  $C_{\text{tr},\boldsymbol{\tau}} > 0$  such that

$$\|(\nabla\varphi \cdot \boldsymbol{\tau})|_{\Sigma}\|_{(H_{00}^{1/2}(\Sigma))'} \leq C_{\text{tr},\boldsymbol{\tau}}\|\varphi\|_{H^1(\Omega_{\text{pm}})} \quad \text{for all } \varphi \in H^1(\Omega_{\text{pm}}). \quad (5.20)$$

Since we have

$$\nabla p^{\text{pm}} \cdot \boldsymbol{\tau} = \frac{\partial p^{\text{pm}}}{\partial x_1} \quad \text{on } \Sigma,$$

for the considered geometrical setting (Figure 5.1) the last integral in (5.17) should be interpreted as the duality pairing

$$\begin{aligned} & \int_{\Sigma} \ell(N_1^{\text{bl}})^{-1} \left( M_1^{1,\text{bl}} \frac{\partial p^{\text{pm}}}{\partial x_1} \right) (\mathbf{w} \cdot \boldsymbol{\tau}) \\ &= \int_{\Sigma} \ell \frac{M_1^{1,\text{bl}}}{N_1^{\text{bl}}} (\nabla p^{\text{pm}} \cdot \boldsymbol{\tau}) (\mathbf{w} \cdot \boldsymbol{\tau}) \\ &:= \ell \frac{M_1^{1,\text{bl}}}{N_1^{\text{bl}}} \langle \nabla p^{\text{pm}} \cdot \boldsymbol{\tau}, \mathbf{w} \cdot \boldsymbol{\tau} \rangle_{(H_{00}^{1/2}(\Sigma))', H_{00}^{1/2}(\Sigma)}. \end{aligned} \quad (5.21)$$

### 5.2.2 Well-posedness of the coupled problem

After having defined the integral over  $\Sigma$  involving  $\partial p^{\text{pm}}/\partial x_1$  in (5.17) by (5.21), we prove the well-posedness of the weak formulation (5.15)–(5.16) corresponding to the Stokes–Darcy problem with the generalized coupling conditions.

**Theorem 5.1 (Well-posedness):** *For homogeneous isotropic porous media with dimensionless permeability  $\tilde{k} > 0$ , the Stokes–Darcy problem given by (5.15)–(5.16) is well-posed under the following assumption*

$$\tilde{k} > \kappa_{\text{pm}} \kappa_{\text{ff}} (C_{\text{tr},\tau} C_{\text{tr},\text{ff}})^2 \left( \frac{M_1^{1,\text{bl}}}{2N_1^{\text{bl}}} \right)^2. \quad (5.22)$$

Here,  $\kappa_i = 1 + C_i^2$ , where  $C_i$  denotes the constant appearing in the Poincaré inequality (A2.1) for  $i \in \{\text{ff}, \text{pm}\}$ , and  $C_{\text{tr},\tau}, C_{\text{tr},\text{ff}} > 0$  are positive constants coming from the trace inequalities (5.20) and (A2.6) in the Appendix A.2.

*Proof.* For the proof we use the classical Babuška–Brezzi theory for the well-posedness of saddle-point problems [24]. The continuity of the linear functionals  $\mathcal{F}$  and  $\mathcal{G}$  in (5.14) is straightforward as well as the continuity and coercivity of the bilinear form  $\mathcal{B}$  presented in (5.13). Thus, it remains to prove the continuity and coercivity of the bilinear form  $\mathcal{A}$  given by (5.17). In the following, we first address the continuity of  $\mathcal{A}$  and show that there exists a constant  $C > 0$  such that

$$|\mathcal{A}(\underline{u}, \underline{w})| \leq C \|\underline{u}\|_W \|\underline{w}\|_W \quad \text{for all } \underline{u}, \underline{w} \in W.$$

Second, we prove the coercivity of  $\mathcal{A}$ , i.e., we show that there exists a constant  $c > 0$  such that

$$\mathcal{A}(\underline{u}, \underline{u}) \geq c \|\underline{u}\|_W^2 \quad \text{for all } \underline{u} \in W.$$

For proving continuity of the bilinear form  $\mathcal{A}$  we use the Cauchy–Schwarz inequality (A2.5), the Poincaré inequality (A2.1), trace inequalities (A2.6),

(A2.7), (5.20), and definition (5.21). Hence, we get

$$\begin{aligned}
 |\mathcal{A}(\underline{u}, \underline{w})| &= \left| \int_{\Omega_{\text{ff}}} \mu \nabla \mathbf{v}_0^{\text{ff}} : \nabla \mathbf{w} + \int_{\Omega_{\text{pm}}} (\mu^{-1} k \nabla p^{\text{pm}}) \cdot \nabla \psi \right. \\
 &\quad - \int_{\Sigma} p^{\text{pm}} (\mathbf{w} \cdot \mathbf{n}) + \int_{\Sigma} (\mathbf{v}_0^{\text{ff}} \cdot \mathbf{n}) \psi \\
 &\quad - \int_{\Sigma} \mu \ell^{-1} (N_1^{\text{bl}})^{-1} (\mathbf{v}_0^{\text{ff}} \cdot \boldsymbol{\tau}) (\mathbf{w} \cdot \boldsymbol{\tau}) \\
 &\quad \left. + \int_{\Sigma} \ell (N_1^{\text{bl}})^{-1} \left( M_1^{1,\text{bl}} \frac{\partial p^{\text{pm}}}{\partial x_1} \right) (\mathbf{w} \cdot \boldsymbol{\tau}) \right| \\
 &\leq \mu \|\mathbf{v}_0^{\text{ff}}\|_{H^1(\Omega_{\text{ff}})^2} \|\mathbf{w}\|_{H^1(\Omega_{\text{ff}})^2} + \mu^{-1} k \|p^{\text{pm}}\|_{H^1(\Omega_{\text{pm}})} \|\psi\|_{H^1(\Omega_{\text{pm}})} \\
 &\quad + C_{\text{tr,ff}} C_{\text{tr,pm}} \|p^{\text{pm}}\|_{H^1(\Omega_{\text{pm}})} \|\mathbf{w}\|_{H^1(\Omega_{\text{ff}})^2} \\
 &\quad + C_{\text{tr,ff}} C_{\text{tr,pm}} \|\mathbf{v}_0^{\text{ff}}\|_{H^1(\Omega_{\text{ff}})^2} \|\psi\|_{H^1(\Omega_{\text{pm}})} \\
 &\quad + \ell C_{\text{tr},\boldsymbol{\tau}} C_{\text{tr,ff}} \left| \frac{M_1^{1,\text{bl}}}{N_1^{\text{bl}}} \right| \|p^{\text{pm}}\|_{H^1(\Omega_{\text{pm}})} \|\mathbf{w}\|_{H^1(\Omega_{\text{ff}})^2} \\
 &\quad + \mu \ell^{-1} (C_{\text{tr,ff}})^2 \frac{1}{|N_1^{\text{bl}}|} \|\mathbf{v}_0^{\text{ff}}\|_{H^1(\Omega_{\text{ff}})^2} \|\mathbf{w}\|_{H^1(\Omega_{\text{ff}})^2}, \tag{5.23}
 \end{aligned}$$

where  $C_{\text{tr,ff}}, C_{\text{tr,pm}} > 0$  are coming from the trace inequalities (A2.6) and (A2.7) provided in the Appendix A.2.

We define

$$\tilde{C} := \max \left\{ \mu^{-1} k, \mu + \mu \ell^{-1} (C_{\text{tr,ff}})^2 \frac{1}{|N_1^{\text{bl}}|}, C_{\text{tr,ff}} C_{\text{tr,pm}} + \ell C_{\text{tr},\boldsymbol{\tau}} C_{\text{tr,ff}} \left| \frac{M_1^{1,\text{bl}}}{N_1^{\text{bl}}} \right| \right\} > 0, \tag{5.24}$$

and using this definition in equation (5.23) yields

$$\begin{aligned}
 |\mathcal{A}(\underline{u}, \underline{w})| &\leq \tilde{C} \left( \|\mathbf{v}_0^{\text{ff}}\|_{H^1(\Omega_{\text{ff}})^2} + \|p^{\text{pm}}\|_{H^1(\Omega_{\text{pm}})} \right) \left( \|\mathbf{w}\|_{H^1(\Omega_{\text{ff}})^2} + \|\psi\|_{H^1(\Omega_{\text{pm}})} \right) \\
 &\leq 2\tilde{C} \|\underline{u}\|_{\mathbf{W}} \|\underline{w}\|_{\mathbf{W}}. \tag{5.25}
 \end{aligned}$$



The second inequality in (5.25) follows from  $(a + b) \leq \sqrt{2}(a^2 + b^2)^{1/2}$  for all  $a, b > 0$ . We have proven estimate (5.25), thus, bilinear form  $\mathcal{A}$  is continuous.

Now, we prove that  $\mathcal{A}$  is coercive. Taking into account the Poincaré inequality (A2.1) and the definition of the  $H^1$ -norm

$$\|u\|_{H^1(\Omega_i)} = (\|u\|_{L^2(\Omega_i)}^2 + \|\nabla u\|_{L^2(\Omega_i)^2}^2)^{1/2}$$

for  $u \in H^1(\Omega_i)$  and  $i \in \{\text{ff}, \text{pm}\}$ , we get

$$\|f\|_{H^1(\Omega_{\text{ff}})^2}^2 \leq \kappa_{\text{ff}} \|\nabla f\|_{L^2(\Omega_{\text{ff}})^4}^2, \quad \|g\|_{H^1(\Omega_{\text{pm}})}^2 \leq \kappa_{\text{pm}} \|\nabla g\|_{L^2(\Omega_{\text{pm}})^2}^2 \quad (5.26)$$

for all  $f \in H_{\text{ff}}$ ,  $g \in H_{\text{pm}}$ . Making use of inequalities (5.21), (5.26) and (A2.6), and recalling that  $N_1^{\text{bl}} < 0$  and  $M_1^{1,\text{bl}} < 0$  (see Sections 3.2.2 and 3.2.3), we obtain

$$\begin{aligned} \mathcal{A}(\underline{u}, \underline{u}) &= \int_{\Omega_{\text{ff}}} \mu \nabla \mathbf{v}_0^{\text{ff}} : \nabla \mathbf{v}_0^{\text{ff}} + \int_{\Omega_{\text{pm}}} (\mu^{-1} k \nabla p^{\text{pm}}) \cdot \nabla p^{\text{pm}} \\ &\quad - \underbrace{\int_{\Sigma} p^{\text{pm}} (\mathbf{v}_0^{\text{ff}} \cdot \mathbf{n}) + \int_{\Sigma} (\mathbf{v}_0^{\text{ff}} \cdot \mathbf{n}) p^{\text{pm}}}_{=0} \\ &\quad - \underbrace{\int_{\Sigma} \mu \ell^{-1} (N_1^{\text{bl}})^{-1} (\mathbf{v}_0^{\text{ff}} \cdot \boldsymbol{\tau})^2}_{\geq 0} + \int_{\Sigma} \ell (N_1^{\text{bl}})^{-1} \left( M_1^{1,\text{bl}} \frac{\partial p^{\text{pm}}}{\partial x_1} \right) (\mathbf{v}_0^{\text{ff}} \cdot \boldsymbol{\tau}) \\ &\geq \mu \|\nabla \mathbf{v}_0^{\text{ff}}\|_{H^1(\Omega_{\text{ff}})^2}^2 + \mu^{-1} k \|\nabla p^{\text{pm}}\|_{H^1(\Omega_{\text{pm}})}^2 \\ &\quad - \ell \frac{M_1^{1,\text{bl}}}{N_1^{\text{bl}}} \|(\nabla p^{\text{pm}} \cdot \boldsymbol{\tau})|_{\Sigma}\|_{(H_0^0)^{1/2}(\Sigma)} \|(\mathbf{v}_0^{\text{ff}} \cdot \boldsymbol{\tau})|_{\Sigma}\|_{H_0^0(\Sigma)} \\ &\geq \kappa_{\text{ff}}^{-1} \mu \|\mathbf{v}_0^{\text{ff}}\|_{H^1(\Omega_{\text{ff}})^2}^2 + \kappa_{\text{pm}}^{-1} \mu^{-1} k \|p^{\text{pm}}\|_{H^1(\Omega_{\text{pm}})}^2 \\ &\quad - \ell C_{\text{tr}, \boldsymbol{\tau}} C_{\text{tr}, \text{ff}} \frac{M_1^{1,\text{bl}}}{N_1^{\text{bl}}} \|p^{\text{pm}}\|_{H^1(\Omega_{\text{pm}})} \|\mathbf{v}_0^{\text{ff}}\|_{H^1(\Omega_{\text{ff}})^2}. \end{aligned} \quad (5.27)$$

We apply the generalized Young’s inequality (A2.3) with  $b = \|\mathbf{v}_0^{\text{ff}}\|_{H^1(\Omega_{\text{ff}})}^2$  and  $a = \ell C_{\text{tr},\tau} C_{\text{tr,ff}} M_1^{1,\text{bl}} (N_1^{\text{bl}})^{-1} \|p^{\text{pm}}\|_{H^1(\Omega_{\text{pm}})}$  to the last term in (5.27). This yields

$$\begin{aligned} \mathcal{A}(\underline{u}, \underline{u}) &\geq \kappa_{\text{ff}}^{-1} \mu \|\mathbf{v}_0^{\text{ff}}\|_{H^1(\Omega_{\text{ff}})}^2 + \kappa_{\text{pm}}^{-1} \mu^{-1} k \|p^{\text{pm}}\|_{H^1(\Omega_{\text{pm}})}^2 \\ &\quad - \frac{\left(\ell C_{\text{tr},\tau} C_{\text{tr,ff}} M_1^{1,\text{bl}} (N_1^{\text{bl}})^{-1}\right)^2}{2\delta} \|p^{\text{pm}}\|_{H^1(\Omega_{\text{pm}})}^2 - \frac{\delta}{2} \|\mathbf{v}_0^{\text{ff}}\|_{H^1(\Omega_{\text{ff}})}^2 \\ &= \left(\kappa_{\text{ff}}^{-1} \mu - \frac{\delta}{2}\right) \|\mathbf{v}_0^{\text{ff}}\|_{H^1(\Omega_{\text{ff}})}^2 \\ &\quad + \left(\kappa_{\text{pm}}^{-1} \mu^{-1} k - \frac{\left(\ell C_{\text{tr},\tau} C_{\text{tr,ff}} M_1^{1,\text{bl}} (N_1^{\text{bl}})^{-1}\right)^2}{2\delta}\right) \|p^{\text{pm}}\|_{H^1(\Omega_{\text{pm}})}^2. \end{aligned}$$

Rewriting the dimensional permeability  $k$  in terms of the nondimensional quantity  $\tilde{k}$ , namely  $k = \ell^2 \tilde{k}$ , we conclude that coercivity of the bilinear form  $\mathcal{A}$  is guaranteed when the following conditions hold true

$$\delta < 2\kappa_{\text{ff}}^{-1} \mu, \quad \kappa_{\text{pm}}^{-1} \mu^{-1} \tilde{k} - \frac{\left(C_{\text{tr},\tau} C_{\text{tr,ff}} M_1^{1,\text{bl}} (N_1^{\text{bl}})^{-1}\right)^2}{2\delta} > 0. \quad (5.28)$$

Combining both inequalities in (5.28) we obtain condition (5.22). Thus, we have proven that  $\mathcal{A}$  is coercive under the assumption (5.22) on the dimensionless permeability  $\tilde{k}$ .  $\square$

Theorem 5.1 states that in case of isotropic porous media the Stokes–Darcy problem with the generalized interface conditions is well-posed if condition (5.22) is fulfilled. This assumption poses a constraint on the nondimensional permeability  $\tilde{k}$  being greater than the ratio of boundary layer constants  $(M_1^{1,\text{bl}}/N_1^{\text{bl}})^2$  multiplied by the constants  $\kappa_{\text{ff}}, \kappa_{\text{pm}}, C_{\text{tr},\tau}$  and  $C_{\text{tr,ff}}$  coming from the inequalities (5.26), (A2.6) and (5.20), respectively. The permeability  $\tilde{k}$  as well as the boundary layer constants  $N_1^{\text{bl}}$  and  $M_1^{1,\text{bl}}$  are computed numerically based on the geometrical configuration of the coupled free-flow and porous-medium system. The constants

$\kappa_{\text{pm}} > 1$  and  $\kappa_{\text{ff}} > 1$  appearing in condition (5.22) depend on the size and geometry of the coupled flow domain [23, 124]. However, to the best of our knowledge, for the constants  $C_{\text{tr},\tau}, C_{\text{tr,ff}} > 0$  coming from the trace inequalities (A2.6) and (5.20), respectively, there exist no estimates. However, in the following section, we demonstrate that the theoretically obtained assumption (5.22) is reasonable and not restrictive for many applications.

**Remark 5.2:** *Note that the permeability  $\tilde{k}$  appearing in (5.22) is dimensionless and depends on the pore geometry within the unit cell  $Y$  only. In particular, assumption (5.22) does not imply that the dimensional permeability  $k = \ell^2 \tilde{k}$  cannot become small.*

## 5.3 Numerical study of theoretical result

In this section, we analyze the validity of condition (5.22) that guarantees well-posedness of the coupled Stokes–Darcy problem with the generalized interface conditions. For the sake of clarity, we reformulate (5.22) as follows

$$\tilde{k} > C_{\kappa,\text{tr}} R^2, \quad (5.29)$$

where  $C_{\kappa,\text{tr}} := \kappa_{\text{pm}} \kappa_{\text{ff}} (C_{\text{tr},\tau} C_{\text{tr,ff}})^2$  and  $R := M_1^{1,\text{bl}} / (2N_1^{\text{bl}})$ . We consider five different geometrical configurations of the coupled flow system, compute  $\tilde{k}$  and  $R$ , and evaluate the resulting restriction on constant  $C_{\kappa,\text{tr}}$ . The computations of all effective coefficients are performed using `FREEFEM++` [86] as described in Section 4.3.

Let us first present the geometrical settings to be studied within this section that only differ in the shape and size of solid obstacles inside the porous domain. We consider homogeneous isotropic porous media, which are constructed by the periodic repetition of the scaled unit cell  $Y^\ell = (0, \ell)^2$ . Such porous structures are fully determined by the characteristic pore size  $\ell$  and the geometry of the solid part  $Y_s$  within the unit cell  $Y$ . Since

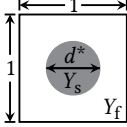
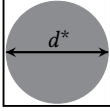
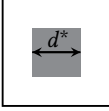
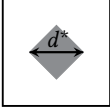
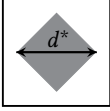
	$G_1$	$G_2$	$G_3$	$G_4$	$G_5$
$Y$					
$d^*$	0.5	0.95	0.4308	0.5	0.7
$\tilde{k}$	1.99e-2	5.59e-5	1.99e-2	2.66e-2	8.64e-3
$R^2$	8.25e-4	5.68e-4	1.66e-4	1.55e-3	1.47e-3

Table 5.1: Size  $d^*$  of the solid grains, permeability  $\tilde{k}$  and squared ratio  $R^2$  for different porous-medium configurations.

the computable parameters  $\tilde{k}$  and  $R$  appearing in (5.29) are independent of the pore size  $\ell$ , it is sufficient to provide the geometrical information for the five considered porous-medium geometries according to the unit cell  $Y$  (Table 5.1).

Now, we focus on the three constants  $\tilde{k}$ ,  $R$  and  $C_{\kappa, \text{tr}}$  appearing in condition (5.29). The nondimensional permeability  $\tilde{k}$  is computed based on the pore geometry within the unit cell  $Y$  by means of homogenization using formula (2.79). We emphasize here that  $\tilde{k}$  is independent of the sharp interface position. The obtained permeability values  $\tilde{k}$  for the considered geometries are presented in Table 5.1. The ratio  $R$  includes the boundary layer constants  $N_1^{\text{bl}}$  and  $M_1^{1, \text{bl}}$  that are computed by solving the cut-off boundary layer problems (4.21)–(4.23) and (4.24)–(4.26) and integrating their solutions afterwards using formulas (4.28) and (4.29), as explained in Section 4.3. Note that we waive the superscripts  $k, m$  and  $a$  for the boundary layer constants here, due to clarity, and we give the information concerning the computational boundary layer stripe in the next paragraph. In Section 4.3, we also showed that constants  $N_1^{\text{bl}}$  and  $M_1^{1, \text{bl}}$  include information about the exact location of the fluid–porous interface. Thus, a change of the interface position leads to the corresponding change of the boundary layer constants and, consequently, also to a change of  $R$ . As mentioned above, constant  $C_{\kappa, \text{tr}}$  in condition (5.29), which contains

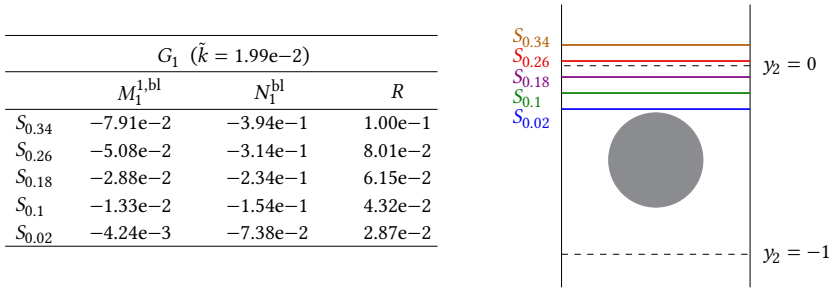
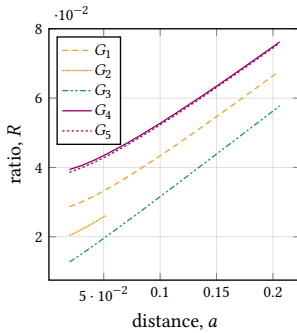


Figure 5.2: Boundary layer constants  $M_1^{bl}$ ,  $N_1^{bl}$  and ratio  $R$  for five interface locations (left) and illustration of these interface locations (right) for geometry  $G_1$ .

$C_{tr,\tau}$  and  $C_{tr,ff}$  coming from the trace inequalities (A2.6) and (5.20), cannot be estimated to the best of the authors' knowledge. Nevertheless, in the following, we show that there is a nontrivial validity range for constant  $C_{\kappa,tr}$  such that condition (5.29) or, equivalently, (5.22) is fulfilled. For this purpose, we minimize the ratio  $R$  of boundary layer constants in (5.29) by an appropriate choice of the fluid–porous interface location.

For the computation of boundary layer constants we use the cut-off boundary layer stripe  $Z_{4,4}$  comprising 4 solid inclusions in the porous part (see Section 4.3). We consider different vertical positions of the interface  $S_a = (0, 1) \times \{\frac{d^* - 1}{2} + a\}$  defined in Section 3.2.2, where  $a \geq 0$  denotes the distance between  $S_a$  and the top of the first row of solid inclusions. For geometry  $G_1$ , five different sharp interface locations are schematically presented in Figure 5.2 (right). The corresponding values of the boundary layer constants  $N_1^{bl}$  and  $M_1^{1,bl}$  as well as the ratio  $R$  are provided in Figure 5.2 (left). We observe that  $R$  monotonically decreases as the interface approaches the top of the solid inclusions, i.e.,  $R$  becomes smaller for  $a \rightarrow 0$  (see also Figure 5.3, left). This correlation between the ratio  $R$  and the interface position  $S_a$  does also hold for other geometrical configurations. For the porous-medium geometries presented in Table 5.1 except for  $G_2$  we consider 30 equidistantly distributed interface locations  $S_a$ . Based



	Interface location $S_{0,02}$		
	$M_1^{1,bl}$	$N_1^{bl}$	$R$
$G_1$	$-4.24e-3$	$-7.38e-2$	$2.87e-2$
$G_2$	$-2.95e-3$	$-6.19e-2$	$2.38e-2$
$G_3$	$-1.12e-3$	$-4.35e-2$	$1.29e-2$
$G_4$	$-7.74e-3$	$-9.84e-2$	$3.93e-2$
$G_5$	$-7.56e-3$	$-9.85e-2$	$3.84e-2$

Figure 5.3: Ratio  $R$  for geometries  $G_1$  to  $G_5$  computed for different interface locations at distance  $a$  from the top of solid obstacles (left). Boundary layer constants  $N_1^{bl}$ ,  $M_1^{1,bl}$  and ratio  $R$  computed for interface  $S_{0,02}$  (right).

on each location we compute the boundary layer constants and obtain the ratio  $R$ . For geometry  $G_2$  a smaller range of  $a$  has been used due to the bigger size of the solid grain. In Figure 5.3 (left), we plot the ratio  $R$  for the porous-medium geometries  $G_1$  to  $G_5$  shown in Table 5.1 versus the distance  $a$ . Based on these results, we position the interface as close as possible to the top of solid inclusions in order to make condition (5.29) or (5.22), respectively, least restrictive. Since restrictions on the meshing in FREEFEM++ do not allow us to locate the interface directly on the top of the first row of solid inclusions, we consider the fluid–porous interface slightly above the solid obstacles taking  $a = 0.02$  for the computation of the boundary layer constants. We provide the computed values  $N_1^{bl}$  and  $M_1^{1,bl}$  as well as the ratio  $R$  in Figure 5.3 (right).

For the ease of analysis of condition (5.29), we present the squared ratio  $R^2$  for the interface location  $S_{0,02}$  next to the nondimensional permeability  $\tilde{k}$  in Table 5.1. For the porous-medium geometries  $G_1$  and  $G_3$ , we have  $\tilde{k} \gg R^2$ . In this case, the constant  $C_{\kappa, tr}$  appearing in condition (5.29) can be of order  $10^2$ , that is not restrictive. For the geometrical configurations  $G_4$  and  $G_5$  we get  $\tilde{k} > R^2$  and the constant  $C_{\kappa, tr}$  can be at most of the

order 10. This is a very mild restriction. However, for geometry  $G_2$  we obtain  $\tilde{k} < R^2$ , that requires  $C_{\kappa, \text{tr}} < 1$  making condition (5.22) a stronger constraint.

**Remark 5.3:** *For orthotropic porous media, i.e.,  $\mathbf{K} = \text{diag}(k_{11}, k_{22})$  and  $N_s^{\text{bl}} = M_1^{2, \text{bl}} = 0$ , the well-posedness of the Stokes–Darcy problem with the generalized interface conditions can be proven in an analogous way to Theorem 5.1. In this case, we obtain a unique solution to problem (5.15)–(5.16) if the following assumption is fulfilled*

$$\tilde{k}_{\min} > CR^2, \quad \tilde{k}_{\min} = \min\{\tilde{k}_{11}, \tilde{k}_{22}\} > 0.$$

**Remark 5.4:** *For anisotropic porous media, all boundary layer constants appearing in the generalized interface conditions (5.3)–(5.5) are nonzero. Therefore, all integral terms in the general expression (5.12) of the bilinear form  $\mathcal{A}$  are present. The additional integral terms in (5.12) in comparison to (5.17), that are nonzero only for anisotropic media, make proving the coercivity of  $\mathcal{A}$  even more challenging than in the isotropic case, where  $\mathcal{A}$  is given by (5.17). The proof of well-posedness of the Stokes–Darcy problem (5.15)–(5.16) for anisotropic porous media is beyond the scope of this thesis and will be addressed in the future.*

## Summary

In this chapter, we derived the weak formulation of the Stokes–Darcy problem with the generalized coupling conditions. We proved the well-posedness of the coupled problem for isotropic porous media under a relationship between the nondimensional permeability and the boundary layer constants appearing in the interface conditions. The theoretically obtained assumption, which guarantees the existence and uniqueness of a weak solution to the Stokes–Darcy problem, is analyzed numerically for several geometrical configurations of the porous domain. We showed

that the assumption is reasonable and not too restrictive for a wide range of porous-medium geometries.



# **6 Model validation**



# Model validation

# 6

The content of this chapter is based on the following original articles and preprints:

- [EE3] E. Eggenweiler and I. Rybak. *Unsuitability of the Beavers–Joseph interface condition for filtration problems*. J. Fluid Mech. 892 (2020), A10, 19. DOI: 10.1017/jfm.2020.194
- [EE4] E. Eggenweiler and I. Rybak. *Effective coupling conditions for arbitrary flows in Stokes–Darcy systems*. Multiscale Model. Simul. 19.2 (2021), pp. 731–757. DOI: 10.1137/20M1346638
- [EE5] F. Mohammadi, E. Eggenweiler, B. Flemisch, S. Oladyshkin, I. Rybak, M. Schneider, and K. Weishaupt. *A surrogate-assisted uncertainty-aware Bayesian validation framework and its application to coupling free flow and porous-medium flow*. Comput. Geosci. (in review). 2022. <https://arxiv.org/abs/2106.13639>

- [EE6] I. Rybak, C. Schwarzmeier, E. Eggenweiler, and R. Rde. *Validation and calibration of coupled porous-medium and free-flow problems using pore-scale resolved models*. Comput. Geosci. 25.2 (2021), pp. 621–635. DOI: 10.1007/s10596-020-09994-x
- [EE7] P. Strohbeck, E. Eggenweiler, and I. Rybak. *A modification of the Beavers–Joseph condition for arbitrary flows to the fluid–porous interface*. Transp. Porous Media (in review). 2022. <https://arxiv.org/abs/2106.15556>

As already stated in Chapter 1, the appropriate choice of interface conditions and the correct determination of effective model parameters for the Stokes–Darcy problem is crucial for accurate numerical simulations of applications. In this chapter, we validate and calibrate the coupled problem with different sets of coupling conditions and analyze the applicability of the considered coupling concepts to various flow directions to the porous bed. For this purpose we compare the solutions of pore-scale resolved models, which serve as reference solutions, to macroscale numerical simulation results. First, we study the Stokes–Darcy problem with the classical interface conditions for unidirectional flows to the porous layer and show its validity in this case (Section 6.1). Second, we demonstrate that the Beavers–Joseph coupling condition and also its simplification by Saffman are unsuitable for general filtration problems with arbitrary flow direction to the interface (Section 6.2). Third, we validate the Stokes–Darcy problem with the generalized interface conditions derived in Chapter 3 and highlight the advantages of the new coupling conditions over the classical ones (Section 6.3).

Below, we summarize the flow models with that we are dealing in this chapter. For all numerical validation cases we work with the dimensionless form of the flow equations. This is reasonable since we study coupled flow problems for the validation of mathematical models, and we

do not simulate real world applications, where the dimensions of physical quantities play a crucial role. Furthermore, we consider porous media constructed by the periodic repetition of the scaled unit cell  $\varepsilon Y = (0, \varepsilon)^2$  as explained in Section 2.3.2 such that permeability and boundary layer constants can be computed via homogenization as described in Section 4.3. The flow region at the pore scale is indicated by  $\Omega^\varepsilon = \Omega_{\text{ff}} \cup \Omega_{\text{pm}}^\varepsilon$  and the macroscopic flow domain is denoted by  $\Omega = \Omega_{\text{ff}} \cup \Omega_{\text{pm}}$  as in Sections 2.3 and 3.1.

### Pore-scale model

The flow at the pore scale is described by the Stokes system (2.42)–(2.44) which reads

$$-\Delta \mathbf{v}^\varepsilon + \nabla p^\varepsilon = \mathbf{0}, \quad \nabla \cdot \mathbf{v}^\varepsilon = 0 \quad \text{in } \Omega^\varepsilon, \quad (6.1)$$

$$\mathbf{v}^\varepsilon = \mathbf{0} \quad \text{on } \partial\Omega^\varepsilon \setminus \partial\Omega, \quad \mathbf{v}^\varepsilon = \bar{\mathbf{v}} \quad \text{on } \Gamma_D, \quad \mathbf{T}(\mathbf{v}^\varepsilon, p^\varepsilon)\mathbf{n} = \bar{\mathbf{h}} \quad \text{on } \Gamma_N. \quad (6.2)$$

Here,  $\bar{\mathbf{v}}$  and  $\bar{\mathbf{h}}$  are prescribed velocity and normal stress on  $\partial\Omega = \Gamma_D \cup \Gamma_N$ , where the subscripts  $D$  and  $N$  denote the parts of the boundary where Dirichlet respective Neumann boundary conditions are applied. Additionally, if different Dirichlet or Neumann boundary values are specified on different parts of  $\Gamma_D$  and  $\Gamma_N$ , respectively, we label the corresponding parts of the boundary using superscripts. For example, we define  $\Gamma_D^{\text{wall}}$  as the external boundary where the Dirichlet condition  $\bar{\mathbf{v}} = \mathbf{0}$  is set. The solution to the pore-scale problem (6.1)–(6.2) serves as a reference solution in order to validate the corresponding coupled Stokes–Darcy model.

### Macroscale Stokes–Darcy models

The flow behavior at the macroscale is modeled by the Stokes–Darcy problem (2.96)–(2.97):

$$-\Delta \mathbf{v}^{\text{ff}} + \nabla p^{\text{ff}} = \mathbf{0}, \quad \nabla \cdot \mathbf{v}^{\text{ff}} = 0 \quad \text{in } \Omega^{\text{ff}}, \quad (6.3)$$

$$-\nabla \cdot (\tilde{\mathbf{K}} \nabla p^{\text{pm}}) = 0 \quad \text{in } \Omega^{\text{pm}}, \quad (6.4)$$

where the dimensionless permeability tensor  $\tilde{\mathbf{K}}$  is computed using formula (2.79). On the external boundary of the coupled flow domain  $\partial\Omega = \Gamma_{\text{ff},D} \cup \Gamma_{\text{ff},N} \cup \Gamma_{\text{pm},D} \cup \Gamma_{\text{pm},N}$  the following conditions are set

$$\mathbf{v}^{\text{ff}} = \bar{\mathbf{v}} \quad \text{on } \Gamma_{\text{ff},D}, \quad \mathbf{T}(\mathbf{v}^{\text{ff}}, p^{\text{ff}})\mathbf{n} = \bar{\mathbf{h}} \quad \text{on } \Gamma_{\text{ff},N}, \quad (6.5)$$

$$p^{\text{pm}} = \bar{p} \quad \text{on } \Gamma_{\text{pm},D}, \quad \mathbf{v}^{\text{pm}} \cdot \mathbf{n} = \bar{\mathbf{v}} \quad \text{on } \Gamma_{\text{pm},N}. \quad (6.6)$$

Additionally, a set of coupling conditions on the fluid–porous interface  $\Sigma$  has to be applied. In this chapter, we consider two different coupling concepts for the Stokes–Darcy problem, namely the classical interface conditions and the generalized coupling conditions. For all validation cases, the fluid–porous interface  $\Sigma$  is assumed to be horizontal and the unit tangential respective unit normal vector is taken  $\mathbf{n} = \mathbf{e}_2$  respective  $\boldsymbol{\tau} = \mathbf{e}_1$ .

The classical set of coupling conditions (2.17)–(2.19) in dimensionless form is given by

$$\mathbf{v}^{\text{ff}} \cdot \mathbf{n} = \mathbf{v}^{\text{pm}} \cdot \mathbf{n} \quad \text{on } \Sigma, \quad (6.7)$$

$$p^{\text{pm}} = -\mathbf{n} \cdot \mathbf{T}(\mathbf{v}^{\text{ff}}, p^{\text{ff}})\mathbf{n} \quad \text{on } \Sigma, \quad (6.8)$$

$$(\mathbf{v}^{\text{ff}} - \mathbf{v}^{\text{pm}}) \cdot \boldsymbol{\tau} = \frac{\varepsilon \sqrt{\tilde{\mathbf{K}}}}{\alpha_{\text{BJ}}} \boldsymbol{\tau} \cdot \nabla \mathbf{v}^{\text{ff}} \mathbf{n} \quad \text{on } \Sigma, \quad (6.9)$$

where  $\alpha_{\text{BJ}} > 0$  is the dimensionless Beavers–Joseph slip coefficient. Instead of condition (6.9) originally proposed by Beavers and Joseph [15] we also consider the following variations of it: the symmetrized version (2.22) of the Beavers–Joseph condition with the rate of strain tensor  $\mathbf{D}(\mathbf{v}^{\text{ff}}) = \frac{1}{2}(\nabla \mathbf{v}^{\text{ff}} + (\nabla \mathbf{v}^{\text{ff}})^\top)$  instead of the velocity gradient  $\nabla \mathbf{v}^{\text{ff}}$  reading

$$(\mathbf{v}^{\text{ff}} - \mathbf{v}^{\text{pm}}) \cdot \boldsymbol{\tau} = \frac{2\varepsilon \sqrt{\tilde{\mathbf{K}}}}{\alpha_{\text{BJ}}} \boldsymbol{\tau} \cdot \mathbf{D}(\mathbf{v}^{\text{ff}})\mathbf{n} \quad \text{on } \Sigma, \quad (6.10)$$

and the Beavers–Joseph–Saffman–Jones condition (2.21), where the porous-medium velocity on the interface is neglected, given by the following formula

$$\mathbf{v}^{\text{ff}} \cdot \boldsymbol{\tau} = \frac{2\varepsilon \sqrt{\tilde{K}}}{\alpha_{\text{BJ}}} \boldsymbol{\tau} \cdot \mathbf{D}(\mathbf{v}^{\text{ff}}) \mathbf{n} \quad \text{on } \Sigma. \quad (6.11)$$

We remind that we take  $\sqrt{\tilde{K}} = \sqrt{\boldsymbol{\tau} \tilde{\mathbf{K}} \boldsymbol{\tau}}$  appearing in conditions (6.9)–(6.11) as it is done in, e.g., [EE4, 107, 141, 165]. Choosing another interpretation of  $\sqrt{\tilde{K}}$  results in an appropriate adjustment of the Beavers–Joseph parameter  $\alpha_{\text{BJ}}$  (see Section 6.1.1, geometry  $G_4$ ).

In addition to the classical coupling concept comprising (6.7), (6.8) and one of the conditions (6.9)–(6.11), we study the validity of the generalized interface conditions (3.95)–(3.97) derived in Chapter 3 for the Stokes–Darcy coupling. These conditions read

$$\mathbf{v}^{\text{ff}} \cdot \mathbf{n} = \mathbf{v}^{\text{pm}} \cdot \mathbf{n} \quad \text{on } \Sigma, \quad (6.12)$$

$$p^{\text{pm}} = -\mathbf{n} \cdot \mathbf{T}(\mathbf{v}^{\text{ff}}, p^{\text{ff}}) \mathbf{n} + N_s^{\text{bl}} \boldsymbol{\tau} \cdot \mathbf{T}(\mathbf{v}^{\text{ff}}, p^{\text{ff}}) \mathbf{n} \quad \text{on } \Sigma, \quad (6.13)$$

$$(\mathbf{v}^{\text{ff}} + \varepsilon^2 \tilde{\mathbf{K}}^{\text{int}} \nabla p^{\text{pm}}) \cdot \boldsymbol{\tau} = -(\varepsilon \mathbf{N}^{\text{bl}} \cdot \boldsymbol{\tau}) (\boldsymbol{\tau} \cdot \nabla \mathbf{v}^{\text{ff}} \mathbf{n}) \quad \text{on } \Sigma, \quad (6.14)$$

where  $N_s^{\text{bl}}$  is a dimensionless constant,  $\mathbf{N}^{\text{bl}}$  is a dimensionless constant vector and  $\tilde{\mathbf{K}}^{\text{int}}$  denotes the interfacial permeability tensor defined in (3.115). All effective coefficients  $N_s^{\text{bl}}$ ,  $\mathbf{N}^{\text{bl}}$  and  $\tilde{\mathbf{K}}^{\text{int}}$  are obtained from the solutions of boundary layer problems as explained in Section 4.3. Furthermore, we introduce the interfacial porous-medium velocity  $\mathbf{v}_{\text{int}}^{\text{pm}} = -\varepsilon^2 \tilde{\mathbf{K}}^{\text{int}} \nabla p^{\text{pm}}$ .

In the following sections, we validate the macroscale Stokes–Darcy model (6.3)–(6.6), either completed with the classical coupling conditions (6.7), (6.8) and one of (6.9)–(6.11) or the generalized conditions (6.12)–(6.14), by comparing the corresponding macroscale simulation results to the ones for the pore-scale resolved model (6.1)–(6.2). For the purpose of comparison, we evaluate macroscale velocity and pressure profiles along different vertical and horizontal cross sections within the coupled domain

according to their agreement with the pore-scale profiles. Additionally, for some validation cases, we compute the relative errors  $\epsilon_{f,c}$  between the pore-scale and macroscale solutions that enables quantitative comparison of competing Stokes–Darcy models. The relative error along the fixed cross section  $x_1 = c$  is defined as follows

$$\epsilon_{f,c} = \frac{\|f(c, \cdot) - f^\varepsilon(c, \cdot)\|}{\|f^\varepsilon(c, \cdot)\|}, \quad \|f(c, \cdot)\|^2 = \int_{-H}^h f(c, x_2)^2 dx_2, \quad (6.15)$$

where  $f^\varepsilon$  denotes the numerical solution to the pore-scale resolved problem,  $f$  is the solution to the macroscale problem,  $h$  is the height of the free-flow region and  $H$  the height of the porous-medium domain with respect to the  $x_2$ -axis.

Numerical methods used for solving the pore-scale and macroscale problems, respectively, and for computing the effective model parameters are described in Section 4. If not stated otherwise, the pore-scale resolved simulations are performed by the use of `FREEFEM++` [86] with Taylor–Hood finite elements and an adaptive mesh (see Section 4.1). The effective properties (permeability and boundary layer constants) are also computed using the software `FREEFEM++` (see Section 4.3). The macroscale problem is discretized using the finite volume method on staggered grids and solved using our in-house C++ code in a monolithic way (see Section 4.2). Details on the mesh size are given in the corresponding sections for each flow problem.

## 6.1 Classical coupling conditions for unidirectional flows to the interface

In this section, we consider the Stokes–Darcy problem (6.3)–(6.6) with the classical coupling conditions including the conservation of mass across the interface (6.7), the balance of normal forces (6.8) and one of the equations (6.10)–(6.11). We validate and calibrate the macroscale coupled problems for unidirectional flows, i.e., parallel or perpendicular to



the fluid–porous interface, and demonstrate the sensitivity of the coupled Stokes–Darcy model to the choice of effective model parameters (Beavers–Joseph slip coefficient  $\alpha_{\text{BJ}}$ , exact interface position). For flows parallel to the porous medium, we show that the optimal value of the Beavers–Joseph slip coefficient can be determined, and that the typically taken value  $\alpha_{\text{BJ}} = 1$  is not appropriate for many flow problems. For perpendicular flows to the porous layer we demonstrate that the value of the parameter  $\alpha_{\text{BJ}}$  is not important, however, the sharp interface location influences the macroscopic flow behavior severely.

In Section 6.1.1, we study pressure driven fluid flow parallel to the interface and show the validity of the original Beavers–Joseph coupling condition (6.10) for the Stokes–Darcy model, however, only if the correct value of the slip coefficient  $\alpha_{\text{BJ}}$  is applied. In Section 6.1.2, we investigate lid driven cavity over a porous bed, where the fluid flows almost parallel to the interface, and demonstrate the sensitivity of the coupled macroscale model to the effective coefficient  $\alpha_{\text{BJ}}$  and the exact location of the sharp fluid–porous interface. In Section 6.1.3, we study forced infiltration of a fluid into a porous medium, where the flow direction is perpendicular to the porous layer and the tangential component of velocity is almost zero. We show that in this case the exact position of the fluid–porous interface is important, but the coupling condition for the tangential velocity component has negligible influence on the performance of the Stokes–Darcy model.

### 6.1.1 Pressure driven flow

In this section, we study the fluid flow parallel to the porous layer that is driven by a pressure gradient. We show that the Beavers–Joseph coupling condition (6.10) is suitable in this case, i.e., it is possible to determine  $\alpha_{\text{BJ}} > 0$  such that microscale and macroscale simulation results are in good agreement. Furthermore, we consider different pore geometries to analyze the dependency of the Beavers–Joseph parameter  $\alpha_{\text{BJ}}$  on the

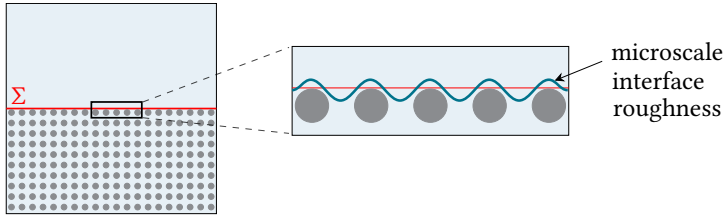


Figure 6.1: Schematic depiction of microscale interface roughness in case of geometry  $G_1$ .

microscale geometrical information (porosity, permeability, arrangement of solid grains and microscale interface roughness).

We consider the sharp fluid–porous interface  $\Sigma = (0, 1) \times \{0\}$  separating the free-flow region  $\Omega_{\text{ff}} = (0, 1) \times (0, 0.5)$  from the porous-medium domain  $\Omega_{\text{pm}} = (0, 1) \times (-0.5, 0)$ . The latter is constructed by  $20 \times 10$  periodically distributed solid inclusions, which are located in the way that the fluid–porous interface is tangent to the top of the first row of solid grains. This interface position is most often considered in case of the classical interface conditions, e.g., [15, EE3, 106, 117]. In order to analyze the influence of microscale interface roughness (Figure 6.1), arrangement of solid grains, permeability  $\tilde{\mathbf{K}}$  and porosity  $\phi$  on the Stokes–Darcy model (6.3)–(6.8), (6.10), we study six porous-medium geometrical configurations characterized by different shapes of solid grains (circular, elliptical, rectangular) and different type of arrangements (in-line, staggered). The unit cells  $Y = (0, 1)^2$  corresponding to the considered pore geometries are presented in Table 6.1. Geometries  $G_1$  and  $G_3$  lead to the same permeability  $\tilde{\mathbf{K}} = \tilde{k}_{11} \mathbf{I}$ , similar porosity  $\phi$ , but to different microscale interface roughness. Geometries  $G_1$ ,  $G_2$  and  $G_4$  are constructed based on the same type of solid inclusions (circular), however, the grains are either arranged in a different manner or have different sizes that result in different permeability and porosity values. Geometries  $G_1$  and  $G_4$  respective  $G_5$  and  $G_6$  yield the same porosity  $\phi$  but different permeability tensors  $\tilde{\mathbf{K}}$ .

To describe pressure driven flow from the pore-scale perspective, we use

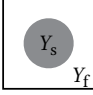
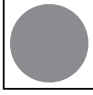
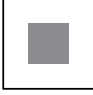
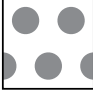
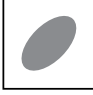
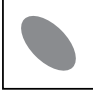
	$G_1$	$G_2$	$G_3$	$G_4$	$G_5$	$G_6$
$Y$						
$\tilde{k}_{11}$	1.99e-2	5.67e-4	1.99e-2	5.63e-3	1.23e-2	1.23e-2
$\tilde{k}_{12}$	0	0	0	0	2.69e-3	-2.69e-3
$k_{22}$	1.99e-2	5.67e-4	1.99e-2	4.44e-3	1.23e-2	1.23e-2
$\phi$	0.804	0.400	0.814	0.804	0.749	0.749

Table 6.1: Unit cells  $Y = Y_f \cup Y_s$  for the considered porous-medium geometries  $G_1$  to  $G_6$  in case of pressure driven flow.

the Stokes equations (6.1)–(6.2) with the following boundary conditions

$$\bar{\mathbf{v}} = \mathbf{0} \text{ on } \Gamma_D, \quad \bar{\mathbf{h}} = (0, -p^{\text{in}})^\top \text{ on } \Gamma_N^{\text{in}}, \quad \bar{\mathbf{h}} = \mathbf{0} \text{ on } \Gamma_N^{\text{out}}, \quad (6.16)$$

where  $\Gamma_N^{\text{in}} = \{0\} \times (-0.5, 0.5)$ ,  $\Gamma_N^{\text{out}} = \{1\} \times (-0.5, 0.5)$ ,  $\Gamma_D = \partial\Omega \setminus (\Gamma_N^{\text{in}} \cup \Gamma_N^{\text{out}})$  and  $p^{\text{in}} = 31.75$  such that  $\max_{\mathbf{x} \in \Omega_{\text{ff}}} |v_1^f(\mathbf{x})| \approx 1.0$ . At the macroscale, the flow is described by the Stokes–Darcy problem (6.3)–(6.8), (6.10) where

$$\bar{\mathbf{v}} = \mathbf{0} \quad \text{on } \Gamma_{\text{ff},D}, \quad \bar{\mathbf{v}} = \mathbf{0} \quad \text{on } \Gamma_{\text{pm},N}, \quad (6.17)$$

$$\bar{\mathbf{h}} = (0, -p^{\text{in}})^\top \quad \text{on } \Gamma_{\text{ff},N}^{\text{in}}, \quad \bar{p} = p^{\text{in}} \quad \text{on } \Gamma_{\text{pm},D}^{\text{in}}, \quad (6.18)$$

$$\bar{\mathbf{h}} = \mathbf{0} \quad \text{on } \Gamma_{\text{ff},N}^{\text{out}}, \quad \bar{p} = 0 \quad \text{on } \Gamma_{\text{pm},D}^{\text{out}}. \quad (6.19)$$

We set  $\Gamma_{\text{ff},D} = \Gamma_D \cap \partial\Omega_{\text{ff}}$ ,  $\Gamma_{\text{pm},N} = \Gamma_D \cap \partial\Omega_{\text{pm}}$ ,  $\Gamma_{N,\text{ff}}^{\text{in/out}} = \Gamma_N^{\text{in/out}} \cap \partial\Omega_{\text{ff}}$  and  $\Gamma_{\text{pm},D}^{\text{in/out}} = \Gamma_N^{\text{in/out}} \cap \partial\Omega_{\text{pm}}$ . Boundary conditions (6.16) and (6.17)–(6.19), respectively, lead to a coupled flow system, where the pressure field is linear and the normal velocity component is zero  $\mathbf{v}^{\text{ff}} \cdot \mathbf{e}_2 = 0$  in  $\Omega_{\text{ff}}$ . We note that due to the latter fact the original Beavers–Joseph coupling condition (6.9) is identical to its symmetrized version (6.10) proposed by Jones. Since the macroscale pressure and the normal velocity component do not depend on the choice of the Beavers–Joseph parameter for this flow problem, we only analyze the tangential velocity component for the determination of the optimal slip coefficient  $\alpha_{\text{BJ}}$ .

In order to find the optimal value of the Beavers–Joseph parameter  $\alpha_{\text{BJ}}$  with respect to geometries  $G_1$  to  $G_6$  we identify the macroscale model that agrees best with the pore-scale resolved model. For this purpose, we minimize the relative error (6.15) between the microscale and macroscale numerical simulation results using an efficient two-level numerical algorithm developed in [EE7] by the coauthor Paula Strohbeck. The proposed two-level algorithm involves Clough–Tocher interpolation and simulated annealing. In Table 6.2 we provide the computed relative errors (6.15) for the typically used value  $\alpha_{\text{BJ}} = 1$  and the determined optimal parameter  $\alpha_{\text{BJ}}^{\text{opt}}$  for the six considered porous-medium geometries depicted in Table 6.1.

For the solution of the microscale problem (6.1)–(6.2), (6.16) we use a grid with approximately 300 000 triangular elements in case of geometry  $G_1$ . To compute the corresponding permeability we solve the cell problems (2.74)–(2.76) using a mesh that consists of approximately 35 000 triangular elements. For solving the macroscale Stokes–Darcy problem (6.3)–(6.8), (6.10), (6.17)–(6.19) we take the grid size  $h_x = h_y = 1/800$  to construct the Cartesian staggered grid.

### Geometry $G_1$

We consider an isotropic porous medium which is constructed by in-line arranged circular solid inclusions as presented in Figure 6.2(a). This yields the characteristic pore size  $\varepsilon = 1/20$ . The radius of the inclusions with respect to the unit cell  $Y$  is taken  $r = 0.25$ . The permeability and porosity values corresponding to geometry  $G_1$  are presented in Table 6.1. We provide the pore-scale velocity field according to problem (6.1)–(6.2), (6.16) in Figure 6.2(a). Using the two-level numerical algorithm developed in [EE7] we determine  $\alpha_{\text{BJ}}^{\text{opt}} = 2.8$  as the optimal value of the Beavers–Joseph parameter for geometry  $G_1$ . The computed relative errors between the pore-scale and macroscale simulation results for the optimal value  $\alpha_{\text{BJ}}^{\text{opt}} = 2.8$  and the standard value  $\alpha_{\text{BJ}} = 1$  are presented in Table 6.2.

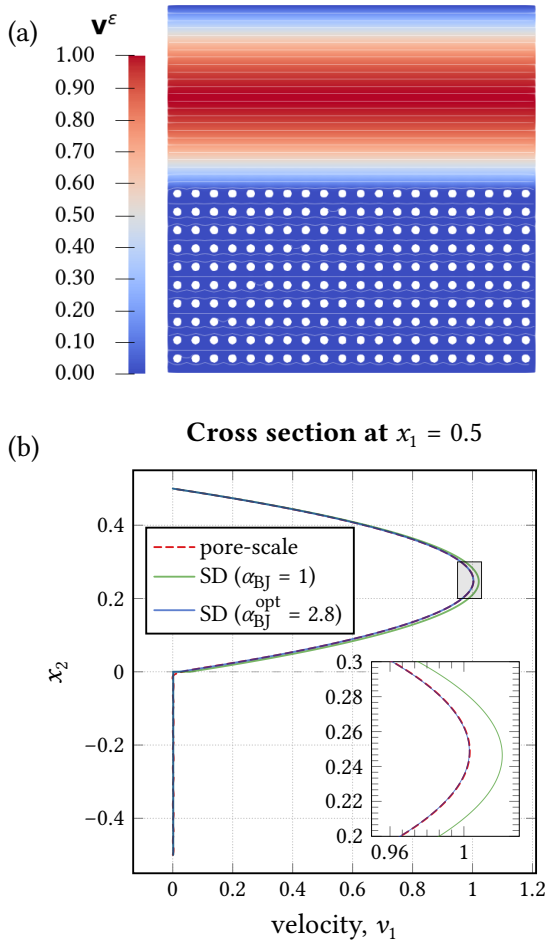


Figure 6.2: (a) Pore-scale velocity field and (b) velocity profiles of the tangential component for pressure driven flow in case of geometry  $G_1$ .

We observe that taking the most accurate value  $\alpha_{\text{BJ}}^{\text{opt}}$  reduces the error between the pore-scale and macroscale solution by factor 8 compared to the typically used  $\alpha_{\text{BJ}} = 1$ . In order to visualize the difference between

the macroscale models with the two different values of Beavers–Joseph parameter, we provide macroscale velocity profiles for  $\alpha_{\text{BJ}} = 1$  (profile: SD ( $\alpha_{\text{BJ}} = 1$ )) and  $\alpha_{\text{BJ}}^{\text{opt}} = 2.8$  (profile: SD ( $\alpha_{\text{BJ}}^{\text{opt}} = 2.8$ )) and compare them to the pore-scale resolved velocity (profile: pore-scale) in Figure 6.2(b). We observe that the macroscale profile for  $\alpha_{\text{BJ}} = 1$  does not fit to the microscale velocity profile, whereas the macroscale model with  $\alpha_{\text{BJ}}^{\text{opt}} = 2.8$  provides excellent agreement with the pore-scale results.

### Geometry $G_2$

For geometry  $G_2$  we study the same shape of solid inclusions as for geometry  $G_1$  and the same type of arrangement (in-line) leading to  $\varepsilon = 1/20$ , however, we consider circular solid inclusions having a bigger radius, i.e.,  $r = \sqrt{(1 - \phi)/\pi}$ . Hence, we constructed a porous medium that has lower porosity ( $\phi = 0.4$ ) and lower permeability ( $\tilde{k}_{11} = 5.67\text{e-}4$ ) in comparison to  $G_1$  (see Table 6.1). We determine the optimal value  $\alpha_{\text{BJ}}^{\text{opt}} = 0.5$  of the Beavers–Joseph parameter for the geometrical configuration  $G_2$  (Table 6.2). When comparing the optimal values of the Beavers–Joseph slip coefficient for geometries  $G_1$  and  $G_2$  we conclude that this coefficient highly depends on the porosity and permeability of the porous structure, as expected and already noticed in [15]. From Table 6.2 we observe that for geometry  $G_2$ , where the porosity and permeability is low, the choice  $\alpha_{\text{BJ}} = 1$  does also provide reasonable macroscale simulation results. Nevertheless, the optimal value  $\alpha_{\text{BJ}}^{\text{opt}} = 0.5$  yield a better performance of the Stokes–Darcy model. We note that in [141] the value  $\alpha_{\text{BJ}}^{\text{opt}} = 0.5$  is also found to be more suitable than the standard value  $\alpha_{\text{BJ}} = 1$  considering the same pore geometry  $G_2$  for a different flow problem.

### Geometry $G_3$

We construct a porous medium that has the same permeability as geometry  $G_1$ , but that is characterized by different interface roughness.

Therefore, we consider the porous-medium domain  $\Omega_{\text{pm}}$  consisting of in-line arranged squared solid inclusions ( $\varepsilon = 1/20$ ) having side length  $d = 0.2154$  with respect to  $Y$ . This yields an isotropic porous medium for which we present the permeability and porosity values in Table 6.1. Besides identical permeability values we observe that geometries  $G_1$  and  $G_3$  have almost the same porosity. Thus, with geometry  $G_3$  we analyze the dependency of the Beavers–Joseph parameter  $\alpha_{\text{BJ}}$  on the pore-scale interface roughness. We determine the optimal value  $\alpha_{\text{BJ}}^{\text{opt}} = 7.1$  for this porous-medium geometrical configuration (Table 6.2) that is noticeably bigger than the value  $\alpha_{\text{BJ}} = 2.8$  which was found to be optimal for geometry  $G_1$ . The error (6.15) between the macroscale and pore-scale model is reduced by factor 14 when applying  $\alpha_{\text{BJ}}^{\text{opt}} = 7.1$  instead of  $\alpha_{\text{BJ}} = 1$  in coupling condition (6.10). Based on these results we conclude that the Beavers–Joseph coefficient  $\alpha_{\text{BJ}}$  is highly affected by the microscale surface roughness.

#### Geometry $G_4$

Next, we study a porous medium having the same microscale interface roughness and the same porosity as geometry  $G_1$  but a different arrangement of solid grains leading to a different permeability tensor  $\tilde{\mathbf{K}}$ . We consider the porous domain  $\Omega_{\text{pm}}$  made of circular solid inclusions with radius  $r = 0.125$  in  $Y$  that are distributed in a staggered manner (Table 6.1). This yields the characteristic pore size  $\varepsilon = 1/10$ , and thus, the radius  $r^\varepsilon = \varepsilon r$  of the solid grains within the flow domain  $\Omega^\varepsilon$  is exactly the same as in case of  $G_1$ . For the geometrical configuration  $G_4$  we obtain an orthotropic permeability tensor  $\tilde{\mathbf{K}} = \text{diag}(\tilde{k}_{11}, \tilde{k}_{22})$ , where the permeability values  $\tilde{k}_{11} \neq \tilde{k}_{22}$  are given in Table 6.1. Using the two-level numerical algorithm from [EE7] we determine  $\alpha_{\text{BJ}}^{\text{opt}} = 3.0$  as the optimal Beavers–Joseph parameter for geometry  $G_4$ . This optimal value provides a relative error (6.15) that is 10 times smaller than in case of the typically applied  $\alpha_{\text{BJ}} = 1$ . We observe that although the interface roughness and the porosity of geometries  $G_1$  and  $G_4$  are identical we obtain optimal

values of the Beavers–Joseph slip coefficient that are not exactly the same. Noting that the value  $\tilde{k}_{11}$  for geometry  $G_4$  is different from  $\tilde{k}_{11}$  for geometry  $G_1$ , we analyze the ratio  $\varepsilon\sqrt{\tilde{K}}\alpha_{\text{BJ}}^{-1}$  appearing in condition (6.10), where we used  $\sqrt{\tilde{K}} = \sqrt{\tilde{k}_{11}}$ . We observe that for both geometrical configurations  $G_1$  and  $G_4$  we have  $\varepsilon\sqrt{\tilde{K}}\alpha_{\text{BJ}}^{-1} \approx 0.0025$ . Moreover, we also consider  $\sqrt{\tilde{K}} = \sqrt{(\tilde{k}_{11} + \tilde{k}_{22})/2}$  in the Beavers–Joseph interface condition (6.10) and determine  $\alpha_{\text{BJ}}^{\text{opt}} = 2.8$  to be the optimal model parameter in this case. Thus, taking  $\sqrt{\tilde{K}} = \sqrt{(\tilde{k}_{11} + \tilde{k}_{22})/2}$  in (6.10) we obtain the same optimal value of the Beavers–Joseph parameter  $\alpha_{\text{BJ}}$  for geometry  $G_4$  as for geometry  $G_1$ . Based on these results we claim that the type of arrangement of the solid grains within the porous medium (in-line or staggered) has negligible influence on the optimal choice for the Beavers–Joseph parameter, if the interface roughness is kept the same.

### Geometries $G_5$ and $G_6$

We consider two anisotropic porous media with full permeability tensors  $\tilde{\mathbf{K}}$ . The porous media are composed by  $20 \times 10$  elliptical solid inclusions arranged in-line ( $\varepsilon = 1/20$ ) tilted to the right (Table 6.1, geometry  $G_5$ ) and tilted to the left (Table 6.1, geometry  $G_6$ ). The boundary of a solid grain within the unit cell  $Y$  for the two pore geometries  $G_5$  and  $G_6$  is described by the ellipse with semi-axes  $r_b = 0.4$  and  $r_c = 0.2$ , with the center at  $(0.5, 0.5)$  and which is rotated clockwise and counter-clockwise by  $45^\circ$ , respectively. Geometries  $G_5$  and  $G_6$  lead to different permeability values  $\tilde{k}_{12}$  (Table 6.1), however, the value of  $\sqrt{\tilde{K}} = \sqrt{\tilde{k}_{11}}$  in the Beavers–Joseph condition (6.10) is the same. Both geometries provide the same interface roughness, and we obtain the same optimal value of the Beavers–Joseph slip coefficient  $\alpha_{\text{BJ}}^{\text{opt}} = 2.0$  (Table 6.2).

In Table 6.2, we summarize the optimal Beavers–Joseph parameters  $\alpha_{\text{BJ}}^{\text{opt}}$  for the considered geometries  $G_1$  to  $G_6$  determined via the two-level



Geometry	$\alpha_{\text{BJ}}^{\text{opt}}$	Error $\epsilon_{v_1,0.5}$ for $\alpha_{\text{BJ}}^{\text{opt}}$	Error $\epsilon_{v_1,0.5}$ for $\alpha_{\text{BJ}} = 1$
$G_1$	2.8	3.401e-3	2.794e-2
$G_2$	0.5	2.838e-3	6.941e-3
$G_3$	7.1	2.632e-3	3.758e-2
$G_4, \sqrt{\tilde{K}} = \sqrt{\tilde{k}_{11}}$	3.0	4.092e-3	3.089e-2
$G_4, \sqrt{\tilde{K}} = \sqrt{\frac{\tilde{k}_{11} + \tilde{k}_{22}}{2}}$	2.8	4.098e-3	2.844e-2
$G_5$	2.0	2.901e-3	1.738e-2
$G_6$	2.0	2.901e-3	1.738e-2

*Table 6.2: Optimal Beavers–Joseph parameters  $\alpha_{\text{BJ}}^{\text{opt}}$  and relative errors between the pore-scale and macroscale simulation results  $\epsilon_{v_1,0.5}$  given in (6.15) for pressure driven flow and different porous-medium geometries.*

numerical algorithm developed in [EE7] for pressure driven flow. In addition, we provide the relative errors  $\epsilon_{v_1,0.5}$  for the tangential velocity in case  $\alpha_{\text{BJ}}^{\text{opt}}$  respective  $\alpha_{\text{BJ}} = 1$  was considered in equation (6.10) for the macroscale model. We observe that taking the most optimal value of the Beavers–Joseph slip coefficient in interface condition (6.10) or, equivalently, in (6.9) results in relative errors between the microscale and macroscale solution given by (6.15) being lower than 0.5% for all considered geometries. However, when taking  $\alpha_{\text{BJ}} = 1$  in condition (6.10) we obtain relative errors up to 3.8%. For many applications it is important to keep the error to a minimum in order to perform numerical simulations as accurately as possible, e.g., in case the coupled model is used to optimize microfluidic experiments [156]. Thus, in case that the classical interface conditions are applied for coupling the Stokes and Darcy flow equations the correct choice of  $\alpha_{\text{BJ}}$  is crucial.

The study of pressure driven flow for geometries  $G_1$  to  $G_6$  showed that the classical coupling conditions are suitable and that the optimal value of the Beavers–Joseph parameter  $\alpha_{\text{BJ}}$  can be determined. We observe

that this parameter is dependent on the microscale interface roughness, permeability and porosity. In contrast, the dependence of  $\alpha_{\text{BJ}}$  on the type of arrangement of solid grains within the porous structure (staggered and in-line) is minor. For this test case, we considered the interface position suggested by Beavers and Joseph [15] and also considered in [106, 117], i.e., tangent to the top of solid grains, and did not investigate the dependence of  $\alpha_{\text{BJ}}$  on the exact position of the sharp interface. This aspect is discussed in Sections 6.1.2 and 6.1.3.

### 6.1.2 Lid driven cavity over porous bed

In this section, we study lid driven cavity over a porous bed and analyze the validity of the Stokes–Darcy problem with the classical coupling concept including the Beavers–Joseph–Saffman–Jones condition (6.11). More precisely, we investigate the performance of the coupled macroscale model (6.3)–(6.8), (6.11) with respect to different locations of the fluid–porous interface  $\Sigma$  and different values of the Beavers–Joseph parameter  $\alpha_{\text{BJ}}$  considering the porous-medium geometries presented in Figure 6.3.

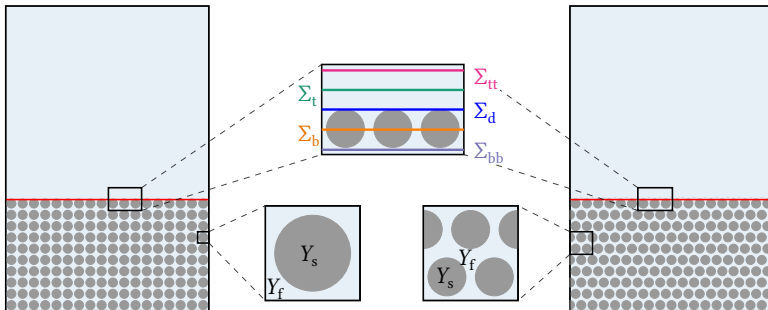


Figure 6.3: Schematic pore-scale setting, unit cell  $Y = (0, 1)^2$  and different interface locations  $\Sigma_i$ ,  $i \in \{b, bb, d, t, tt\}$  for the isotropic (left) and orthotropic (right) porous medium.

We consider the macroscopic flow domain  $\Omega = (0, 1) \times (-0.5, 1)$  consisting of the free-flow region  $\Omega_{\text{ff}}$  and the porous part  $\Omega_{\text{pm}}$ . We study two geometrical configurations of the porous structure: an isotropic porous medium with in-line arranged solid inclusions (Figure 6.3, left) and an orthotropic medium, where the obstacles are arranged in a staggered manner (Figure 6.3, right). These porous media are constructed by  $40 \times 20$  circular solid inclusions yielding the characteristic pore size  $\varepsilon = 1/40$  in the isotropic case and  $\varepsilon = 1/20$  in the orthotropic case. For both porous structures the porosity is  $\phi = 0.4$  and the radius of the circular solid grains within the unit cell  $Y$  is  $r = \sqrt{(1 - \phi)/\pi}$ . The permeability tensor  $\tilde{\mathbf{K}}$  is computed numerically by means of homogenization theory using formula (2.79) and the entries  $\tilde{k}_{11}$ ,  $\tilde{k}_{12}$  and  $\tilde{k}_{22}$  are presented in Table 6.3 for the two geometries.

The fluid–porous interface  $\Sigma$  is an idealized representation of the interfacial region between the free-flow region and the porous medium where the properties of the medium, as well as the fluid velocity and pressure, encounter strong but nevertheless continuous variations. Beavers and Joseph [15] already noted that the exact position of the sharp interface is ambiguous. They defined the line tangent to the uppermost row of solid obstacles as the ‘nominal’ interface (blue line in Figure 6.3) and considered this interface location in their studies. In the literature the interface position is typically assumed to lie within the range of the order of characteristic pore size  $\varepsilon$  from the nominal interface [10, 35, 36]. For the Stokes–Darcy model (6.3)–(6.8), (6.11) we consider five different locations of the fluid–porous interface (Figure 6.3) within the typical range:  $\Sigma_{\text{bb}}$  at  $x_2 = -0.025$ ,  $\Sigma_{\text{b}}$  at  $x_2 = -0.01$ ,  $\Sigma_{\text{t}}$  at  $x_2 = 0.01$ ,  $\Sigma_{\text{tt}}$  at  $x_2 = 0.025$  and  $\Sigma_{\text{d}}$  at  $x_2 = 0$ , which is the line tangent to the first row of solid inclusions. In the definition of interface and boundary conditions  $\Sigma$  stands for any choice of  $\Sigma_i$ ,  $i \in \{\text{bb}, \text{b}, \text{d}, \text{t}, \text{tt}\}$ .

Fluid flow at the pore scale is described by the nondimensional Stokes equations (6.1)–(6.2) completed with the following boundary conditions

$$\bar{\mathbf{v}} = (1, 0)^\top \quad \text{on } \Gamma_D, \quad \bar{\mathbf{v}} = \mathbf{0} \quad \text{on } \partial\Omega \setminus \Gamma_D, \quad (6.20)$$

where  $\Gamma_D = (0, 1) \times \{1\}$ . Moreover, to define the pressure uniquely we impose  $\int_{\Omega_{\text{ff}}} p^\varepsilon \, dx = 0$ . The boundary conditions presented in (6.20) yield lid driven cavity flow over a porous medium, where the fluid flows parallel to the interface near the horizontal middle of the coupled domain. To obtain the corresponding macroscale model, we use equations (6.3)–(6.6) and set the following conditions on the external boundary  $\partial\Omega$ :

$$\begin{aligned} \bar{\mathbf{v}} &= (1, 0)^\top & \text{on } \Gamma_{D,\text{ff}}, & & \bar{\mathbf{v}} &= \mathbf{0} & \text{on } \partial\Omega_{\text{ff}} \setminus (\Gamma_{D,\text{ff}} \cup \Sigma), \\ \bar{\mathbf{v}} &= 0 & \text{on } \partial\Omega_{\text{pm}} \setminus \Sigma, & & & & \end{aligned} \quad (6.21)$$

together with the constraint for the pressure  $\int_{\Omega_{\text{ff}}} p_{\text{ff}} \, dx = 0$ , and for  $\Gamma_{D,\text{ff}} = \Gamma_D$ . In addition to the boundary conditions specified in (6.21) coupling conditions (6.7), (6.8) and (6.11) are applied on the fluid–porous interface.

This section is based on [EE6], where we use the trial and error method to identify the parameter  $\alpha_{\text{BJ}} \in \{0.1, 0.2, \dots, 4\}$  and the interface location  $\Sigma_i$ ,  $i \in \{\text{b}, \text{bb}, \text{d}, \text{t}, \text{tt}\}$ , that yield the Stokes–Darcy model, which provides numerical simulation results that are in the best agreement with the pore-scale results. Some of our findings are later confirmed using the two-level numerical algorithm developed in [EE7].

The pore-scale problem (6.1)–(6.2), (6.20) is solved using the lattice Boltzmann method (LBM). The LBM simulations have been performed by the coauthors Christoph Schwarzmeier and Ulrich Rude (Friedrich-Alexander-Universitt Erlangen-Nrnberg) using the open-source software framework WALBERLA [13] ([www.walberla.net](http://www.walberla.net)). The cell problems (2.74)–(2.76) are solved using FREEFEM++ with an adaptive mesh and approximately 40 000 elements. For the discretization of the macroscale problem we use our in-house C++ code taking the grid size  $h_x = h_y = 1/800$ .

### Isotropic porous medium

We study the sensitivity of the macroscale model (6.3)–(6.6), (6.21) with coupling conditions (6.7), (6.8) and (6.11) to the location of the sharp fluid–

	<table style="width: 100%; border-collapse: collapse;"> <tr> <td style="padding-right: 10px;"><math>\tilde{k}_{11}</math></td> <td>5.67e-4</td> </tr> <tr> <td><math>\tilde{k}_{12}</math></td> <td>0</td> </tr> <tr> <td><math>\tilde{k}_{22}</math></td> <td>5.67e-4</td> </tr> </table>	$\tilde{k}_{11}$	5.67e-4	$\tilde{k}_{12}$	0	$\tilde{k}_{22}$	5.67e-4		<table style="width: 100%; border-collapse: collapse;"> <tr> <td style="padding-right: 10px;"><math>\tilde{k}_{11}</math></td> <td>4.15e-4</td> </tr> <tr> <td><math>\tilde{k}_{12}</math></td> <td>0</td> </tr> <tr> <td><math>\tilde{k}_{22}</math></td> <td>1.33e-4</td> </tr> </table>	$\tilde{k}_{11}$	4.15e-4	$\tilde{k}_{12}$	0	$\tilde{k}_{22}$	1.33e-4
$\tilde{k}_{11}$	5.67e-4														
$\tilde{k}_{12}$	0														
$\tilde{k}_{22}$	5.67e-4														
$\tilde{k}_{11}$	4.15e-4														
$\tilde{k}_{12}$	0														
$\tilde{k}_{22}$	1.33e-4														

Table 6.3: Permeability for the isotropic (left) and orthotropic (right) porous medium.

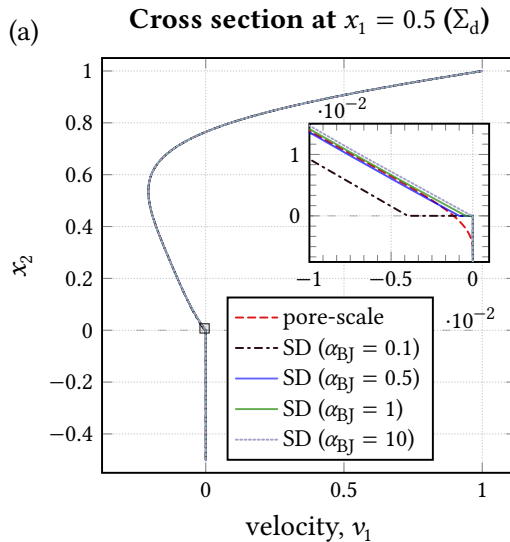
porous interface and to the Beavers–Joseph parameter  $\alpha_{BJ}$  considering the isotropic porous medium (Figure 6.3, left). We make cross sections in the horizontal middle of the coupled domain, at  $x_1 = 0.5$  (between two columns of solid inclusions) and at  $x_1 = 0.4875$  (intersecting solid inclusions), where the flow is almost parallel to the fluid–porous interface, and in the interfacial zone at  $x_2 = 0$ . Note that the velocity profiles corresponding to the pore-scale resolved model (profile: pore-scale) fluctuate in the porous medium and near the interface (Figure 6.4(b)) due to the presence of solid inclusions. Since the Stokes–Darcy model is an upscaled formulation of the pore-scale problem it does not see the microscopic details. Hence, to guarantee a fair and reasonable comparison of microscale and macroscale numerical simulation results, we average the pore-scale velocity whenever it is necessary.

In Figure 6.4(a) we provide profiles of the tangential velocity component corresponding to the pore-scale problem (6.1)–(6.2), (6.20) and Stokes–Darcy problem (6.3)–(6.8), (6.11), (6.21) for different values of the Beavers–Joseph slip coefficient  $\alpha_{BJ}$  at  $x_1 = 0.5$ . We consider the interface  $\Sigma_d$  positioned tangent to the first row of solid obstacles as in [15]. The best agreement between macroscale and pore-scale resolved simulation results is obtained for  $\alpha_{BJ} = 0.5$  (profile: SD,  $\alpha_{BJ} = 0.5$ ). In [EE6], the same observation is also made for other vertical cross sections.

To demonstrate the sensitivity of the coupled Stokes–Darcy model to the choice of  $\alpha_{BJ}$  in the Beavers–Joseph–Saffman–Jones condition (6.11), we evaluate cross sections for the tangential velocity component along the fluid–porous interface at  $x_2 = 0$ . In Figure 6.4(b) we present macroscale velocity profiles for different values of the Beavers–Joseph slip coefficient  $\alpha_{BJ}$

and the pore-scale velocity profile resulting from the LBM simulations, that fluctuates due to the presence of solid inclusions. In this case, averaging of the pore-scale simulation results is needed. The averaging has been performed by the coauthor Christoph Schwarzmeier who used a simple unweighted moving average of 50 values, i.e., lattice cells, to filter the low and high frequency components of the pore-scale velocity. For details on the pore-scale averaging we refer to [EE6]. In addition to the macroscale and LBM velocity profiles we also provide the profile for the tangential component of the averaged pore-scale velocity (profile: pore-scale (avg.)) in Figure 6.4(b). Here, it is clearly visible that the macroscale velocity profile with  $\alpha_{\text{BJ}} = 0.5$  fits well to the averaged microscale result, whereas the profile according to the standard value  $\alpha_{\text{BJ}} = 1$  does not agree. This finding confirms the results from Section 6.1.1 that the typically used value for the Beavers–Joseph parameter  $\alpha_{\text{BJ}} = 1$  is in general not the most accurate choice.

We verify our findings later by applying the two-level numerical algorithm that is developed in [EE7]. We determine  $\alpha_{\text{BJ}}^{\text{opt}} = 0.4$  as the optimal



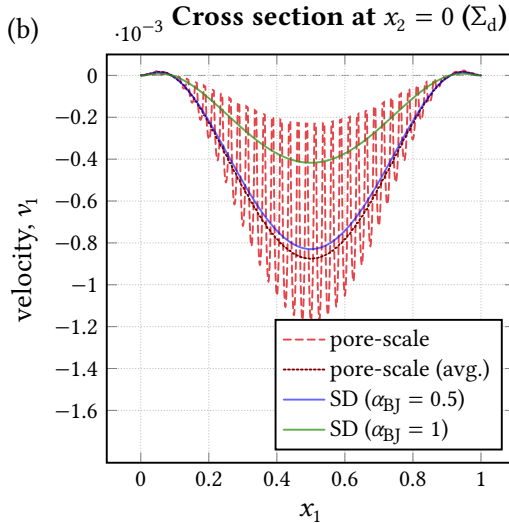


Figure 6.4: Velocity profiles of the tangential component for the lid driven cavity case (a) at  $x_1 = 0.5$  and (b) at  $x_2 = 0$  for different values of the Beavers–Joseph slip coefficient  $\alpha_{BJ}$  in case of the isotropic porous medium.

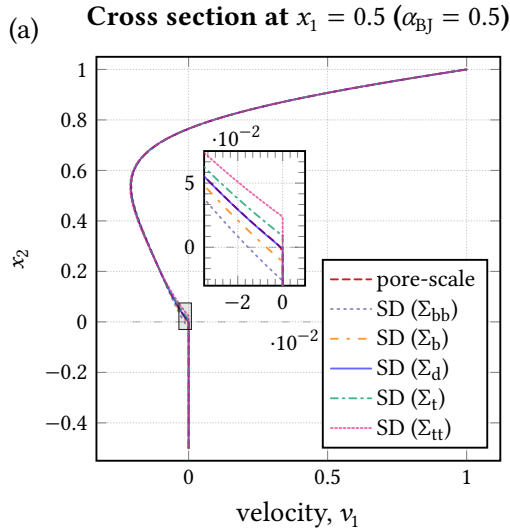
Beavers–Joseph parameter for lid driven cavity flow and the isotropic porous medium (Figure 6.3, left). We note that the value  $\alpha_{BJ} = 0.5$ , which we found to be the best choice using the trial and error method [EE6], is very close to the optimal parameter  $\alpha_{BJ}^{\text{opt}} = 0.4$ . Furthermore, the choice  $\alpha_{BJ} = 0.5$  leads to a relative error between the pore-scale and macroscale simulation results given by (6.15) that is similar to the one for  $\alpha_{BJ}^{\text{opt}} = 0.4$ . The errors for the two different values of the Beavers–Joseph parameter are provided in Table 6.4.

To evaluate the dependence of the coupled Stokes–Darcy model on the exact position of the sharp fluid–porous interface, we study further interface locations in addition to  $\Sigma_d$ , namely  $\Sigma_{bb}$ ,  $\Sigma_b$ ,  $\Sigma_t$  and  $\Sigma_{tt}$ . In Figure 6.5, we present the tangential and normal velocity profiles considering the five different positions of the fluid–porous interface and  $\alpha_{BJ} = 0.5$ , which we

Value of the Beavers–Joseph parameter	Error $\epsilon_{v_1,0.5}$
$\alpha_{BJ} = 0.4$	1.071e-3
$\alpha_{BJ} = 0.5$	1.237e-3

Table 6.4: Relative errors between the pore-scale and macroscale simulation results  $\epsilon_{v_1,0.5}$  given in (6.15) for lid driven cavity over porous bed and the isotropic porous medium considering different values of the Beavers–Joseph parameter.

previously found to be the best choice for the Beavers–Joseph parameter. The velocity profiles related to the Stokes–Darcy models differ from one another especially in the interfacial zone but also in the free-flow region. From Figure 6.5(a) we observe that the best fit of the macroscale profile to the pore-scale resolved simulation result for the tangential velocity component is obtained for the interface  $\Sigma_d$  located directly on top of the first row of solid inclusions. This is what we expected, since  $\Sigma_d$  was considered earlier when we determined  $\alpha_{BJ} = 0.5$  as the optimal value





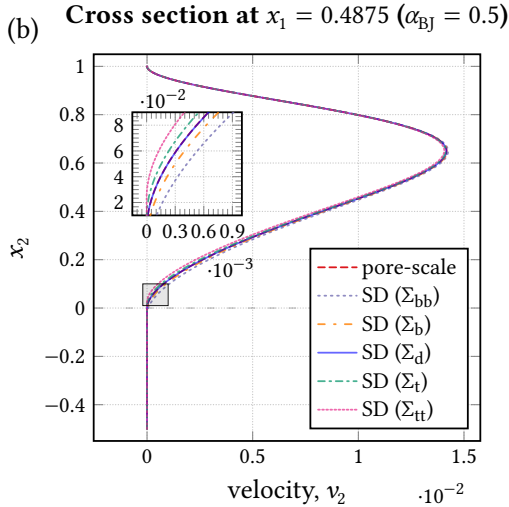


Figure 6.5: Velocity profiles of the (a) tangential and (b) normal component for the lid driven cavity case for different locations of the sharp interface in case of the isotropic porous medium.

for the slip coefficient. Therefore, if one considers an interface position different from  $\Sigma_d$ , the model parameter  $\alpha_{BJ}$  needs be adjusted such that pore-scale and macroscale simulation results fit best. This finding reveals that the Beavers–Joseph parameter is dependent on the exact interface location. In Figure 6.5(b) we provide profiles corresponding to the normal velocity component. Again, we observe that the best agreement between the macroscale and pore-scale profiles is obtained in case the interface position  $\Sigma_d$  is considered for the Stokes–Darcy model.

Based on our studies, we recommend locating the fluid–porous interface tangent to the uppermost row of solid obstacles if the classical interface conditions (6.7), (6.8) and (6.11) are used for the coupling of Stokes and Darcy flow equations. We recall that this interface position is also considered in the work of Beavers and Joseph [15] and in [106, 152].

### Orthotropic porous medium

Since the Beavers–Joseph slip coefficient  $\alpha_{\text{BJ}}$  contains geometrical information about the interfacial region, we consider an orthotropic porous medium (Figure 6.3, right) for the lid driven cavity test case. The orthotropic medium is characterized by the same microscale interface roughness as the isotropic one (Figure 6.3, left) but the permeability tensor  $\tilde{\mathbf{K}}$  is different (Table 6.3). We test various values for the Beavers–Joseph parameter  $\alpha_{\text{BJ}}$  and obtain the same optimal slip coefficient  $\alpha_{\text{BJ}} = 0.5$  as in the isotropic case (Figure 6.4). In Figure 6.6, we present tangential velocity profiles in the middle of the domain at  $x_1 = 0.5$  for the typically used value  $\alpha_{\text{BJ}} = 1$  and the most accurate value  $\alpha_{\text{BJ}} = 0.5$  of the Beavers–Joseph parameter considering the interface location  $\Sigma_d$ .

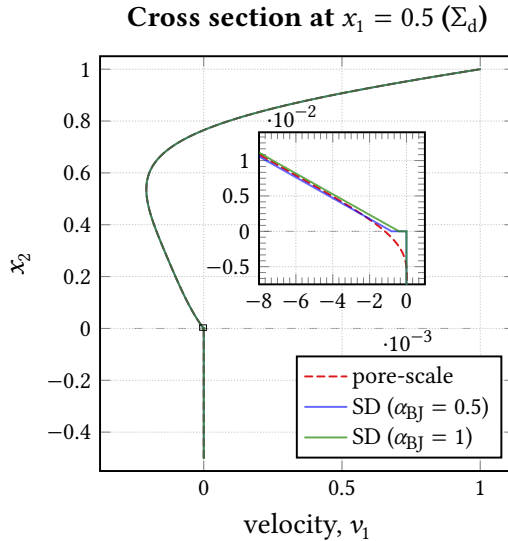


Figure 6.6: Velocity profiles of the tangential component for the lid driven cavity case in case of the orthotropic porous medium.

By consideration of the orthotropic porous medium presented in Figure 6.3

(right), we showed that the microscale interface roughness is an important aspect for the determination of the optimal Beavers–Joseph parameter, but the arrangement type of solid grains plays a less significant role if the porosity of different porous media is kept the same. This finding is in agreement with the results from Section 6.1.1, where the influence of different parameters (pore-scale interface roughness, permeability, porosity, arrangement of inclusions) is intensively studied.

### 6.1.3 Forced infiltration

In this section, we study forced infiltration of a fluid into a porous medium, where the flow is mainly perpendicular to the porous bed and the tangential velocity component in the free-flow region and in the porous-medium domain is negligible small. We consider coupling conditions (6.7), (6.8) and (6.11) for the macroscale problem (6.3)–(6.6), evaluate the importance of the Beavers–Joseph parameter  $\alpha_{BJ}$  and study the sensitivity of the coupled flow model to the fluid–porous interface.

We consider the same computational domain  $\Omega = \Omega_{ff} \cup \Omega_{pm} = (0, 1) \times (-0.5, 1)$  as for the lid driven cavity problem (Section 6.1.2) and apply equal notations for the different interface locations, i.e.,  $\Sigma_i$  and  $i \in \{b, bb, d, t, tt\}$ . The porous medium is constructed by staggered arranged solid obstacles as schematically presented in Figure 6.3 (right) and the corresponding permeability values are provided in Table 6.3 (right). Such a pore geometry avoids channel flow in the vertical direction between the columns of solid inclusions that would happen if the isotropic medium (Figure 6.3, left) would be considered for the forced infiltration problem.

To describe infiltration of a fluid into a porous medium, we impose the following boundary conditions for the pore-scale problem (6.1)–(6.2):

$$\begin{aligned} \bar{\mathbf{v}} &= (0, -0.1 \sin(\pi x_1))^T & \text{on } \Gamma_D, & \qquad \bar{\mathbf{h}} = (0, -100)^T & \text{on } \Gamma_N, \\ \bar{\mathbf{v}} &= \mathbf{0} & \text{on } \partial\Omega \setminus (\Gamma_D \cup \Gamma_N), & \end{aligned} \tag{6.22}$$

where  $\Gamma_D = (0, 1) \times \{1\}$  and  $\Gamma_N = (0, 1) \times \{-0.5\}$ . For the corresponding macroscale Stokes–Darcy problem (6.3)–(6.8), (6.11) we set

$$\bar{\mathbf{v}} = (0, -0.1 \sin(\pi x_1))^T \text{ on } \Gamma_{D,\text{ff}}, \quad \bar{\mathbf{v}} = \mathbf{0} \text{ on } \partial\Omega_{D,\text{ff}} \setminus (\Gamma_D \cup \Sigma), \quad (6.23)$$

$$\bar{p} = 100 \text{ on } \Gamma_{D,\text{pm}}, \quad \bar{\mathbf{v}} = \mathbf{0} \text{ on } \Gamma_{N,\text{pm}}, \quad (6.24)$$

with  $\Gamma_{D,\text{ff}} = \Gamma_D$ ,  $\Gamma_{D,\text{pm}} = \Gamma_N$ ,  $\Gamma_{N,\text{pm}} = \partial\Omega_{\text{pm}} \setminus (\Gamma_{D,\text{pm}} \cup \Sigma)$  and  $\Sigma$  stands for any choice of  $\Sigma_i$  for  $i \in \{\text{b}, \text{bb}, \text{d}, \text{t}, \text{tt}\}$ .

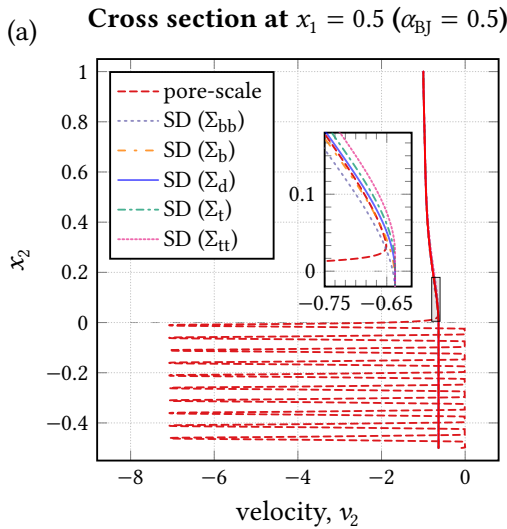
As in Section 6.1.2, the pore-scale problem (6.1)–(6.2), (6.22) is solved using the lattice Boltzmann method. For the solution of the cell problems (2.74)–(2.76) via FREEFEM++ approximately 40 000 elements are used. For solving the macroscale Stokes–Darcy problem we take the grid size  $h_x = h_y = 1/800$ .

Since the flow, specified by boundary conditions (6.22) and (6.23)–(6.24), is almost perpendicular to the porous bed, we have  $(\partial v_{\text{ff}}/\partial x_2) \cdot \boldsymbol{\tau} \approx 0$  and  $(\partial v_{\text{ff}}/\partial x_1) \cdot \mathbf{n} \approx 0$ , where  $\boldsymbol{\tau}$  and  $\mathbf{n}$  denote the tangential respective normal unit vector on the fluid–porous interface. Recalling that these partial derivatives appear on the right hand side of the Beavers–Joseph–Saffman–Jones condition (6.11) we find that for any choice of the Beavers–Joseph parameter in its typical range [15] equation (6.11) reduces approximately to the no-slip condition  $\mathbf{u}^{\text{ff}} \cdot \boldsymbol{\tau} = 0$  on  $\Sigma$ . Consequently, the slip coefficient  $\alpha_{\text{BJ}}$  has negligible impact on the performance of the coupled Stokes–Darcy model. Therefore, we do not investigate different values of the Beavers–Joseph parameter  $\alpha_{\text{BJ}}$  but simply take  $\alpha_{\text{BJ}} = 0.5$  as in Section 6.1.2. Forced infiltration of a fluid into a porous structure is also considered in [34], where the no-slip condition  $\mathbf{u}^{\text{ff}} \cdot \boldsymbol{\tau} = 0$  is proposed as the effective interface condition for the tangential velocity on  $\Sigma$ .

In order to study the applicability of the Stokes–Darcy problem (6.3)–(6.6), (6.23)–(6.24) with the classical interface conditions (6.7), (6.8) and (6.11) and analyze the sensitivity of the coupled problem to the location of the sharp fluid–porous interface, we evaluate cross sections at  $x_1 = 0.5$  considering the interface positions  $\Sigma_{\text{bb}}$ ,  $\Sigma_{\text{b}}$ ,  $\Sigma_{\text{d}}$ ,  $\Sigma_{\text{t}}$  and  $\Sigma_{\text{tt}}$  (Figure 6.3). In Figure 6.7(a), profiles of the normal velocity component for the macroscale

model and the pore-scale resolved model are shown. We observe that all the macroscale simulation results for the normal velocity are in acceptable agreement with the microscale results. In Figure 6.7(b), we provide pressure profiles at  $x_1 = 0.5$ . We observe that the pressure field is very sensitive to the exact location of the sharp fluid–porous interface, more precisely, the interface position highly influences the pressure in the free-flow region. As in Section 6.1.2, the best fit between macroscale and pore-scale simulation results is obtained for the interface  $\Sigma_d$  located tangent to the first row of solid inclusions (Figure 6.7(b)).

We find out that in case of forced infiltration of a fluid into a porous material the classical coupling conditions (6.7), (6.8) and (6.11), where the latter condition is originally developed for flows parallel to the interface, can be applied and provide physically reasonable results. As already mentioned earlier, the interface condition (6.11) has almost no effect on the performance of the coupled Stokes–Darcy system due to the negligible small tangential velocity component.



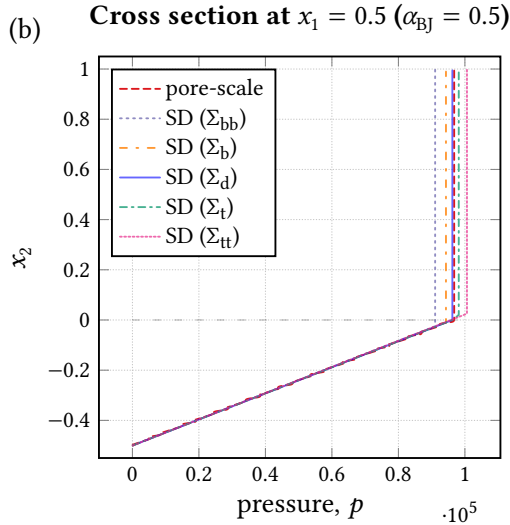


Figure 6.7: (a) Velocity profiles of the normal component and (b) pressure profiles for the infiltration problem at  $x_1 = 0.5$  zoomed near the interface.

### Summary of Section 6.1

We demonstrated that the Stokes–Darcy problem with the classical set of coupling conditions is very sensitive to the choice of model parameter  $\alpha_{\text{BJ}}$  and the exact location of the sharp fluid–porous interface. We showed that the typically used value  $\alpha_{\text{BJ}} = 1$  of the Beavers–Joseph slip coefficient is often not the correct choice, and that this coefficient highly depends on porosity, permeability and microscale interface roughness. To determine the optimal value of the Beavers–Joseph parameter for flows parallel to the porous layer we developed the two-level numerical algorithm [EE7]. This algorithm computes the optimal value  $\alpha_{\text{BJ}}^{\text{opt}}$  via minimizing the relative error between pore-scale and macroscale numerical simulation results. In case of forced infiltration of a fluid into a porous structure, i.e., when the fluid flow is perpendicular to the interface, the classical coupling conditions, which are proposed for flows parallel to the porous medium,

can be applied and provide a physically consistent representation of the pore-scale processes. Furthermore, based on the flow problems studied in this section, we recommend locating the sharp interface directly on top of the first row of solid obstacles in case the classical interface conditions are used.

## 6.2 Classical coupling conditions for arbitrary flows to the interface

In this section, we demonstrate that the Beavers–Joseph interface condition (6.10) and its simplification by Saffman (6.11) are unsuitable for the Stokes–Darcy coupling in case of arbitrary flow directions to the fluid–porous interface. For this purpose, we compare macroscale numerical simulation results for various choices of  $\alpha_{\text{BJ}}$  to pore-scale results at different cross sections. Dependent on the cross section we identify the model parameter  $\alpha_{\text{BJ}}$  that leads to the best agreement of microscale and macroscale solution. Since the porous media studied in this section are homogeneous and the properties of the fluid–porous interface do not change, the Beavers–Joseph parameter  $\alpha_{\text{BJ}}$ , which contains the geometrical information about the interfacial region (see Section 6.1.1), is supposed to be constant along the interface. However, we demonstrate that different values of the Beavers–Joseph slip coefficient are optimal for different cross sections. Thus, we conclude that it is not possible to find a global constant  $\alpha_{\text{BJ}}$  such that microscale and macroscale simulation results fit well.

We study two flow problems, where the fluid flow is arbitrary to the porous medium, and consider several porous-medium configurations. In Section 6.2.1, we analyze the coupled Stokes–Darcy model in case of filtration of a fluid through a T-shaped domain inspired by [80], and in Section 6.2.2, we study a general filtration problem similar to the one in Section 6.3.3.

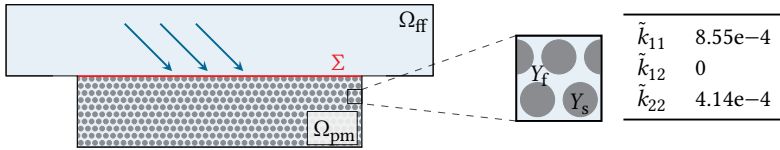


Figure 6.8: Geometrical setting for filtration through T-shaped domain in case of circular inclusions (left), corresponding unit cell and permeability values (right).

### 6.2.1 Filtration through T-shaped domain

We investigate filtration of a fluid through a T-shaped coupled free-flow and porous-medium domain  $\Omega = \Omega_{\text{ff}} \cup \Omega_{\text{pm}}$  where the flow is arbitrary to the fluid–porous interface. We consider the free-flow region  $\Omega_{\text{ff}} = (0, 3) \times (0, 0.5)$  separated by the interface  $\Sigma = (0.5, 2.5) \times \{0\}$  from the porous-medium domain  $\Omega_{\text{pm}} = (0.5, 2.5) \times (-0.5, 0)$ . The latter is constructed by 80 solid inclusions in  $x_1$ -direction and 20 inclusions in  $x_2$ -direction that are arranged in a staggered manner. Consequently, the unit cell  $Y$  contains  $2 \times 2$  solid grains and the characteristic pore size is  $\varepsilon = 1/20$ . Different shapes of solid grains (circular, elliptical tilted to the right, elliptical tilted to the left) are studied, and the corresponding permeability values and unit cells  $Y = Y_f \cup Y_s$  are provided in Figure 6.8 (right) and Table 6.6. For each geometrical configuration the sharp interface  $\Sigma$  is located directly on top of the solid inclusions as proposed in [15, 106, EE6, 152]. The geometrical setting of the coupled flow domain is schematically presented in Figure 6.8 (left) for circular solid grains.

The flow at the pore scale is described by the nondimensional Stokes equations (6.1)–(6.2) completed with the following set of boundary conditions on the external boundary

$$\bar{\mathbf{v}} = (0.1 \sin(2\pi x_2), 0)^\top \quad \text{on } \Gamma_D^{\text{in}}, \quad \bar{\mathbf{h}} = (0, -10)^\top \quad \text{on } \Gamma_N, \quad (6.25)$$

$$\bar{\mathbf{v}} = \mathbf{0} \quad \text{on } \Gamma_D^{\text{wall}}, \quad (6.26)$$



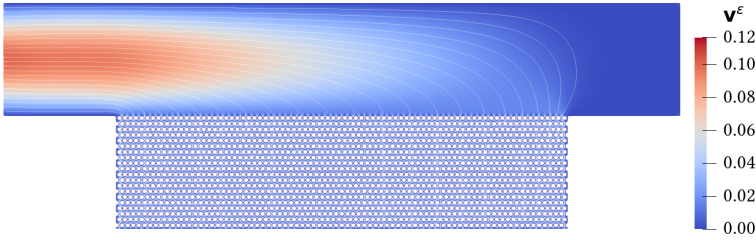


Figure 6.9: Pore-scale velocity field for filtration through T-shaped domain in case of circular solid inclusions.

where  $\Gamma_D^{\text{in}} = \{0\} \times (0, 0.5)$ ,  $\Gamma_N = (0.5, 2.5) \times \{-0.5\}$  and  $\Gamma_D^{\text{wall}} = \partial\Omega \setminus (\Gamma_D^{\text{in}} \cup \Gamma_N)$ . For the coupled Stokes–Darcy problem (6.3)–(6.8) with either (6.10) or (6.11) we specify the corresponding boundary conditions

$$\bar{\mathbf{v}} = (0.1 \sin(2\pi x_2), 0)^\top \quad \text{on } \Gamma_{D,\text{ff}}^{\text{in}}, \quad \bar{\mathbf{v}} = \mathbf{0} \quad \text{on } \Gamma_{D,\text{ff}}^{\text{wall}}, \quad (6.27)$$

$$\bar{\mathbf{v}} = 0 \quad \text{on } \Gamma_{N,\text{pm}}^{\text{wall}}, \quad \bar{p} = 10 \quad \text{on } \Gamma_{D,\text{pm}}. \quad (6.28)$$

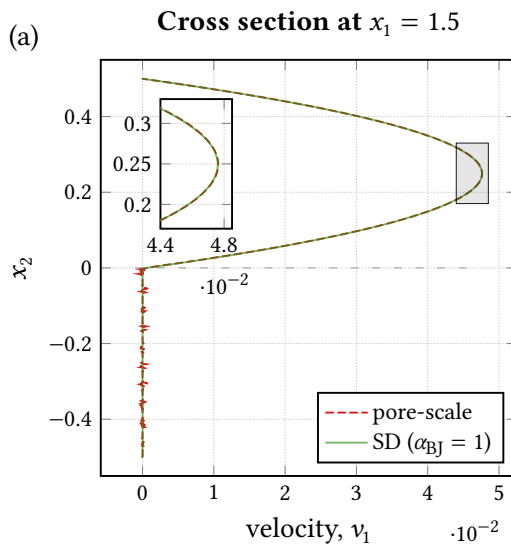
Here, we define  $\Gamma_{D,\text{ff}}^{\text{in}} = \Gamma_D^{\text{in}}$ ,  $\Gamma_{D,\text{ff}}^{\text{wall}} = \Gamma_D^{\text{wall}} \cap \partial\Omega_{\text{ff}}$ ,  $\Gamma_{N,\text{pm}}^{\text{wall}} = \Gamma_D^{\text{wall}} \cap \partial\Omega_{\text{pm}}$  and  $\Gamma_{D,\text{pm}} = \Gamma_N$ . The pore-scale problem (6.1)–(6.2), (6.25)–(6.26) and the Stokes–Darcy problem (6.3)–(6.8), (6.27)–(6.28) with (6.10) or (6.11), respectively, describe a flow system where the fluid flow is arbitrary to the porous medium (Figure 6.9).

We solve the microscale problem (6.1)–(6.2), (6.25)–(6.26) using FREEFEM++ where approximately 360 000 finite elements are used to partition the flow domain  $\Omega^\varepsilon$  such that at least three triangular elements are between two solid obstacles. The permeability is computed according to equation (2.79) using the solution of the cell problems (2.74)–(2.76), which are solved on a mesh that consists of approximately 50 000 triangular elements. For the solution of the Stokes–Darcy problem (6.3)–(6.8), (6.27)–(6.28) with (6.10) or (6.11) the grid size  $h_x = h_y = 1/400$  is taken.

### Staggered circular inclusions

In this section, we consider the porous medium consisting of circular solid grains that are arranged in a staggered way (Figure 6.8). The boundaries of the solid inclusions within the unit cell  $Y$  are described by circles with the centers at  $(m_1, m_2) \in \{(0, 0.25), (0.5, 0.25), (1, 0.25), (0.25, 0.75), (0.75, 0.75)\}$  and radius  $r = 0.2$ .

In order to analyze the applicability of the Beavers–Joseph condition (6.10) for this test case we make vertical cross sections at  $x_1 = 1.5$  (center of the flow domain) and at  $x_1 = 2.2$ . We observe that the physically reasonable fluctuations of the pore-scale velocity profiles near the interface and in the porous layer are negligible small, and therefore, there is no need to average the pore-scale results. In Figure 6.10 we present profiles of the tangential velocity component  $v_1$  for the two considered cross sections. We test various values for the Beavers–Joseph parameter in the range  $\alpha_{\text{BJ}} \in \{0.1, 0.2, \dots, 4\}$  and compare the corresponding macroscale simulation result to the pore-scale result with respect to the cross section



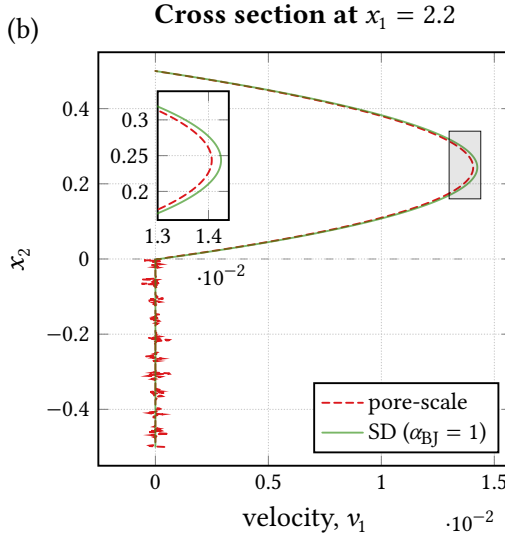


Figure 6.10: Velocity profiles of the tangential component (a) at  $x_1 = 1.5$  and (b) at  $x_1 = 2.2$  for filtration through T-shaped domain in case of circular inclusions.

at  $x_1 = 1.5$ . We find out that the pore-scale profile (profile: pore-scale) and the velocity profile corresponding to the coupled Stokes–Darcy model fit well for the typically chosen value  $\alpha_{\text{BJ}} = 1$  (profile: SD ( $\alpha_{\text{BJ}} = 1$ )) in the middle of the domain (Figure 6.10(a)). For the cross section at  $x_1 = 2.2$ , where the flow is nonparallel to the porous layer, the macroscale profile for the same choice of the Beavers–Joseph parameter differs from the pore-scale velocity profile (Figure 6.10(b)). Also, for other cross sections we observe that the pore-scale and macroscale simulation results for  $\alpha_{\text{BJ}} = 1$  do not match as well as they do at  $x_1 = 1.5$ .

In Table 6.5 we provide the relative errors (6.15) with respect to the tangential velocity  $v_1$  and the value  $\alpha_{\text{BJ}} = 1$  for the cross sections at  $x_1 = 1.5$  and  $x_1 = 2.2$ . We observe that the error  $\epsilon_{v_1, 2.2}$  is more than two times bigger compared to the error  $\epsilon_{v_1, 1.5}$ . This indicates that taking  $\alpha_{\text{BJ}} = 1$ , which leads to the best agreement of microscale and macroscale velocity profiles

Value of the Beavers–Joseph parameter	Error $\epsilon_{v_1,1.5}$	Error $\epsilon_{v_1,2.2}$
$\alpha_{\text{BJ}} = 1$	7.455e–3	1.778e–2

*Table 6.5: Relative errors (6.15) with respect to  $v_1$  for filtration through T-shaped domain in case of circular inclusions at two different cross sections.*

at  $x_1 = 1.5$ , is not the optimal choice for the Beavers–Joseph parameter considering the simulation results for the cross section at  $x_1 = 2.2$ .

Additionally, we tested the Beavers–Joseph–Saffman–Jones condition (6.11) instead of the more general Beavers–Joseph condition (6.10) and observed that there is only a slight difference between the resulting macroscopic profiles at all considered cross sections. This is physically consistent since the tangential porous-medium velocity is negligible small compared to the tangential free-flow velocity for this test case. Therefore, we do not provide the results related to Saffman’s version of the Beavers–Joseph condition given by (6.11).

To summarize, for the considered filtration problem and geometrical setting we find out that for different cross sections different values for the slip coefficient  $\alpha_{\text{BJ}}$  need to be applied such that pore-scale and macroscale velocity profiles fit best. Thus, we conclude that the Beavers–Joseph type conditions (6.10) and (6.11) are not the most accurate interface conditions for the Stokes–Darcy coupling.

**Remark 6.1:** *This flow problem was the first example [EE3], for which we found out that the Beavers–Joseph interface condition (6.10) and the condition proposed by Saffman (6.11) are not optimal for coupling the Stokes and Darcy equations. Since the considered porous medium is isotropic and densely packed with solid grains (see Figures 6.8 and 6.9) the differences between the pore-scale velocity profile and the macroscale velocity profile are relatively small, even for a value of the Beavers–Joseph parameter which is not the optimal one. However, if we consider a porous medium with higher*

porosity (see Section 6.2.2) or with anisotropic permeability (e.g., staggered elliptical inclusions) these differences become more significant.

### Staggered elliptical inclusions tilted to the right

Pore-scale interface roughness, porosity and permeability highly influence the optimal choice of the model parameter  $\alpha_{\text{BJ}}$  (see Section 6.1.1). Consequently, these properties of the porous medium also play a crucial role for the performance of the coupled Stokes–Darcy model with the classical set of interface conditions (6.7), (6.8) and (6.10) or (6.11). In order to study the applicability of the Beavers–Joseph type conditions (6.10) and (6.11) for anisotropic porous media in case of arbitrary flow directions to the porous layer, we consider the porous-medium domain  $\Omega_{\text{pm}}$  constructed based on the unit cell  $Y$  presented in Table 6.6 (middle). The unit cell contains  $2 \times 2$  elliptical solid obstacles that are tilted to the right and arranged in a staggered way. More precisely, the semi-major axis of a single ellipse is positioned at  $\gamma = \pi/4$  counterclockwise to the positive part of the  $x_1$ -axis as presented in Table 6.6 (left). The boundary curves of the solid obstacles within the unit cell  $Y$  are given by

$$e(t) = (m_1, m_2) + 0.092(\cos(t) + 2 \sin(t), -\cos(t) + 2 \sin(t)), \quad (6.29)$$

with the center at  $(m_1, m_2) \in \{(0, 0.25), (0.5, 0.25), (1, 0.25), (0.25, 0.75), (0.75, 0.75)\}$ , and further we have  $t \in [0, 2\pi)$  for  $m_1 \in \{0.25, 0.5, 0.75\}$ ,  $t \in [-0.463648, \pi - 0.463648)$  for  $m_1 = 0$  and  $t \in [\pi - 0.463648, 2\pi - 0.463648)$  for  $m_1 = 1$ . For the prescribed anisotropic porous medium having a full permeability tensor  $\tilde{\mathbf{K}}$  we provide the entries  $\tilde{k}_{11}$ ,  $\tilde{k}_{12}$  and  $\tilde{k}_{22}$  in Table 6.6 (middle). As before, we have  $80 \times 20$  solid grains within the porous domain  $\Omega_{\text{pm}} = (0.5, 2.5) \times (-0.5, 0)$ .

We solve the pore-scale problem (6.1)–(6.2), (6.25)–(6.26) in the perforated domain  $\Omega^\varepsilon$  and observe physically reasonable fluctuations of the pore-scale velocity field in the interior of the porous bulk and near the fluid–porous interface that is a consequence of the anisotropic porous-medium geometrical configuration (Table 6.6, middle). In order to make

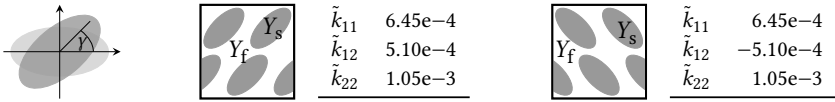
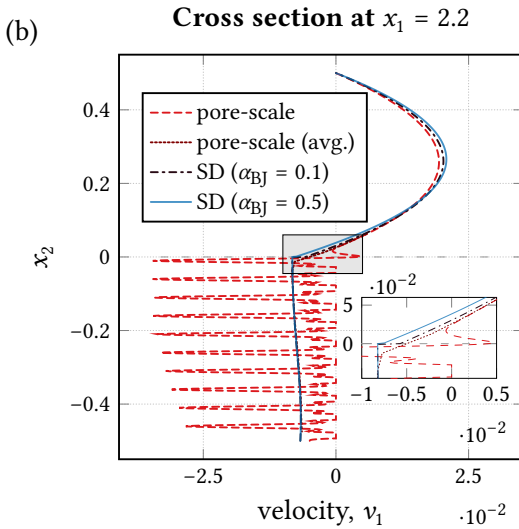
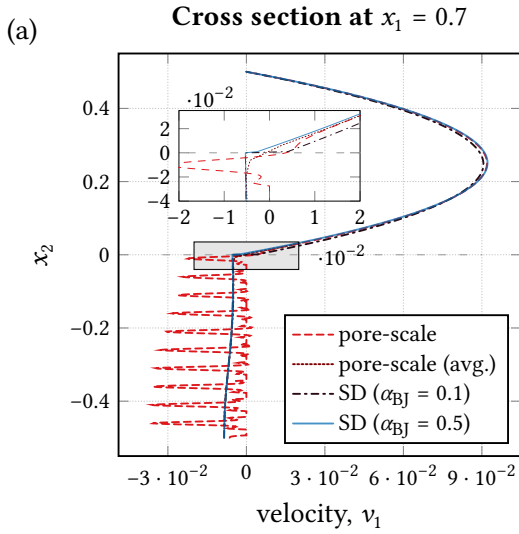


Table 6.6: Ellipse rotated by angle  $\gamma$  counterclockwise to the positive part of the  $x_1$ -axis (left) and permeability values for two anisotropic porous-medium geometries (middle and right).

the comparison of microscale to macroscale numerical simulation results easier, we provide the averaged pore-scale velocity (profile: pore-scale (avg.)) in addition to the velocity profile without averaging. We spatially average the microscale velocity field using adaptive volume averaging described in Section 4.1. The averaging volume  $V^{\text{avg}}$  within the porous medium away from the interface is of size  $(0, \varepsilon)^2$ . For averaging the velocity in the uppermost unit cell, close to the free-flow region, we consider one averaging volume of size  $(0, \varepsilon) \times (0, 0.5\varepsilon)$  and two volumes of size  $(0, \varepsilon) \times (0, 0.25\varepsilon)$ . Additionally, we average the pore-scale velocity also slightly above the fluid-porous interface using  $V^{\text{avg}} = (0, \varepsilon) \times (0, 0.25\varepsilon)$ . From Figure 6.11 we observe that the resulting averaged pore-scale velocity profiles match well to all the macroscale velocity profiles in the interior of the porous medium away from the interface. This is also what we expect since we know from classical averaging theories (e.g., homogenization, volume averaging) that Darcy's law accurately describes the fluid flow in the porous medium in an averaged sense.

We make vertical cross sections at  $x_1 = 0.7$ ,  $x_1 = 1.5$  and  $x_1 = 2.2$  in order to analyze the agreement between the pore-scale and different macroscale profiles of the tangential velocity component  $v_1$  (Figure 6.11). For the Stokes–Darcy model we applied various values  $\alpha_{\text{BJ}} \in \{0.1, 0.2, \dots, 4\}$  and identified the values which provided the best agreement of macroscale and microscale simulation results for the cross sections at  $x_1 = 0.7$  and at  $x_1 = 2.2$ . In Figure 6.11(a) we present the macroscale profile for  $\alpha_{\text{BJ}} = 0.5$ , that we found to be the best candidate for the Beavers–Joseph parameter at  $x_1 = 0.7$ , and the profile for  $\alpha_{\text{BJ}} = 0.1$  which is the most suitable value for the Stokes–Darcy coupling considering the cross section at  $x_1 = 2.2$ .



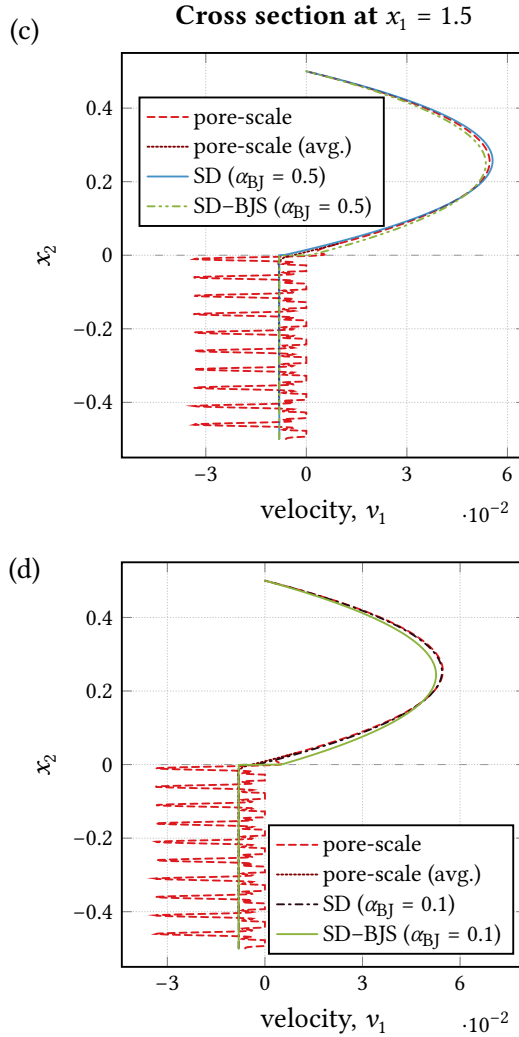


Figure 6.11: Velocity profiles of the tangential component (a) at  $x_1 = 0.7$ , (b) at  $x_1 = 2.2$  and (c), (d) at  $x_1 = 1.5$  for filtration through T-shaped domain in case of elliptical inclusions tilted to the right.



Although the choice  $\alpha_{\text{BJ}} = 0.1$  provides a better fit of pore-scale and macroscale results at  $x_1 = 2.2$  than for any other value  $\alpha_{\text{BJ}} > 0.1$ , none of the considered values for the Beavers–Joseph parameter is optimal for this cross section. Velocity profiles for the cross section at  $x_1 = 1.5$  are presented in Figures 6.11(c) and 6.11(d). Here, the macroscale velocity profiles for the previously found optimal values  $\alpha_{\text{BJ}} = 0.1$  and  $\alpha_{\text{BJ}} = 0.5$  both do not agree well with the pore-scale resolved solution. Thus, the most appropriate choice for the Beavers–Joseph slip coefficient at  $x_1 = 1.5$  is different from these two values. Due to the fact that we found different parameters  $\alpha_{\text{BJ}}$  to be optimal at the three different locations, we conclude that there exist no global constant  $\alpha_{\text{BJ}}$  along the whole interface that should be used in the Beavers–Joseph interface condition (6.10).

Besides the Beavers–Joseph coupling condition (6.10) we apply Saffman’s version (6.11) for the Stokes–Darcy coupling. We numerically solve the macroscale problem (6.3)–(6.8), (6.11), (6.27)–(6.28) taking  $\alpha_{\text{BJ}} = 0.1$  and  $\alpha_{\text{BJ}} = 0.5$  and make cross sections at  $x_1 = 1.5$  (profiles: SD–BJS, see Figures 6.11(c) and 6.11(d)). We observe that the macroscale simulation results obtained by using the Beavers–Joseph–Saffman–Jones condition (6.11) fit even worse to the pore-scale simulation results than the results obtained by using condition (6.10) for the macroscale model. The reason for this is a relatively high tangential Darcy velocity inside the porous medium due to the anisotropic structure. Thus, for such flow problems the filtration velocity in the coupling condition for the tangential velocity cannot be neglected as proposed by Saffman.

Summing up, considering the anisotropic geometrical configuration of the porous medium (Table 6.6, middle) for the filtration through a T-shaped domain, one cannot identify any constant value  $\alpha_{\text{BJ}}$  as the best choice for the Beavers–Joseph parameter. Thus, the commonly used Beavers–Joseph type interface conditions (6.10) and (6.11) are not suitable in this case to couple the Stokes equations to the Darcy flow equations accurately.

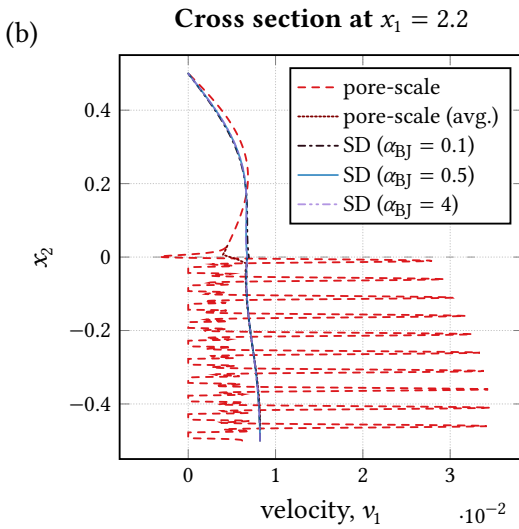
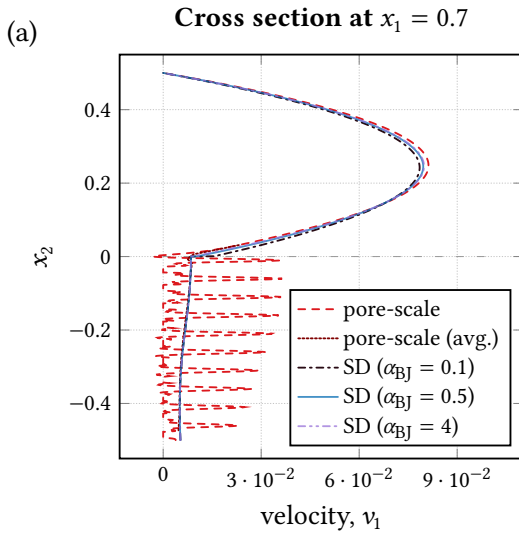
### Staggered elliptical inclusions tilted to the left

We consider a second anisotropic porous medium composed of  $80 \times 20$  elliptical solid inclusions distributed in a staggered manner, where the semi-major axis of an ellipse within the unit cell  $Y$  is rotated by  $\gamma = \pi/4$  clockwise to the negative part of the  $x_1$ -axis as depicted in Table 6.6 (right). In this case, the borders of the solid obstacles within the unit cell  $Y$  are given by

$$e(t) = (m_1, m_2) + 0.092(2 \cos(t) + \sin(t), -2 \cos(t) + \sin(t)), \quad (6.30)$$

with the center at  $(m_1, m_2) \in \{(0, 0.25), (0.5, 0.25), (1, 0.25), (0.25, 0.75), (0.75, 0.75)\}$ , and it is  $t \in [0, 2\pi)$  for  $m_1 \in \{0.25, 0.5, 0.75\}$ ,  $t \in [-1.107149, \pi - 1.107149)$  for  $m_1 = 0$  and  $t \in [\pi - 1.107149, 2\pi - 1.107149)$  for  $m_1 = 1$ . This pore geometry leads to a full permeability tensor  $\tilde{\mathbf{K}}$  which is given in Figure 6.6 (right).

We consider cross sections at  $x_1 = 0.7$ ,  $x_1 = 1.5$  and  $x_1 = 2.2$  to evaluate the microscale and macroscale numerical simulation results. As in the case of elliptical solid inclusions tilted to the right, we observe fluctuations in the pore-scale velocity profiles that appear naturally due to the presence of solid obstacles. We therefore provide in Figure 6.12 the averaged velocity profiles additionally to the nonaveraged ones. The averaged velocity field is obtained by means of adaptive volume averaging (Section 4.1). In Figure 6.12(a) velocity profiles in the left part of the coupled domain at  $x_1 = 0.7$  are presented. We investigated different values of the Beavers–Joseph parameter  $\alpha_{\text{BJ}} \in \{0.1, 0.2, \dots, 4\}$ , however, for all choices the macroscale velocity profiles significantly differ from the pore-scale solution. We provide profiles for the three representative values  $\alpha_{\text{BJ}} = 0.1$  (smallest value),  $\alpha_{\text{BJ}} = 0.5$  (optimal value at  $x_1 = 0.7$  in case of elliptical solid inclusions tilted to the right) and  $\alpha_{\text{BJ}} = 4$  (biggest value). Tangential velocity profiles in the horizontal center are presented in Figure 6.12(c). Here, we also cannot achieve a good match between the microscale and macroscale simulation results no matter which value of  $\alpha_{\text{BJ}}$  is chosen.



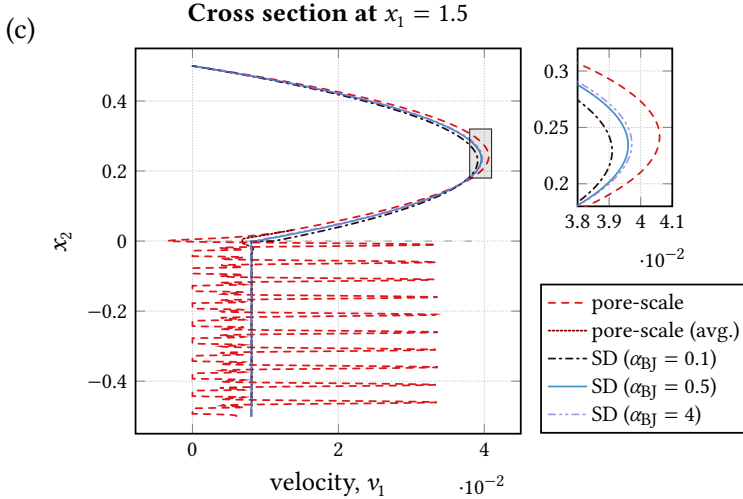


Figure 6.12: Velocity profiles of the tangential component (a) at  $x_1 = 0.7$ , (b) at  $x_1 = 2.2$  and (c) at  $x_1 = 1.5$  for filtration through T-shaped domain in case of elliptical inclusions tilted to the left.

Additionally, we provide velocity profiles at  $x_1 = 2.2$  (Figure 6.12(b)). In this case, the profile obtained from the pore-scale resolved simulations disagree completely with all profiles corresponding to the macroscale model independent of the choice of parameter  $\alpha_{BJ}$ . We claim that the main factor for these differences is the unsuitable coupling (6.10) at the fluid–porous interface  $\Sigma$ . To summarize, for this pore geometry the slip coefficient  $\alpha_{BJ}$  cannot be adjusted such that microscale and macroscale velocity profiles agree.

**Remark 6.2:** Considering the profiles in Figure 6.12, one could speculate that for the solid inclusions described by equation (6.30) the fluid–porous interface  $\Sigma$  is located at the wrong vertical position. To the best of our knowledge, there is no recommendation concerning the interface location for noncircular solid inclusions. Therefore, we cannot claim that the location on top of solid grains is valid for all porous structures and all flow regimes. However, we justify our choice as follows: i) interface location should be

*the same over the whole length of the porous-medium domain since the medium is periodic; ii) interface position should be chosen independently on the explicit geometrical configuration of the porous medium while the microscale interface roughness is the same. Since for oval inclusions tipped to the right (6.29) and tipped to the left (6.30) the pore-scale interface roughness is the same and for some cross sections the interface location seems to be correct (Figure 6.11), we place the interface directly on the top of the first row of solid inclusions.*

### 6.2.2 General filtration problem

In this section, we study a general filtration problem, where the flow direction is arbitrary to the porous medium, based on the problem analyzed in [EE7]. We consider the Stokes–Darcy model (6.3)–(6.6) with the classical interface conditions (6.7), (6.8) and (6.10) and use the two-level numerical algorithm from [EE7] to determine the optimal value  $\alpha_{\text{BJ}}^{\text{opt}}$  at various vertical cross sections. For every cross section, we find a different value for the Beavers–Joseph coefficient to be optimal, and thus, we conclude that there exists no global optimal value  $\alpha_{\text{BJ}}$ .

We consider the free-flow region  $\Omega_{\text{ff}} = (0, 1) \times (0, 0.5)$ , the fluid–porous interface  $\Sigma = (0, 1) \times \{0\}$  and the porous medium  $\Omega_{\text{pm}} = (0, 1) \times (-0.5, 0)$ . The latter includes  $20 \times 10$  circular solid inclusions ( $\varepsilon = 1/20$ ) with radius  $r = 0.25$  and the fluid–porous interface  $\Sigma$  is located directly on top of the inclusions. The corresponding unit cell  $Y$  and the permeability values are presented in Figure 6.7, where we also provide a depiction of the flow domain.

We impose the following boundary conditions for the pore-scale problem (6.1)–(6.2):

$$\bar{\mathbf{v}} = (0, -0.7 \sin(\pi x_1))^{\top} \quad \text{on } \Gamma_D^{\text{in}}, \quad \bar{\mathbf{v}} = \mathbf{0} \quad \text{on } \Gamma_D^{\text{wall}}, \quad (6.31)$$

$$\bar{\mathbf{v}} \cdot \mathbf{e}_2 = 0, \quad \bar{\mathbf{h}} \cdot \mathbf{e}_1 = 0 \quad \text{on } \Gamma_{D/N}^{\text{out}}, \quad (6.32)$$

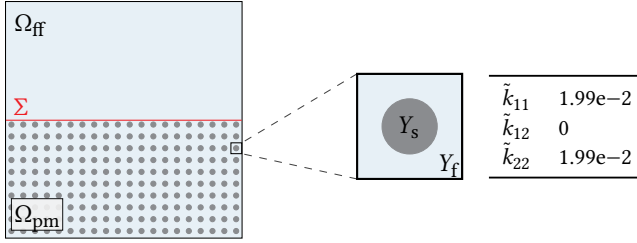


Table 6.7: Schematic setting of the flow domain (left), unit cell  $Y$  and permeability values (right) that are considered for the general filtration problem.

where  $\Gamma_D^{\text{in}} = (0, 1) \times \{0.5\}$ ,  $\Gamma_{D/N}^{\text{out}} = (\{0\} \times (0, 0.5)) \cup (\{1\} \times (0, 0.225))$ , and  $\Gamma_D^{\text{wall}} = \partial\Omega \setminus (\Gamma_D^{\text{in}} \cup \Gamma_D^{\text{out}})$ . We provide the pore-scale velocity field in Figure 6.13(a) and observe that the flow is nonparallel to the porous bed especially for  $x_1 > 0.5$ . The macroscale Stokes–Darcy model (6.3)–(6.8) and (6.10) is complemented with the following boundary conditions

$$\bar{\mathbf{v}} = (0, -0.7 \sin(\pi x_1))^T \quad \text{on } \Gamma_{D,ff}^{\text{in}}, \quad \bar{\mathbf{v}} = \mathbf{0} \quad \text{on } \Gamma_{D,ff}^{\text{wall}}, \quad (6.33)$$

$$\bar{\mathbf{v}} \mathbf{e}_2 = 0, \quad \bar{\mathbf{h}} \cdot \mathbf{e}_1 = 0 \quad \text{on } \Gamma_{D/N,ff}^{\text{out}}, \quad \bar{\mathbf{v}} = 0 \quad \text{on } \Gamma_{N,pm}^{\text{wall}}, \quad (6.34)$$

where  $\Gamma_{D,ff}^{\text{in}} = \Gamma_D^{\text{in}}$ ,  $\Gamma_{D/N,ff}^{\text{out}} = \Gamma_{D/N}^{\text{out}}$ ,  $\Gamma_{D,ff}^{\text{wall}} = \Gamma_D^{\text{wall}} \cap \partial\Omega_{ff}$  and  $\Gamma_{N,pm}^{\text{wall}} = \Gamma_D^{\text{wall}} \cap \partial\Omega_{pm}$ .

The microscale problem (6.1)–(6.2), (6.31)–(6.32) is solved using FREEFEM++ and we used approximately 330 000 finite elements to partition the computational domain  $\Omega^\varepsilon$ . The permeability values are obtained from the solutions to problems (2.74)–(2.76) that are solved on a mesh consisting of approximately 50 000 triangular elements. For the solution of the Stokes–Darcy problem (6.3)–(6.8), (6.33)–(6.34) with (6.10) we take the grid size  $h_x = h_y = 1/800$ .

The pore-scale velocity field according to problem (6.1)–(6.2), (6.31)–(6.32) is presented in Figure 6.13(a). Since the flow direction with respect to the

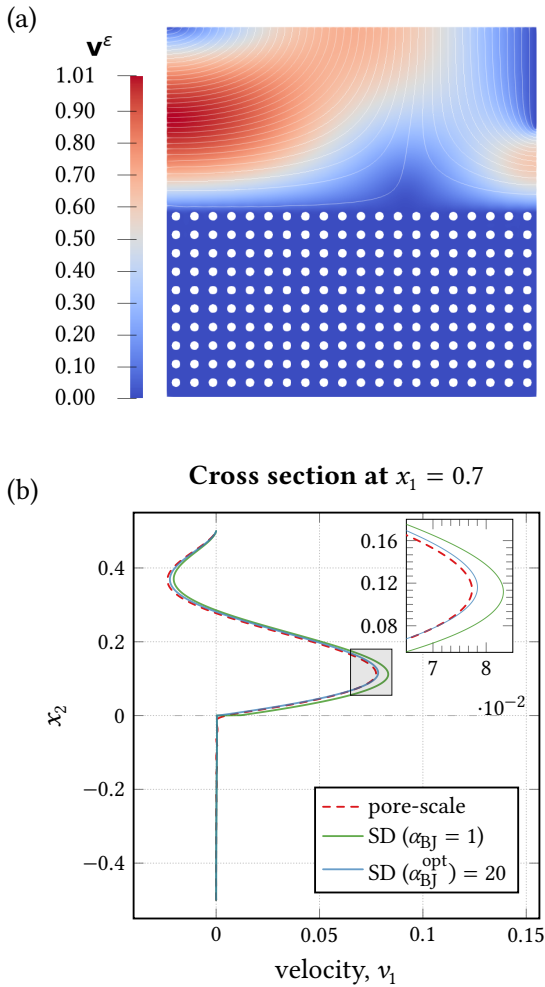


Figure 6.13: (a) Pore-scale velocity field and (b) tangential velocity profiles for the general filtration problem with geometry  $G_1$  and  $\varepsilon = 1/20$ .

porous layer is nonparallel and changes along the fluid–porous interface, we consider different cross sections for the determination of the optimal

value  $\alpha_{\text{BJ}}^{\text{opt}}$  of the Beavers–Joseph parameter in condition (2.19). Furthermore, we assume a broader range of the slip coefficient  $\alpha_{\text{BJ}} \in [0.01, 100]$  to allow for more flexibility. For this flow problem, both velocity components are nonzero on the fluid–porous interface, and thus, both are influenced by the choice of the Beavers–Joseph parameter. Therefore, in addition to the determination of  $\alpha_{\text{BJ}}^{\text{opt}}$  based on the minimal relative error (6.15) with respect to the tangential velocity  $v_1$ , we also determine  $\alpha_{\text{BJ}}^{\text{opt}}$  with respect to the normal velocity  $v_2$ .

Before, we present the optimal values  $\alpha_{\text{BJ}}^{\text{opt}}$  and the corresponding relative errors (6.15) for different cross sections (Table 6.8) we provide velocity profiles for the tangential component at  $x_1 = 0.7$  (Figure 6.13(b)). The macroscale tangential velocity profile with the typically used value  $\alpha_{\text{BJ}} = 1$  does not fit well to the pore-scale resolved model. Applying the two-level numerical algorithm [EE7], we found that the difference between the microscale and macroscale simulation results for the tangential velocity given by (6.15) becomes smaller for bigger values of the Beavers–Joseph slip coefficient  $\alpha_{\text{BJ}}$ . However, these improvements are minor for  $\alpha_{\text{BJ}} \in [20, 100]$ . Therefore, we take  $\alpha_{\text{BJ}}^{\text{opt}} = 20$  at  $x_1 = 0.7$  for the tangential velocity. As can be seen from Figure 6.13(b), the macroscale profile for  $\alpha_{\text{BJ}}^{\text{opt}} = 20$  fits much better to the pore-scale resolved model than for the traditionally used value  $\alpha_{\text{BJ}} = 1$ .

In total, we consider four different cross sections for the general filtration problem. The optimal values  $\alpha_{\text{BJ}}^{\text{opt}}$  and the corresponding errors (6.15) for both velocity components  $v_1$  and  $v_2$  and each cross section are provided in Table 6.8. Additionally, we compute the relative errors according to the value  $\alpha_{\text{BJ}} = 1$  that is often one order of magnitude bigger than the error for  $\alpha_{\text{BJ}} = \alpha_{\text{BJ}}^{\text{opt}}$ . We observe that the optimal value of Beavers–Joseph parameter is different for every cross section and each velocity component. Thus, for arbitrary flow directions to the porous bed the Beavers–Joseph slip coefficient  $\alpha_{\text{BJ}}$  is not constant along the interface and the optimal value cannot be found globally. This fact indicates that



Cross section	Velocity	$\alpha_{\text{BJ}}^{\text{opt}}$	Error $\epsilon_{v_i, x_1}$ for $\alpha_{\text{BJ}} = \alpha_{\text{BJ}}^{\text{opt}}$	Error $\epsilon_{v_i, x_1}$ for $\alpha_{\text{BJ}} = 1$
$x_1 = 0.5$	$v_1$	5.0	6.620e-3	2.484e-2
$x_1 = 0.5$	$v_2$	3.9	1.283e-3	8.858e-3
$x_1 = 0.7$	$v_1$	20.0	3.468e-2	9.901e-2
$x_1 = 0.7$	$v_2$	3.3	1.638e-3	1.087e-2
$x_1 = 0.8$	$v_1$	3.7	1.510e-2	4.039e-2
$x_1 = 0.8$	$v_2$	4.1	1.691e-3	1.108e-2
$x_1 = 0.9$	$v_1$	3.2	1.215e-2	3.529e-2
$x_1 = 0.9$	$v_2$	3.6	4.638e-3	9.416e-3

Table 6.8: Optimal Beavers–Joseph parameters and relative errors for the general filtration problem and geometry  $G_1$ .

the Beavers–Joseph condition (6.10) is not suitable for arbitrary flows in Stokes–Darcy systems.

### Summary of Section 6.2

We studied two flow problems, where the flow is arbitrary, i.e., neither parallel nor perpendicular to the porous layer, and analyzed the suitability of the Beavers–Joseph condition. Hereby, we considered homogeneous porous media and the interface positioned tangent to the top of solid grains. We demonstrated that it is not possible to find a constant Beavers–Joseph parameter  $\alpha_{\text{BJ}}$  along the fluid–porous interface such that pore-scale and macroscale numerical simulation results are in good agreement. However, this should be the case since the effective porous-medium properties such as microscale surface roughness, permeability and porosity do not change along the sharp interface. Thus, we showed that the Beavers–Joseph

condition and its modification by Saffman are unsuitable for the accurate coupling of the Stokes and Darcy flow equations.

### 6.3 Generalized coupling conditions

In this section, we validate the generalized coupling conditions (6.12)–(6.14) derived in Chapter 3 both for unidirectional and arbitrary flows to the fluid–porous interface, and compare them with the classical interface conditions. We consider various configurations of the porous medium and study three flow problems with different flow direction to the porous bed (parallel, slightly nonparallel, arbitrary). For all considered validation scenarios, we show that the Stokes–Darcy problem with the generalized interface conditions describes the fluid flow accurately. We compare the macroscale model with the generalized conditions (6.12)–(6.14) to the one with the classical coupling conditions (6.7)–(6.9) or (6.7), (6.8), (6.10) in order to highlight the advantages of the newly derived interface concept in case of unidirectional flows to the interface. Moreover, comparing the performance of both coupled Stokes–Darcy models confirms the findings from Section 6.2, i.e., the unsuitability of the classical conditions in case of arbitrary flow directions to the porous bed.

In Section 6.3.1, we consider pressure driven flow, where the flow is parallel to the fluid–porous interface. We demonstrate that the generalized interface conditions are valid and lead to a more accurate macroscale model in comparison to the classical coupling concept even if the most optimal Beavers–Joseph parameter  $\alpha_{\text{BJ}}$  is considered. In Section 6.3.2, we study double lid driven cavity flow over a porous medium, where the flow is nonparallel to the porous bed near the lateral boundaries and in the middle of the domain. This flow problem corresponds to the theoretical derivation of the generalized coupling conditions in Section 3.1. We validate the proposed conditions and show that they yield a more reliable macroscale model than the classical coupling conditions. In Section 6.3.3, we consider a general filtration problem, where the fluid flow is arbitrary to

the porous bed. We demonstrate that the generalized interface conditions are valid and that the classical coupling concept cannot be used to obtain a physically reasonable Stokes–Darcy model.

### 6.3.1 Pressure driven flow

We study the pore-scale flow problem (6.1)–(6.2), (6.16) describing pressure driven flow as in Section 6.1.1, where the classical coupling concept is validated. In this section, we apply the generalized interface conditions (6.12)–(6.14) on the fluid–porous interface in order to couple the Stokes and Darcy flow equations. In Section 6.3.1.1, we show that the corresponding Stokes–Darcy model is in very good agreement with the pore-scale model, and thus, the generalized interface conditions are valid in this case. Further, using the results from Section 6.1.1, we demonstrate that the classical coupling conditions yield a less accurate macroscale model even if the optimal slip coefficient  $\alpha_{\text{BJ}}^{\text{opt}}$  is considered. We recall that this value is determined by minimizing the error between the pore-scale and macroscale simulation results before the classical conditions are applied. Section 6.3.1.2 is dedicated to the question of when the generalized condition (6.14) reduces to the Beavers–Joseph condition (6.9). We show that this can happen only in case of very specific porous-medium geometrical configurations as already indicated in Section 3.2.3.

The pore-scale problem (6.1)–(6.2), (6.16) and the cell problems (2.74)–(2.76) are solved using `FREEFEM++`. The number of grid cells are the same as in Section 6.1.1. For the boundary layer problems (4.21)–(4.23) and (4.24)–(4.26) we use approximately 280 000 elements to resolve the flow domain  $Z_4$ . For the solution of the macroscale Stokes–Darcy problem given by (6.3)–(6.6), (6.17)–(6.19) with the generalized interface conditions (6.12)–(6.14) we take the grid size  $h_x = h_y = 1/800$ .

### 6.3.1.1 Validity of generalized interface conditions

In this section, we first show that the generalized interface conditions (6.12)–(6.14) are valid in case of pressure driven flow and that the exact interface location, which can be chosen in a certain range (see Section 3.2.2), influences the performance of the corresponding Stokes–Darcy model negligibly. Second, we use the results obtained in Section 6.1.1 to highlight the better suitability of the generalized conditions for the Stokes–Darcy coupling than the classical coupling concept. In order to address both aspects, we compare microscale and macroscale numerical simulation results along a fixed cross section and compute the relative errors (6.15).

The microscopic flow region  $\Omega^f$  is constructed by  $20 \times 10$  in-line arranged solid obstacles based on one of the representative geometries  $G_1$  to  $G_6$  described in Section 6.1.1. The corresponding unit cells  $Y = (0, 1)^2$  are presented in Table 6.1. The line tangent to the first row of solid grains is given by  $\{x_2 = 0\}$ . We consider the macroscopic domain  $\Omega$  consisting of the free-flow region  $\Omega_{\text{ff}} = (0, 1) \times (\gamma, 0.5)$  and the porous medium  $\Omega_{\text{pm}} = (0, 1) \times (-0.5, \gamma)$  separated by the horizontal interface  $\Sigma = (0, 1) \times \{\gamma\}$ . We investigate different vertical positions  $\gamma$  of the sharp interface within the coupled domain to illustrate the fact that the effective coefficients in the generalized conditions (6.12)–(6.14) include the information on the exact interface position. Thus, we show that the validity of the generalized coupling concept is independent of the choice of this position as mentioned in Section 3.2.2.

First, we study pressure driven flow described at the macroscale by (6.3)–(6.6), (6.17)–(6.17), (6.12)–(6.14) and consider the same fluid–porous interface as in Section 6.1.1, which is located on top of the solid inclusions. For the generalized interface conditions (6.12)–(6.14) effective coefficients are computed from the solutions of boundary layer problems (4.21)–(4.23) and (4.24)–(4.26), where the same interface location as for the macroscale model needs to be applied (see Section 4.3). Due to limitations on the mesh generation in FREEFEM++, which is used for the solution of boundary layer problems, it is not possible to place the interface directly on top of

	$G_1$	$G_2$	$G_3$	$G_4$	$G_5$	$G_6$
$\tilde{k}_{11}$	1.99e-2	5.67e-4	1.99e-2	5.63e-3	1.23e-2	1.23e-2
$\tilde{k}_{12}$	0	0	0	0	2.69e-3	-2.69e-3
$\tilde{k}_{22}$	1.99e-2	5.67e-4	1.99e-2	4.44e-3	1.23e-2	1.23e-2
$N_1^{\text{bl}}$	-5.48e-2	-4.44e-2	-2.44e-2	-2.82e-2	-5.68e-2	-5.68e-2
$N_s^{\text{bl}}$	0	0	0	0	-2.72e-2	2.72e-2
$M_1^{1,\text{bl}}$	-3.02e-3	-2.10e-3	-4.52e-4	-7.82e-4	-3.95e-3	-3.95e-3
$M_1^{2,\text{bl}}$	0	0	0	0	-3.34e-3	3.34e-3

Table 6.9: Permeability values (see Table 6.1) and boundary layer constants appearing in the generalized coupling conditions for geometries  $G_1$  to  $G_6$  and interface  $\Sigma_d$ .

the solid grains. However, we position the interface as close as possible at distance  $\gamma = 5e-5$  above the solid obstacles and denote it by  $\Sigma_d$ . The permeability values and the boundary layer constants appearing in conditions (6.12)–(6.14) corresponding to the sharp location  $\Sigma_d$  are provided in Table 6.9 for all considered geometries. The values  $\tilde{k}_{11}$ ,  $\tilde{k}_{12}$  and  $\tilde{k}_{22}$  for geometries  $G_1$  to  $G_6$  are already given in Table 6.1, but we included them also in Table 6.9 for the ease of comparison with the effective coefficients  $M_1^{j,\text{bl}}$  for  $j = 1, 2$  later. We recall that the permeability tensor  $\tilde{\mathbf{K}}$  is not dependent on the exact interface position.

In Table 6.10 (last column), we present the errors between the pore-scale and the macroscale simulation results introduced in (6.15) for the representative pore geometries  $G_1$  to  $G_6$  in case the generalized interface conditions (GIC) are applied. Additionally, we provide the errors obtained in Section 6.1.1 (Table 6.2) for the classical interface conditions both with the optimal value  $\alpha_{\text{BJ}}^{\text{opt}}$  of the Beavers–Joseph parameter, which needs to be determined (e.g., using the two-scale numerical algorithm from [EE7]), and the typically used value  $\alpha_{\text{BJ}} = 1$ . Note that  $\alpha_{\text{BJ}}^{\text{opt}}$  is different for the geometries  $G_1$  to  $G_6$  and is provided in Table 6.2. From Table 6.9, we observe that the errors in case of the generalized coupling conditions are

Geometry	Error $\epsilon_{v_1,0.5}$ for $\alpha_{\text{BJ}} = \alpha_{\text{BJ}}^{\text{opt}}$	Error $\epsilon_{v_1,0.5}$ for $\alpha_{\text{BJ}} = 1$	Error $\epsilon_{v_1,0.5}$ for GIC
$G_1$	3.401e-3	2.794e-2	1.205e-3
$G_2$	2.838e-3	6.941e-3	1.044e-3
$G_3$	2.632e-3	3.758e-2	1.176e-3
$G_4, \sqrt{\tilde{K}} = \sqrt{\tilde{k}_{11}}$	4.092e-3	3.089e-2	1.257e-3
$G_5$	2.901e-3	1.738e-2	7.779e-4
$G_6$	2.901e-3	1.738e-2	8.253e-4

*Table 6.10: Relative errors (6.15) with respect to  $v_1$  in case of different coupling conditions for the Stokes–Darcy problem describing pressure driven flow: classical conditions with  $\alpha_{\text{BJ}} = \alpha_{\text{BJ}}^{\text{opt}}$ ; classical conditions with  $\alpha_{\text{BJ}} = 1$ ; and generalized interface conditions (GIC).*

significantly smaller than for the classical interface conditions if  $\alpha_{\text{BJ}} = 1$  is taken. Moreover, even if the most optimal value  $\alpha_{\text{BJ}}^{\text{opt}}$  of the Beavers–Joseph parameter is applied, the generalized interface conditions lead to a more accurate Stokes–Darcy model than the classical coupling concept.

In Section 3.2.2, we explained how the exact location of the fluid–porous interface is included in the boundary layer coefficients and that one has freedom to choose this interface location within a certain range. In order to demonstrate the validity of the generalized interface conditions independent of the chosen interface position, we investigate a second interface location  $\Sigma_0$  (in case of geometry  $G_1$ ) that is also considered in [34, 97]. The interface  $\Sigma_0$  is located on top of the uppermost unit cell within the porous-medium domain at  $\gamma = 1/2(\varepsilon - d^\varepsilon)$ , where  $d^\varepsilon = d^* \varepsilon$  is the diameter of the solid inclusions within the flow domain  $\Omega^\varepsilon$  (Figure 6.14). We recall that in our case, for geometry  $G_1$ , the diameter of the grains within unit cell  $Y$  is  $d^* = 0.5$  and the characteristic pore size is  $\varepsilon = 1/20$ . For the interface location  $\Sigma_0$  and geometry  $G_1$ , we obtain the following boundary

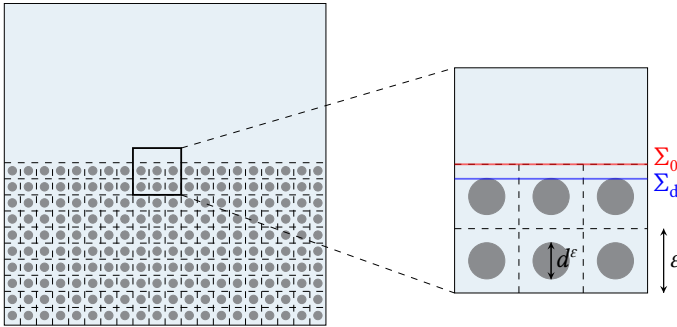


Figure 6.14: Interface locations  $\Sigma_d$  (blue) and  $\Sigma_0$  (red) in case of geometry  $G_1$ .

layer constants

$$N_1^{\text{bl}} = -3.04\text{e-}1, \quad N_s^{\text{bl}} = 0, \quad M_1^{1,\text{bl}} = -4.77\text{e-}2, \quad M_1^{2,\text{bl}} = 0. \quad (6.35)$$

We observe that the values for  $N_1^{\text{bl}}$  and  $M_1^{1,\text{bl}}$  in case of  $\Sigma_d$  (Table 6.9) are bigger as the values provided in (6.35) according to  $\Sigma_0$ . This is in agreement with our findings in Section 3.2.2.

We compare tangential velocity profiles of the pore-scale and macroscale solution in Figure 6.15. The profiles corresponding to the Stokes–Darcy problem with the generalized interface conditions for the two interface locations  $\Sigma_d$  (profile: SD–GIC ( $\Sigma_d$ )) and  $\Sigma_0$  (profile: SD–GIC ( $\Sigma_0$ )) coincide in the free-flow region and porous-medium domain. Minor differences between these two profiles are observable very close to the interface that is expected since the exact position of the fluid–porous interface is different. Moreover, both macroscale velocity profiles corresponding to the generalized interface conditions fit very well to the pore-scale results. Hence, for different choices of the sharp interface position one obtains an accurate Stokes–Darcy model. This finding confirms the theoretical arguments from Section 3.2.2 that the boundary layer constants incorporate the information of the exact interface location. In addition, Figure 6.15 shows velocity profiles in case the classical interface conditions are consid-

ered for the Stokes–Darcy coupling. For the classical conditions we first consider the recommended interface  $\Sigma_d$  (Figure 6.14, blue line) for two values of the Beavers–Joseph parameter:  $\alpha_{\text{BJ}} = \alpha_{\text{BJ}}^{\text{opt}} = 2.8$ , the optimal one for geometry  $G_1$ , and the commonly applied one  $\alpha_{\text{BJ}} = 1$ . We observe that the macroscale profile for  $\alpha_{\text{BJ}} = 2.8$  (profile: SD ( $\alpha_{\text{BJ}} = 2.8, \Sigma_d$ )) is in good agreement with the pore-scale profile whereas this is not the case for the profile that belongs to  $\alpha_{\text{BJ}} = 1$  (profile: SD ( $\alpha_{\text{BJ}} = 1, \Sigma_d$ )). Second, for the sake of completeness, we apply the classical coupling concept also on the interface  $\Sigma_0$ . We observe from Figure 6.15 that the typically used value  $\alpha_{\text{BJ}} = 1$  (profile: SD ( $\alpha_{\text{BJ}} = 1, \Sigma_0$ )) is unsuitable for the Stokes–Darcy coupling in this case since the corresponding macroscale profile does not agree at all with the pore-scale result. However, due to the fact that the flow is parallel to the porous bed, an optimal value  $\alpha_{\text{BJ}}^{\text{opt}}$  can be determined (see Section 6.1.1). In this case, for geometry  $G_1$  and the interface position  $\Sigma_0$ , we find  $\alpha_{\text{BJ}}^{\text{opt}} = 0.4$  (profile: SD ( $\alpha_{\text{BJ}} = 0.4, \Sigma_0$ )).

Thus, we found out that the Stokes–Darcy problem (6.3)–(6.6) with the generalized interface conditions (6.12)–(6.14) represent the fluid flow very accurately in case of pressure driven flow. The performance of

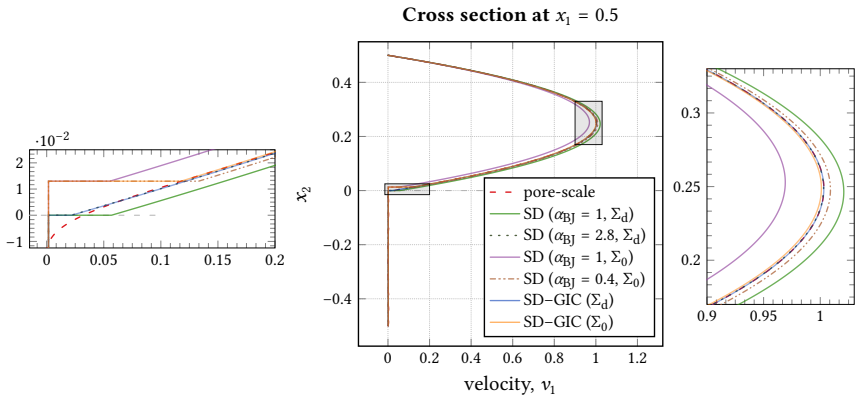


Figure 6.15: Velocity profiles for the tangential component at  $x_1 = 0.5$  for pressure driven flow and geometry  $G_1$ .



the macroscale model with the classical interface conditions (6.7)–(6.9) can be nearly as good as in case of the generalized conditions, however, only if the optimal Beavers–Joseph parameter  $\alpha_{\text{BJ}}$  is used. The typical choice  $\alpha_{\text{BJ}} = 1$  is not suitable for many problems, and thus, the correct determination of the Beavers–Joseph slip coefficient is crucial. To overcome this task, we recommend using the generalized interface conditions, where all parameters are computed, instead of applying the classical coupling concept.

### 6.3.1.2 Recovery of original Beavers–Joseph condition

In Section 3.2.3, we have shown that the generalized condition for the tangential velocity can be written in the same form (6.14) as the Beavers–Joseph condition (6.9). Moreover, we mentioned that for some specific porous-medium geometries it is possible to find a sharp interface location such that  $\mathbf{v}^{\text{pm}} \cdot \boldsymbol{\tau} = \mathbf{v}_{\text{int}}^{\text{pm}} \cdot \boldsymbol{\tau}$ , and thus, equations (6.9) and (6.14) are the same. In the following, we focus on this aspect.

First, we define the nondimensional velocity  $\mathbf{v}_{\text{int}}^{\text{pm}}$  in analogy to the interfacial porous-medium velocity that was introduced in Section 3.2.3 for the dimensional setting. In case of a horizontal fluid–porous interface the interfacial porous-medium velocity reads

$$\mathbf{v}_{\text{int}}^{\text{pm}} = -\varepsilon^2 \begin{pmatrix} -M_1^{1,\text{bl}} & -M_1^{2,\text{bl}} \\ -M_2^{1,\text{bl}} & -M_2^{2,\text{bl}} \end{pmatrix} \nabla p^{\text{pm}}.$$

Thus, in order to obtain  $\mathbf{v}^{\text{pm}} \cdot \boldsymbol{\tau} = \mathbf{v}_{\text{int}}^{\text{pm}} \cdot \boldsymbol{\tau}$  on  $\Sigma$  we need to have  $-M_1^{1,\text{bl}} = \tilde{k}_{11}$  and  $-M_1^{2,\text{bl}} = \tilde{k}_{12}$ . Second, we recall from Section 3.2.2 that the boundary layer constants  $N_1^{\text{bl}}$  and  $M_1^{1,\text{bl}}$  increase monotonically for  $a \rightarrow 0$ , where  $a$  denotes the distance of the interface  $S$  within the boundary layer stripe from the top of solid grains (Figure 4.7). Thus, for the interface tangent to the solid inclusions we obtain the greatest values for the coefficients  $N_1^{\text{bl}}$  and  $M_1^{1,\text{bl}}$ . Here, this interface is denoted by  $S_{0,001}$  and corresponds to the interface  $\Sigma_d$  within the macroscopic domain  $\Omega$ . The computed values

for the boundary layer constants with respect to  $S_{0.001}$ , or equivalently,  $\Sigma_d$  are provided in Table 6.9. Furthermore, in Section 3.2.2 we found out that the constants  $N_s^{\text{bl}}$  and  $M_1^{2,\text{bl}}$  are not affected by a change of the sharp interface location.

Analyzing the permeability values and boundary layer constants in Table 6.9 for the geometries  $G_1$  to  $G_6$ , we observe that: i) for geometries  $G_1$ ,  $G_3$  and  $G_4$  we have  $\tilde{k}_{11} > -M_1^{1,\text{bl}}$ , and thus, it is possible to find a sharp interface location above the solid obstacles such that  $\tilde{k}_{11} = -M_1^{1,\text{bl}}$  that leads to  $\mathbf{v}^{\text{pm}} \cdot \boldsymbol{\tau} = \mathbf{v}_{\text{int}}^{\text{pm}} \cdot \boldsymbol{\tau}$ ; ii) for geometry  $G_2$  it is  $\tilde{k}_{11} < -M_1^{1,\text{bl}}$  yielding  $\mathbf{v}^{\text{pm}} \cdot \boldsymbol{\tau} \neq \mathbf{v}_{\text{int}}^{\text{pm}} \cdot \boldsymbol{\tau}$  for any interface location; and iii) for the anisotropic porous-medium geometries  $G_5$  and  $G_6$  we have  $\tilde{k}_{12} \neq -M_1^{2,\text{bl}}$ , hence, we always have  $\mathbf{v}^{\text{pm}} \cdot \boldsymbol{\tau} \neq \mathbf{v}_{\text{int}}^{\text{pm}} \cdot \boldsymbol{\tau}$ .

Further numerical experiments revealed that for each shape and arrangement of the solid inclusions, which lead to an orthotropic porous medium (e.g., circular, square, rhombus), there exists a critical value of porosity  $\phi_0^{\text{shape, arrangement}}$  such that  $\mathbf{v}^{\text{pm}} \cdot \boldsymbol{\tau} = \mathbf{v}_{\text{int}}^{\text{pm}} \cdot \boldsymbol{\tau}$  for the interface  $S_{0.001}$  tangent to the solid obstacles. Then, for all porous structures with  $\phi < \phi_0^{\text{shape, arrangement}}$ , which are characterized by the same shape of solid grains and same type of arrangement, it is not possible to obtain  $\mathbf{v}^{\text{pm}} \cdot \boldsymbol{\tau} = \mathbf{v}_{\text{int}}^{\text{pm}} \cdot \boldsymbol{\tau}$  for any interface location  $S_a$ , and thus, condition (6.14) does not simplify to the Beavers–Joseph condition (6.9). For in-line arranged circular solid grains we find  $\phi_0 = \phi_0^{\text{circular, in-line}} \approx 0.5211$ .

We consider geometry  $G_1$  having  $\phi \approx 0.80365 > \phi_0^{\text{circular, in-line}}$  exemplary to determine the interface location  $S_a$  at distance  $a$  above the solid inclusions such that  $\tilde{k}_{11} = -M_1^{1,\text{bl}}$ . For this purpose, we start with the interface  $S_{0.001}$ , move it stepwise by distance 0.001 away from the solid obstacles and for each location we compute the constant  $M_1^{1,\text{bl}}$  until we have  $-\tilde{k}_{11} = M_1^{1,\text{bl}}$ . This equality of effective coefficients for  $G_1$  is obtained if  $S_{0.138}$  is considered. According to the determined interface location  $S_{0.138}$ , we compute the boundary layer constant  $N_1^{\text{bl}}$  and obtain the

slip coefficient  $\alpha_{\text{BJ}}$  appearing in (6.9) via  $\alpha_{\text{BJ}} = -\sqrt{\tilde{k}_{11}}/N_1^{\text{bl}}$ . For geometry  $G_1$ , we get  $N_1^{\text{bl}} = -1.92\text{e}-2$  leading to  $\alpha_{\text{BJ}} = 7.3$ .

Based on the observations we made in this section, we conclude that for some orthotropic porous-medium geometries it is possible to obtain  $\mathbf{v}^{\text{pm}} = \mathbf{v}_{\text{int}}^{\text{pm}}$  by the appropriate choice of interface location. However, this is in general not the case (see geometry  $G_2$ ). For anisotropic porous media having a full tensor  $\tilde{\mathbf{K}}$  the Darcy velocity  $\mathbf{v}^{\text{pm}}$  appearing in the Beavers–Joseph condition (6.9) is always different from  $\mathbf{v}_{\text{int}}^{\text{pm}}$  in the generalized condition (6.14).

### 6.3.2 Double lid driven cavity over porous bed

In this section, we consider a flow problem that corresponds to the problem considered for the theoretical derivation of the generalized conditions (see Section 3.1.1). Here, the fluid flow is arbitrary to the fluid–porous interface near the horizontal middle and lateral boundaries of the flow domain, and in between it is almost parallel to the porous bed (Figure 6.16, right). We validate the generalized interface conditions (6.12)–(6.14) and show that they are more accurate than the classical set of coupling conditions (6.7)–(6.9). The free-flow region  $\Omega_{\text{ff}} = (0, 1) \times (\gamma, 0.5)$  and the porous-medium domain  $\Omega_{\text{pm}} = (0, 1) \times (-0.5, \gamma)$  are divided by the sharp interface  $\Sigma = (0, 1) \times \{\gamma\}$ , where  $\gamma$  determines the exact location of the interface in vertical direction. The porous medium is isotropic, constructed by  $20 \times 10$  circular solid obstacles with radius  $r^\varepsilon = 0.25\varepsilon$ , where  $\varepsilon = 1/20$ . Permeability values and boundary layer constants appearing in the macroscopic flow models are provided in Figure 6.16 (left). We introduce two different positions of the fluid–porous interface (Figure 6.14):  $\Sigma_0$  taking  $\gamma = 0$  that is located at the top of the upper unit cell, at distance  $(1/2 - r)\varepsilon$  above the top of the solid grains,  $\Sigma_{\text{d}}$  taking  $\gamma = -\varepsilon/2 + r$  that is located directly on top of the solid inclusions.

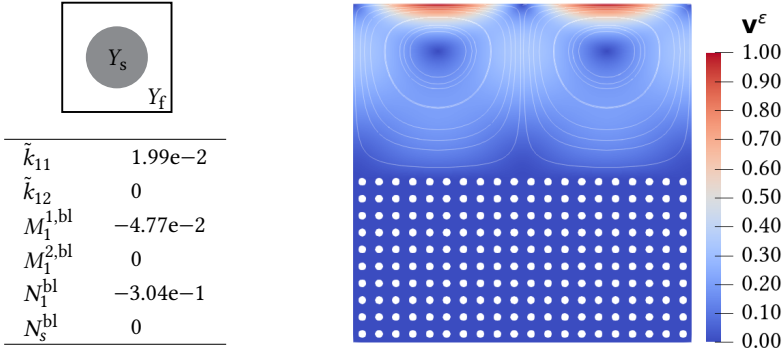


Figure 6.16: Effective coefficients appearing in the generalized conditions (left) and pore-scale velocity field for double lid driven cavity flow over porous bed (right).

The pore-scale problem (6.1)–(6.2) is completed with the following conditions on the external boundary

$$\begin{aligned} \bar{\mathbf{v}} &= (\sin(2\pi x_1), 0)^\top \text{ on } \Gamma_D^{\text{in}}, & \bar{\mathbf{v}}\mathbf{n} &= \bar{\mathbf{h}}\cdot\boldsymbol{\tau} = 0 \text{ on } \Gamma_{D/N}^{\text{out}}, \\ \{\mathbf{v}^\epsilon, p^\epsilon\} & \text{ is 1-periodic,} \end{aligned} \quad (6.36)$$

where  $\Gamma_D^{\text{in}} = (0, 1) \times \{0.5\}$  and  $\Gamma_{D/N}^{\text{out}} = (0, 1) \times \{-0.5\}$ . The pore-scale velocity field is shown in Figure 6.16 (right). The boundary conditions for the Stokes–Darcy model (6.3)–(6.6) corresponding to (6.36) read

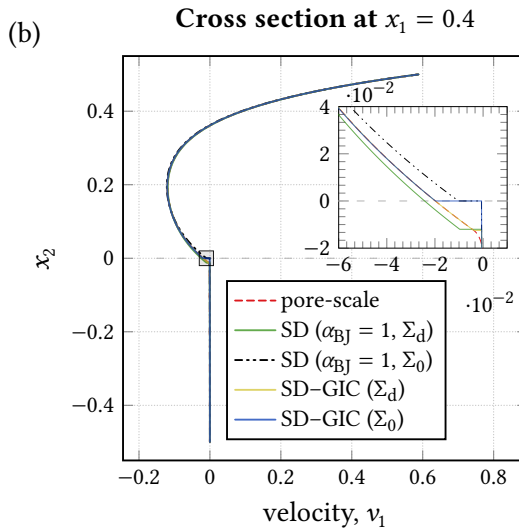
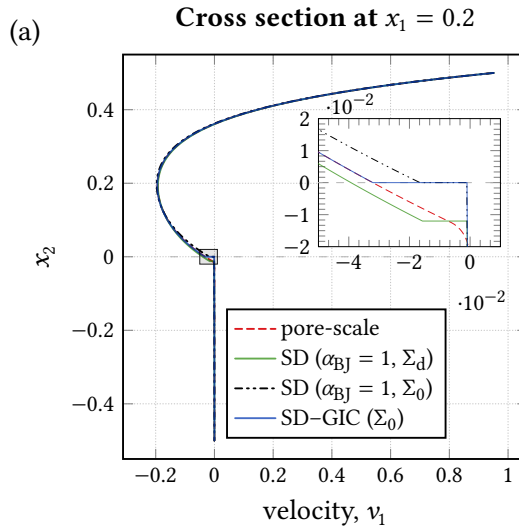
$$\begin{aligned} \bar{\mathbf{v}} &= (\sin(2\pi x_1), 0)^\top \text{ on } \Gamma_{D,ff}^{\text{in}}, & \bar{\mathbf{v}} &= 0 \text{ on } \Gamma_{N,pm}^{\text{out}}, \\ \{\mathbf{v}^{\text{ff}}, p^{\text{ff}}, p^{\text{pm}}\} & \text{ is 1-periodic,} \end{aligned} \quad (6.37)$$

where we set  $\Gamma_{D,ff}^{\text{in}} = \Gamma_D^{\text{in}}$  and  $\Gamma_{N,pm}^{\text{out}} = \Gamma_{D/N}^{\text{out}}$ . We apply both the generalized coupling conditions (6.12)–(6.14) and the classical ones (6.7)–(6.9) taking  $\alpha_{\text{BJ}} = 1$  on the fluid–porous interface to obtain a closed macroscale model formulation. Without the loss of generality, we consider the interface location  $\Sigma_0$  for the generalized interface conditions, if not stated otherwise. This position of the fluid–porous interface is also consid-

ered in, e.g., [33, 34, 96, 97], where effective interface conditions for the Stokes–Darcy problem are derived using the same averaging techniques as in Chapter 3. For the classical set of coupling conditions, we apply both interface locations  $\Sigma_0$  and  $\Sigma_d$  since  $\Sigma_d$  is recommended to use in [15, 106, EE6].

The Stokes system (6.1)–(6.2), (6.36) is solved using an adaptive mesh with approximately 330 000 triangular elements. For the numerical solution of the cell problems (2.74)–(2.76) approximately 30 000 triangular elements are considered. The boundary layer problems given by (4.21)–(4.23) and (4.24)–(4.26) are solved taking approximately 120 000 elements. For solving the coupled Stokes–Darcy problems (6.3)–(6.6), (6.37) with interface conditions (6.7)–(6.9) or (6.12)–(6.14) we apply a staggered grid with mesh size  $h_x = h_y = 1/800$ .

Figure 6.17 provides velocity and pressure profiles for two vertical cross sections, where the flow is nonparallel to the porous layer. We observe that the velocity profiles corresponding to the pore-scale model and the macroscale model with both, the classical and the generalized coupling conditions, agree to a large extent (Figures 6.17(a), 6.17(b) and 6.17(c)). We further analyze the different coupled Stokes–Darcy models by assessing the conformance of corresponding macroscale simulation results and pore-scale results above the fluid–porous interface as it is done in [EE4]. Taking into account the zoomed regions in Figures 6.17(a) and 6.17(b), we find out that the newly derived interface conditions lead to tangential velocity profiles that fit almost perfectly to the pore-scale profiles. Such a good match between pore-scale and macroscale velocity  $v_1$  above the interface cannot be achieved with the classical coupling concept for the standard choice  $\alpha_{\text{BJ}} = 1$ , no matter which interface location is considered.



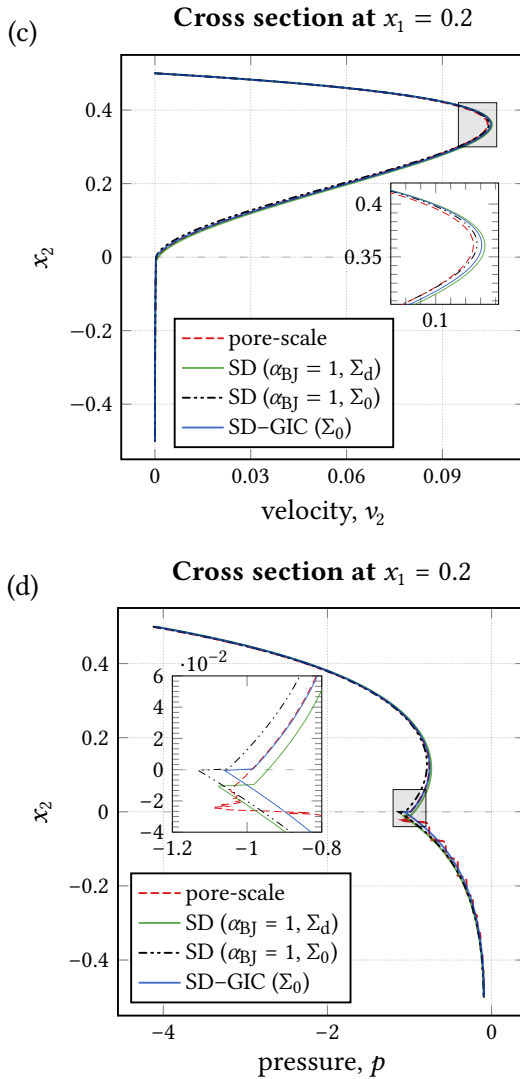


Figure 6.17: Velocity and pressure profiles for double lid driven cavity over porous bed.

Interface location	Error $\epsilon_{v_1,0.4}$ ( $\alpha_{BJ} = 1$ )	Error $\epsilon_{v_1,0.4}$ for GIC
$\Sigma_0$	2.003e-2	1.176e-2
$\Sigma_d$	9.567e-3	2.373e-3

*Table 6.11: Relative errors (6.15) with respect to  $v_1$  and the cross section at  $x_1 = 0.4$  in case of different coupling conditions and different interface locations for the Stokes–Darcy problem describing double lid driven cavity over a porous bed: classical conditions with  $\alpha_{BJ} = 1$  and generalized conditions (GIC) on  $\Sigma_0$  and  $\Sigma_d$ , respectively.*

In addition to these observations, we quantify the differences between the microscale and macroscale simulation results by computing the relative errors (6.15) with respect to  $v_1$  for the cross section at  $x_1 = 0.4$  (Table 6.11). We observe that the error  $\epsilon_{v_1,0.4}$  for the generalized conditions on  $\Sigma_0$  is smaller than the one for the classical conditions on  $\Sigma_0$ , but a little larger than the error for the classical conditions on  $\Sigma_d$ . The reason for that is the better agreement of pore-scale and macroscale profiles for  $x_2 < 0$  in case of  $\Sigma_d$  compared to  $\Sigma_0$  for this validation case. Therefore, to make a fair comparison, we consider the interface  $\Sigma_d$  also for the generalized conditions and compute the corresponding relative error  $\epsilon_{v_1,0.4}$  (Table 6.11). The boundary layer constants according to  $\Sigma_d$  read

$$N_1^{\text{bl}} = -5.48\text{e-}2, \quad N_s^{\text{bl}} = 0, \quad M_1^{1,\text{bl}} = -3.02\text{e-}3, \quad M_1^{2,\text{bl}} = 0.$$

From Table 6.11 we observe that the newly derived interface conditions applied on  $\Sigma_d$  lead to the smallest relative error. The same observation are made for the cross section at  $x_1 = 0.2$ . We provide the corresponding tangential velocity profile (profile: SD–GIC ( $\Sigma_d$ )) for the cross section at  $x_1 = 0.4$  in Figure 6.17(b). This profile already fits to the pore-scale profile directly above  $\Sigma_d$ .

Differences between the pore-scale pressure and the macroscale pressure corresponding to the classical interface conditions for both interface locations are more evident than for the velocity (Figure 6.17(d)). We



observe that the pressure profile corresponding to the Stokes–Darcy model with the generalized interface conditions is in very good agreement with the pore-scale results and that the performance of the macroscale model with the classical coupling conditions and the interface  $\Sigma_0$  is worst.

To summarize, for double lid driven cavity flow over a porous medium we observed that the error (6.15) with respect to the tangential velocity and the interface position  $\Sigma_i$ ,  $i \in \{0, d\}$  is smaller for the generalized conditions than for the classical coupling conditions. Furthermore, we found out that the macroscale simulation results applied on the interface  $\Sigma_d$ , which is located tangent to the solid inclusions, agree better with the pore-scale results than for the interface  $\Sigma_0$  for this validation case. We showed that the Stokes–Darcy model with the new interface conditions (6.12)–(6.14) applied on  $\Sigma_d$  is the most accurate coupled model.

### 6.3.3 General filtration problem

In this section, we demonstrate that the newly developed interface conditions (6.12)–(6.14) are also valid for general coupled problems, where the fluid flow is arbitrary to the porous medium, but which are not restricted to periodic conditions on the lateral boundaries. Furthermore, we show that the classical interface conditions (6.7)–(6.9) are not suitable in this case that confirms our findings from Section 6.2. We consider the free-flow region  $\Omega_{\text{ff}} = (0, 1) \times (\gamma, 0.5)$  overlying the porous domain  $\Omega_{\text{pm}} = (0, 1) \times (-0.5, \gamma)$  and the sharp interface  $\Sigma$  located at  $x_2 = \gamma$ . For the porous domain we study two different geometries leading to an isotropic or anisotropic porous medium, respectively. Both geometrical configurations are constructed based on the periodic repetition of the scaled unit cell  $\varepsilon Y = (0, \varepsilon)^2$  that includes one circular respective elliptical solid grain. The corresponding unit cells  $Y$  and the nondimensional effective coefficients for the two porous-medium geometries are presented in Figures 6.18 (left) and 6.20 (left). In total, there are  $20 \times 10$  solid obstacles present in the porous region  $\Omega_{\text{pm}}$  leading to the nondimensional characteristic pore size  $\varepsilon = 1/20$ .

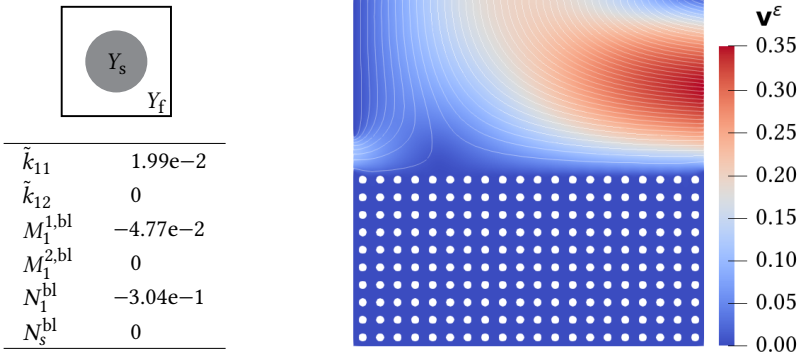


Figure 6.18: Effective coefficients (left) and pore-scale velocity field for the general filtration problem (right) in case of the isotropic porous medium.

At the pore scale, the general filtration problem is described by the Stokes equations (6.1)–(6.2) with the following boundary conditions

$$\bar{\mathbf{v}} = (0, -0.2 \sin(\pi x_1))^T \quad \text{on } \Gamma_D^{\text{in}}, \quad \bar{\mathbf{v}} = \mathbf{0} \quad \text{on } \Gamma_D^{\text{wall}}, \quad (6.38)$$

$$\bar{\mathbf{h}} = \mathbf{0} \quad \text{on } \Gamma_{N,ff}, \quad \bar{\mathbf{h}} = (0, -p_b)^T \quad \text{on } \Gamma_{N,pm}, \quad (6.39)$$

where  $\Gamma_D^{\text{in}} = (0, 1) \times \{0.5\}$ ,  $\Gamma_{N,ff} = (\{0\} \times (0, 0.1)) \cup (\{1\} \times (0, 0.5))$ ,  $\Gamma_{N,pm} = (0, 1) \times \{-0.5\}$  and  $\Gamma_D^{\text{wall}} = \partial\Omega \setminus (\Gamma_D^{\text{in}} \cup \Gamma_{N,ff} \cup \Gamma_{N,pm})$ .

The corresponding flow problem at the macroscale is given by the Stokes–Darcy problem (6.3)–(6.5) either with conditions (6.7)–(6.9) or (6.12)–(6.14) and completed with the following conditions on the external boundary

$$\bar{\mathbf{v}} = (0, -0.2 \sin(\pi x_1))^T \quad \text{on } \Gamma_D^{\text{in}}, \quad \bar{\mathbf{v}} = \mathbf{0} \quad \text{on } \Gamma_{D,ff}^{\text{wall}}, \quad (6.40)$$

$$\bar{\mathbf{h}} = \mathbf{0} \quad \text{on } \Gamma_{N,ff}, \quad \bar{\mathbf{v}} = \mathbf{0} \quad \text{on } \Gamma_{N,pm}^{\text{wall}}, \quad \bar{p} = p_b \quad \text{on } \Gamma_{D,pm}. \quad (6.41)$$

Here, we set  $\Gamma_{D,ff}^{\text{wall}} = \Gamma_D^{\text{wall}} \cup \partial\Omega_{ff}$ ,  $\Gamma_{D,pm}^{\text{wall}} = \Gamma_D^{\text{wall}} \cup \partial\Omega_{pm}$  and  $\Gamma_{D,pm} = \Gamma_{N,pm}$ . Boundary conditions (6.38)–(6.39) and (6.40)–(6.41) yield a flow system where the flow direction is arbitrary to the porous medium. We provide the

pore-scale flow field in case of the isotropic porous medium in Figure 6.18 (right) and in case of the anisotropic medium in Figure 6.20 (right). We observe that within the left part of the flow region ( $x_1 < 0.5$ ) the flow is highly nonparallel to the fluid–porous interface, whereas in the right part ( $x_1 > 0.5$ ) the flow becomes increasingly parallel to the porous medium.

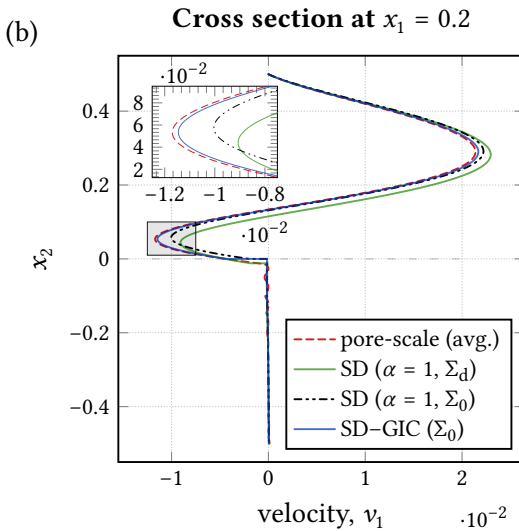
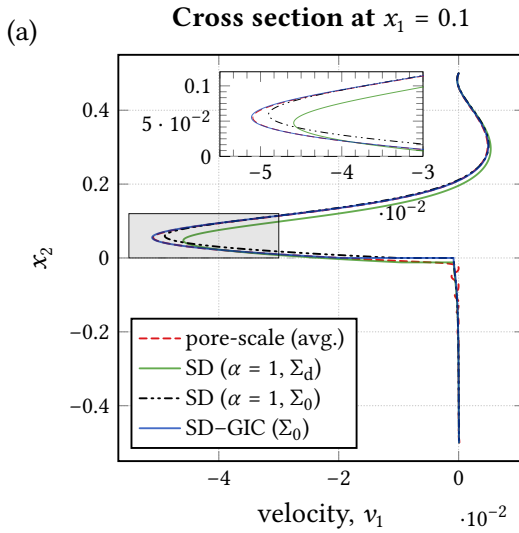
For the classical set of coupling conditions (6.7)–(6.9) we consider two different choices for the fluid–porous interface as in Section 6.3.2:  $\Sigma_0$  located at  $x_2 = 0$  and  $\Sigma_d$  located directly on top of the solid inclusions that is recommended in case of circular solid grains [106, 117, EE6]. Note that the vertical position  $\Sigma_d$  is different for the two porous-medium geometries we study within this section since the size  $d^*$  of the solid obstacles is different. For the set of generalized interface conditions (6.12)–(6.14) we chose the interface  $\Sigma_0$ .

The pore-scale problem (6.1)–(6.2), (6.38)–(6.39) is solved using approximately 330 000 triangular elements in case of the isotropic geometry to resolve the flow domain  $\Omega^\varepsilon$ . Due to the presence of solid obstacles in the porous medium, the pore-scale solution fluctuates. To make the comparison of microscale and macroscale simulation results easier, the pore-scale simulations are averaged using ensemble averaging as described in Section 4.1.2. The cell problems (2.74)–(2.76) are solved with a mesh consisting of approximately 30 000 elements and for the boundary layer problems (4.21)–(4.23) and (4.24)–(4.26) we use approximately 120 000 elements. For solving the macroscale Stokes–Darcy problems (6.3)–(6.6), (6.40)–(6.41) with (6.7)–(6.9) or (6.12)–(6.14) we take the grid size  $h_x = h_y = 1/800$ .

### Isotropic porous medium

We consider the porous-medium constructed based on the unit cell  $Y = (0, 1)^2$  that includes one circular solid grain with the center at  $(0.5, 0.5)$  and radius  $r = 0.25$ . This yields an isotropic porous medium and the corresponding permeability and boundary layer constants are presented in Figure 6.18 (left).

Figure 6.19 shows velocity and pressure profiles corresponding to the pore-scale and macroscale problems at different vertical cross sections. We provide profiles for the tangential velocity component at  $x_1 = 0.1$  and  $x_1 = 0.2$  where the flow is nonparallel to the interface. The velocity profiles corresponding to the generalized interface conditions provide a very good agreement with the averaged pore-scale velocity profiles (profile: pore-scale (avg.)) as can be observed from Figures 6.19(a) and 6.19(b). Numerical simulation results for the Stokes–Darcy model with the classical coupling conditions do not match to the pore-scale results no matter which interface location,  $\Sigma_0$  or  $\Sigma_d$ , is chosen (Figures 6.19(a) and 6.19(b)). We observe that the results for the classical interface conditions and location  $\Sigma_0$  provide a slightly better fitting than the results for the interface position  $\Sigma_d$ . In Figure 6.19(c) we provide the profiles for the normal component of velocity at  $x_1 = 0.1$ . The macroscale simulation result corresponding to the newly derived interface conditions is in very good agreement with the averaged pore-scale velocity profile. The velocity computed using the classical set of interface conditions, where the interface  $\Sigma_0$  is considered, does not match as well to the pore-scale results as the profile for the generalized conditions. However, when we apply the classical interface conditions on the interface  $\Sigma_d$ , the normal velocity profile according to the macroscale simulation results has a completely different shape (Figure 6.19(c)). In Figure 6.19(d) we present the pressure profiles at  $x_1 = 0.2$ . The pressure computed using the generalized conditions agrees very well with the averaged pore-scale pressure that is not the case for the classical conditions. We observe, that the choice of  $\Sigma_d$  provides a better agreement of pore-scale and macroscale solution for the pressure, whereas for the velocity the interface location  $\Sigma_0$  seems to be more suitable. Similar observations are obtained for other cross sections.



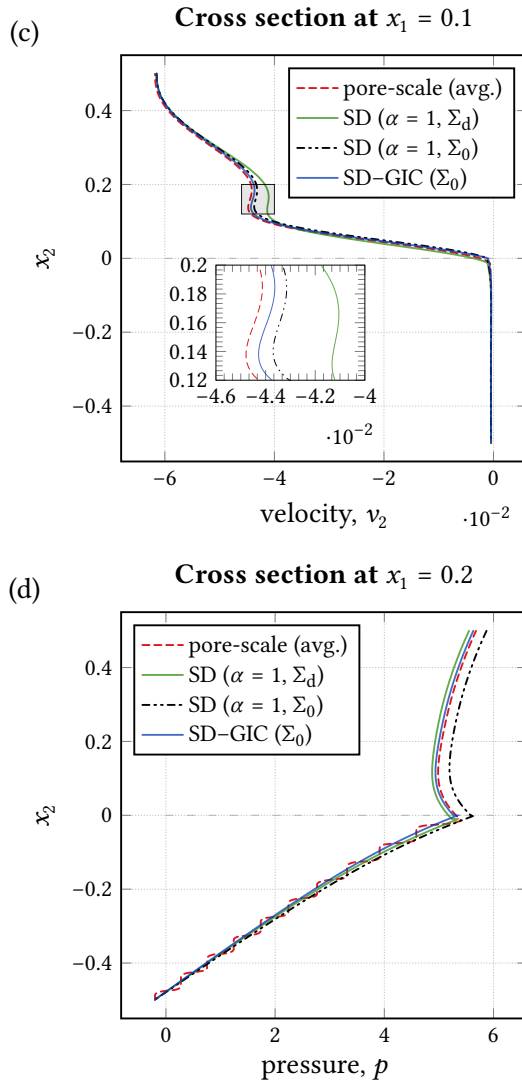


Figure 6.19: Velocity and pressure profiles for the general filtration problem in case of the isotropic porous medium.

### Anisotropic porous medium

In order to validate the generalized interface conditions in case of the general filtration problem for anisotropic porous media, we consider the porous medium made up of  $20 \times 10$  elliptical solid inclusions distributed periodically (Figure 6.20). In this case, the boundary of the solid part  $Y_s$  within the unit cell  $Y = (0, 1)^2$  is described by the ellipse

$$e(t) = (0.5, 0.5) + \cos(0.25\pi)(0.2 \cos(t) + 0.4 \sin(t), -0.2 \cos(t) + 0.4 \sin(t)),$$

for  $t \in [0, 2\pi)$ . These inclusions are neither symmetric with respect to the  $x_1$ - nor  $x_2$ -axis. Therefore, we obtain a full permeability tensor  $\tilde{\mathbf{K}}$  and all boundary layer constants are nonzero as presented in Figure 6.20 (left). Such elliptical obstacles are also considered in [34], where equal permeability values are obtained. We study the same flow problem as in the isotropic case, i.e., we have the same flow domains and boundary conditions (6.38)–(6.39) and (6.40)–(6.41) for the pore-scale respective macroscale problem, only a different porous-medium morphology.

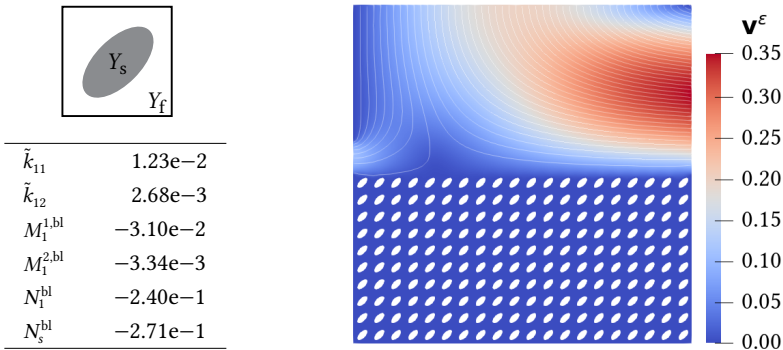


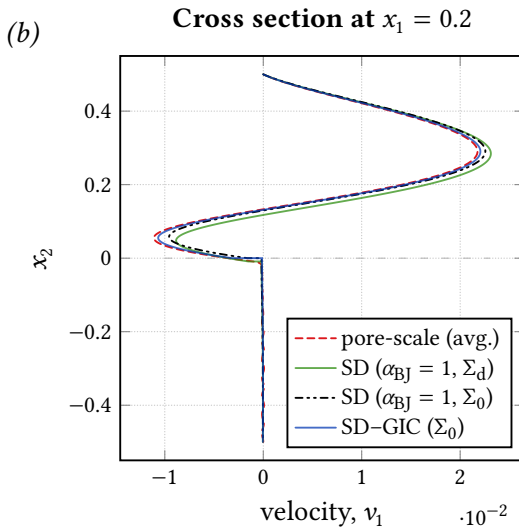
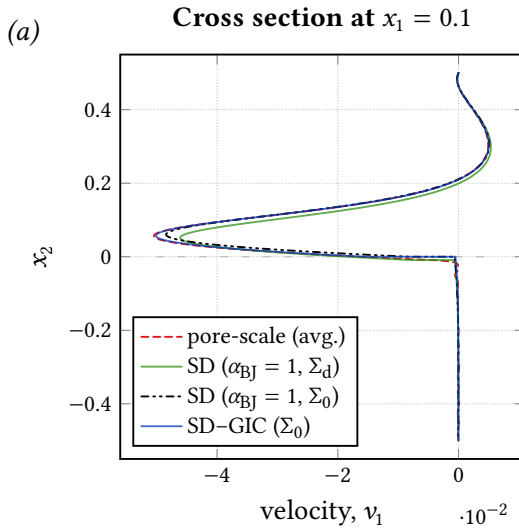
Figure 6.20: Effective coefficients (left) and pore-scale velocity field for the general filtration problem (right) in case of the anisotropic porous medium.

In Figure 6.21 we present profiles for the velocity and pressure at  $x_1 = 0.1$  and  $x_1 = 0.2$ . We observe that the macroscale simulation results with respect to the set of generalized interface conditions (6.12)–(6.14) agree very well with the pore-scale results, whereas the results corresponding to the classical interface conditions (6.7)–(6.9) do not fit. The profiles are similar to those presented in Figure 6.19, the differences are due to different porous-medium morphology. Again, in case the classical interface concept is applied, we find out that different interface locations are more suitable for the velocity components ( $\Sigma_0$ ) and the pressure ( $\Sigma_d$ ), respectively. However, for both interface positions the Stokes–Darcy model with the classical set of coupling conditions cannot capture the pore-scale effects. The macroscale model with the generalized interface conditions yields velocity and pressure profiles that coincide very well with the profiles according to the pore-scale model.

For the general filtration problem, where the flow is highly arbitrary to the interface, the generalized interface conditions provide a coupled Stokes–Darcy model that reflect the pore-scale flow processes accurately for all considered geometries. In contrast to the generalized conditions, the classical coupling conditions fail to represent fluid flow in the coupled system. If the classical coupling concept is applied, different interface locations seem to be optimal for the velocity and pressure, however, that should not be the case.

**Remark 6.3:** *In [EE5] we perform a benchmark study considering a coupled problem, where the flow direction is arbitrary to the porous bed and the porous medium is constructed of in-line arranged squared solid inclusions. The corresponding pore-scale velocity field is presented in Figure 6.22. In this benchmark study the performance of three different coupled models (Stokes–Darcy model with classical respective generalized interface conditions, Stokes equations coupled to pore network model from [161, 162]) is compared quantitatively using the uncertainty-aware validation framework developed by the coauthor Farid Mohammadi. Application of the validation framework to the considered benchmark problem reveals that the Stokes–*





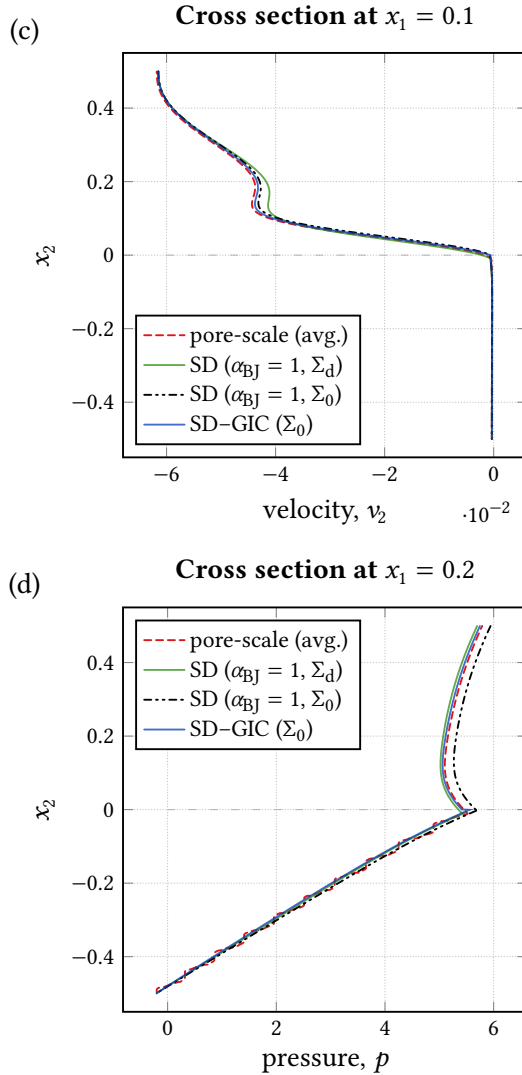


Figure 6.21: Velocity and pressure profiles for the general filtration problem in case of the anisotropic porous medium.

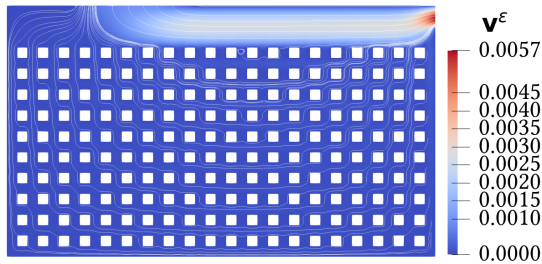


Figure 6.22: Pore-scale velocity field according to the flow problem studied in [EE5].

*Darcy model with the generalized interface conditions represents the fluid flow through the coupled system best compared to the two other coupled models. The same observations are made if the squared solid obstacles are replaced by circular solid inclusions [EE5].*

### Summary of Section 6.3

We studied three flow problems to validate the generalized coupling conditions derived in Chapter 3, and to demonstrate their advantage over the classical conditions. In case of pressure driven flow we observed that the Stokes–Darcy model with the generalized interface conditions provides simulation results that agree very well to the pore-scale model, and we showed that it is more accurate compared to the macroscale model with the classical interface conditions, even if the most optimal Beavers–Joseph parameter is applied. Moreover, we demonstrated that for a few special orthotropic porous-medium configurations, the generalized condition (6.14) for the tangential component reduces to the Beavers–Joseph interface condition (6.9). In case of double lid driven cavity flow over a porous medium we observed that the generalized interface conditions lead to a Stokes–Darcy model that describes the fluid flow very precisely, and that the macroscale model with the classical conditions do not agree so well. For a general filtration problem with arbitrary flow direction to the

interface, we demonstrated that the newly derived coupling conditions are suitable, whereas the classical conditions cannot represent the coupled system accurately.

# **7** Conclusions and perspectives



# Conclusions and perspectives

# 7

This dissertation is devoted to the derivation, analysis and validation of coupling conditions for the Stokes–Darcy problem that account for arbitrary flow directions to the interface. In order to derive these conditions we used homogenization and boundary layer theory allowing the rigorous formulation of macroscale equations based on the underlying pore-scale model. We applied the newly derived conditions to couple the Stokes and Darcy flow equations, and proved existence and uniqueness of a weak solution for the resulting macroscale problem. We developed numerical methods to compute all effective model parameters and to solve the coupled Stokes–Darcy problem. Finally, we validated the generalized coupling conditions by comparing pore-scale resolved to macroscale numerical simulations.

Below, we summarize the conclusions for the individual chapters, put them into the context of the dissertation, and discuss perspectives for future work including potential extensions of the developed models, analytical results and numerical schemes.

In Chapter 1, we highlighted the importance of free-flow and porous-medium flow systems for industry, environment and biology, introduced different approaches to model such coupled flow systems and motivated the goal of the thesis.

In Chapter 2, we provided the pore-scale flow model and the subdomain flow models we are dealing with in this thesis. We introduced the classical coupling conditions for the macroscale problem as well as some alternative coupling concepts available in the literature and specified their limitations. We presented the state of the art in terms of analysis, numerical methods and model validation of coupled Stokes–Darcy problems. Additionally, we introduced homogenization and boundary layer theory based on examples from the literature, where these averaging techniques have been successfully applied to derive interface conditions for unidirectional flows in coupled flow systems.

In Chapter 3, we rigorously derived generalized coupling conditions using homogenization with two-scale asymptotic expansions and boundary layer theory. These conditions are valid for arbitrary flows in coupled systems and, unlike the classical interface conditions, do not contain any unknown parameters. All coefficients can be computed based on the pore geometry in the vicinity of the fluid–porous interface. We showed that the information concerning the exact interface location is also included in the coefficients and that this location can be chosen with some freedom. Moreover, we analyzed the effective coefficients for various porous-medium geometries, and found out that some coefficients are zero in case of isotropic porous media and others are always negative. These findings made the physical interpretation of the generalized interface conditions, as well as their comparison to the classical coupling approach, easier. For the derivation of the generalized coupling conditions in Section 3.1, we started from the pore-scale description of the coupled flow system in form of the Stokes equations. Hereby, we considered a flat interface, the stress tensor in its nonsymmetric form and assumed that no external forces are present. Thus, the corresponding macroscale Stokes–Darcy model with the derived coupling conditions is also based on these assumptions. Currently, we are working on the extension of the generalized interface conditions to the case of the symmetric stress tensor and a nonzero external force term. Future work could also extend the developed coupling concept to inertial flows and arbitrary interface. Another task that could be addressed in the future is the derivation of estimates for the velocity



---

and pressure error functions defined in Section 3.1. This could serve as a further confirmation of the validity of the developed interface conditions besides their numerical validation in Chapter 6. Further research is also needed for the development of interface conditions for two-phase fluid flows in coupled free-flow and porous-medium systems.

In Chapter 4, we developed numerical methods to solve the pore-scale and macroscale problems as well as to compute effective parameters appearing in the macroscale model. For the discretization and solution of the pore-scale problem we used the finite element software `FREEFEM++` and applied Taylor–Hood finite elements to partition the perforated domain. The cell and boundary layer problems, whose solutions are needed to compute the effective parameters, are also solved via `FREEFEM++`. The solution to the macroscale Stokes–Darcy problem is computed monolithically using our in-house C++ code, which is based on the finite volume method on staggered grids and multipoint flux approximation in the porous medium. The monolithic solution strategy is well suited for rapid validation of new interface concepts as these conditions can be easily implemented. To make the generalized interface conditions directly available to other researchers we also implemented them into the open-source simulator `DuMux`. Future work could include the development of more efficient numerical methods such as domain decomposition schemes.

In Chapter 5, we analyzed the Stokes–Darcy problem with the generalized interface conditions with respect to existence and uniqueness of a weak solution. We derived the variational formulation of the coupled problem and proved its well-posedness for isotropic porous media. Well-posedness could be guaranteed under a suitable relationship between the permeability and the boundary layer constants which contain the geometrical information within the interfacial region. In order to examine the validity of the obtained assumption we considered several representative porous-medium configurations and analyzed the resulting relationship. We found that for a wide range of pore geometries the assumption, needed to guarantee well-posedness, is not restrictive. For anisotropic porous media all effective coefficients appearing in the generalized coupling conditions are

nonzero. Therefore, further integral terms over the interface appear in the bilinear form, for which coercivity and continuity need to be proven. Proving the coercivity was already challenging in the isotropic case since the term that includes the boundary layer constants is not necessarily positive. Thus, further research is needed to prove coercivity for the bilinear form in the more complex anisotropic case.

In Chapter 6, we validated the Stokes–Darcy problem with the classical and the generalized coupling conditions by comparison of pore-scale to macroscale numerical simulations. First, we showed that the classical coupling conditions are suitable for flows parallel to the interface since the optimal Beavers–Joseph parameter can be determined such that the error between pore-scale and macroscale simulation results is minimal. Moreover, we found that these conditions can also be applied for perpendicular flows to the interface. In this case, the value taken for the Beavers–Joseph slip coefficient has almost no effect on the behavior of the coupled system, since the tangential velocity is negligible. Second, we demonstrated that the classical coupling concept is unsuitable for arbitrary flow directions to the porous layer. We showed that it is not possible to determine a constant Beavers–Joseph parameter along the fluid–porous interface such that pore-scale and macroscale simulations agree. Third, we validated the Stokes–Darcy model with the generalized coupling conditions developed in Chapter 3. We showed that in case of pure parallel fluid flow, the generalized conditions provide more accurate results than the classical interface conditions even if the optimal Beavers–Joseph slip coefficient is considered. For arbitrary flow directions to the interface, where the classical conditions are not suitable, we demonstrated the validity of the generalized coupling conditions for the Stokes–Darcy problem. Further comparison of the developed conditions with other alternative coupling conditions presented in Chapter 1, which are supposed to account for arbitrary flows, remains open for future work. This will be a major task since these conditions have not been validated for nonparallel flows so far. Moreover, some alternative coupling concepts contain unknown parameters that need to be determined before the conditions can be used in numerical simulations. For the determination of these

unknown model parameters the generalized coupling conditions might be useful, i.e., parameters in the alternative conditions that correspond to those in the generalized conditions can be computed based on the pore geometry. The comparison of different alternative interface conditions could bring meaningful insight into the physically important terms for the accurate coupling of free-flow and porous-medium flow that might also be interesting for the development of coupling concepts for the inertial flow regime.



# Appendix



## A.1 Functional spaces and norms

In the following, we introduce the functional spaces and norms that are used within this thesis based on [109, Chapter 3] and [EE1, EE4].

For the definition of spaces and norms we consider an open subset  $\Omega \subset \mathbb{R}^d$ , where  $d = 1, 2, 3$  is the dimension of space, and a scalar function  $\varphi : \Omega \rightarrow \mathbb{R}$ , if not stated otherwise. For vector-valued functions  $\boldsymbol{\varphi} : \Omega \rightarrow \mathbb{R}^d$  the below defined spaces and norms are denoted by the superscript  $d$ , for example,  $\boldsymbol{\varphi} \in L^2(\Omega)^d$  and  $\|\boldsymbol{\varphi}\|_{L^2(\Omega)^d}$ , where  $L^2(\Omega)^d$  denotes the space of vector-valued functions that are componentwise in  $L^2(\Omega)$ . Accordingly, for a tensor  $\mathbf{T} : \Omega \rightarrow \mathbb{R}^{d \times d}$  we use the superscript  $d \times d$ , e.g.,  $\mathbf{T} \in H^1(\Omega)^{d \times d}$  and  $\|\mathbf{T}\|_{H^1(\Omega)^{d \times d}}$ .

First, we introduce the following standard functional spaces and Lebesgue spaces with their corresponding norms

- $C^\infty(\Omega)$ : space of smooth functions ;
- $C_{\text{loc}}^\infty(\Omega)$ : space of smooth functions whose derivatives are allowed to be unbounded ;
- $C_{\text{per}}^\infty(Y)$ : function space defined in Definition 2.4 ;
- $C_0^\infty(\Omega)$ : space of smooth functions with compact support ;

- $C_0^\infty(\Omega; C_{\text{per}}^\infty(Y))$ : test function space with fast and slow variables,

$$C_0^\infty(\Omega; C_{\text{per}}^\infty(Y)) = \left\{ \varphi : \Omega \rightarrow C_{\text{per}}^\infty(Y) : \varphi(\mathbf{x}, \cdot) \in C_0^\infty(\Omega) \right\};$$

- $L^2(\Omega)$ : space of square-integrable functions  $\varphi$ ,

$$L^2(\Omega) = \left\{ \varphi : \Omega \rightarrow \mathbb{R} \text{ measurable} : \int_{\Omega} |\varphi|^2 dV < \infty \right\},$$

$$\|\varphi\|_{L^2(\Omega)} = \left( \int_{\Omega} \varphi^2 dV \right)^{1/2};$$

- $L_{\text{per}}^2(\Omega)$ : space of  $L^2$ -functions that are  $L$ -periodic in  $x_1$ , defined by equation (2.51);

- $L_{\text{loc}}^2(\Omega)$ : space of locally square-integrable functions,

$$L_{\text{loc}}^2(\Omega) = \left\{ \varphi : \Omega \rightarrow \mathbb{R} \text{ measurable} : \varphi|_K \in L^2(K) \text{ for all } K \subset \Omega, \right. \\ \left. K \text{ compact} \right\};$$

- $L^2(\Omega_{\text{pm}}^\varepsilon)/\mathbb{R}$ : function space defined by equation (2.53);

- $L^2(\Omega \times Y) = L^2(\Omega; L^2(Y)) = \left\{ \varphi : \Omega \rightarrow L^2(Y) : \varphi(\mathbf{x}, \cdot) \in L^2(\Omega) \right\}$ .

Further, we denote the Sobolev spaces and norms by

- $W^{k,p}(\Omega)$ ,  $1 \leq p \leq \infty$ : space of functions  $\varphi \in L^p(\Omega)$  having weak derivatives up to order  $k \in \mathbb{N}$  with finite  $L^p$  norm;

- $H^1(\Omega)$ : space of functions  $\varphi \in L^2(\Omega)$  having distributional gradients  $\nabla\varphi$  in  $L^2(\Omega)^2$ ,

$$H^1(\Omega) = \left\{ \varphi \in L^2(\Omega) : \nabla\varphi \in L^2(\Omega)^2 \right\},$$

$$\|\varphi\|_{H^1(\Omega)} = \left( \|\varphi\|_{L^2(\Omega)}^2 + \|\nabla\varphi\|_{L^2(\Omega)^2}^2 \right)^{1/2};$$

- $H_{\text{per}}^1(\Omega)/\mathbb{R}$ : function space defined in Section 2.3.2 (Step 5);

- $H_0^1(\Omega)$ : space of functions  $\varphi \in H^1(\Omega)$  that vanish on the boundary,

$$H_0^1(\Omega) = \{\varphi \in H^1(\Omega) : \varphi = 0 \text{ on } \partial\Omega\};$$

- $H^{1/2}(\partial\Omega)$ : trace space of functions  $\varphi \in L^2(\partial\Omega)$ ,

$$H^{1/2}(\partial\Omega) = \{\varphi \in L^2(\partial\Omega) : \varphi = u|_{\partial\Omega} \text{ for some } u \in H^1(\Omega)\};$$

- $H_{00}^{1/2}(\Sigma)$ : trace space of functions  $\varphi \in H^{1/2}(\partial\Omega_{\text{pm}})$  with  $\text{supp } \varphi \subset \bar{\Sigma}$ ,

$$H_{00}^{1/2}(\Sigma) = \{\varphi \in H^{1/2}(\partial\Omega_{\text{pm}}) : \text{supp } \varphi \subset \bar{\Sigma}\};$$

- $H^{-1}(\Omega)$ : dual space of  $H_0^1(\Omega)$ ;
- $H^{-1/2}(\partial\Omega)$ : dual space of  $H^{1/2}(\partial\Omega)$ ,

$$\|\varphi\|_{H^{-1/2}(\partial\Omega)} = \sup_{f \in H^{1/2}(\partial\Omega)} \frac{\langle \varphi, f \rangle_{\partial\Omega}}{\|f\|_{H^{1/2}(\partial\Omega)}};$$

- $(H_{00}^{1/2}(\Sigma))'$ : dual space of  $H_{00}^{1/2}(\Sigma)$ .

Specific test function spaces defined in context with homogenization are

- $V_{\text{per}}(\Omega^\varepsilon)^2$ : test function space defined by equation (3.5);
- $W_{\text{per}}(\Omega_{\text{pm}}^\varepsilon)^d$ : test function space defined by equation (2.50);
- $V(Z^{\text{bl}})^2$ : test function space,

$$V(Z^{\text{bl}})^2 = \{\mathbf{u} \in L_{\text{loc}}^2(Z^{\text{bl}})^2 : \nabla_{\mathbf{y}} \mathbf{u} \in L^2(Z^{\text{bl}})^{2 \times 2}, \mathbf{u} \in L^2(Z^-)^2, \mathbf{u} = \mathbf{0} \text{ on } \partial Z_s^{\text{bl}}, \\ \nabla_{\mathbf{y}} \boldsymbol{\varphi} = 0 \text{ in } Z^{\text{bl}}, \mathbf{u} \text{ is } y_1\text{-periodic}\}.$$

Finally, we summarize the functional spaces and norms defined in Chapter 5 of this thesis

- $H_{\text{ff}} = \{\boldsymbol{\varphi} \in H^1(\Omega_{\text{ff}})^2 : \boldsymbol{\varphi} = \mathbf{0} \text{ on } \partial\Omega_{\text{ff}} \setminus \Sigma\}$  ;
- $H_{\text{ff},\Sigma} = \{\boldsymbol{\varphi} \in H^1(\Omega_{\text{ff}})^2 : \boldsymbol{\varphi} = \mathbf{0} \text{ on } \Gamma_{\text{ff},D}^{\text{wall}} \cup \Sigma\}$  ;
- $Q_{\text{ff}} = L^2(\Omega_{\text{ff}})$  ;
- $H_{\text{pm}} = \{\psi \in H^1(\Omega_{\text{pm}}) : \psi = 0 \text{ on } \Gamma_{\text{pm},D}\}$  ;
- $W = H_{\text{ff}} \times H_{\text{pm}}$ ,  $\|\underline{\mathbf{w}}\|_W^2 = \|\mathbf{w}\|_{H^1(\Omega_{\text{ff}})}^2 + \|\psi\|_{H^1(\Omega_{\text{pm}})}^2$  for all  $\underline{\mathbf{w}} = (\mathbf{w}, \psi) \in W$  ;
- $H(\text{div}; \Omega)^2 = \{\boldsymbol{\varphi} \in L^2(\Omega)^2 : \nabla \cdot \boldsymbol{\varphi} \in L^2(\Omega)\}$ .

## A.2 Inequalities

Below, we provide elementary inequalities which have been used throughout this thesis. Let the domain  $\Omega \subset \mathbb{R}^d$  denote a bounded, connected and open subset of  $\mathbb{R}^d$ .

**Lemma A.1 (Poincaré inequality):** *Let  $\varphi \in H^1(\Omega)$  with  $\varphi = 0$  on  $\Gamma$ ,  $\Gamma \subset \partial\Omega$  and  $\Gamma \neq \emptyset$ . Then, there exists a constant  $C > 0$  such*

$$\|\varphi\|_{L^2(\Omega)} \leq C \|\nabla\varphi\|_{L^2(\Omega)}. \quad (\text{A2.1})$$

*Proof.* See, e.g., [59, Chapters 5.6 and 5.8] or [132, Property 2.4].  $\square$

**Lemma A.2 (Poincaré-type inequalities):** *Let the scale separation parameter  $\varepsilon$  and the pore space  $\Omega_{\text{pm}}^\varepsilon$  w.r.t. the porous-medium domain  $\Omega_{\text{pm}}$  be defined as in Section 2.3.2. For  $\varphi \in H^1(\Omega_{\text{pm}}^\varepsilon)$  and  $\varphi = 0$  on  $\partial\Omega_{\text{pm}}^\varepsilon \setminus \partial\Omega_{\text{pm}}$ . Then, we have the following Poincaré-type inequalities*

$$\|\varphi\|_{L^2(\Sigma)} \leq C\varepsilon^{1/2} \|\nabla\varphi\|_{L^2(\Omega_{\text{pm}}^\varepsilon)}, \quad \|\varphi\|_{L^2(\Omega_{\text{pm}}^\varepsilon)} \leq C\varepsilon \|\nabla\varphi\|_{L^2(\Omega_{\text{pm}}^\varepsilon)}. \quad (\text{A2.2})$$



*Proof.* These estimates are well-known consequences of the Poincaré inequality (A2.1) and the proofs can be found in, e.g., [120, Lemma 4.10], [153, Lemma 1] or [120, Lemma 4.10].  $\square$

**Lemma A.3 (Generalized Young’s inequality):** For  $a, b > 0$  and  $\delta > 0$  it holds

$$ab \leq \frac{a^2}{2\delta} + \frac{\delta b^2}{2}. \quad (\text{A2.3})$$

*Proof.* See, e.g., [59, Appendix B].  $\square$

**Lemma A.4 (Minkowski inequality):** Let  $\Omega$  be a measure space,  $1 \leq p < \infty$  and  $\varphi, \psi \in L^p(\Omega)$ . Then, the sum  $\varphi + \psi$  is an element of  $L^p(\Omega)$ , and we have

$$\|\varphi + \psi\|_{L^2(\Omega)} \leq \|\varphi\|_{L^2(\Omega)} + \|\psi\|_{L^2(\Omega)}. \quad (\text{A2.4})$$

*Proof.* See, e.g., [59, Appendix B].  $\square$

**Lemma A.5 (Cauchy–Schwarz inequality):** For all vectors  $\mathbf{u}$  and  $\mathbf{v}$  elements of a real linear space  $H$  with inner product  $\langle \cdot, \cdot \rangle$  it holds

$$|\langle \mathbf{u}, \mathbf{v} \rangle|^2 \leq \langle \mathbf{u}, \mathbf{u} \rangle \cdot \langle \mathbf{v}, \mathbf{v} \rangle. \quad (\text{A2.5})$$

*Proof.* See, e.g., [59, Appendix B, D].  $\square$

**Lemma A.6 (Trace inequalities):** Let  $\Omega_i \subset \mathbb{R}^2$  a bounded domain with a smooth or locally Lipschitz boundary  $\partial\Omega_i$  for  $i \in \{\text{ff}, \text{pm}\}$ ,  $H_{\text{ff}}$  and  $H_{\text{pm}}$  defined as in Section 5.1.2. Then, for  $\Sigma \subset \partial\Omega_i$  there exist  $C_{\text{tr,ff}}, C_{\text{tr,pm}} > 0$  such that

$$\|\mathbf{v}|_{\Sigma}\|_{H_{00}^{1/2}(\Sigma)} \leq C_{\text{tr,ff}} \|\mathbf{v}\|_{H^1(\Omega_{\text{ff}})} \quad \forall \mathbf{v} \in H_{\text{ff}}, \quad (\text{A2.6})$$

$$\|\psi|_{\Sigma}\|_{H_{00}^{1/2}(\Sigma)} \leq C_{\text{tr,pm}} \|\psi\|_{H^1(\Omega_{\text{pm}})} \quad \forall \psi \in H_{\text{pm}}. \quad (\text{A2.7})$$

*Proof.* These are results of the trace theorem for Sobolev spaces proven in [110, Chapter 3, 4, 12] and [59, Chapter 5].  $\square$

### A.3 Lax–Milgram theorem

**Theorem A.7 (Lax–Milgram):** *Let  $H$  be a real Hilbert space with norm  $\|\cdot\|$  and inner product  $(\cdot, \cdot)$ . Further,  $\langle \cdot, \cdot \rangle$  denotes the pairing of  $H$  with its dual space. Assume that*

$$\mathcal{B} : H \times H \rightarrow \mathbb{R}$$

*is a bilinear mapping, for which there exist constants  $c, C > 0$  such that*

$$|\mathcal{B}(u, v)| \leq C\|u\|\|v\|, \quad u, v \in H, \quad (\text{i})$$

*and*

$$\mathcal{B}(u, u) \geq c\|u\|^2, \quad u \in H. \quad (\text{ii})$$

*We say bilinear form  $\mathcal{B}$  is bounded after (i) and coercive after (ii). Finally, let  $f : H \rightarrow \mathbb{R}$  be a bounded linear functional on  $H$ . Then, there exists a unique element  $u \in H$  such that*

$$\mathcal{B}(u, v) = \langle f, v \rangle$$

*for all  $v \in H$ .*

*Proof.* See, e.g., [59, Chapter 6, Section 6.2.1, Theorem 1].  $\square$

# Publications by the author

- [EE1] E. Eggenweiler, M. Discacciati, and I. Rybak. *Analysis of the Stokes–Darcy problem with generalised interface conditions*. ESAIM Math. Model. Numer. Anal. 56 (2022), pp. 727–742. DOI: 10.1051/m2an/2022025.
- [EE2] E. Eggenweiler and I. Rybak. *Interface conditions for arbitrary flows in coupled porous-medium and free-flow systems. Finite Volumes for Complex Applications IX – Methods, Theoretical Aspects, Examples. FVCA 9, Bergen, Norway, 2020*. Vol. 323. Springer Proc. Math. Stat. Springer, 2020, pp. 345–353. DOI: 10.1007/978-3-030-43651-3\\_31.
- [EE3] E. Eggenweiler and I. Rybak. *Unsuitability of the Beavers–Joseph interface condition for filtration problems*. J. Fluid Mech. 892 (2020), A10, 19. DOI: 10.1017/jfm.2020.194.
- [EE4] E. Eggenweiler and I. Rybak. *Effective coupling conditions for arbitrary flows in Stokes–Darcy systems*. Multiscale Model. Simul. 19.2 (2021), pp. 731–757. DOI: 10.1137/20M1346638.
- [EE5] F. Mohammadi, E. Eggenweiler, B. Flemisch, S. Oladyshkin, I. Rybak, M. Schneider, and K. Weishaupt. “A surrogate-assisted uncertainty-aware bayesian validation framework and its application to coupling free flow and porous-medium flow”. 2022. URL: <https://arxiv.org/abs/2106.13639>.

- [EE6] I. Rybak, C. Schwarzmeier, E. Eggenweiler, and U. Rde. *Validation and calibration of coupled porous-medium and free-flow problems using pore-scale resolved models*. *Comput. Geosci.* 25.2 (2021), pp. 621–635. DOI: 10 . 1007/s10596-020-09994-x.
- [EE7] P. Strohbeck, E. Eggenweiler, and I. Rybak. “A modification of the Beavers–Joseph condition for arbitrary flows to the fluid–porous interface”. 2022. URL: <https://arxiv.org/abs/2106.15556>.
- [EE8] A. Wagner, E. Eggenweiler, F. Weinhardt, Z. Trivedi, D. Krach, C. Lohrmann, K. Jain, N. Karadimitriou, C. Bringedal, P. Volland, C. Holm, H. Class, H. Steeb, and I. Rybak. *Permeability estimation of regular porous structures: a benchmark for comparison of methods*. *Transp. Porous Media* 138.1 (2021), pp. 1–23. DOI: 10 . 1007 / s 11242-021-01586-2.

# Bibliography

- [1] G. Allaire. *Homogenization of the Navier–Stokes equation with a slip boundary condition*. *Comm. Pure Appl. Math.* 44.6 (1991), pp. 605–641. DOI: 10.1002/cpa.3160440602.
- [2] G. Allaire. *Homogenization of the Stokes flow in a connected porous medium*. *Asymptotic Anal.* 2.3 (1989), pp. 203–222. DOI: 10.3233/ASY-1989-2302.
- [3] G. Allaire. *Homogenization and two-scale convergence*. *SIAM J. Math. Anal.* 23.6 (1992), pp. 1482–1518. DOI: 10.1137/0523084.
- [4] P. R. Amestoy, I. S. Duff, J.-Y. L’Excellent, and J. Koster. *A fully asynchronous multifrontal solver using distributed dynamic scheduling*. *SIAM J. Matrix Anal. Appl.* 23.1 (2001), pp. 15–41. DOI: 10.1137/S0895479899358194.
- [5] P. Angot. “Solvability of the variable-viscosity fluid–porous flows coupled with an optimal stress jump interface condition”. 2021. URL: <https://hal.archives-ouvertes.fr/hal-03172378/>.
- [6] P. Angot. *A fictitious domain model for the Stokes/Brinkman problem with jump embedded boundary conditions*. *C. R. Math. Acad. Sci. Paris* 348.11-12 (2010), pp. 697–702. DOI: 10.1016/j.crma.2010.04.022.
- [7] P. Angot. *On the well-posed coupling between free fluid and porous viscous flows*. *Appl. Math. Lett.* 24.6 (2011), pp. 803–810. DOI: 10.1016/j.aml.2010.07.008.

- [8] P. Angot. *Well-posed Stokes/Brinkman and Stokes/Darcy coupling revisited with new jump interface conditions*. ESAIM Math. Model. Numer. Anal. 52.5 (2018), pp. 1875–1911. DOI: 10.1051/m2an/2017060.
- [9] P. Angot, F. Boyer, and F. Hubert. *Asymptotic and numerical modelling of flows in fractured porous media*. M2AN Math. Model. Numer. Anal. 43.2 (2009), pp. 239–275. DOI: 10.1051/m2an/2008052.
- [10] P. Angot, B. Goyeau, and J. A. Ochoa-Tapia. *Asymptotic modeling of transport phenomena at the interface between a fluid and a porous layer: jump conditions*. Phys. Rev. E 95.6 (2017), p. 063302, 16. DOI: 10.1103/physreve.95.063302.
- [11] J. K. Arthur. *Experimental investigation of porous medium structural effects on a coupled porous media-free zone laminar flow*. SN Appl. Sci. 1 (2019), p. 1062. DOI: 10.1007/s42452-019-1070-7.
- [12] J. K. Arthur, D. W. Ruth, and M. F. Tachie. *PIV measurements of flow through a model porous medium with varying boundary conditions*. J. Fluid Mech. 629 (2009), pp. 343–374. DOI: 10.1017/S0022112009006405.
- [13] M. Bauer, S. Eibl, C. Godenschwager, N. Kohl, M. Kuron, C. Rettinger, F. Schornbaum, C. Schwarzmeier, D. Thönnies, H. Köstler, and U. Rüdiger. *WaLBerla: a block-structured high-performance framework for multiphysics simulations*. Comput. Math. Appl. 81 (2021), pp. 478–501. DOI: 10.1016/j.camwa.2020.01.007.
- [14] L. Beaudin, K. Brenner, S. Lopez, R. Masson, and F. Smai. *Non-isothermal compositional liquid gas Darcy flow: formulation, soil-atmosphere boundary condition and application to high-energy geothermal simulations*. Comput. Geosci. 23 (2019), pp. 443–470. DOI: 10.1007/s10596-018-9794-9.
- [15] G. S. Beavers and D. D. Joseph. *Boundary conditions at a naturally permeable wall*. J. Fluid Mech. 30.1 (1967), pp. 197–207. DOI: 10.1017/S0022112067001375.

- [16] A. Y. Beliaev and S. M. Kozlov. *Darcy equation for random porous media*. Commun. Pure Appl. Math. 49.1 (1996), pp. 1–34. DOI: 10.1002/(SICI)1097-0312(199601)49:1<1::AID-CPA1>3.0.CO;2-J.
- [17] C. Bernardi, T. C. Rebollo, F. Hecht, and Z. Mghazli. *Mortar finite element discretization of a model coupling Darcy and Stokes equations*. ESAIM. Math. Model. Numer. Anal. 42.3 (2008), pp. 375–410. DOI: 10.1051/m2an:2008009.
- [18] S. Beyhaghi, Z. Xu, and K. M. Pillai. *Achieving the inside–outside coupling during network simulation of isothermal drying of a porous medium in a turbulent flow*. Transp. Porous Media 114.6 (2016), pp. 823–842. DOI: 10.1007/s11242-016-0746-3.
- [19] M. J. Blunt. *Multiphase flow in permeable media: a pore-scale perspective*. Cambridge University Press, 2017. DOI: 10.1017/9781316145098.
- [20] M. J. Blunt, B. Bijeljic, H. Dong, O. Gharbi, S. Iglauer, P. Mostaghimi, A. Paluszny, and C. Pentland. *Pore-scale imaging and modelling*. Adv. Water Resour. 51 (2013), pp. 197–216. DOI: 10.1016/j.advwatres.2012.03.003.
- [21] Y. Boubendir and S. Tlupova. *Domain decomposition methods for solving Stokes–Darcy problems with boundary integrals*. SIAM J. Sci. Comput. 35.1 (2013), B82–B106. DOI: 10.1137/110838376.
- [22] S. Brdar, A. Dedner, R. Klöforn, M. Kränkel, and D. Kröner. *Simulation of geophysical problems with dune-fem*. Computational science and high performance computing iv. Ed. by E. Krause, Y. Shokin, M. Resch, D. Kröner, and N. Shokina. Springer Berlin Heidelberg, 2011, pp. 93–106. DOI: 10.1007/978-3-642-17770-5\_8.
- [23] H. Brezis. *Functional analysis, sobolev spaces and partial differential equations*. Springer, 2011.
- [24] F. Brezzi. *On the existence, uniqueness and approximation of saddle-point problems arising from Lagrange multipliers*. Rev. Française Automat. Informat. Recherche Opérationnelle, sér. Rouge 8 (1974), pp. 129–151. DOI: 10.1051/m2an/197408R201291.

- [25] F. Brezzi and M. Fortin. *Mixed and hybrid finite element methods*. Springer, 1991.
- [26] H. C. Brinkman. *A calculation of the viscous force exerted by a flowing fluid on a dense swarm of particles*. Appl. Sci. Res. 1.27 (1949), pp. 27–34. DOI: 10.1007/BF02120313.
- [27] E. Burman and P. Hansbo. *Stabilized Crouzeix–Raviart element for the Darcy–Stokes problem*. Numer. Methods Partial Differ. Equations 21.5 (2005), pp. 986–997. DOI: 10.1002/num.20076.
- [28] E. Burman and P. Hansbo. *A unified stabilized method for Stokes’ and Darcy’s equations*. J. Comput. Appl. Math. 198.1 (2007), pp. 35–51. DOI: 10.1016/j.cam.2005.11.022.
- [29] M. Cai, M. Mu, and J. Xu. *Preconditioning techniques for a mixed Stokes/Darcy model in porous media applications*. J. Comput. Appl. Math. 233.2 (2009), pp. 346–355. DOI: 10.1016/j.cam.2009.07.029.
- [30] Y. Cao, M. Gunzburger, F. Hua, and X. Wang. *Coupled Stokes–Darcy model with Beavers–Joseph interface boundary condition*. Commun. Math. Sci. 8.1 (2010), pp. 1–25. DOI: 10.4310/CMS.2010.v8.n1.a2.
- [31] Y. Cao, M. Gunzburger, X. Hu, F. Hua, X. Wang, and W. Zhao. *Finite element approximations for Stokes–Darcy flow with Beavers–Joseph interface conditions*. SIAM J. Numer. Anal. 47.6 (2010), pp. 4239–4256. DOI: 10.1137/080731542.
- [32] P. Carman. *Fluid flow through granular beds*. Chem. Eng. Res. Des. 75 (1997), pp. 32–48. DOI: 10.1016/S0263-8762(97)80003-2.
- [33] T. Carraro, C. Goll, A. Marciniak-Czochra, and A. Mikelić. *Pressure jump interface law for the Stokes–Darcy coupling: confirmation by direct numerical simulations*. J. Fluid Mech. 732 (2013), pp. 510–536. DOI: 10.1017/jfm.2013.416.
- [34] T. Carraro, C. Goll, A. Marciniak-Czochra, and A. Mikelić. *Effective interface conditions for the forced infiltration of a viscous fluid into a porous medium using homogenization*. Comput. Methods Appl. Mech. Engrg. 292 (2015), pp. 195–220. DOI: 10.1016/j.cma.2014.10.050.



- [35] M. Chandesris and D. Jamet. *Boundary conditions at a planar fluid–porous interface for a Poiseuille flow*. Int. J. Heat Mass Transfer 49.13-14 (2006), pp. 2137–2150. doi: 10.1016/j.ijheatmasstransfer.2005.12.010.
- [36] M. Chandesris and D. Jamet. *Boundary conditions at a fluid–porous interface: an a priori estimation of the stress jump coefficients*. Int. J. Heat Mass Transfer 50.17-18 (2007), pp. 3422–3436. DOI: 10.1016/j.ijheatmasstransfer.2007.01.053.
- [37] V. P. Chauhan, T. Stylianopoulos, Y. Boucher, and R. K. Jain. *Delivery of molecular and nanoscale medicine to tumors: transport barriers and strategies*. Annu. Rev. Chem. Biomol. Eng. 2.1 (2011), pp. 281–298. DOI: 10.1146/annurev-chembioeng-061010-114300.
- [38] W. Chen, M. Gunzburger, F. Hua, and X. Wang. *A parallel Robin–Robin domain decomposition method for the Stokes–Darcy system*. SIAM J. Numer. Anal. 49.3 (2011), pp. 1064–1084. DOI: 10.1137/080740556.
- [39] P. Chidyagwai, S. Ladenheim, and D. B. Szyld. *Constraint preconditioning for the coupled Stokes–Darcy system*. SIAM J. Sci. Comput. 38.2 (2016), A668–A690. DOI: 10.1137/15M1032156.
- [40] P. Chidyagwai and B. Rivière. *On the solution of the coupled Navier–Stokes and Darcy equations*. Comput. Methods Appl. Mech. Engrg. 198.47-48 (2009), pp. 3806–3820. DOI: 10.1016/j.cma.2009.08.012.
- [41] J. A. Cunge and F. M. Holly. *Practical aspects of computational river hydraulics*. Pitman Advanced Publishing Program, 1980.
- [42] C. D’Angelo and P. Zunino. *Robust numerical approximation of coupled Stokes’ and Darcy’s flows applied to vascular hemodynamics and biochemical transport*. ESAIM Math. Model. Numer. Anal. 45.3 (2011), pp. 447–476. DOI: 10.1051/m2an/2010062.
- [43] H. Darcy. *Les fontaines publiques de la ville de Dijon*. Dalmont, 1856.

- [44] D. Das, V. Nassehi, and R. Wakeman. *A finite volume model for the hydrodynamics of combined free and porous flow in sub-surface regions*. Adv. Environ. Res. 7.1 (2002), pp. 35–58. DOI: 10.1016/S1093-0191(01)00108-3.
- [45] R. Dautray and J. Lions. *Mathematical analysis and numerical methods for science and technology*. Springer, 1990.
- [46] T. Defraeye, B. Nicolai, D. Mannes, W. Aregawi, P. Verboven, and D. Derome. *Probing inside fruit slices during convective drying by quantitative neutron imaging*. J. Food Eng. 178 (2016), pp. 198–202. DOI: 10.1016/j.jfoodeng.2016.01.023.
- [47] M. Discacciati. *Modelli di accoppiamento fra le equazioni di Stokes e quelle di Darcy per lo studio di problemi di idrodinamica*. Università degli Studi dell’Insubria, Como, Italy, 2001.
- [48] M. Discacciati. *Domain decomposition methods for the coupling of surface and groundwater flows*. Ecole Polytechnique Fédérale de Lausanne, Switzerland, 2004. DOI: 10.5075/epfl-thesis-3117.
- [49] M. Discacciati and L. Gerardo-Giorda. *Optimized Schwarz methods for the Stokes–Darcy coupling*. IMA J. Numer. Anal. 38.4 (2018), pp. 1959–1983. DOI: 10.1093/imanum/drx054.
- [50] M. Discacciati, E. Miglio, and A. Quarteroni. *Mathematical and numerical models for coupling surface and groundwater flows*. Appl. Numer. Math. 43.1-2 (2002), pp. 57–74. DOI: 10.1016/S0168-9274(02)00125-3.
- [51] M. Discacciati and R. Oyarzúa. *A conforming mixed finite element method for the Navier–Stokes/Darcy coupled problem*. Numer. Math. 135.2 (2017), pp. 571–606. DOI: 10.1007/s00211-016-0811-4.
- [52] M. Discacciati and A. Quarteroni. *Navier–Stokes/Darcy coupling: modeling, analysis, and numerical approximation*. Rev. Mat. Complut. 22.2 (2009), pp. 315–426. DOI: 10.5209/rev\ \_REMA.2009.v22.n2.16263.
- [53] M. Discacciati, A. Quarteroni, and A. Valli. *Robin–Robin domain decomposition methods for the Stokes–Darcy coupling*. SIAM J. Numer. Anal. 45.3 (2007), pp. 1246–1268. DOI: 10.1137/06065091X.

- [54] L. Durlofsky and J. F. Brady. *Analysis of the Brinkman equation as a model for flow in porous media*. Phys. Fluids 30.11 (1987), p. 3329. DOI: 10.1063/1.866465.
- [55] M. G. Edwards and C. F. Rogers. *Finite volume discretization with imposed flux continuity for the general tensor pressure equation*. Comput. Geosci. 2.4 (1998), pp. 259–290. DOI: 10.1023/A:1011510505406.
- [56] Y. Efendiev and T. Y. Hou. *Multiscale finite element methods*. Vol. 4. Surveys and Tutorials in the Applied Mathematical Sciences. Springer, New York, 2009. DOI: 10.1007/978-0-387-09496-0.
- [57] K. Erbertseder, J. Reichold, B. Flemisch, P. Jenny, and R. Helmig. *A coupled discrete/continuum model for describing cancer-therapeutic transport in the lung*. PLoS ONE 7 (3 2012), e31966. DOI: 10.1371/journal.pone.0031966.
- [58] H. Erfani, N. Karadimitriou, A. Nissan, M. S. Walczak, S. An, B. Berkowitz, and V. Niasar. *Process-dependent solute transport in porous media*. Transp. Porous Media 140 (2021), pp. 421–435. DOI: 10.1007/s11242-021-01655-6.
- [59] L. C. Evans. *Partial differential equations*. American Mathematical Society, 2010.
- [60] J. Faulkner, B. X. Hu, S. Kish, and F. Hua. *Laboratory analog and numerical study of groundwater flow and solute transport in a karst aquifer with conduit and matrix domains*. J. Contam. Hydrol. 110.1 (2009), pp. 34–44. DOI: 10.1016/j.jconhyd.2009.08.004.
- [61] P. Forchheimer. *Wasserbewegung durch boden*. Z. Ver. Deutsch. Ing. 45 (1901), pp. 1782–1788.
- [62] G. Fu and C. Lehrenfeld. *A strongly conservative hybrid DG/mixed FEM for the coupling of Stokes and Darcy flow*. J. Sci. Comput. 77.3 (2018), pp. 1605–1620. DOI: 10.1007/s10915-018-0691-0.
- [63] J. Galvis and M. Sarkis. *Non-matching mortar discretization analysis for the coupling Stokes–Darcy equations*. Electron. Trans. Numer. Anal. 26 (2007), pp. 350–384. URL: <http://eudml.org/doc/130540>.

- [64] B. Ganis, D. Vassilev, C. Wang, and I. Yotov. *A multiscale flux basis for mortar mixed discretizations of Stokes–Darcy flows*. *Comput. Methods Appl. Mech. Engrg.* 313 (2017), pp. 259–278. DOI: 10.1016/j.cma.2016.09.037.
- [65] G. N. Gatica, S. Meddahi, and R. Oyarzúa. *A conforming mixed finite-element method for the coupling of fluid flow with porous media flow*. *IMA J. Numer. Anal.* 29.1 (2009), pp. 86–108. DOI: 10.1093/imanum/drm049.
- [66] G. N. Gatica, R. Oyarzúa, and F.-J. Sayas. *Analysis of fully-mixed finite element methods for the Stokes–Darcy coupled problem*. *Math. Comput.* 80.276 (2011), pp. 1911–1948. DOI: 10.1090/S0025-5718-2011-02466-X.
- [67] G. N. Gatica, R. Oyarzúa, and F.-J. Sayas. *Convergence of a family of Galerkin discretizations for the Stokes–Darcy coupled problem*. *Numer. Methods Partial Differ. Equations* 27.3 (2011), pp. 721–748. DOI: 10.1002/num.20548.
- [68] G. N. Gatica and F. A. Sequeira. *Analysis of the HDG method for the Stokes–Darcy coupling*. *Numer. Methods Partial Differ. Equations* 33.3 (2017), pp. 885–917. DOI: 10.1002/num.22128.
- [69] P. George. *Automatic mesh generation and finite element computation. Finite element methods (part 2), numerical methods for solids (part 2)*. Vol. 4. *Handbook of Numerical Analysis*. Elsevier, 1996, pp. 69–190. DOI: 10.1016/S1570-8659(96)80003-2.
- [70] P. George, F. Hecht, and E. Saltel. *Automatic mesh generator with specified boundary*. *Comput. Methods Appl. Mech. Eng.* 92.3 (1991), pp. 269–288. DOI: 10.1016/0045-7825(91)90017-Z.
- [71] V. Girault and B. Rivière. *DG approximation of coupled Navier–Stokes and Darcy equations by Beaver–Joseph–Saffman interface condition*. *SIAM J. Numer. Anal.* 47.3 (2009), pp. 2052–2089. DOI: 10.1137/070686081.
- [72] A. Goharzadeh, A. Khalili, and B. B. Jørgensen. *Transition layer thickness at a fluid–porous interface*. *Phys. Fluids* 17.5 (2005), p. 057102. DOI: 10.1063/1.1894796.

- [73] B. Goyeau, D. Lhuillier, D. Gobin, and M. Velarde. *Momentum transport at a fluid–porous interface*. Int. J. Heat Mass Transfer 46.21 (2003), pp. 4071–4081. DOI: 10 . 1016 / S0017 - 9310 (03 ) 00241-2.
- [74] W. G. Gray and C. T. Miller. *Thermodynamically constrained averaging theory approach for modeling flow and transport phenomena in porous medium systems: 1. motivation and overview*. Adv. Water Resour. 28.2 (2005), pp. 161–180. DOI: 10 . 1016 / j . advwatres . 2004 . 09 . 005.
- [75] G. Guennebaud, B. Jacob, et al. *Eigen v3*. 2010. URL: <http://eigen.tuxfamily.org>.
- [76] R. Guibert, M. Nazarova, P. Horgue, G. Hamon, P. Creux, and G. Debenest. *Computational permeability determination from pore-scale imaging: sample size, mesh and method sensitivities*. Transp. Porous Media 107 (2015), pp. 641–656. DOI: 10 . 1007/s11242-015-0458-0.
- [77] V. Gurau and J. A. Mann. *A critical overview of computational fluid dynamics multiphase models for proton exchange membrane fuel cells*. SIAM J. Appl. Math. 70.2 (2009), pp. 410–454. DOI: 10 . 1137 / 080727993.
- [78] H. Versteeg and W. Malalasekera. *An introduction to computational fluid dynamics: the finite volume method*. Prentice Hall, 2007.
- [79] N. S. Hanspal, A. N. Waghode, V. Nassehi, and R. J. Wakeman. *Numerical analysis of coupled Stokes/Darcy flows in industrial filtrations*. Transp. Porous Media 64 (2006), pp. 73–101. DOI: 10 . 1007/s11242-005-1457-3.
- [80] N. Hanspal, A. Waghode, V. Nassehi, and R. Wakeman. *Development of a predictive mathematical model for coupled Stokes/Darcy flows in cross-flow membrane filtration*. Chem. Eng. J. 149.1 (2009), pp. 132–142. DOI: 10 . 1016 / j . cej . 2008 . 10 . 012.
- [81] F. H. Harlow and J. E. Welch. *Numerical calculation of time-dependent viscous incompressible flow of fluid with free surface*. Phys. Fluids 8.12 (1965), pp. 2182–2189. DOI: 10 . 1063 / 1 . 1761178.

- [82] G. Harper, J. Liu, S. Tavener, and T. Wildey. *Coupling Arbogast–Correa and Bernardi–Raugel elements to resolve coupled Stokes–Darcy flow problems*. *Comput. Methods Appl. Mech. Eng.* 373 (2021), p. 113469. DOI: 10.1016/j.cma.2020.113469.
- [83] S. Hasan, V. Niasar, N. K. Karadimitriou, J. R. A. Godinho, N. T. Vo, S. An, A. Rabbani, and H. Steeb. *Direct characterization of solute transport in unsaturated porous media using fast X-ray synchrotron microtomography*. *Proc. Natl. Acad. Sci. U.S.A.* 117 (38 2020), pp. 23443–23449. DOI: 10.1073/pnas.2011716117.
- [84] S. M. Hassanizadeh and W. G. Gray. *Boundary and interface conditions in porous media*. *Water Resour. Res.* 25.7 (1989), pp. 1705–1715. DOI: 10.1029/WR025i007p01705.
- [85] S. M. Hassanizadeh and T. Leijnse. *On the modeling of brine transport in porous media*. *Water Resour. Res.* 24.3 (1988), pp. 321–330. DOI: 10.1029/WR024i003p00321.
- [86] F. Hecht. *New development in FREEFEM++*. *J. Numer. Math.* 20 (2012), pp. 251–265. DOI: 10.1515/jnum-2012-0013.
- [87] R. Helmig. *Multiphase flow and transport processes in the subsurface: a contribution to the modeling of hydrosystems*. Springer-Verlag, 1997.
- [88] P. Henning, M. Oehlberger, and B. Schweizer. *Homogenization of the degenerate two-phase flow equations*. *Math. Models Methods Appl. Sci.* 23.12 (2013), pp. 2323–2352. DOI: 10.1142/S0218202513500334.
- [89] K. E. Holter, M. Kuchta, and K.-A. Mardal. *Robust preconditioning for coupled Stokes–Darcy problems with the Darcy problem in primal form*. *Comput. Math. Appl.* 91 (2021), pp. 53–66. DOI: 10.1016/j.camwa.2020.08.021.
- [90] U. Hornung. *Homogenization and porous media*. Springer, 1997. DOI: 10.1007/978-1-4612-1920-0.
- [91] Y. Hou and Y. Qin. *On the solution of coupled Stokes/Darcy model with Beavers–Joseph interface condition*. *Comput. Math. Appl.* 77.1 (2019), pp. 50–65. DOI: 10.1016/j.camwa.2018.09.011.

- [92] X. Hu, X. Wang, M. Gunzburger, F. Hua, and Y. Cao. *Experimental and computational validation and verification of the Stokes–Darcy and continuum pipe flow models for karst aquifers with dual porosity structure*. *Hydrol. Processes* 26.13 (2012), pp. 2031–2040. DOI: 10.1002/hyp.8308.
- [93] R. Huber and R. Helmig. *Node-centered finite volume discretizations for the numerical simulation of multiphase flow in heterogeneous porous media*. *Comput. Geosci.* 4 (2020), pp. 141–164. DOI: 10.1023/A:1011559916309.
- [94] A. Jackson, I. Rybak, R. Helmig, W. Gray, and C. Miller. *Thermodynamically constrained averaging theory approach for modeling flow and transport phenomena in porous medium systems: 9. transition region models*. *Adv. Water Resour.* 42 (2012), pp. 71–90. DOI: 10.1016/j.advwatres.2012.01.006.
- [95] W. Jäger and A. Mikelić. *On the boundary conditions at the contact interface between a porous medium and a free fluid*. *Ann. Scuola Norm. Sup. Pisa Cl. Sci.* 23.3 (1996), pp. 403–465. URL: [http://www.numdam.org/item/ASNSP\\_1996\\_4\\_23\\_3\\_403\\_0/](http://www.numdam.org/item/ASNSP_1996_4_23_3_403_0/).
- [96] W. Jäger and A. Mikelić. *On the interface boundary condition of Beavers, Joseph, and Saffman*. *SIAM J. Appl. Math.* 60.4 (2000), pp. 1111–1127. DOI: 10.1137/S003613999833678X.
- [97] W. Jäger and A. Mikelić. *Modeling effective interface laws for transport phenomena between an unconfined fluid and a porous medium using homogenization*. *Transp. Porous Media* 78 (2009), pp. 489–508. DOI: 10.1007/s11242-009-9354-9.
- [98] W. Jäger, A. Mikelić, and N. Neuss. *Asymptotic analysis of the laminar viscous flow over a porous bed*. *SIAM J. Sci. Comput.* 22.6 (2001), pp. 2006–2028. DOI: 10.1137/S1064827599360339.
- [99] C. G. Jean-Louis Auriault and Claude Boutin. *A trivariate Clough–Tocher scheme for tetrahedral data*. Wiley-ISTE, 2009. DOI: 10.1002/9780470612033.
- [100] I. P. Jones. *Low reynolds number flow past a porous spherical shell*. *Proc. Camb. Phil. Soc.* 73.1 (1973), pp. 231–238. DOI: 10.1017/S0305004100047642.

- [101] G. Kanschat and B. Rivière. *A strongly conservative finite element method for the coupling of Stokes and Darcy flow*. J. Comput. Phys. 229.17 (2010), pp. 5933–5943. DOI: 10.1016/j.jcp.2010.04.021.
- [102] T. Karper, K.-A. Mardal, and R. Winther. *Unified finite element discretizations of coupled Darcy–Stokes flow*. Numer. Methods Partial Differ. Equations 25.2 (2009), pp. 311–326. DOI: 10.1002/num.20349.
- [103] M. Keskin and N. Ağiralioğlu. *A simplified dynamic model for flood routing in rectangular channels*. J. Hydrol. 202.1 (1997), pp. 302–314. DOI: 10.1016/S0022-1694(97)00072-3.
- [104] J. Kozeny. *Über die kapillare Leitung des Wassers im Boden*. Sitzungsber. Akad. Wiss. Wien 136 (1927), pp. 271–306.
- [105] U. Lācis and S. Bagheri. *A framework for computing effective boundary conditions at the interface between free fluid and a porous medium*. J. Fluid Mech. 812 (2017), pp. 866–889. DOI: 10.1017/jfm.2016.838.
- [106] U. Lācis, Y. Sudhakar, S. Pasche, and S. Bagheri. *Transfer of mass and momentum at rough and porous surfaces*. J. Fluid Mech. 884 (2020), A21, 34. DOI: 10.1017/jfm.2019.897.
- [107] W. Layton, F. Schieweck, and I. Yotov. *Coupling fluid flow with porous media flow*. SIAM J. Numer. Anal. 40.6 (2003), pp. 2195–2218. DOI: 10.1137/S0036142901392766.
- [108] M. Le Bars and M. G. Worster. *Interfacial conditions between a pure fluid and a porous medium: implications for binary alloy solidification*. J. Fluid Mech. 550 (2006), pp. 149–173. DOI: 10.1017/S0022112005007998.
- [109] J.-L. Lions. *Some methods in the mathematical analysis of systems and their control*. Kexue Chubanshe (Science Press), Beijing; Gordon & Breach Science Publishers, New York, 1981.
- [110] J. Lions and E. Magenes. *Non-homogeneous boundary problems and applications*. Springer, 1972.



- [111] K. Lipnikov, D. Vassilev, and I. Yotov. *Discontinuous Galerkin and mimetic finite difference methods for coupled Stokes–Darcy flows on polygonal and polyhedral grids*. Numer. Math. 126.2 (2014), pp. 321–360. DOI: 10.1007/s00211-013-0563-3.
- [112] R. Lipton and M. Avellaneda. *Darcy’s law for slow viscous flow past a stationary array of bubbles*. Proc. Roy. Soc. Edinburgh Sect. A 114.1-2 (1990), pp. 71–79. DOI: 10.1017/S0308210500024276.
- [113] Q. Liu, L. Chen, J. Li, and V. Singh. *Two-dimensional kinematic wave model of overland-flow*. J. Hydrol. 291.1 (2004), pp. 28–41. DOI: 10.1016/j.jhydrol.2003.12.023.
- [114] A. Marciniak-Czochra and A. Mikelić. *Effective pressure interface law for transport phenomena between an unconfined fluid and a porous medium using homogenization*. Multiscale Model. Simul. 10.2 (2012), pp. 285–305. DOI: 10.1137/110838248.
- [115] E. Marušić-Paloka and A. Mikelić. *An error estimate for correctors in the homogenization of the Stokes and the Navier–Stokes equations in a porous medium*. Boll. Unione Mat. Ital. A(7) 10.3 (1996), pp. 661–671.
- [116] W. McMinin and T. Magee. *Principles, methods and applications of the convective drying of foodstuffs*. Food Bioprod. Process. 77.3 (1999), pp. 175–193. DOI: 10.1205/096030899532466.
- [117] M. Mierzwiczak, A. Fraska, and J. K. Grabski. *Determination of the slip constant in the Beavers–Joseph experiment for laminar fluid flow through porous media using a meshless method*. Math. Probl. Eng. (2019), Art. ID 1494215, 12. DOI: 10.1155/2019/1494215.
- [118] A. Mikelić. *Homogenization of nonstationary Navier–Stokes equations in a domain with a grained boundary*. Ann. Mat. Pura Appl. (4) 158 (1991), pp. 167–179. DOI: 10.1007/BF01759303.
- [119] A. Mikelić and I. Aganović. *Homogenization in a porous media under a nonhomogeneous boundary condition*. Boll. U.M.I. 7 (1987), pp. 171–180.

- [120] A. Mikelić. *Homogenization theory and applications to filtration through porous media. Filtration in porous media and industrial application (Cetraro, 1998)*. Vol. 1734. Lecture Notes in Math. Springer, Berlin, 2000, pp. 127–214. DOI: 10.1007/BFb0103977.
- [121] L. Mosser, O. Dubrule, and M. J. Blunt. *Reconstruction of three-dimensional porous media using generative adversarial neural networks*. Phys. Rev. E 96 (4 2017), p. 043309. DOI: 10.1103/PhysRevE.96.043309.
- [122] M. Mu and J. Xu. *A two-grid method of a mixed Stokes–Darcy model for coupling fluid flow with porous media flow*. SIAM J. Numer. Anal. 45.5 (2007), pp. 1801–1813. DOI: 10.1137/050637820.
- [123] S. B. Naqvi and A. Bottaro. *Interfacial conditions between a free-fluid region and a porous medium*. Int. J. Multiph. Flow 141 (2021), p. 103585. DOI: 10.1016/j.ijmultiphaseflow.2021.103585.
- [124] A. I. Nazarov and S. I. Repin. *Exact constants in Poincaré type inequalities for functions with zero mean boundary traces*. Math. Meth. Appl. Sci. 38.15 (2015), pp. 3195–3207. DOI: 10.1002/mma.3290.
- [125] G. Neale and W. Nader. *Practical significance of Brinkman’s extension of Darcy’s law: coupled parallel flows within a channel and a bounding porous medium*. Can. J. Chem. Eng. 52.4 (1974), pp. 475–478. DOI: 10.1002/cjce.5450520407.
- [126] D. A. Nield. *The Beavers–Joseph boundary condition and related matters: a historical and critical note*. Transp. Porous Media 78 (2009), pp. 537–540. DOI: 10.1007/s11242-009-9344-y.
- [127] J. Ochoa-Tapia and S. Whitaker. *Momentum transfer at the boundary between a porous medium and a homogeneous fluid – I. theoretical development*. Int. J. Heat Mass Transfer 38.14 (1995), pp. 2635–2646. DOI: 10.1016/0017-9310(94)00346-w.
- [128] M. Ohlberger and B. Schweizer. *Modelling of interfaces in unsaturated porous media*. Discrete Contin. Dyn. Syst. Special (2007), pp. 794–803.

- [129] D. Or, P. Lehmann, E. Shahraeeni, and N. Shokri. *Advances in soil evaporation physics – a review*. Vadose Zone J. 12.4 (2013), vj2012.0163. DOI: 10.2136/vzj2012.0163.
- [130] G. F. Pinder and M. A. Celia. *Subsurface hydrology*. John Wiley & Sons, 2006.
- [131] A. Quarteroni, A. Manzoni, and C. Vergara. *The cardiovascular system: mathematical modelling, numerical algorithms and clinical applications*. 26 (2017), pp. 365–590. DOI: 10.1017/S0962492917000046.
- [132] A. Quarteroni. *Elements of functional analysis. Numerical models for differential problems*. Springer Milan, 2014, pp. 11–29. DOI: 10.1007/978-88-470-5522-3\_2.
- [133] R. R. Hernandez-Rodriguez, B. Goyeau, P. Angot, and J. A. Ochoa-Tapia. *Average velocity profile between a fluid layer and a porous medium: Brinkman boundary layer*. Rev. Mex. Ing. Chim. 19 (2020), pp. 495–520. DOI: 10.24275/rmiq/Fen843.
- [134] L. A. Richards. *Capillary conduction of liquids through porous mediums*. J. Appl. Phys. 1.5 (1931), pp. 318–333. DOI: 10.1063/1.1745010.
- [135] A. Rinehart, U. Lācis, and S. Bagheri. “The Brinkman viscosity for porous media exposed to a free flow”. 2021. URL: <https://arxiv.org/abs/2106.01879>.
- [136] B. Rivière. *Analysis of a discontinuous finite element method for the coupled Stokes and Darcy problems*. J. Sci. Comput. 22/23 (2005), pp. 479–500. DOI: 10.1007/s10915-004-4147-3.
- [137] B. Rivière and I. Yotov. *Locally conservative coupling of Stokes and Darcy flows*. SIAM J. Numer. Anal. 42.5 (2005), pp. 1959–1977. DOI: 10.1137/S0036142903427640.
- [138] M. Rozložník. *Saddle-point problems and their iterative solution*. Nečas Center Series. Birkhäuser/Springer, Cham, 2018. DOI: 10.1007/978-3-030-01431-5.
- [139] H. Rui and Y. Sun. *A MAC scheme for coupled Stokes–Darcy equations on non-uniform grids*. J. Sci. Comput. 82 (2020), p. 79. DOI: 10.1007/s10915-020-01181-5.

- [140] I. Rybak. *Mathematical modeling of coupled free flow and porous medium systems*. University of Stuttgart, Germany, 2015.
- [141] I. Rybak, J. Magiera, R. Helmig, and C. Rohde. *Multirate time integration for coupled saturated/unsaturated porous medium and free flow systems*. *Comput. Geosci.* 19 (2015), pp. 299–309. DOI: 10.1007/s10596-015-9469-8.
- [142] P. G. Saffman. *On the boundary condition at the surface of a porous medium*. *Stud. Appl. Math.* 50.2 (1971), pp. 93–101. DOI: 10.1002/sapm197150293.
- [143] E. Sanchez-Palencia. *Non-homogeneous media and vibration theory*. Springer, 1980.
- [144] M. Schneider, D. Gläser, K. Weishaupt, E. Coltman, B. Flemisch, and R. Helmig. “Coupling staggered-grid and vertex-centered finite-volume methods for coupled porous-medium free-flow problems”. 2021. URL: <https://arxiv.org/abs/2112.11089>.
- [145] M. Schneider, K. Weishaupt, D. Gläser, W. M. Boon, and R. Helmig. *Coupling staggered-grid and mpfa finite volume methods for free flow/porous-medium flow problems*. *J.Comput. Phys.* 401 (2020), p. 109012. DOI: 10.1016/j.jcp.2019.109012.
- [146] B. Schweizer. *Homogenization of a fluid problem with a free boundary*. *Comm. Pure Appl. Math.* 53.9 (2000), pp. 1118–1152. DOI: 10.1002/1097-0312(200009)53:9<1153::AID-CPA4>3.0.CO;2-R.
- [147] M. Shiue, K. C. Ong, and M. Lai. *Convergence of the MAC scheme for the stokes/ darcy coupling problem*. *J. Sci. Comput.* 76.2 (2018), pp. 1216–1251. DOI: 10.1007/s10915-018-0660-7.
- [148] J. H. Smith and J. A. Humphrey. *Interstitial transport and transvascular fluid exchange during infusion into brain and tumor tissue*. *Microvasc. Res.* 73.1 (2007), pp. 58–73. DOI: 10.1016/j.mvr.2006.07.001.

- [149] P. Sochala, A. Ern, and S. Piperno. *Mass conservative BDF-discontinuous Galerkin/explicit finite volume schemes for coupling subsurface and overland flows*. *Comput. Methods Appl. Mech. Engrg.* 198.27-29 (2009), pp. 2122–2136. DOI: 10 . 1016 / j . cma . 2009 . 02 . 024.
- [150] R. Song, Y. Wang, J. Liu, M. Cui, and Y. Lei. *Comparative analysis on pore-scale permeability prediction on micro-ct images of rock using numerical and empirical approaches*. *Energy Sci. Eng.* 7.6 (2019), pp. 2842–2854. DOI: 10 . 1002 / ese3 . 465.
- [151] A. Stefansson, P. R. Di Palma, N. Guyennon, A. Parmigiani, C. Huber, F. Heße, and E. Romano. *Impact of synthetic porous medium geometric properties on solute transport using direct 3d pore-scale simulations*. *Geofluids Volume 2019* (2019), p. 6810467. DOI: 10 . 1155 / 2019 / 6810467.
- [152] Y. Sudhakar, U. Laxis, S. Pasche, and S. Bagheri. *Higher-order homogenized boundary conditions for flows over rough and porous surfaces*. *Transp. Porous Media* 136 (2021), pp. 1–42. DOI: 10 . 1007 / s11242-020-01495-w.
- [153] L. Tartar. *Incompressible fluid in a porous medium - convergence of the homogenization process*. Springer-Verlag, Berlin Appendix of [143], 1979.
- [154] L. Tartar. *An introduction to sobolev spaces and interpolation spaces*. Lecture Notes of the Unione Matematica Italiana, 2007.
- [155] R. Temam. *Navier–Stokes equations*. Revised. Vol. 2. *Studies in Mathematics and its Applications*. North-Holland Publishing Co., Amsterdam-New York, 1979.
- [156] A. Terzis, I. Zarikos, K. Weishaupt, G. Yang, X. Chu, R. Helmig, and B. Weigand. *Microscopic velocity field measurements inside a regular porous medium adjacent to a low reynolds number channel flow*. *Phys. Fluids* 31.4 (2019), p. 042001. DOI: 10 . 1063 / 1 . 5092169.
- [157] J. M. Urquiza, D. N’Dri, A. Garon, and M. C. Delfour. *Coupling Stokes and Darcy equations*. *Appl. Numer. Math.* 58.5 (2008), pp. 525–538. DOI: 10 . 1016 / j . apnum . 2006 . 12 . 006.

- [158] P. Verboven, D. Flick, B. Nicolai, and G. Alvarez. *Modelling transport phenomena in refrigerated food bulks, packages and stacks: basics and advances*. Int. J. Refrig. 29.6 (2006), pp. 985–997. DOI: 10.1016/j.ijrefrig.2005.12.010.
- [159] C. Vreugdenhil. *Numerical methods for shallow-water flow*. Kluwer Academic Publishers, 1994.
- [160] G. Wang, F. Wang, and Y. He. *A divergence free weak virtual element method for the stokes–darcy problem on general meshes*. Comput. Methods Appl. Mech. Eng. 344 (2019), pp. 998–1020. DOI: 10.1016/j.cma.2018.10.022.
- [161] K. Weishaupt, A. Terzis, I. Zarikos, G. Yang, B. Flemisch, D. A. M. de Winter, and R. Helmig. *A hybrid-dimensional coupled pore-network/free-flow model including pore-scale slip and its application to a micromodel experiment*. Transp. Porous Media 135.1 (2020), pp. 243–270. DOI: 10.1007/s11242-020-01477-y.
- [162] K. Weishaupt, V. Joekar-Niasar, and R. Helmig. *An efficient coupling of free flow and porous media flow using the pore-network modeling approach*. J. Comput. Phys. 1 (2019), p. 100011. DOI: 10.1016/j.jcp.2019.100011.
- [163] S. Whitaker. *The method of volume averaging*. Vol. 13. Springer Netherlands, 1999. DOI: 10.1007/978-94-017-3389-2.
- [164] D. Wildenschild and A. P. Sheppard. *X-ray imaging and analysis techniques for quantifying pore-scale structure and processes in subsurface porous medium systems*. Adv. Water Resour. 51 (2013), pp. 217–246.
- [165] G. Yang, E. Coltman, K. Weishaupt, A. Terzis, R. Helmig, and B. Weigand. *On the Beavers–Joseph interface condition for non-parallel coupled channel flow over a porous structure at high Reynolds numbers*. Transp. Porous Media 128 (2019), pp. 431–457. DOI: 10.1007/s11242-019-01255-5.
- [166] P. Zunino. *Mathematical and numerical modeling of mass transfer in the vascular system*. Ecole Polytechnique Fédérale de Lausanne, Switzerland, 2002.



## Abstract

Coupled free-flow and porous-medium flow systems occur in nature as well as in a wide range of technical applications, for example, groundwater filtration or water management in fuel cells. The free flow is typically described by the Stokes equations and the flow through the porous medium by Darcy's law. One of the major challenges in modeling such flow systems is the accurate coupling of both mathematical models across the fluid–porous interface. Traditional coupling concepts are developed for unidirectional flows, parallel or perpendicular to the porous layer, however, they are not applicable if arbitrary flow directions occur, such as in industrial filtration. This fact significantly restricts the amount of applications that can be accurately modeled. Therefore, new interface conditions accounting for arbitrary flows in Stokes–Darcy systems are needed.

In this dissertation, we develop generalized coupling conditions that are valid for arbitrary flow directions to the fluid–porous interface. These conditions are rigorously derived using homogenization with two-scale asymptotic expansions and boundary layer theory. All coefficients appearing in the generalized interface conditions are computed based on the pore geometry in the vicinity of the interface. This is a great advantage over the traditionally applied coupling conditions, which are limited to unidirectional flows and contain unknown model parameters that must be fitted before the conditions can be used in numerical simulations. We derive the variational formulation of the Stokes–Darcy problem with the newly derived coupling conditions and prove existence and uniqueness of a weak solution. We develop a finite volume discretization scheme to solve the coupled problem numerically and employ finite element methods to compute all effective model parameters and to solve the pore-scale problem. To validate the generalized coupling conditions we compare microscale and macroscale numerical simulation results. We demonstrate that the derived interface conditions are more accurate than the classical conditions in case of unidirectional flows, and that they are valid in case of arbitrary flow directions to the interface, whereas the classical conditions fail.